

R-10-71

Darcy Tools version 3.4

Verification, validation and demonstration

Urban Svensson, Computer-aided Fluid Engineering AB

December 2010

Svensk Kärnbränslehantering AB

Swedish Nuclear Fuel
and Waste Management Co

Box 250, SE-101 24 Stockholm
Phone +46 8 459 84 00



ISSN 1402-3091

SKB R-10-71

Darcy Tools version 3.4

Verification, validation and demonstration

Urban Svensson, Computer-aided Fluid Engineering AB

December 2010

This report concerns a study which was conducted for SKB. The conclusions and viewpoints presented in the report are those of the author. SKB may draw modified conclusions, based on additional literature sources and/or expert opinions.

A pdf version of this document can be downloaded from www.skb.se.

Contents

1	Introduction	5
1.1	Background	5
1.2	Objective and outline	5
2	Confidence building	7
2.1	Background	7
2.2	General aspects	7
2.3	DarcyTools	7
2.4	Confidence building	8
3	Verification	9
3.1	Cases considered	9
3.2	Objectives of the verification study	9
4	Validation	11
4.1	Introduction	11
4.2	Validation versus calibration	11
4.3	Cases considered	12
5	Demonstration	13
6	Concluding remarks	15
7	References	17
Appendix 1	Verification cases	21
	Case A1: One-dimensional transient diffusion	21
	Case A2: One-dimensional steady advection/diffusion	23
	Case A3: Two-dimensional pressure problem	26
	Case A4: Tests of grid, fractures as objects	28
	Case A5: Test of grid, cell removal	29
	Case B1: Regional groundwater circulation, /Tóth 1963/	30
	Case B2: Steady groundwater table	32
	Case B3: Theis problem	34
	Case B4: Water inflow to a circular tunnel	36
	Case B5: Specific yield, /Neuman 1975/	38
	Case B6: Transient groundwater table	40
	Case B7: Water inflow to a grouted tunnel	42
	Case C1: Three fractures in a 2D domain	45
	Case C2: A multi-fracture fracture zone	47
	Case C3: Single fracture in a box	49
	Case C4: Many fractures in a box	52
	Case C5: Percolation theory	54
	Case C6: Diffusion in a dead-end fracture	57
	Case C7: Matrix-fracture temperature problem	60
	Case D1: Taylor dispersion, PARTRACK	63
	Case D2: Breakthrough curve, PARTRACK	65
	Case D3: Breakthrough curve, adv/diff eqn	70
	Case D4: Seven fractures in a 2D domain, PARTRACK	72
	Case D5: Three fractures in a 2D domain	74
	Case D6: Single fracture in a box, PARTRACK	77
	Case E1: Henry's problem	79
	Case E2: Two-fluid problem	82
	Case E3: Coupled temperature and salinity fields	85
	Case E4: Upconing	87
	Case E5: The floating island	89

Appendix 2	Case V1: A site scale validation	93
	Case V2: A laboratory scale validation	107
	Case V3: A repository scale validation	116
	Case V4: An experimental scale validation	124
	Case V5: A pump test	131
Appendix 3	Case De0: The base case	143
	Case De1: The open repository	147
	Case De2: Transport from a canister to ground level	154
	Case De3: Transient paleo simulation	159
	Case De4: A steady state pump test	163
	Case De5: Hydration of the tunnel backfill	168
	Case De6: Surface hydrology	174
	Case De7: Glaciation	181

1 Introduction

1.1 Background

DarcyTools is a computer code for simulation of flow and transport in porous and/or fractured media. The fractured media in mind is a fractured rock and the porous media the soil cover on the top of the rock; it is hence groundwater flows, which is the class of flows in mind.

A number of novel methods and features form the present version of DarcyTools. In the verification studies, these methods are evaluated by comparisons with analytical solutions for idealized situations. The five verification groups (see Table 3-1 below), thus reflect the scope of DarcyTools.

The present report will focus on the Verification, Validation and Demonstration of DarcyTools. Two accompanying reports cover other aspects:

- Concepts, Methods and Equations, /Svensson et al. 2010/ (Hereafter denoted Report 1).
- User's Guide, /Svensson and Ferry 2010/ (Hereafter denoted Report 2).

1.2 Objective and outline

The objective of this report is to compile all verification, validation and demonstration studies that have been carried out so far. After some brief introductory sections, all cases will be reported in Appendix 1 (verification cases), Appendix 2 (validation cases) and Appendix 3 (demonstration cases).

2 Confidence building

2.1 Background

During the last twenty years CFD (Computational Fluid Dynamics) has become a standard simulation tool in most engineering problems, dealing with groundwater flow and transport. This development has been driven by readily available software packages and the significant increase in affordable computer speed and memory capacity. CFD is however not a simple technique to use; generally speaking a basic understanding of several subjects like fluid mechanics, numerical analysis and computer software programming is required. For groundwater modelling an understanding of hydrogeology is of course also needed.

2.2 General aspects

In a recent project, ERCOFTAC /Casey and Wintergerste 2000/, guidelines for CFD simulations are discussed and summarised. Partly based on this report, the following main sources of errors and uncertainties in groundwater simulations can be identified:

- Mathematical model. The mathematical model does not describe the real flow exactly. For example, in textbooks the approximations inherent in the Darcy equation are often analyzed and listed. Another often used approximation is that the water is incompressible.
- Discretization. Numerical solutions are performed on a grid in space and time. The difference between the solution on this grid and the exact solution of the modelled equations is called the discretization error.
- Convergence and round-off errors. Typically a CFD simulation involves iterative procedures. Convergence errors occur because these iterations are stopped by a certain criteria before they are completed. Round-off errors are due to the limited number of digits when a number is stored in the computer memory.
- Application uncertainties. These include uncertainties about the geometry of the domain (for example a fracture network), boundary conditions, fluid properties, etc.
- Code errors. It is difficult to get software “bug-free”.
- User errors. These are the errors that result from mistakes or carelessness by the user.

More points could have been listed (errors in post processing, interpretation of results, etc) but the list given probably gives the most important ones. In this context it may be of interest to refer to the following definitions (from ERCOFTAC):

Error: A recognizable deficiency that is not due to lack of knowledge.

Uncertainty: A potential deficiency that is due to lack of knowledge.

2.3 DarcyTools


As DarcyTools is a groundwater code, one should view the list of points given from this perspective. The significance of the different points may still vary depending on the modelling approach chosen and the problem studied. Here we mainly concern ourselves with a fracture network, as represented in a continuum model. All of the above discussed errors and uncertainties may still be relevant to consider and it is not easy to neglect (or set priority to) any of the points. For the modelling approach chosen it is however expected that the “quality” of a simulation is strongly dependent on how well the fracture network is represented in the continuum model. The fracture network is however only partly known (geometry, properties, etc) and we therefore need to consider the uncertainty introduced. For the class of flows considered, one can hence conclude that the main uncertainty is due to the incomplete knowledge of the fracture network, while a major technical issue is how a fracture network should be represented in a continuum model.

2.4 Confidence building

The question whether a computer code is credible or not and methods to answer this question are given in an issue of the /AIAA Journal 1998/. Based on the papers presented, Table 2-1 has been created. The table is an attempt to illustrate the actions involved in the confidence building process. A few comments to the table:

- The order (from top to bottom) is essential. It is not possible to achieve certification without having demonstrated verification and validation.
- There is a consensus in the literature about the definitions of verification and validation. Additional steps and actions in the confidence building are still open to discussion.
- Some authors emphasize that it is important to distinguish between confidence building in a computer code and in a specific application. Related to this issue is the concept “fitness for purpose”. It is for example of little value to have a very accurate numerical solution if the algorithm is so slow that the code is impractical for its intended use.

Table 2-1. Processes and actions involved in confidence building.

C o n f i d e n c e b u i l d i n g 	Process	Definition	Action
	Verification	Demonstrate that the equations are solved correctly.	Comparison with analytical solutions and other models.
	Validation	Demonstrate that the right equations are solved.	Comparison with measurements (laboratory and field data).
	Certification	Assess whether the right things are done and whether they are done right.	Evaluate software construction and working procedures.
More (QA-systems, wide range of applications, publications in international journals, etc).			

3 Verification

3.1 Cases considered

The verification cases performed can be found in Appendix 1 and are summarized in Table 3-1.

All cases tested show “good result”, i.e. the comparison with the corresponding analytical solution, or another model study, is satisfactory; the reader is referred to the cases to study the details.

3.2 Objectives of the verification study

A few words may however be needed to explain the objectives when selecting the test cases and the way the comparisons have been carried out.

- The test cases should include one, two and three dimensional, steady and transient cases.
- A wide range of relevant physical processes should be included, i.e. density stratification, unsaturated zones, storativity effects, etc.
- The representation of fractures in a continuum model is a key feature of DarcyTools and should be well covered by the test cases.

Some verification studies described in the literature are focused on grid refinement studies. Here the listed objectives have however been considered to be more important with the “fitness for purpose” argument in mind.

Table 3-1. Compilation of verification cases.

Group	Case	Comment
A. Numerical methods	A1. One dimensional transient diffusion	This group of cases intends to show that the numerical methods work as expected.
	A2. One dimensional steady advection/diffusion	
	A3. Two-dimensional pressure problem	
	A4. Test of grid, fractures as objects	
	A5. Test of grid, cell removal	
B. Porous media	B1. Regional groundwater circulation	This group considers some classical hydrogeological test cases.
	B2. Steady groundwater table	
	B3. Theis problem	
	B4. Water inflow to a circular tunnel	
	B5. Specific yield, /Neuman 1975/	
	B6. Transient groundwater table	
	B7. Water inflow to a grouted tunnel.	
C. Fractured media	C1. Three fractures in a two dimensional domain	This group of cases deals with the representation of fractures in a continuum model.
	C2. A multi-fracture fracture zone	
	C3. Single fracture in a box	
	C4. Many fractures in a box	
	C5. Percolation theory	
	C6. Diffusion in a dead-end fracture	
	C7. Matrix-fracture temperature problem	
D. Transport and dispersion	D1. Taylor dispersion	This group considers transport, retention, dispersion and particle tracking cases.
	D2. Breakthrough curve, PARTRACK	
	D3. Breakthrough curve, adv/diff eqn.	
	D4. Seven fractures in a 2D domain, PARTRACK	
	D5. Three fractures in a 2D domain, PARTRACK	
	D6. Single fracture in a box, PARTRACK	
E. Buoyancy effects	E1. Henry's problem	This group considers comparisons where density stratification, due to salinity and temperature gradients, is a key factor.
	E2. Two fluid problem	
	E3. Coupled temperature- salinity fields	
	E4. Upconing	
	E5. The floating island	

4 Validation

4.1 Introduction

As validation should be concerned with comparisons with measurements and DarcyTools has not yet been widely used for real world applications, it is not surprising that very few such comparisons can be reported at this stage. However, as discussed in Report 1, it is relevant to include cases that were carried out with PHOENICS as the equation solver, as it has been carefully evaluated that the two solvers give very similar solutions. Note that the descriptions of the fracture network (GEHYCO) and other descriptions of physical processes are in most respects the same in the PHOENICS /Spalding 1981/ cases to be discussed, as in the present version of DarcyTools.

4.2 Validation versus calibration

For simulations of flow and transport in a fractured rock, it is difficult to separate the steps “validation” and “calibration”. To discuss this, we first need to define “calibration” (following /AIAA 1998/):

- **Calibration** is the process of tuning a code, in order to improve its prediction of global quantities, for realistic geometries, of design interest.

If we require that validation studies should be concerned with comparisons with field measurements, we also need to accept that these measurements are obtained in conditions that are to a large extent unknown. We do not know the fracture network (its geometry, fracture properties, boundary conditions, etc). We therefore have to accept the following tentative definition of validation:

- For the flow and transport in a fractured rock, **validation** of a simulation can be claimed if calibration can be performed with all adjustable parameters within realistic limits.

This definition immediately raises the question “what are realistic limits?”. For major deformation zones we may be able to define bounds for properties (thickness, transmissivity, porosity, etc) and these bounds then define the “realistic limits”. However, for most applications properties and boundary conditions can not be given with error bounds and we have to accept the admittedly weak definition given. Flow and transport around a repository introduce a number of special considerations (for a discussion see /Cliffe et al. 1998/). As one example we may mention the analysis of the impact of an inland ice on the performance of a repository. It is not possible to validate a model, by comparisons with field data, for such a case; still predictions are needed.

4.3 Cases considered

Validation cases are described in Appendix 2 and summarized in Table 4-1. As can be seen the validation cases are taken from calibration studies in various projects. We thus follow the definition of validation given above.

Table 4-1. Compilation of validation cases.

Case	Project (Reference)	Comments
A site scale validation (Case V1)	Impact of the tunnel construction on the groundwater system at Äspö. Task #5 /Svensson et al. 2002/.	Calibration focuses on: <ul style="list-style-type: none"> • Groundwater table. • Pressure in boreholes. • Kinematic porosity. • Water composition. Code: PHOENICS.
A laboratory scale validation (Case V2)	A laboratory scale analysis of flow and salinity distribution in the Äspö area, /Svensson 1999/.	Calibration focuses on: <ul style="list-style-type: none"> • Fracture transmissivities. • Pressure in boreholes. • Conductivity distributions. Code: PHOENICS.
A repository scale validation (Case V3)	Prototype Repository. Groundwater flow, pressure and salinity distributions around the Prototype Repository. Continuum model No1, /Svensson 2001/.	Calibration focuses on: <ul style="list-style-type: none"> • Tunnel inflows (skin). • Pressure in boreholes. • Conductivity distributions. Code: DarcyTools.
An experimental scale validation (Case V4)	Simulation of tracer transport considering both experimental and natural, i.e. long, time scales, /Svensson and Follin 2004/.	Calibration focuses on: <ul style="list-style-type: none"> • PARTRACK. • Sorbing and non-sorbing tracer retention. Code: DarcyTools.
A pump test (Case V5)	The Olkiluoto site, Finland. <ul style="list-style-type: none"> • Numerical simulations of the pump tests in boreholes KR14-KR18. Äspö Task Force; Task7B, /Svensson 2010/. 	Calibration focuses on: <ul style="list-style-type: none"> • Pump tests. • Representation of boreholes in a large scale model. Code: DarcyTools.

5 Demonstration

A set of demonstration cases has been developed. The main objective of the demo cases is to provide starting points for site models of various kinds (surface hydrology, open repository, glaciations, etc). All cases have a common base with respect to the computational domain and the fracture network. Another common feature is that no input files are required; all set-ups are hence easy to run and understand.

Demonstration cases are described in Appendix 3 and summarized in Table 5-1. Case De0 gives the common base for all cases.

Table 5-1. Compilation of demonstration cases.

Case	Comments
The base case (Case De0)	Provides the common features of all demo cases.
The open repository (Case De1)	Illustrates a wide range of issues relevant for an open repository.
Transport from a canister to ground level (Case De2)	Trajectories from a single canister to ground level are calculated.
Transient paleo simulation (Case De3)	The transient development of the salinity field during the last 10 000 years is studied.
A steady state pump test (Case De4)	It is shown how pumped and observation boreholes can be simulated.
Hydration of the tunnel backfill (Case De5)	A simple model to simulate the transient hydration of the tunnel backfill is illustrated.
Surface hydrology (Case De6)	The coupled surface ground water problem is solved.
Glaciation (Case De7)	The flow around a canister is related to an advancing inland ice.

6 Concluding remarks

It is clear from Chapter 2 that the process of confidence building is complex and involves many aspects. The bottom line is if a particular simulation is credible or not. The computer code, and its verification and validation, is of course a key factor when credibility is judged, but the user of the code is also important. CFD simulations are still far from routine calculations and the modeller normally takes a number of decisions when formulating the problem conceptually and mathematically. The “credibility of the modeller” is hence also a factor to consider.

The number and range of verification, validation and demonstration cases presented is a good indication of the qualities of DarcyTools. More cases are not urgently needed; real world applications would however contribute to the confidence building. As DarcyTools is one of the codes used for the SKB Site Investigations, such applications are now emerging.

7 References

SKB's (Svensk Kärnbränslehantering AB) publications can be found at www.skb.se/publications.

- AIAA Journal, 1998.** Special issue. Vol 36, No 5. The American Institute of Aeronautics and Astronautics.
- Barten W, 1996.** Linear response concept combining advection and limited rock matrix diffusion in a fracture network transport model. *Water Resources Research*, 32, pp 3285–3296.
- Bour O, Davy P, 1998.** On the connectivity of three-dimensional fault networks. *Water Resources Research*, 34, pp 2611–2622.
- Börgesson L, Fälth B, Hernelind J, 2006.** Water saturation phase of the buffer and backfill in the KBS-3V concept. Special emphasis given to the influence of the backfill on the wetting of the buffer. SKB TR-06-14, Svensk Kärnbränslehantering AB.
- Casey M, Wintergerste T (eds), 2000.** Best practice guidelines. ERCOFTAC Special Interest Group on “Quality and Trust in Industrial CFD”.
- Charlaix E, Guyon E, Rivier N, 1984.** A criterion for percolation threshold in a random array of plates. *Solid State Communications*, 50, pp 999–1002.
- Claesson J, Hellström G, Probert T, 1992.** Buoyancy flow in fractured rock with a salt gradient in the groundwater. A second study of coupled salt and thermal buoyancy. SKB TR 92-41, Svensk Kärnbränslehantering AB.
- Cliffe K A, Morris S T, Porter J D, 1998.** Assessment model validity document. NAMMU: A program for calculating groundwater flow and transport through porous media. SKB R-99-51, Svensk Kärnbränslehantering AB.
- Cvetkovic V, Selroos J O, Cheng H, 1999.** Transport of reactive tracers in rock fractures. *Journal of Fluid Mechanics*, 378, pp 335–356.
- Domenico P A, Schwartz F W, 1990.** *Physical and Chemical Hydrogeology*. New York: Wiley.
- Elert M, Svensson H, 1999.** Äspö Hard Rock Laboratory. Deconvolution of breakthrough curves from TRUE-1 tracer tests (STT-1 and STT-1b) with sorbing tracers. Äspö Task Force, Task 4E. SKB IPR-99-35, Svensk Kärnbränslehantering AB.
- El Tani M, 2003.** Circular tunnel in a semi-infinite aquifer. *Tunneling and Underground Space Technology*, 18, pp 49–55.
- Fetter C W, 1994.** *Applied Hydrogeology*. 3rd ed. Upper Saddle River: Prentice Hall.
- Follin S, Hermanson J, 1996.** A discrete fracture network model of the Äspö TBM tunnel rock mass. SKB AR D-97-001, Svensk Kärnbränslehantering AB.
- Forsmark T, Rhén I, 1999.** Äspö Hard Rock Laboratory. Prototype repository. Hydrogeology interference test campaign 1 after drill campaign 3. SKB IPR-00-07, Svensk Kärnbränslehantering AB.
- Forsmark T, Rhén I, Andersson C, 2001.** Äspö Hard Rock Laboratory. Prototype repository. Hydrology – deposition- and lead-through boreholes: inflow measurements, hydraulic responses and hydraulic tests. SKB IPR-00-33, Svensk Kärnbränslehantering AB.
- Gurban I, Laaksoharju M, Andersson C, 1998.** Influences of the tunnel construction on the groundwater chemistry at Äspö. SKB TN-98-16g, Svensk Kärnbränslehantering AB.
- Haggerty R, McKenna S A, Meigs L C, 2000.** On the late-time behavior of tracer test breakthrough curves. *Water Resources Research*, 36, pp 3467–3479.
- Hellström G, Tsang C-F, Claesson J, 1988.** Buoyancy flow at a two-fluid interface in a porous medium: Analytical studies. *Water Resources Research*, 24, pp 493–506.
- La Pointe P R, 1994.** Evaluation of stationary and non-stationary geostatistical models for inferring hydraulic conductivity values at Äspö. SKB TR 94-22, Svensk Kärnbränslehantering AB.

- Neretnieks I, 2002.** A stochastic multi-channel model for solute transport - analysis of tracer tests in fractured rock. *Journal of Contaminant Hydrology*, 55, pp 175–211.
- Neuman S P, 1975.** Analysis of pumping tests data from anisotropic unconfined aquifers considering delayed gravity response. *Water Resources Research*, 11, pp 329–342.
- Painter S, 1999.** Long-range spatial dependence in fractured rock. Empirical evidence and implications for tracer transport. SKB R-00-03, Svensk Kärnbränslehantering AB.
- Park Y-J, Lee K-K, 1999.** Analytical solutions for solute transfer characteristics at continuous fracture junctions. *Water Resources Research*, 35, pp 1531–1537.
- Probert T, Claesson J, 1997.** Heat as a tracer in fractured rock. SKB Progress Report HRL-97-29, Svensk Kärnbränslehantering AB.
- Raudkivi A J, Callander R A, 1976.** Analysis of groundwater flow. London: Arnold.
- Rhén I, Forsmark T, 2000.** Äspö Hard Rock Laboratory. High-permeability features (HPF). SKB IPR-00-02, Svensk Kärnbränslehantering AB.
- Rhén I (ed), Gustafson G, Stanfors R, Wikberg P, 1997.** Äspö HRL – Geoscientific evaluation 1997/5. Models based on site characterization 1986–1995. SKB TR 97-06, Svensk Kärnbränslehantering AB.
- Robinson P C, 1984.** Numerical calculations of critical densities for lines and planes. *Journal of Physics A: Mathematical and General*, 17, pp 2823–2830.
- Sahimi M, 1995.** Flow and transport in porous media and fractured rock: from classical methods to modern approaches. Weinheim: VCH.
- Ségol G, 1994.** Classic groundwater simulations. Englewood Cliffs, NJ: PTR Prentice Hall.
- Stigsson M, Outters N, Hermanson J, 2000.** Äspö Hard Rock Laboratory. Prototype Repository. Hydraulic DFN model no:2. SKB PR IPR-01-39, Svensk Kärnbränslehantering AB.
- Svensson U, 1999.** A laboratory scale analysis of groundwater flow and salinity distribution in the Äspö area. SKB TR-99-24, Svensk Kärnbränslehantering AB.
- Svensson U, 2001.** Äspö Hard Rock Laboratory. Prototype Repository. Groundwater flow, pressure and salinity distributions around the Prototype Repository. Continuum model No 1. SKB IPR-01-40, Svensk Kärnbränslehantering AB.
- Svensson U, 2006.** The Forsmark repository. Modelling changes in flow, pressure and salinity fields, due to a repository for spent nuclear fuel. SKB R-05-57, Svensk Kärnbränslehantering AB.
- Svensson U, 2010.** Äspö Task Force on modelling of groundwater flow and transport of solutes. Task 7A, 7B and 7C. Numerical simulations of flow and transport at the Olkiluoto site, Finland. SKB P-11-17, Svensk Kärnbränslehantering AB.
- Svensson U, Ferry M, 2010.** DarcyTools, Version 3.4. User's guide. SKB R-10-72, Svensk Kärnbränslehantering AB.
- Svensson U, Follin S, 2004.** Äspö Hard Rock Laboratory. Äspö Task Force. Task 6A, 6B and 6B2. Simulation of tracer transport considering both experimental and natural time scales. SKB IPR-04-42, Svensk Kärnbränslehantering AB.
- Svensson U, Laaksoharju M, Gurban, 2002.** Äspö Hard Rock Laboratory. Impact of the tunnel construction on the groundwater system at Äspö. Task 5. Äspö Task Force on groundwater flow and transport of solutes. SKB IPR-02-45, Svensk Kärnbränslehantering AB.
- Svensson U, Ferry M, Kuylenstierna H-O, 2010.** DarcyTools, Version 3.4. Concepts, methods and equations. SKB R-07-38, Svensk Kärnbränslehantering AB.
- Tóth J A, 1963.** A theoretical analysis of ground-water flow in small drainage basins. *Journal of Geophysical Research*, 68, pp 4795–4811.
- Versteeg H K, Malalasekera W, 1995.** An introduction to computational fluid dynamics: The finite volume method. Harlow: Longman Scientific & Technical.

Verification cases

Case A1: One-dimensional transient diffusion

Introduction

The simplest possible test case is perhaps the one-dimensional transient diffusion problem. In order to relate this problem to fractured rocks, we will choose diffusion coefficients and dimension that describe “diffusive exchange with a dead-end fracture”. However, the chosen simulation parameters are of course of no significance for the test problem, i.e. we may equally well study the non-dimensional problem.

The situation considered is outline in Figure A1-1. Initially the concentration in the 1D domain is 1.0. At time = 0.0 the concentration at the left boundary is suddenly reduced to 0.0, while the right boundary is of the zero flux type.

The analytical solution to this problem can be found in /Versteeg and Malalasekera 1995/:

$$C(x,t) = C_0 \frac{4}{\pi} \sum_{n=1}^{\infty} \frac{(-1)^{n+1}}{2n-1} \exp(-\alpha \lambda_n^2 t) \cos(\lambda_n x) \quad (A1-1)$$

where $\lambda_n = \frac{(2n-1)}{2L} \pi$ and α denotes diffusion coefficient, t time and C_0 initial concentration.

The objective of the test case is to verify that DarcyTools can predict one-dimensional transient diffusion correctly.

Numerical simulation

Three different diffusion coefficients will be evaluated. With the coefficients and dimensions chosen, see Table A1-1, the time scale of the problem will be about 10^4 years.

Simulation parameters are summarised in Table A1-1.

Table A1-1. Simulation parameters.

Domain	1D, 10 metres.
Initial condition	$c = 1.0$.
Boundary conditions	$c = 0$ at $x = 0$, $\partial c / \partial x = 0$ at $x = L$, for $t > 0$.
Diffusion coefficients	Varied: 0.5, 1.0 and $2.0 \cdot 10^{-10}$ m ² /s.
Grid	Space: $dx_{max} = 0.05$. Time: $\Delta t = 5$ years, uniform.

Results/discussion

The concentration at $x = L$ was used for the comparison with the analytical solution, see Figure A1-2. A near perfect agreement is found.

Conclusion

DarcyTools can calculate one-dimensional transient diffusion, with high accuracy.

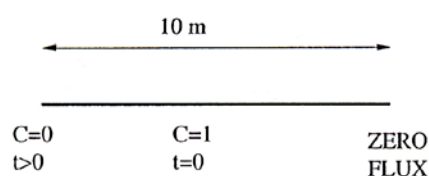


Figure A1-1. One-dimensional transient diffusion. Outline of situation studied.

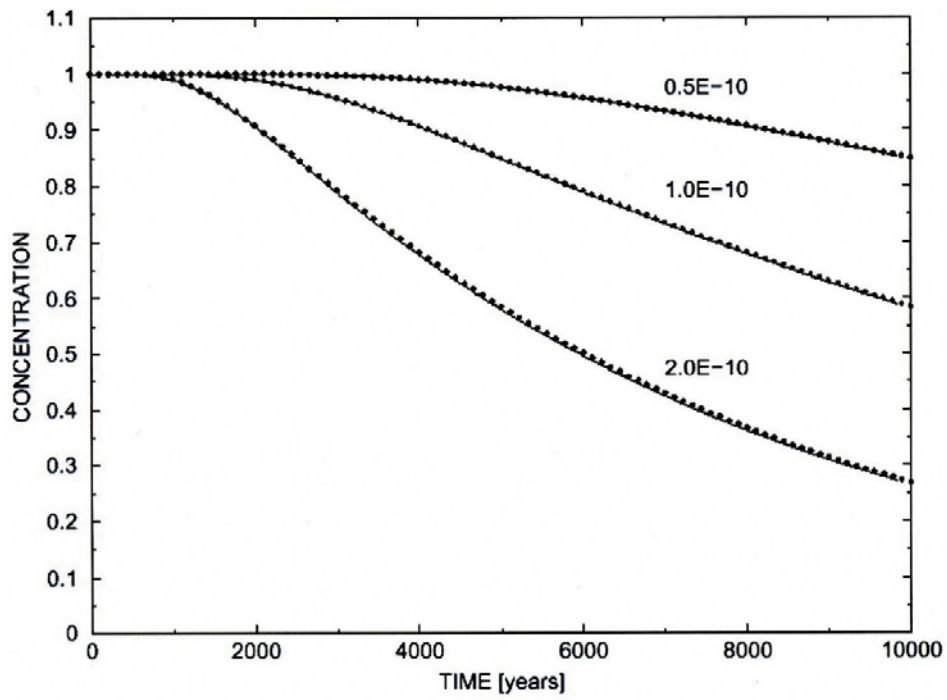


Figure AI-2. One-dimensional transient diffusion. Comparison of the concentration at $x = L$ as given by the analytical solution (—) and DarcyTools (•••).

Case A2: One-dimensional steady advection/diffusion

Introduction

The situation studied is outlined in Figure A2-1. A steady flow, with a velocity of 2 m/s along the x -axis, is convecting a property ϕ . The property ϕ is subject to sources and sinks and is also diffused along the x -axis. The steady state distribution of ϕ is the solution of interest. This distribution is given by the following equation:

$$\frac{\partial}{\partial x}(\rho u \phi) = \frac{\partial}{\partial x} \left(\Gamma \frac{\partial \phi}{\partial x} \right) + s \quad (\text{A2-1})$$

where u denotes velocity, Γ diffusion coefficient and s sources and sinks.

This test case has been presented in the book by /Versteg and Malalasekera 1995/, where also an analytical solution is given. An attempt was made to calculate the ϕ -distribution from the analytical solution. This was however not successful; one possible reason for this is that there may be a printing error in the equations presented. The analytical solution was therefore taken from the graphical presentation, given by /Versteg and Malalasekera 1995/.

The objective of the test case is to see how well DarcyTools predicts the ϕ distribution when both convection and diffusion are significant in the flow direction.

Numerical simulations

Some of data specifying the problem are given in Figure A2-1; a complete account is given in Table A2-1.

Three grid sizes will be tested in order to evaluate if a grid independent solution can be obtained.

Table A2-1. Simulation parameters.

Domain	1D, Length = 1.5 metres
Velocity	2.0 m/s, uniform
Boundary conditions	$\phi = 0$ at $x = 0$, $d\phi/dx = 0$ at $x = L$
Source/Sink	$a = -200$, $b = 100$ (see Figure A2-1)
Properties	$\Gamma = 0.03$ kg/m/s, $\rho = 1$ kg/m ³
Grid	$dx_{\max} = 0.006$, which gives $NX = 256$

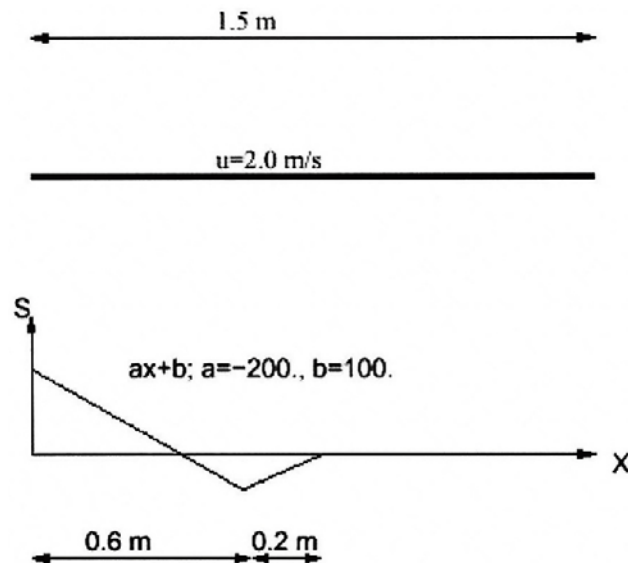


Figure A2-1. The situation considered.

Results/discussion

A comparison with the analytical solution and a grid independence test can be found in Figure A2-2.

Starting with the comparison with the analytical solution, it is seen that a close agreement is achieved. As mentioned above, the analytical solution was taken from a figure given by /Versteg and Malalasekera 1995/ and there is of course some uncertainty involved in that procedure. The agreement is thus concluded to be acceptable.

The grid independence test shows that $NX = 100$ is not enough to generate a grid independent solution. Solutions for $NX = 256$ and 300 are however very close. The reason for the fairly fine discretization needed is probably the use of a hybrid difference scheme. This scheme has been chosen for its many favourable properties (conservative, stable, etc) but it is a first-order scheme in terms of the Taylor series truncation error. In practical groundwater simulations it is however not expected that “diffusion in the flow direction” is a significant process and there is hence no strong reason to abandon the hybrid scheme, based on the results from the present test case.

Conclusion

DarcyTools predicts a correct steady state distribution of a scalar, subject to the combined effects of convection and diffusion. A fairly large number of grid cells is however needed to obtain a grid independent solution.

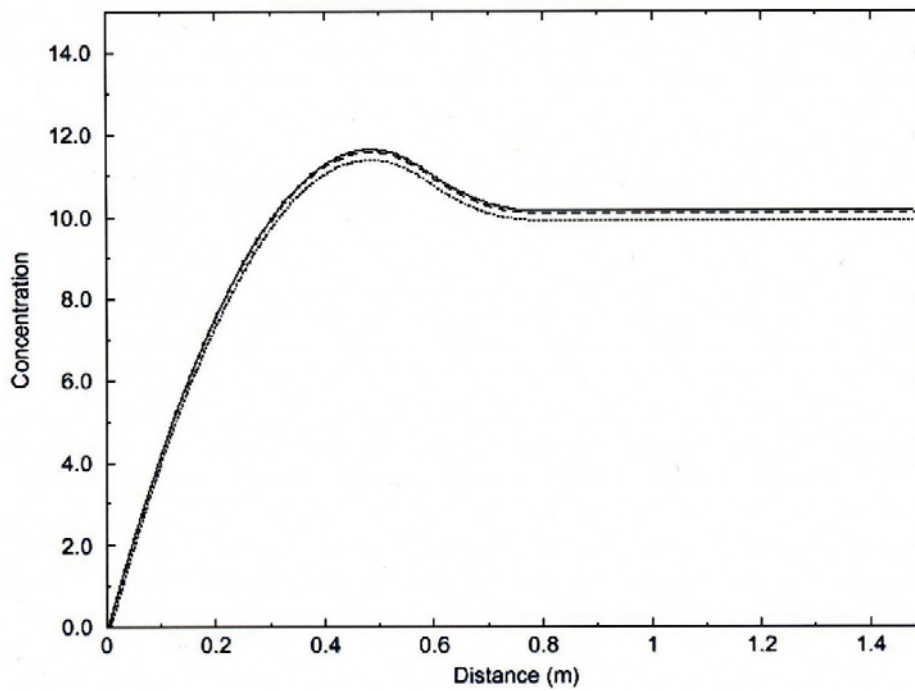
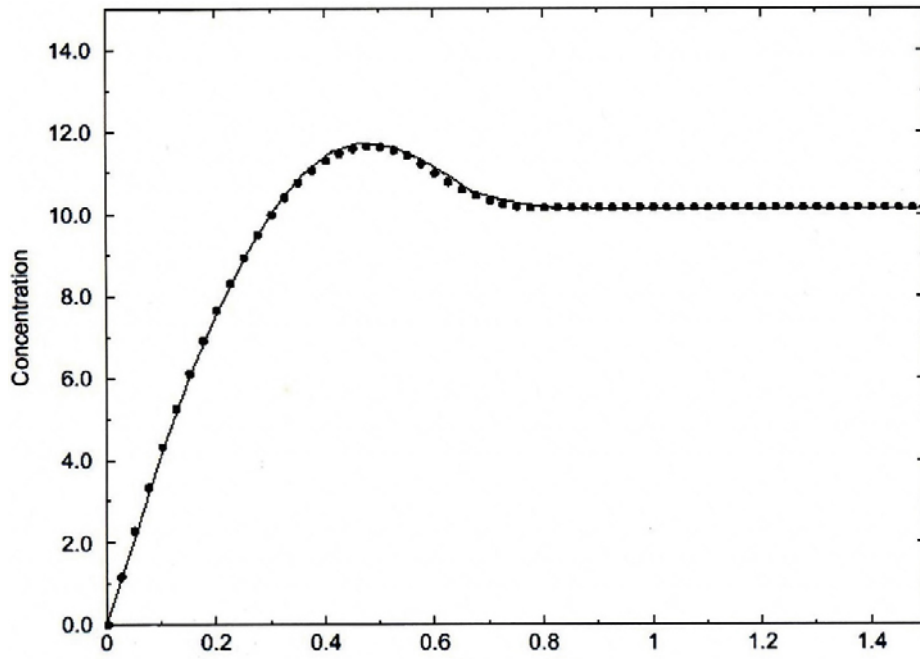


Figure A2-2. Comparison with analytical solution (top) and grid independence test.

Symbols top: — Analytical solution
 Numerical solution
 bottom: — Numerical solution $NX = 300$
 ---- Numerical solution $NX = 256$
 Numerical solution $NX = 100$

Case A3: Two-dimensional pressure problem

Introduction

In this test the pressure solver in DarcyTools will be used to predict the flow through a channel that has a complex pattern, see Figure A3-1. The channel will be given a much higher conductivity than the background and the flow through the domain will hence be restricted to the channel. A pressure drop from the lower left corner to the upper right is prescribed through the boundary conditions. In the channel a linear pressure drop is the correct solution.

The objective of the test case is to verify that DarcyTools predicts a correct flow and pressure distribution for the situation described.

Numerical simulation

The channel will be implemented by simply specifying the relevant cell wall conductivities. The general method in DarcyTools for describing a fracture in a continuum model (GEHYCO) will hence not be used here; a number of other test cases are devoted to GEHYCO.

As we follow the grid system, the length of the channel will not be exactly the same as shown in Figure A3-1 (360 metres in the figure as compared to 359 in the numerical representation). This will be taken into account when calculating the through-flow analytically, Q_a .

Most of the test case specification is given in Figure A3-1; same additional data are given in Table A3-1.

Table A3-1. Simulation parameters.

Domain	100·100·1 metres.
Conductivity (channel)	10^{-5} m/s.
Grid	$\Delta = 1.0$ m, uniform.

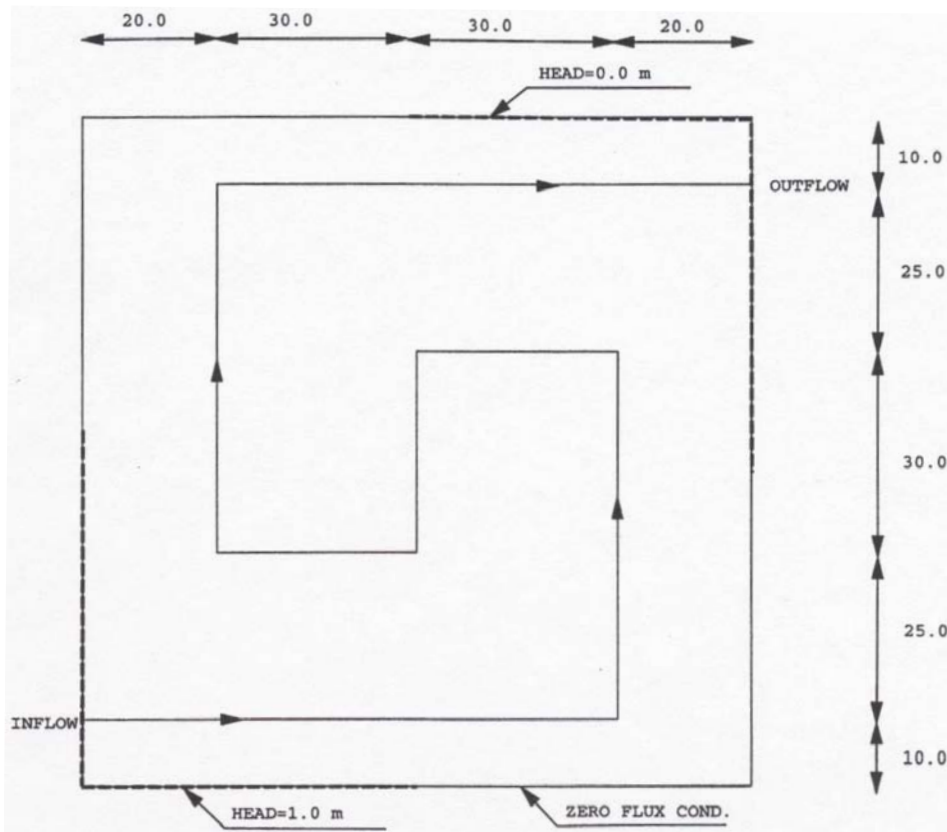


Figure A3-1. Flow through a complex channel. Outline of situation studied and coordinates for the centre line of the channel.

Results/discussion

The through-flow was predicted with an accuracy of 5 correct digits ($Q_a/Q_{calc} = 1.00001$, where Q_{calc} is the predicted flow).

The calculated pressure distribution is shown in Figure A3-2. As can be seen a complex pattern is obtained, but the pressure drop along the channel is linear, as expected.

Conclusion

It is concluded that the flow through a channel that runs along the coordinate directions can be calculated with high accuracy.

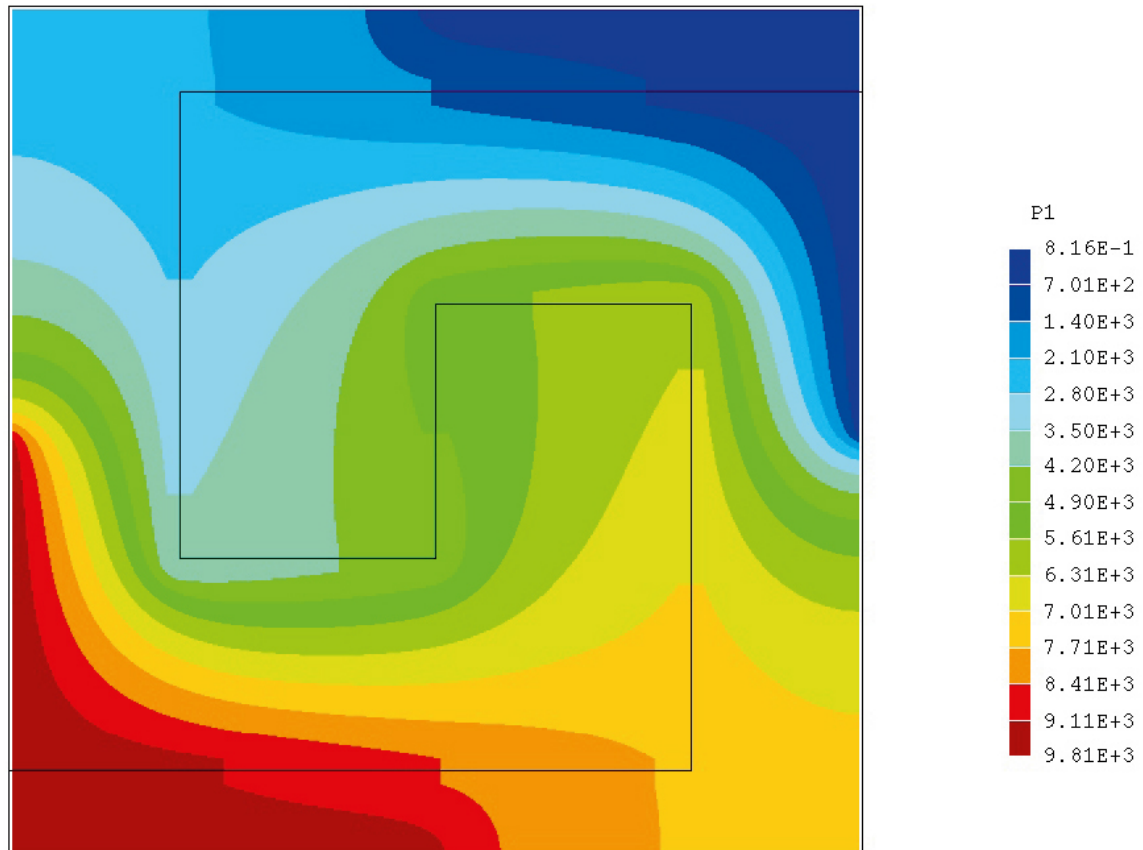


Figure A3-2. A channel in a 2D domain. Pressure distribution. The solid line indicates the centreline of the fracture.

Case A4: Tests of grid, fractures as objects

Introduction

This case is a variant of Case C4 and the reader is referred to this case for a full description. In summary the case considers the flux through 25 fractures that connect two opposite sides of a box with dimensions 100·100·100 metres.

The objective of the test case is to demonstrate how the computational grid can be generated with respect to the fracture network; a fine grid is needed to resolve the fractures, while a coarser grid can be specified for the rest of the domain

Numerical Simulation

A grid with $dx_{\max} = dy_{\max} = dz_{\max} = 0.5$ m was specified for the fractures, while the maximum cell size for the rest of the domain was set to 2.0 m, see Figure A4-1.

Results/discussion

The grid specification results in a grid with 576,345 cells. The mass flux through the domain in Case C4 was 0.0140 kg/s (fracture thickness 0.125 m), for the present grid the mass flux is 0.0139 kg/s. The difference is hence insignificant.

Conclusion

A grid, which resolves the fracture network with a higher resolution than the rest of the domain, has been shown to produce correct results.

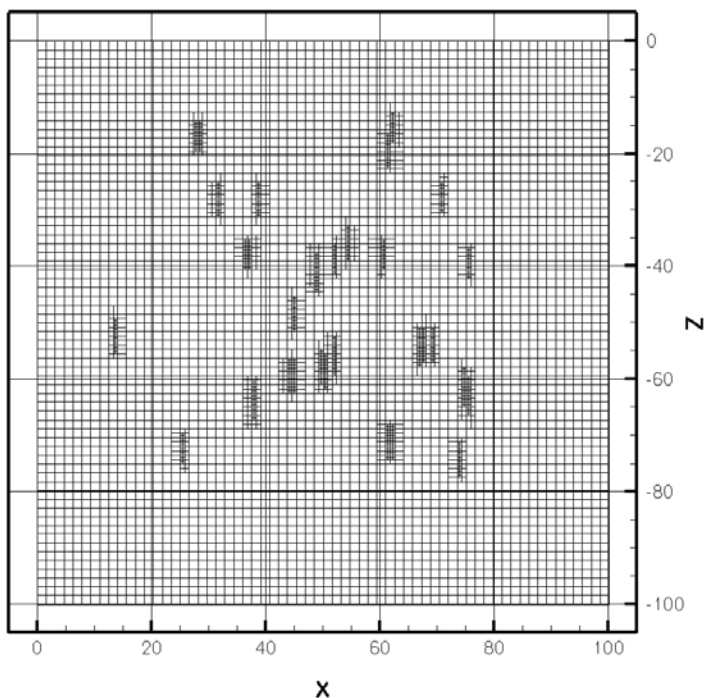


Figure A4-1. Illustration of a grid that resolves fractures with a higher resolution. View perpendicular to flow direction.

Case A5: Test of grid, cell removal

Introduction

This case is a variant of Case C4 and the reader is referred to this case for a full description. In summary the case considers the flux through 25 fractures that connect two opposite sides of a box with dimension 100·100·100 metres.

The objective of the test case is to demonstrate how a computational grid can be generated with respect to the fracture network; a fine grid is needed to resolve the fractures. In this case all cells that are not in contact with the fractures will be removed.

Numerical simulation

A grid with cell size $dx_{\max} = dy_{\max} = dz_{\max} = 0.5$ m was specified for the whole domain. A uniform grid with 2,097,152 cells was the result. All cells that are not in contact with the fractures were then removed; 2,033,279 cells were removed. An illustration of the final grid is given by Figure A5-1.

Results/discussion

The mass flux through the domain in Case C4 was 0.0140 kg/s (fracture thickness 0.125 m), for the present grid the mass flux is 0.0139 kg/s. The difference is hence insignificant.

Conclusion

A grid which resolves the fracture network with a high resolution and removes cells in the rest of the domain, has been shown to produce correct results.

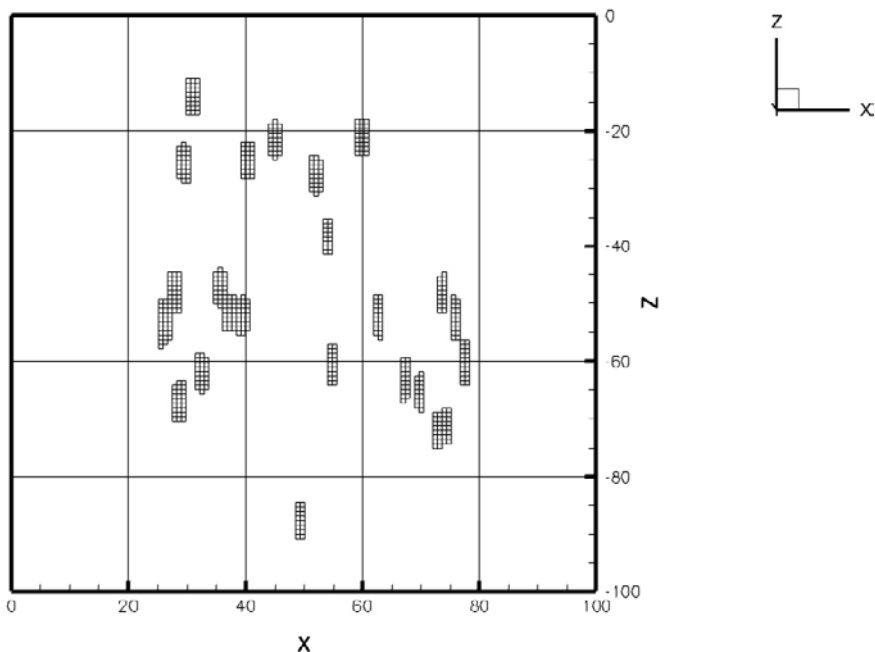


Figure A5-1. Illustration of a grid that resolves fractures with a high resolution and removes cells that are not in contact with the fracture. View perpendicular to flow direction.

Case B1: Regional groundwater circulation, /Tóth 1963/

Introduction

The natural ground water table often follows the topography. If one assumes that the ground water table coincides with the topography it is possible, under some further assumptions, to predict the ground water circulation.

/Tóth 1963/ (as described in /Fetter 1994/) provides an analytical solution for the case of a linear slope with an over-laying undulating sin-wave shaped upper boundary. This solution is illustrated in Figure B1-1.

The objective of this test case is to compare the numerical solution by the analytical solution, as given in Figure B1-1. The comparison will only be qualitative.

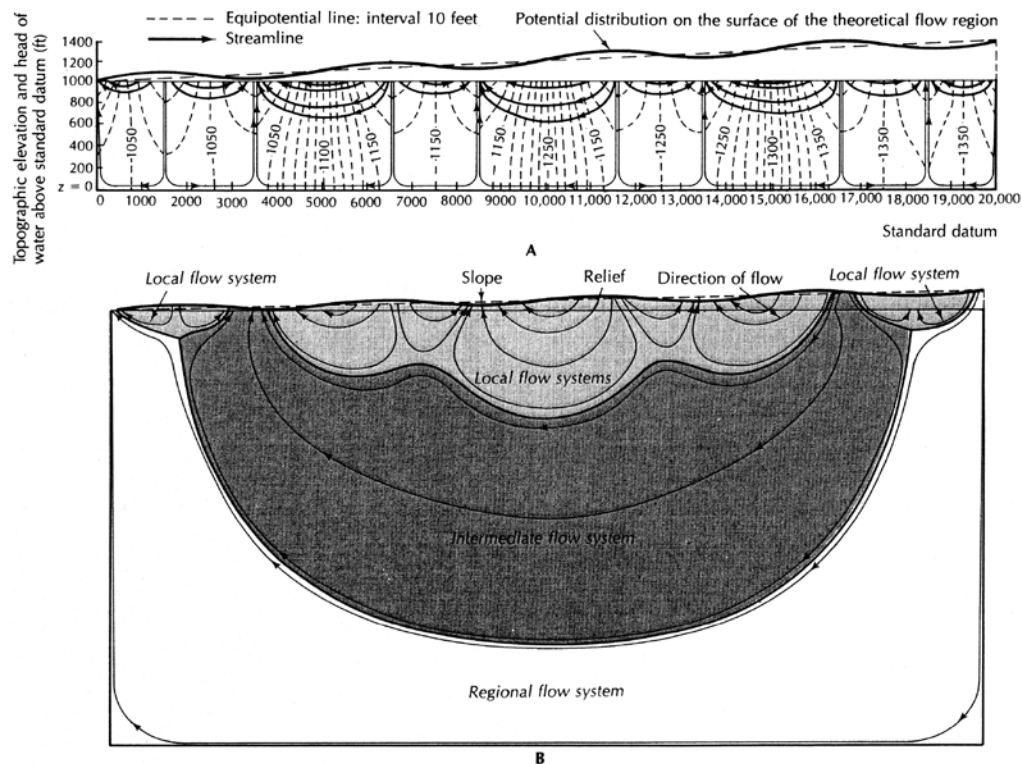


Figure B1-1. The effect of increased basin depth is shown on these two figures. In Part A, the basin depth/length ratio is 1:20; in Part B, it is 1:2. The shallow basin has only local flow systems, whereas the deep basin has local, intermediate, and regional flow systems. The water-table configuration is the same for both basins. From /Fetter 1994/.

Numerical simulation

A computational domain of length 20 km and depth 10 km is specified, i.e. a two-dimensional situation is studied.

The linear part of the slope has a total elevation of 400 metres, while the undulating part has an amplitude of 50 metres.

Further details are given in Table B1-1.

Table B1-1. Simulation parameters.

Domain	2D, 20·10 [km ²]
Boundary conditions	Zero flux on all boundaries except for the top boundary where a fixed pressure, according to the topography, is prescribed.
Properties	Permeability = $2 \cdot 10^{-16}$ [m ²] Porosity = 10^{-3} Viscosity = $2 \cdot 10^{-3}$ [kg/ms] Density = 1,000 [kg/km ³]
Grid	$dx_{\max} = dz_{\max} = 100$ m

Results/discussion

The predicted ground water circulation is shown in Figure B1-2, which can be compared with the lower figure in Figure B1-1. A close agreement is found.

Conclusion

A qualitative agreement with the solution by /Tóth 1963/ has been demonstrated.

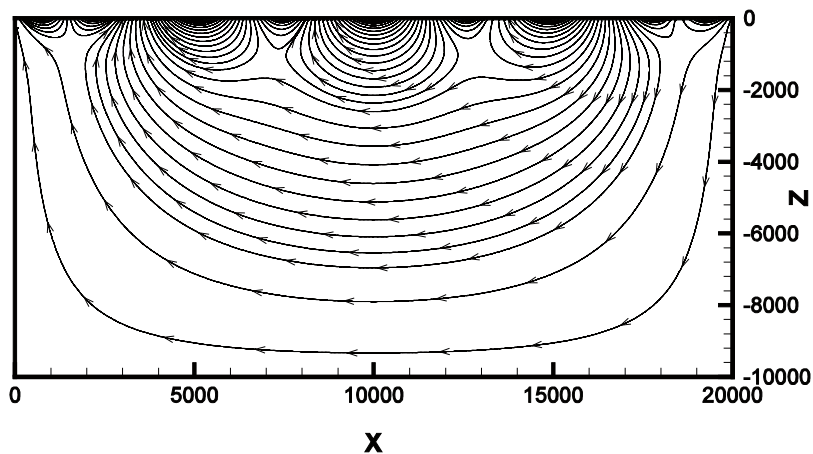


Figure B1-2. Simulated groundwater circulation below an undulating topography.

Case B2: Steady groundwater table

Introduction

The problem addressed is illustrated in Figure B2-1. In a two-dimensional vertical section the ground water elevation is sought. The groundwater flow may be forced by a pressure difference between the boundaries $h_1 - h_2$ or a vertical inflow at the top boundary, or both simultaneously. Only the steady state solution is to be considered.

The groundwater level, h , at distance, x , is given by (from Fetter 1994/):

$$h = \sqrt{h_1^2 - \frac{(h_1^2 - h_2^2)x}{L} + \frac{w}{K}(L-x)x} \quad (\text{B2-1})$$

where K is conductivity and other notation as given in Figure B2-1.

The objective of the test case is to verify that the algorithm used in DarcyTools (GRWT) predicts a groundwater table that is in agreement with the analytical solution.

Numerical simulation

The analytical solution is based on the Dupuit assumptions; a fact that needs to be considered in the numerical model set-up. One way to simulate the Dupuit assumptions is to introduce a higher conductivity in the vertical direction (as compared to the horizontal ones). This will make the vertical pressure distribution close to the hydrostatic one. A few test calculations revealed that increasing the vertical conductivity by a factor of 100 would “do the trick”.

Further details of the test case are given in Table B2-1.

Table B2-1. Simulation parameters.

Domain	100 (horizontal)·50 (vertical) metres.
Conductivity	10^{-8} (horizontal), 10^{-6} (vertical) m/s.
Boundary conditions	Bottom: Zero flux. Top: Prescribed flux (base case 100 mm/year or $3.2 \cdot 10^{-9}$ m/s). Left: Hydrostatic pressure, $h_1 = 30$ m. Right: Hydrostatic pressure, $h_2 = 20$ m.
Grid	$dx_{\max} = dz_{\max} = 1$ m.

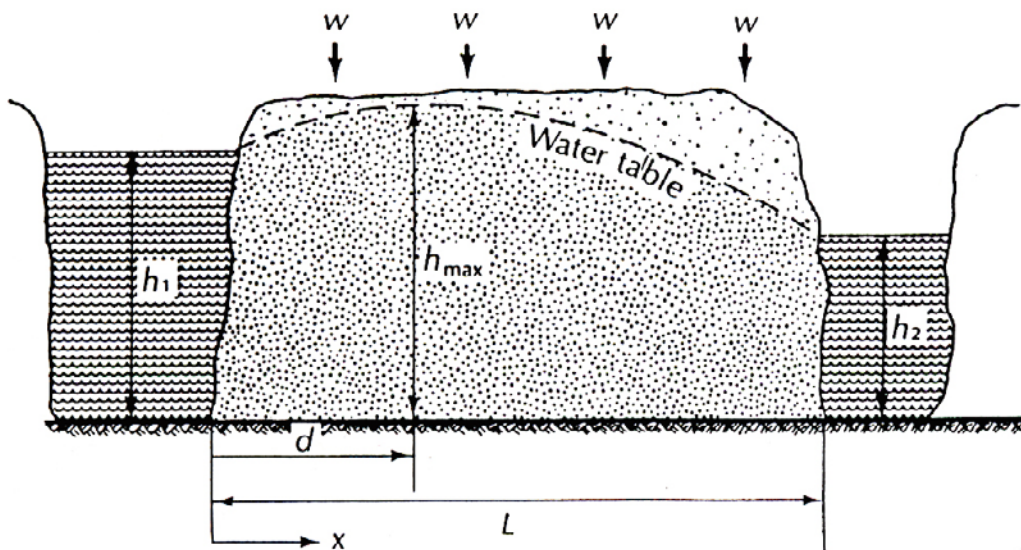


Figure B2-1. The groundwater table problem. Illustration of the situation and notation used.

Results/discussion

The comparison with the analytical solution is shown in Figure B2-2. The agreement is very close and needs no further comments. Figure B2-3 shows the flow pattern.

Conclusion

The steady state groundwater table, as predicted by DarcyTools, is in good agreement with the corresponding analytical solution.

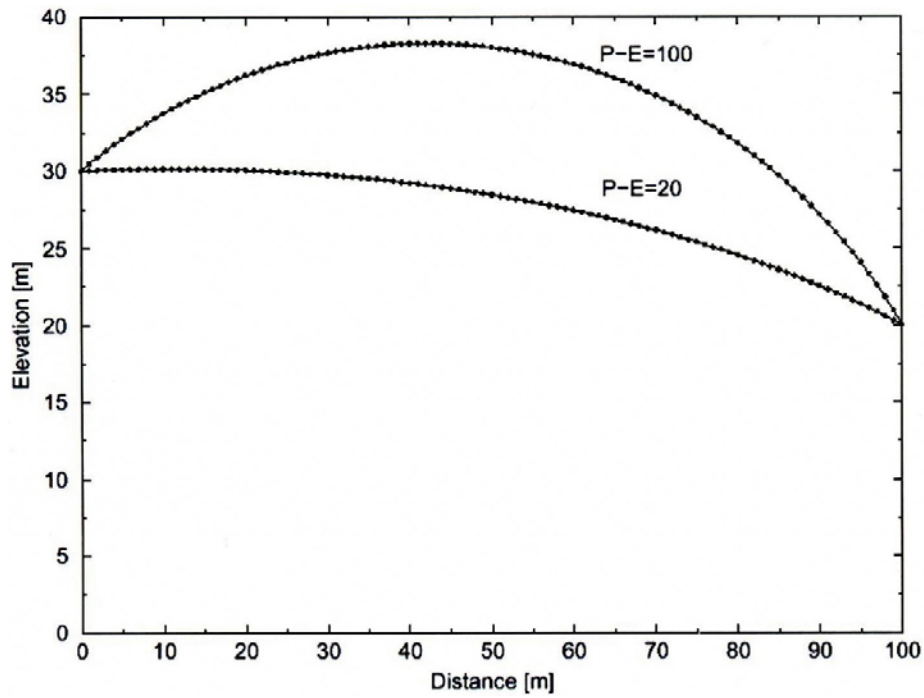


Figure B2-2. Comparison between analytically (—) and numerically (•••) calculated groundwater table for two P-E values.

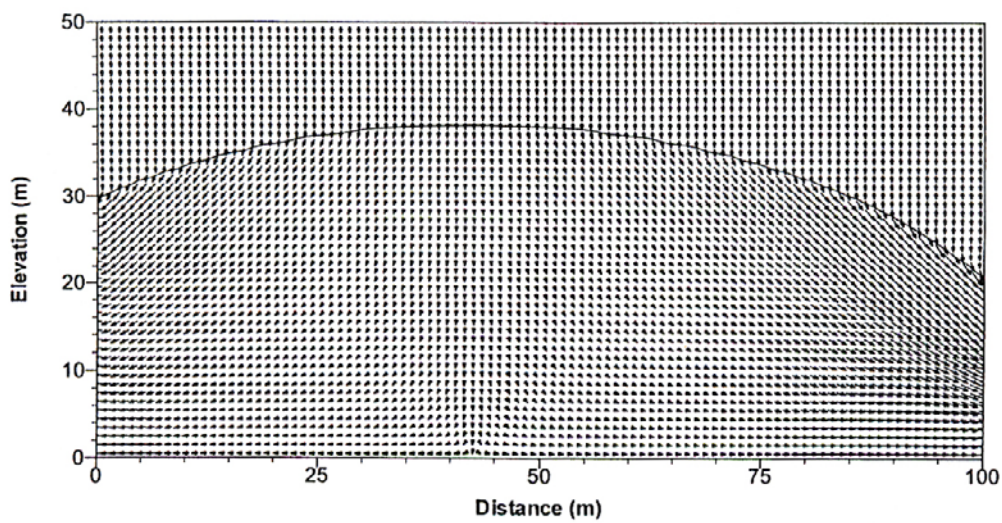


Figure B2-3. Predicted flow and groundwater table.

Case B3: Theis problem

Introduction

Theis problem deals with the transient drawdown due to a well that is discharging at a constant rate, Q , from an areally extensive confined aquifer. The situation considered is outlined in Figure B3-1. Some further specification:

- The potentiometric surface is initially horizontal.
- There is no source of recharge to the aquifer.
- The aquifer is compressible and water is released instantaneously from the aquifer, as the head is lowered.

The analytical solution to this problem is given by the following relations (as presented in Fetter 1994):

$$h_0 - h = \frac{Q}{4\pi T} \int_u^\infty \frac{e^{-u}}{u} du \quad (\text{B3-1})$$

The integral in Equation B3-1 can be replaced with an infinite series so that the

This equation becomes:

$$h_0 - h = \frac{Q}{4\pi T} \left[-0.5772 - \ln u + u - \frac{u^2}{2 \cdot 2!} + \frac{u^3}{3 \cdot 3!} - \frac{u^4}{4 \cdot 4!} + \dots \right] \quad (\text{B3-2})$$

The argument u is given as

$$u = \frac{r^2 S}{4Tt} \quad (\text{B3-3})$$

where h is hydraulic head, T transmissivity, b the aquifer thickness, r radial distance and S aquifer storativity (product of the specific storativity and aquifer thickness).

In DarcyTools the relation between the porosity, ϕ , and pressure, p , is expressed as a state law (see main report). It can be shown that the two ways of expressing the storativity effect are related as follows:

$$\sigma_0 = S/(b\theta_0) \quad (\text{B3-4})$$

where σ_0 is the coefficient in the state law and θ_0 the porosity before pumping starts.

The objective of the test case is to demonstrate that the storativity effect, as expressed in DarcyTools, is in accordance with Theis analytical solution.

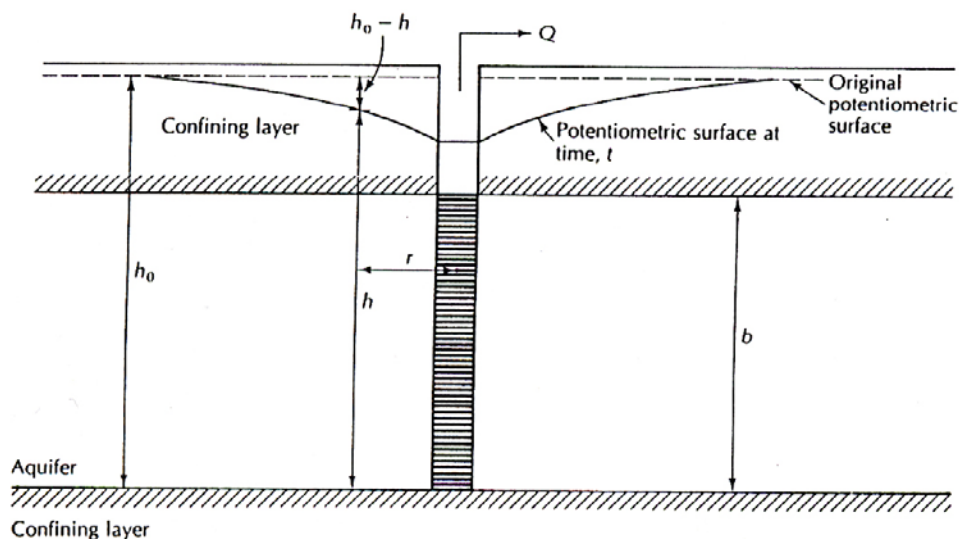


Figure B3-1. Fully penetrating well pumping from a confined aquifer (from Fetter 1994/).

Numerical simulation

The flow towards the well will be radial and the problem is hence best handled in polar coordinates. This system is however not provided in DarcyTools and we thus need to simulate the problem as a 2D problem (it is 1D in polar coordinates) in Cartesian coordinates. Due to symmetry conditions we need however only to consider one quarter of the domain and the “pumped cell” is hence placed in the lower left corner of the domain.

Further details of the simulations are given in Table B3-1.

Table B3-1. Simulation parameters.

Domain	2D, 1,000·1,000·10 metres.
Transmissivity	10^{-3} m ² /s.
Pumping rate	$2.5 \cdot 10^{-3}$ m ³ /s.
Storativity	Varied: 0.005, 0.01 and 0.02.
Boundary conditions	Zero flux condition on all boundaries.
Grid	Expanding in x and y directions, one cell in z-direction . Time direction: Ten days of integration time, subdivided into 1,000 steps.

Results/discussion

The comparison between the analytical and numerical solution, for three storativity values, is shown in Figure B3-2. A point at a radius of 100 metres from the well was chosen for the comparison. It is clear from the figure that a near perfect agreement is achieved (the error is always less than 1%).

Conclusion

It has been shown that DarcyTools is in good agreement with the analytical solution of Thies problem.

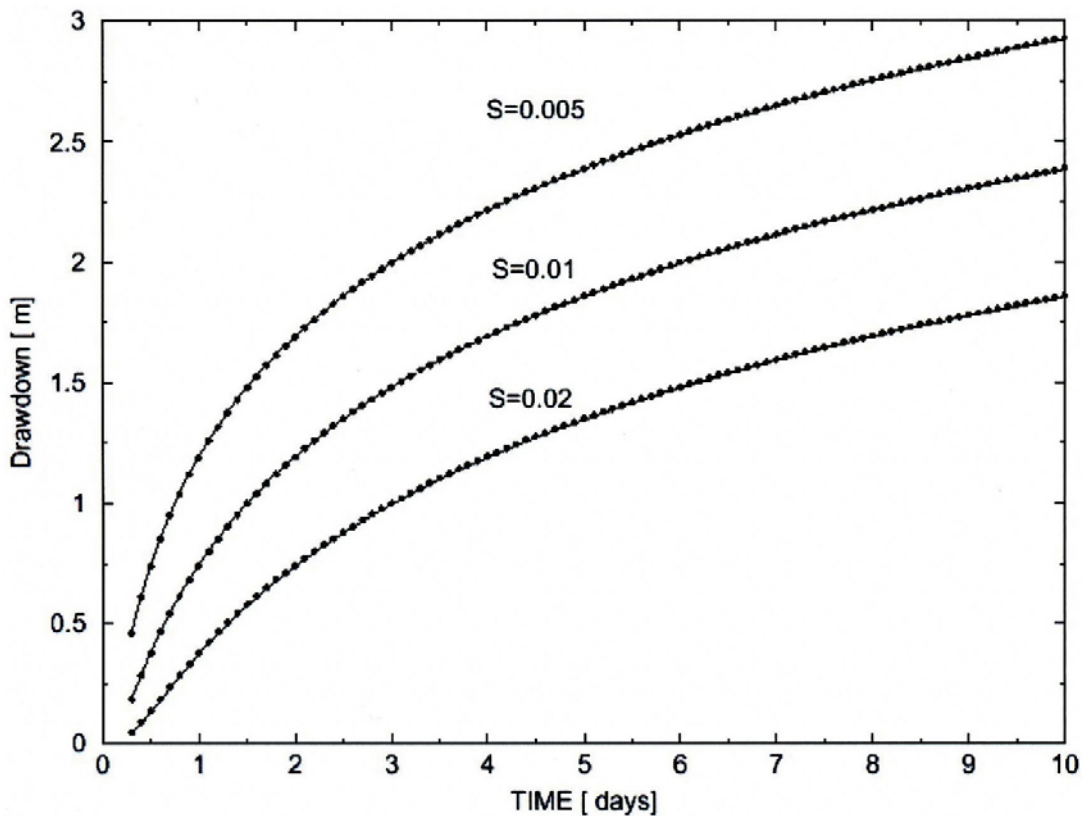


Figure B3-2. Comparison between analytically (—) and numerically (•••) calculated drawdown at a radius of 100 metres from a well.

Case B4: Water inflow to a circular tunnel

Introduction

The steady state flow towards a circular tunnel in a semi-infinite isotropic and homogeneous aquifer will be investigated. If the radius of the tunnel is denoted r and the depth h it is well established that the inflow, q , is given by

$$q = 2\pi k \frac{h}{\ln \frac{2h}{r}} \quad (\text{B4-1})$$

where k is the hydraulic conductivity. A review of analytical solutions is provided by /El Tani 2003/ and in this paper it is shown that (B4-1) is valid if $r/h \ll 1$ (if $r/h \approx 0.1$, the error in q is of the order of 1 %).

The objective of this test case is to verify that the numerical solution is in agreement with (B4-1).

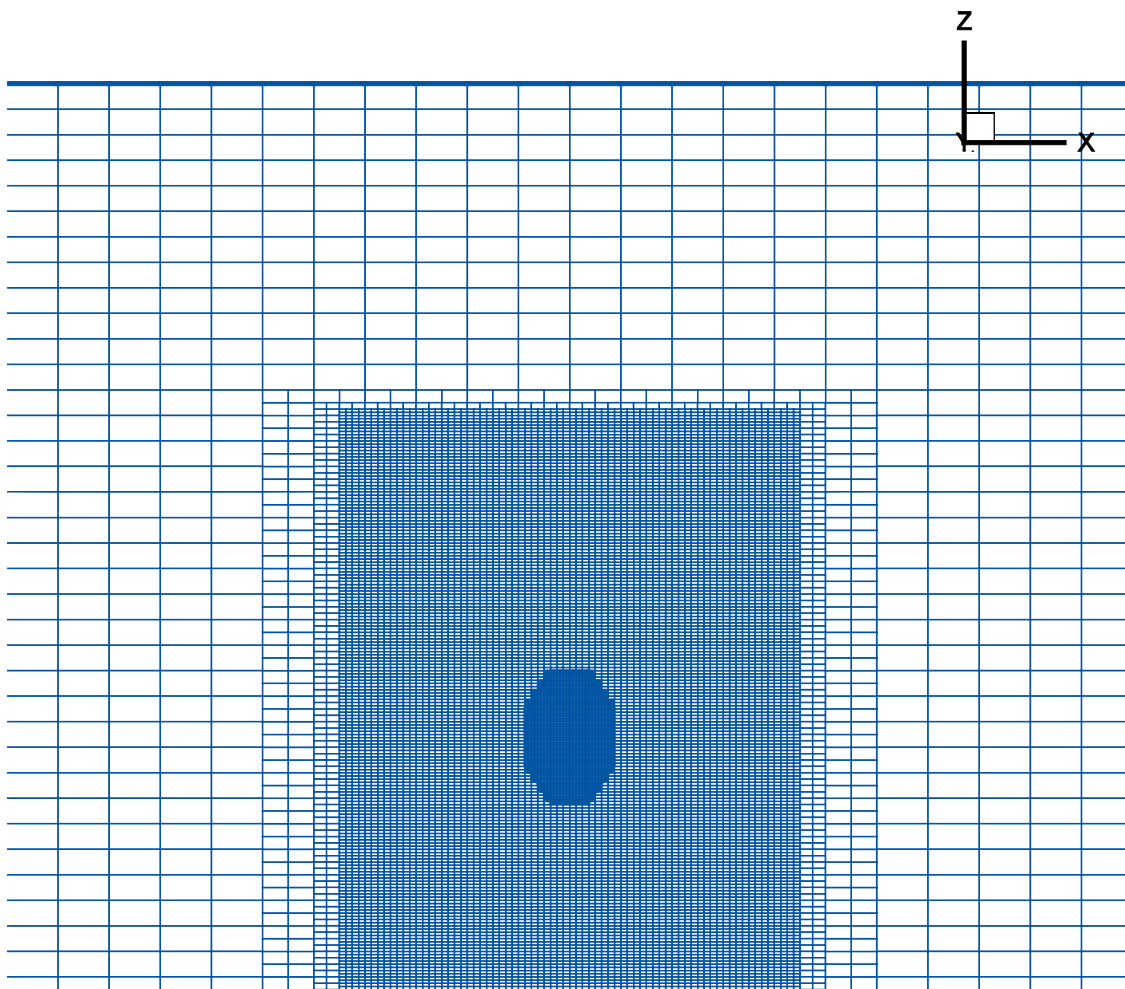


Figure B4-1. The grid close to the tunnel.

Numerical simulation

The simulation parameters are summarized in Table B4-1. A vertical plane (the simulation is 2D) with dimensions 3,000 m (horizontal) and 1,000 m (vertical) specifies the computational domain. Part of the grid is shown in Figure B4-1.

Table B4-1. Simulation parameters.

Domain	3,000·1,000·1 metres.
Boundary conditions	Fixed pressure at ground. Zero flux on all other boundaries. Atmospheric pressure in tunnel.
Properties	Conductivity = 10^{-5} m/s.
Tunnel	Centre at a depth of 100 metres. Radius varied: 2.5, 5.0, 10.0 metres.
Grid	Tunnel: $\Delta_{\max} = 1.0$. Near field: $\Delta_{\max} = 2.0$. Far field: $\Delta_{\max} = 20$.

Results/discussion

The inflow to the tunnel, as calculated by Equation (B4-1) and by the numerical simulation, is shown in Figure B4-2. A close agreement is found for the three tunnel radius tested.

In /El Tani 2003/ corrections for a finite r/h value are given. For the present cases it is found that the corrections are smaller than 0.5%; however they do act to bring the analytical results even closer to the numerical ones. It was found that the horizontal size of the domain needed to be quite large (3,000 metres). A smaller size (1,000 m) affected the inflow with several percent.

Conclusion

It has been demonstrated that water inflow to a circular tunnel with atmospheric pressure can be calculated with good accuracy.

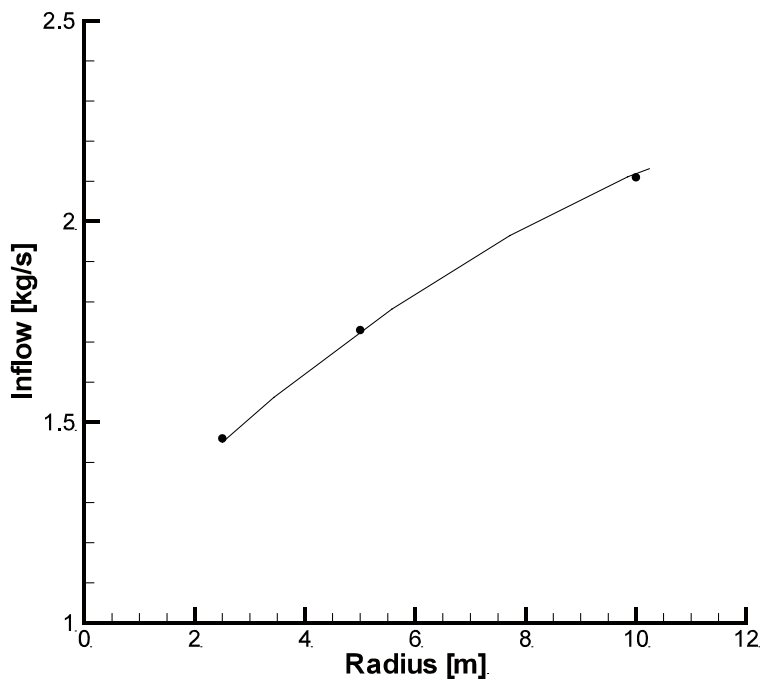


Figure B4-2. Analytically (line) and numerically (symbols) determined relation between tunnel radius and inflow.

Case B5: Specific yield, /Neuman 1975/

Introduction

The pumping of an unconfined aquifer generates a characteristic time-drawdown curve in a near borehole piezometer; first a steep part, then an almost flat part and finally a relatively steep late-time segment. The flat part is attributed to “delayed yield”, which is the gravitational drainage of the unsaturated zone.

/Neuman 1975/ gives an analytical solution which covers all three parts. The assumptions of this solution are different to the ones in the numerical technique embodied in DarcyTools (see Part A). In particular, /Neuman 1975/ assumes that the water table remains at its original position, while the numerical model considers a moving ground water table.

The objective of this case is to compare the first two parts of the drawdown curve and in particular the levels of the flat part. For longer pumping (and larger drawdowns) the two solutions may not be comparable, but this point will not be investigated here.

Numerical simulation

The problem will be specified as a three dimensional one in Cartesian coordinates, although a two dimensional solution in cylindrical coordinates would have been more appropriate. An outline is given in Figure B5-1; we are hence only studying one quarter of the complete domain (due to symmetry conditions).

Input data are given in Figure B5-1 and Table B5-1.

Table B5-1. Simulation parameters.

Domain	250·250·10 [m ³].
Boundary conditions	Zero flux.
Sink due to pumping	5·10 ⁻³ [m ³ /s].
Properties	Permeability = 2·10 ⁻¹¹ [m ²]. Porosity = 10 ⁻² . Density = 1,000 [kg/km ³]. Spec. storativity = 2·10 ⁻⁵ . Delay time = 50 s. Specific yield = 0.2.
Grid	x and y: Expanding from the well. z: Uniform. dz _{max} = 1.0 m.

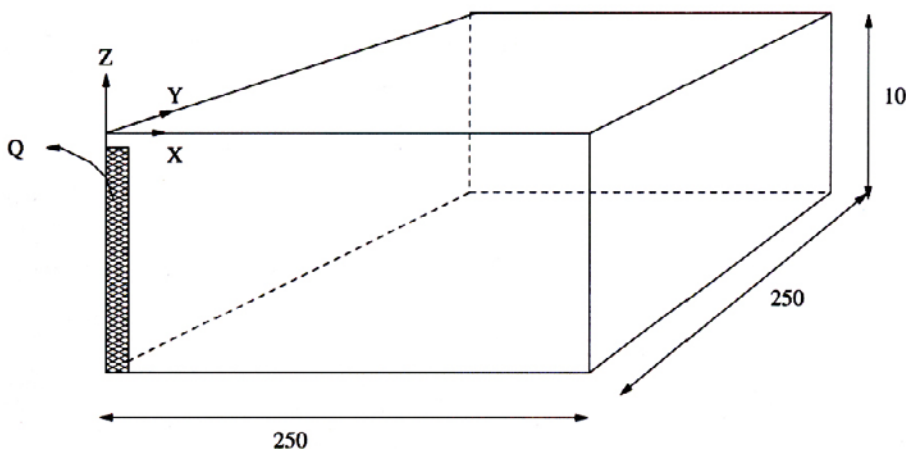


Figure B5-1. Outline of situation studied.

Result/discussion

The simulated time-drawdown curves in three points (at different distances from the well) are shown in Figure B5-2. The levels of the flat part, as given by the analytical solution, is also given in the figure. As can be seen a surprisingly close agreement, considering the different basic assumptions, is found.

Conclusion

It is found that the flat part of the time-drawdown curve is in agreement with the analytical solution by /Neuman 1975/.

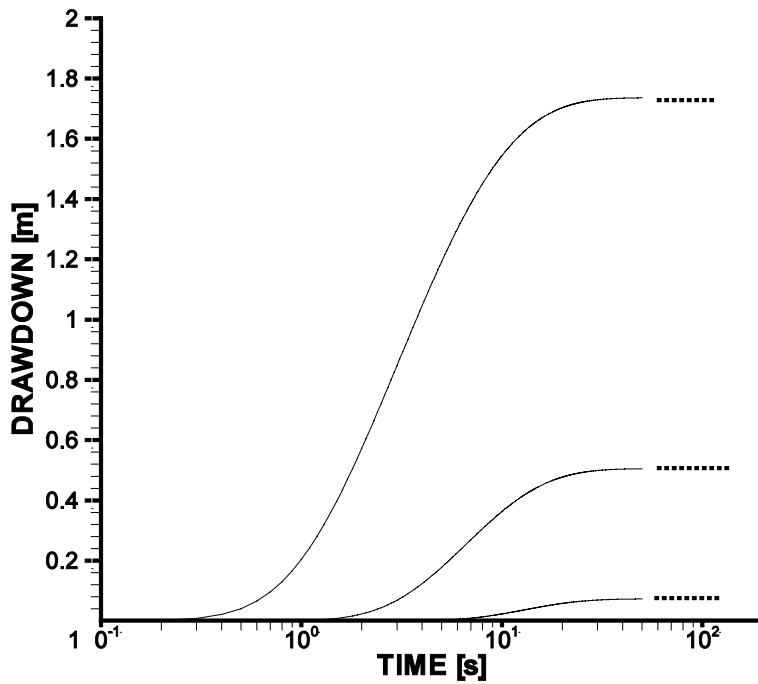


Figure B5-2. Time-drawdown at distances 4.5 (top), 10 (middle) and 20 (bottom) metres from the well. Dotted lines give the corresponding analytical solutions for the flat part.

Case B6: Transient groundwater table

Introduction

In Report 1 it has been suggested that the storativity term alone could account for the free surface dynamics. In Figure B6-1 a case considered by /Raudkivi and Callander 1976/ is outlined. They apply the one-dimensional diffusion equation to this problem:

$$\frac{\partial y}{\partial t} = \frac{Kd}{n} \frac{\partial^2 y}{\partial x^2} \quad (5-1)$$

where K is conductivity, d depth and n porosity. Obviously no “delayed drainage” is considered by this equation, instead it is assumed that the advancing or retreating GRWT interacts with the unsaturated zone instantaneously.

Numerical simulation

The method based on the storativity term will now be applied to this case. However, we will not solve the one-dimensional diffusion equation (it has earlier been demonstrated that DarcyTools solves this equation correctly), but instead apply the suggested method as a 2D case. Hence the free surface is identified by $p = 0$ and the horizontal conductivity is reduced above this level. The storativity term is used to simulate the storage of water. It should however be noted that the storage term apply all over the domain (also above the grwt) and the simulation is thus not directly comparable to the case outlined in Figure B6-1, where storage is due to the GRWT rising into the unsaturated zone. Applying a storativity term over the whole domain was however the pragmatic assumption adopted and it is this we will test. The data used for the simulation are summarised in Table B6-1.

Table B6-1. A transient case. Simulation parameters.

Domain	11.2 (vertical)-50.0 (horizontal) metres.
Conductivity	10^{-6} (horizontal), 10^{-4} (vertical) m/s.
Storativity	$S_l = 0.035 \text{ m}^{-1}$.
Boundary conditions	Prescribed pressure at left boundary, according to water level. Zero flux condition on all other boundaries.
Grid	Non uniform Cartesian.

Results/discussion

The main result of the simulation is shown in Figure B6-2, where the predicted GRWT (lines) is compared with the analytical solution (symbols) As can be seen the agreement is good for 30 and 32 days, but less good for 40 days. The reason for the disagreement at 40 days is probably that the numerical model will release water also above the grwt and hence delay the lowering. It should once again be emphasized that we are not trying to solve the one-dimensional diffusion equation, which is the analytical solution in this case, and we should therefore not expect a perfect agreement.

Conclusion

A qualitative agreement with the analytical solution for a transient ground water table has been demonstrated. The suggested method, based on the storativity term, needs further evaluation.

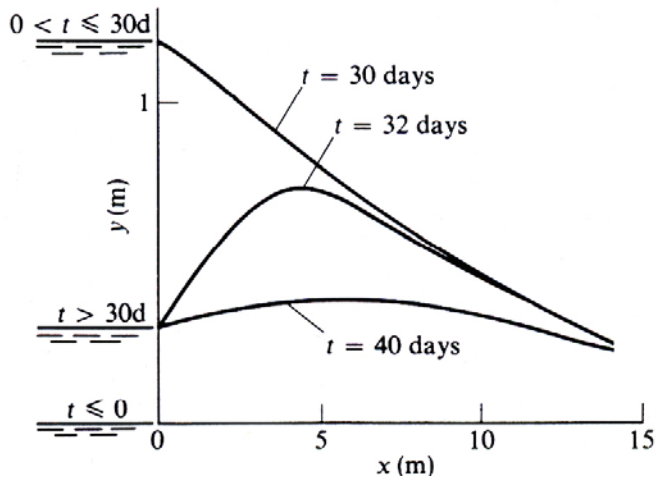
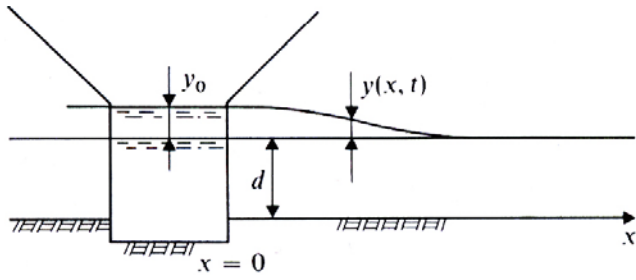


Figure B6-1. The transient GRWT. Situation considered (top). Lower figure: the analytical result for a momentarily changed water level at the left boundary. (From /Raudkivi and Callander 1976/.

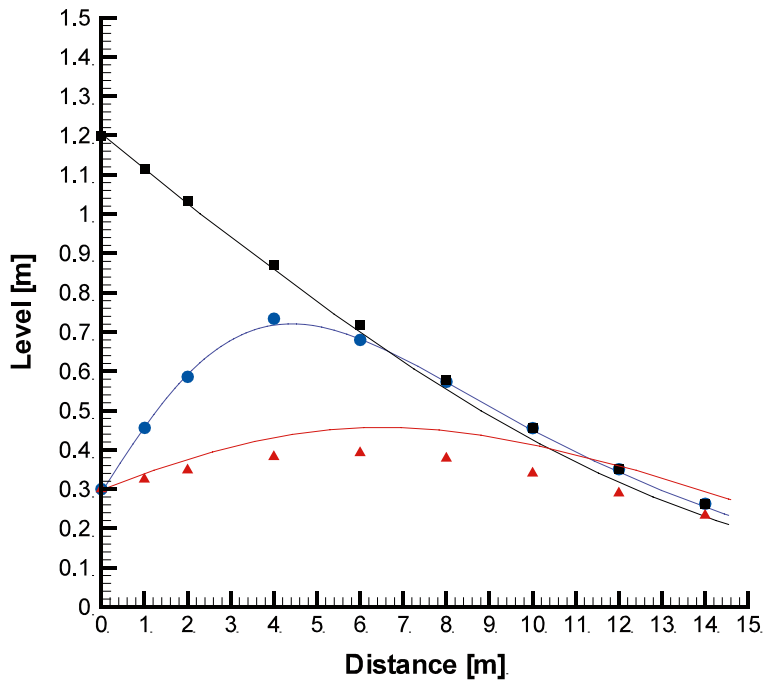


Figure B6-2. Comparison between numerical (lines) and analytical (symbols) solution. GRWT at 30 (black), 32 (blue) and 40 (red) days.

Case B7: Water inflow to a grouted tunnel

Introduction

The steady state flow towards a circular grouted tunnel in a semi-infinite isotropic and homogeneous aquifer will be investigated. If the radius of the tunnel is denoted r , the thickness of the grout t and the depth h , it is well established that the inflow, q , is given by

$$q = 2\pi k \frac{h}{\ln \frac{2h}{r} + \left(\frac{k}{k_g} - 1 \right) \left(\ln \left(1 + \frac{t}{r} \right) \right)} \quad (\text{B7-1})$$

where k is the hydraulic conductivity and k_g the conductivity of the grouted region.

The objective of this test case is to verify that the numerical solution is in agreement with (B7-1).

Numerical simulation

The simulation parameters are summarized in Table B7-1. A vertical plane (the simulation is 2D) with dimensions 3,000 m (horizontal) and 1,000 m (vertical) specifies the computational domain. Part of the grid is shown in Figure B7-1.

Table B7-1. Simulation parameters.

Domain	3,000·1,000·1 metres.
Boundary conditions	Fixed pressure at ground. Zero flux on all other boundaries. Atmospheric pressure in tunnel.
Properties	Conductivity = 10^{-5} m/s. Grouting in a 2 metres thick layer. Grouting conductivity varied.
Tunnel	Centre at a depth of 100 metres. Radius 10.0 metres.
Grid	Tunnel: $\Delta_{\max} = 0.5$. Near field: $\Delta_{\max} = 2.0$. Far field: $\Delta_x = 16$, $\Delta_z = 2$.

Results/discussion

The inflow to the tunnel, as calculated by Equation (B7-1) and by the numerical simulation, is shown in Figure B7-2. A close agreement is found for the grouting conductivities studied.

Conclusion

It has been demonstrated that water inflow to a grouted circular tunnel with atmospheric pressure can be calculated with good accuracy.

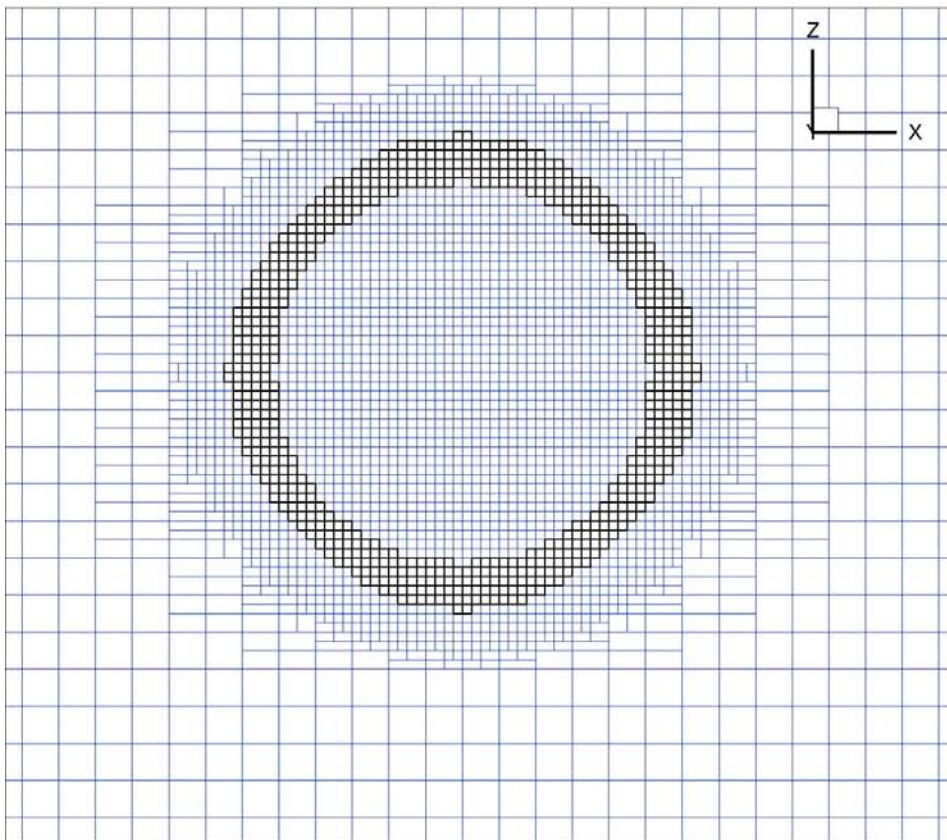
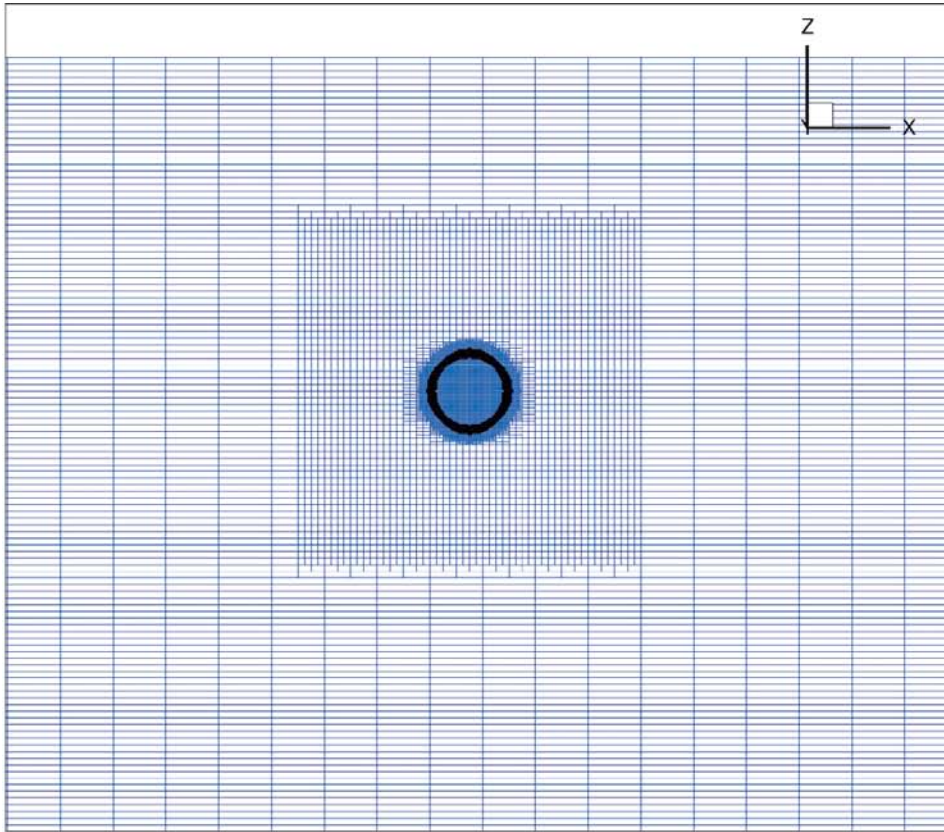


Figure B7-1. The grid close to the tunnel. Black colour indicates the grouted region.

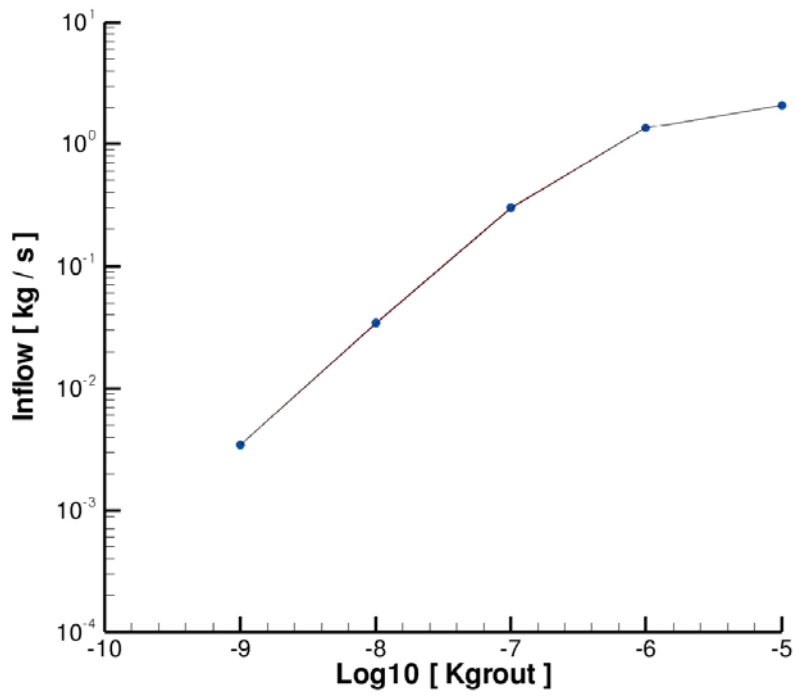


Figure B7-2. Analytically (line) and numerically (symbols) determined relation between grouting conductivity and inflow.

Case C1: Three fractures in a 2D domain

Introduction

This case considers the steady flow through three crossing fractures in a 2D domain, see Figure C1-1. Pressure is prescribed on the left and right boundaries, while the top and bottom boundaries are of zero flux type.

It is possible to determine the flow in all individual parts of the network analytically, as well as the pressure in the fracture crossings; these data will be used for verification of the numerical results. It is of special interest to study the accuracy of the numerical solution as a function of the fracture thickness, b , in relation to the cell size, Δ .

The objective of the test case is to verify that DarcyTools is in agreement with the analytical solution for the case considered.

Numerical simulation

The computational domain is specified in Figure C1-1 and some further details are given in Table C1-1. The pressure difference ($P_1 - 0$) and the fracture conductivity are of no importance, as we will normalize all results with the data from the analytical solution. The number of grid cells is held constant and the ratio b/Δ is hence varied by varying the fracture thickness b .

A test with a fracture network, where all the fractures do not directly connect the two sides with prescribed pressure, will also be carried out. In this test part of fracture c (from inlet to point 2 and part of fracture b (from point 3 to outlet) will be removed.

Table C1-1. Simulation parameters.

Domain	2D 10·5 metres.
P_1	9,810 Pa.
Fracture Conductivity	$5 \cdot 10^{-5}$ m/s.
Fracture thickness	b/Δ varied: 0.1, 0.5, 1.0 and 2.0.
Grid	$dx_{\max} = dy_{\max} = 0.02$.

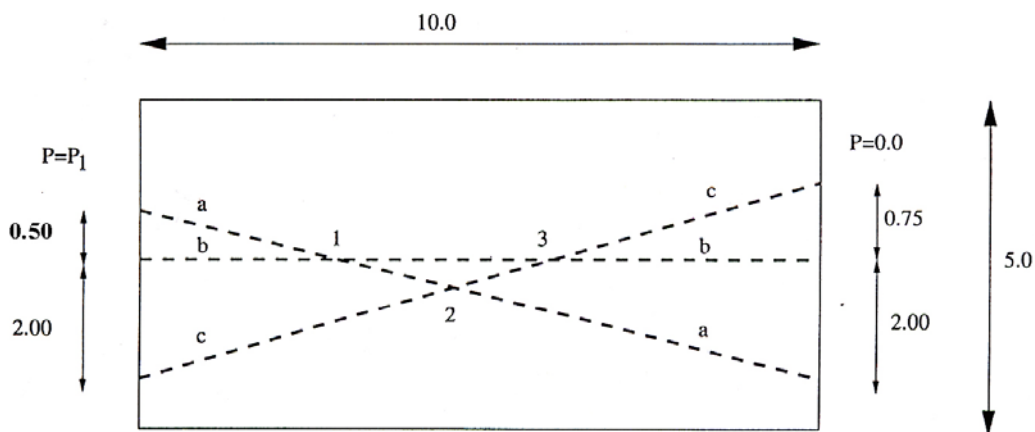


Figure C1-1. Flow in a two-dimensional fracture system. Outline of situation considered.

Results/discussion

All results are summarised in Table C1-2. Both the total flux through the domain, Q , and the pressures in points 1, 2 and 3 have been normalised with the corresponding values from the analytical solution. The general picture is that the numerical solution is in close agreement with the analytical one, it should however be noted that calculated flow decreases, in relation to the analytically calculated, with a decreasing ratio b/Δ .

Table C1-2. Flow and pressure in a fracture network. Values calculated with DarcyTools have been normalised with the corresponding values from the analytical solution.

Parameter	Fracture thickness normalised with Δ (b/Δ).				
	0.1	0.5	1.0	2.0	1.0, fractures removed
Q	0.960	0.987	0.997	1.001	0.998
P_1	1.000	1.001	1.001	1.001	0.998
P_2	0.998	0.999	0.999	1.000	1.005
P_3	0.998	1.000	1.000	1.000	0.982

Conclusion

Flow and pressure in three crossing fractures in a 2D domain can be accurately calculated by DarcyTools.

Case C2: A multi-fracture fracture zone

Introduction

A fracture zone is a region of high fracture intensity. Whenever possible, one should hence generate fracture zones as a sub domain in which a fracture network is specified.

This test case intends to show how this is done in DarcyTools and also demonstrate that a correct solution is obtained.

The situation considered is outlined in Figure C2-1. In a box with dimensions 100·100·100 metres a sub domain (the fracture zone) with dimensions 50·100·5 metres is specified. Within the sub domain fractures with dimension 2·2·0.1 metres are generated; the fractures are given random orientation and position. If a large number, n , of fractures are placed in the zone the fracture zone conductivity, $Cond_{zone}$, will be :

$$Cond_{zone} = \frac{nCond_{fr}V_{fr}}{V_{zone}} \quad (C2-1)$$

where $Cond_{fr}$ and V_{fr} are the conductivity and volume of a fracture and V_{zone} the volume of the fracture zone. By choosing $Cond_{fr} = Cond_{ref}/n$, where $Cond_{ref}$ is a constant, we find that $Cond_{zone}$ is constant and the flux through the fracture zone should also be constant for a given head difference between the two opposite faces of the box. However, it is clear that this will only be true when the number of fractures is large.

In the numerical simulation, a range of n -values will be tested and the flux through the fracture zone will be the parameter that we compare with the theoretical value.

Numerical simulation

The situation considered is given by Figure C2-1 and some complementary data are found in Table C2-1.

Table C2-1. Simulation parameters.

Domain	100·100·100 metres.
Boundary conditions	Fixed pressure difference (= 1 metre head) between two opposite faces. Zero flux on other faces.
Fracture zone dimensions	50·100·5 metres.
Fracture dimensions	2·2·0.1 metres.
Fracture conductivity	$Cond_{ref} = 1.0$ m/s.
Grid	$dx_{max} = dy_{max} = dz_{max} = 0.5$ in fracture zone.

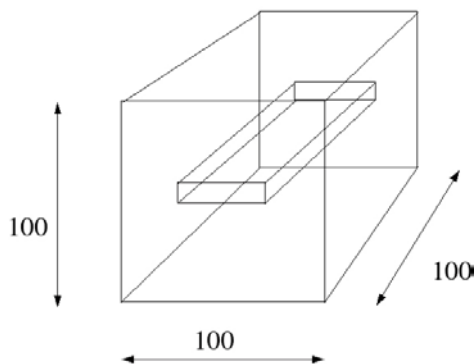


Figure C2-1. Illustration of a fracture zone in a box.

Results/discussion

The flux through the domain as a function of the number of fractures, n , is shown in Figure C2-2. When n is small the two sides of the box are not connected and the flux is zero. When n is large we see that the flux approaches the theoretical value; for $n \approx 400,000$ a flux that is 99 % of the theoretical value is calculated. It may be the case that the flux will always be somewhat lower than the theoretical value as the fracture zone will get irregular boundaries with parts that do not contribute to the flux.

Conclusion

The multi-fracture fracture zone has been shown to give the expected average transmissivity.

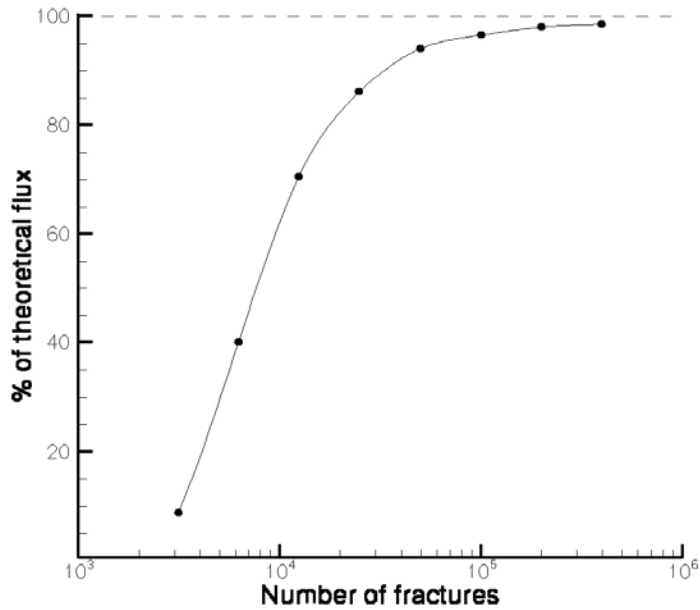


Figure C2-2. The flux through the fracture zone as a function of the number of fractures in the zone.

Case C3: Single fracture in a box

Introduction

It was noted in Report 1 that the accuracy of the representation of a fracture depends on the angles the fracture forms with the coordinate directions and the thickness of the fracture (in relation to the cell size Δ). The purpose of this test case is to establish the magnitude of the errors that can be expected due to these effects.

The situation studied is outlined in Figure C3-1. The pressure is held constant on two opposite faces ($y = 0.0$ m and $y = 100.0$ m) and a zero flux condition is used on all other boundaries. At the inflow boundary the position of the fracture is fixed, with centreline coordinates (10.0, 0.0, 10.0). The fracture position at the downstream boundary is varied in order to test a wide range of angles to the coordinate directions. Also a range of thicknesses was tested, but the height of the fracture, H , was kept constant at 5 metres.

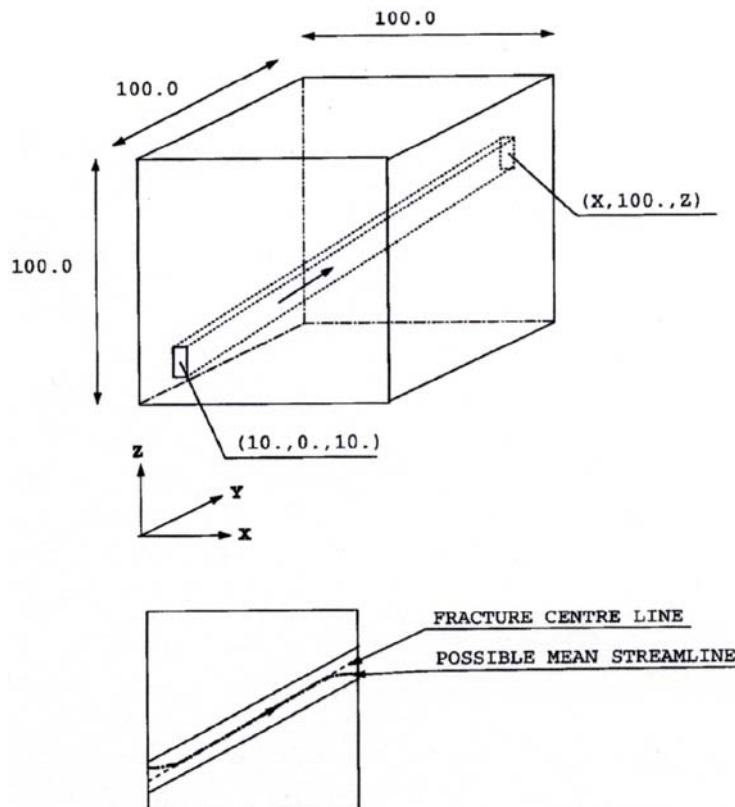


Figure C3-1. A single fracture in a 3D domain. Outline of situation studied (top) and illustration of fracture centre line and mean streamline. All distances in metres.

Numerical simulations

Most of the simulations parameters are introduced in Figure C3-1, some further details are summarised in Table C3-1.

A systematic variation of the fracture thickness and the downstream position will be in focus in the simulations.

Table C3-1. Simulation parameters.

Domain	100·100·100 metres.
Boundary conditions	Fixed pressure difference (= 1 metre head) between two opposite faces. Zero flux on other faces.
Fracture dimensions	Height = 5 metres, thickness varied (see Result section).
Fracture position	Fixed at inflow boundary (see Figure C3-1), varied at outflow boundary (see Result section).
Fracture conductivity	10^{-4} m/s.
Grid	$dx_{\max} = dy_{\max} = dz_{\max} = 2.0$

Results/discussion

Results are presented in Table C3-2. Five downstream fracture positions and five fracture thicknesses were tested. The five downstream fracture positions will give a fracture that, for the first position, is parallel to the y -coordinate while the last position gives a fracture that almost follows a diagonal in the box. Note also that the x - and z -coordinates for the downstream positions are different; this ensures that the fracture will have different angles to all three coordinate directions (except for the first position). The grid representation of the transmissivity, T , is obtained from the calculated flow rate, Q_c , the head difference, dh , between the inlet and outlet planes, the fracture height, H , and the centre line length of the fracture, L .

$$T = \frac{Q_c}{H} \frac{L}{dh} \quad (\text{C3-1})$$

In Table C3-2 the ratio T/T_0 , where T_0 is the true, prescribed, transmissivity, is given for the five downstream positions and fracture thicknesses, b . For the first position, i.e. the fracture that is parallel to the y -coordinate, the transmissivity is represented exactly in the grid. For other angles it is found, as expected, that the error generally increases with decreasing b/Δ . In Table C3-2 also the average T/T_0 as a function of b/Δ can be found. The average ratio for all 25 tested situations is 0.984.

A comment may be needed to the value 1.007 ($x = 90$, $z = 70$, $b/\Delta = 2.0$) in Table C3-2. It is expected that the method gives $T/T_0 \leq 1.0$ for all thicknesses and all angles the fracture forms with the coordinate directions. The explanation for values larger than 1.0 is that the mean streamline may be shorter than the centreline of the fracture, see Figure C3-1. The T -values in Table C3-2 were all calculated using the centreline of the fracture as the distance between the inlet and outlet plane and may hence overestimate the length somewhat.

Table C3-2. Single fracture in a 3D domain. The transmissivity as represented in the computational grid, T , normalised with the true transmissivity, T_0 , for various fracture thicknesses and orientations.

Fracture coordinates at downstream boundary [m]	Transmissivity ratio, T/T_0				
	Fracture thicknesses, b/Δ				
	2.0	1.0	0.5	0.25	0.125
x = 10.0, z = 10.0	1.000	1.000	1.000	1.000	1.000
x = 30.0, z = 25.0	0.997	0.993	0.981	0.953	0.949
x = 50.0, z = 40.0	0.997	0.989	0.970	0.947	0.926
x = 70.0, z = 55.0	1.001	0.995	0.983	0.969	0.966
x = 90.0, z = 70.0	1.007	1.002	0.996	0.993	0.989
Average	1.000	0.996	0.986	0.972	0.966

Conclusion

It is concluded that the flow through a single fracture, with arbitrary orientation to the coordinate directions, can be expected to be accurately predicted (maximum error about 1%) provided that $b/\Delta > 1.0$. If $b/\Delta = 0.125$ the average error is about 3%, but for some fracture orientations an error of 5% can result.

Case C4: Many fractures in a box

Introduction

This case is based on the same computational domain as Case C3 (see Figure C3-1). It is thus a box with dimensions 100·100·100 metres, which is discretized using a maximum cell size, Δ , of 2 metres. A range of thicknesses, b , will be considered, but the height, H , of the fractures will be held constant and equal to 5 metres. 25 fractures will be generated with start and end positions randomly distributed on the squares $10.0 < x < 90.0$, $10.0 < z < 90.0$. The total flow rate, Q_t , will be equal to the sum of the flow in each fracture:

$$Q_t = \sum Q = \sum HT \frac{dh}{L} = HTdh \sum \frac{1}{L} \quad (\text{C4-1})$$

where dh is the applied head difference, T the fracture transmissivity and L the length of a fracture.

The objective of the test case is to evaluate how well we can represent the transmissivity of several, randomly oriented, crossing fractures.

Numerical simulation

In order to calculate the average fracture transmissivity as represented in the grid, T , we need to know the total flow rate and the sum of L^{-1} , where L is the fracture length. These lengths are calculated and stored during the generation of the fractures. The generated fracture system, consisting of 25 fractures, is shown in Figure C4-1. As can be seen a complex system of crossing fractures is generated. Simulations were carried out for a range of fracture thicknesses and the average fracture transmissivity, T , was estimated from Equation C4-1.

The simulation parameters are summarised in Table C4-1.

Results/discussion

Results from simulations are found in Table C4-2. As for the previous test cases we find that the error increases with decreasing fracture thickness. For $b/\Delta = 2.0$ the ratio $T/T_0 > 1$; this is probably due to the estimate of the mean streamline length, discussed in the previous test cases.

Conclusion

It is concluded that the flow rate through a fracture network in 3D is calculated correctly by DarcyTools, provided the fracture thickness (b/Δ) is not too small.

Table C4-1 Simulation parameters.

Domain	100·100·100 metres.
Boundary conditions	Fixed pressure on two opposite faces ($y=0.0$ and 100 metres).
Fracture thickness	Varied; $b/\Delta = 0.125, 0.25, 0.5, 1.0$ and 2.0.
Fracture transmissivity	$b \cdot 10^{-4}$ m ² /s.
Grid	$dx_{\max} = dy_{\max} = dz_{\max} = 2$ m.

Table C4-2. Many fractures in a 3D domain. The average transmissivity as represented in the computational grid, T , normalised with the true transmissivity, T_0 , for a range of fracture thicknesses.

Fracture thickness/ Δ	Average transmissivity
2.0	1.011
1.0	1.000
0.5	0.990
0.25	0.971
0.125	0.960

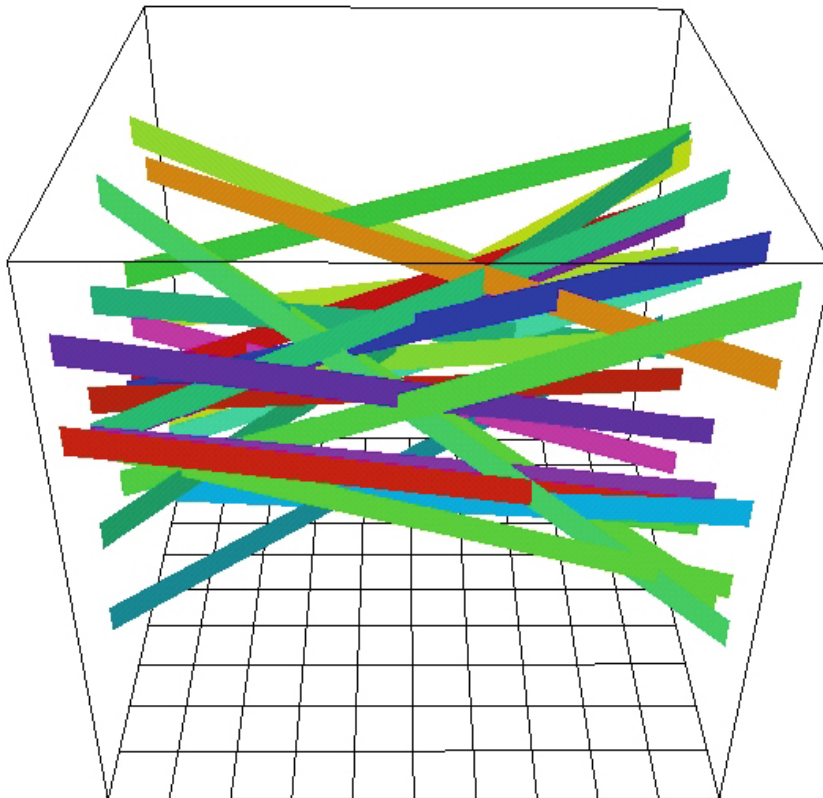


Figure C4-1. 25 fractures in a 3D domain. Illustration of the fracture system. The bottom of the box has been marked with a grid. Colours do not indicate any varying property.

Case C5: Percolation theory

Introduction

Percolation theory deals with the question whether two, or more, faces of a box are connected through a fracture network. Below a certain fracture density, d , (number of fractures per unit volume) the box faces are not connected, while they are connected above this value. The critical density, d_c , is called the percolation threshold. Estimates of d_c for various fracture networks can be found in the percolation literature and we want to ensure that our fracture network connects the box faces at the correct fracture density.

In a numerical simulation only finite size systems can be considered, while theoretical estimates of d_c often assume infinite systems. Many studies are also restricted to orthogonal fracture sets; a recent example is /Bour and Davy 1998/. Fewer results are available for the situation we have in mind. However, in /Robinson 1984/ randomly oriented square planes in a finite volume are studied and a critical density is given. The percolation criterion was that all six faces should be connected by one single cluster. The critical density given by Robinson for a box of 20·20·20 m³ filled with thin squares of side length one metre is 1.231 planes per unit volume; this value will be used as a reference.

A fracture network, at the critical fracture density, is shown in Figure C5-1. The fractures have random positions and orientations and a side length of 10 metres; all isolated fractures and fracture clusters have been removed.

The objective of the case is to show that a fracture network at the percolation threshold results in connected flow channels, when the network has been represented as grid cell conductivities.

Numerical simulations

Thin (thickness = 0.1 m) squares (1·10 m) will be distributed randomly in a box with dimensions 100·100·100 metres. Also the orientation of the fractures will be random.

A range of fracture densities will be tested and for each a flow calculation will be carried out. The relation between the flow rate, Q , and the fracture density is sought.

The simulation parameters are summarised in Table C5-1.

Table C5-1 Simulation parameters.

Domain	100·100·100 metres.
Boundary conditions	Fixed pressure on two opposite faces ($y = 0.0$ and 100 metres).
Fracture size	10·10·0.1 metres.
Fracture transmissivity	10^{-4} m ² /s.
Fracture density	Varied: $0.8 \cdot 10^{-3} \rightarrow 1.5 \cdot 10^{-3}$ m ⁻³ .
Grid	$dx_{\max} = dy_{\max} = dz_{\max} = 2$ m.

Results/discussion

The main result is given in Figure C5-2, where the flow rate versus the fracture density is shown. The two vertical lines give the estimated critical density as given by /Robinson 1984/ (discussed above) and /Charlaix et al. 1984/:

$$p = d \cdot (\text{average area of the fractures}) \cdot (\text{average half perimeter}) \quad (\text{C5-1})$$

/Charlaix et al. 1984/ proposed that the dimensionless number p must lie between 1.5 and 3 at the percolation threshold. The line in Figure C5-2 was based on a $p = 2.25$, which is in the middle of the range given.

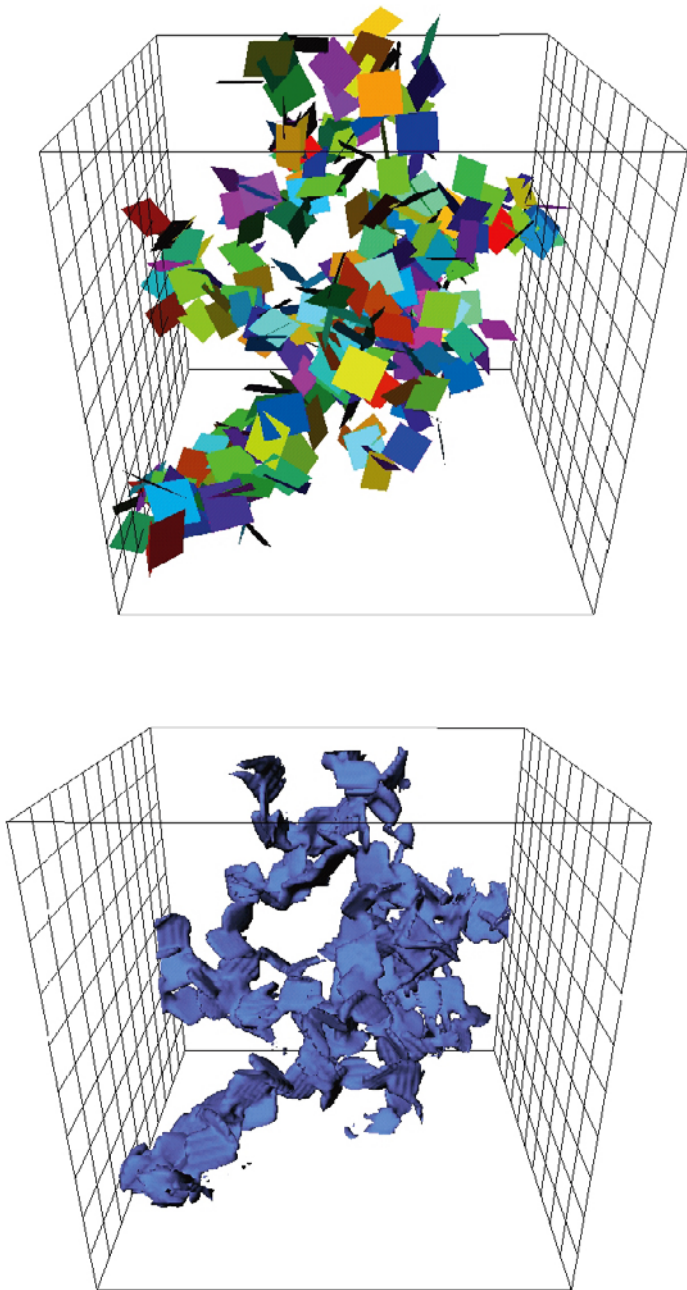


Figure C5-1. A fracture network that connects two opposite faces of the box (top) and the corresponding flow channels. Fracture density at the percolation threshold. Fracture size is 10 metres. The two connected sides of the box have been marked with grids.

The results are regarded as evidence that fracture connectivity is maintained when a network is represented as grid cell conductivities. As we are using networks at the percolation threshold, the network represents the weakest possible connection between the two box faces; still flow channels are generated.

An important aspect of the problem considered is the probabilistic nature of d_c (both position and orientation are random variables). It is hence not possible to estimate d_c from a single realisation of the network. An analysis that considers this aspect, and also analyses a network with fractures of a side length 5 metres, is given in /Svensson 2001/.

Conclusion

It has been shown that, a fracture network at the percolation threshold, represented as grid cell conductivities, results in a connected flow system.

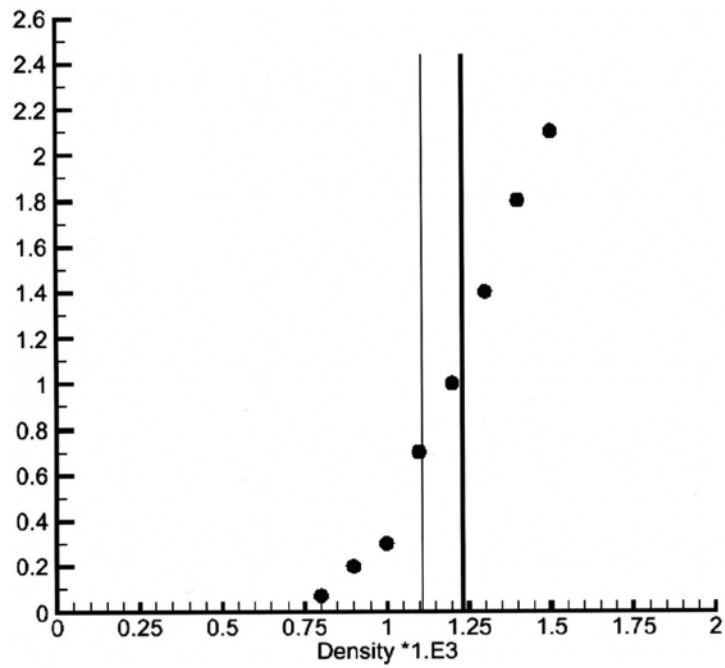


Figure C5-2. Predicted (• • •) relation between fracture density and flow through the domain. Lines represent estimates of d_c from the literature; (—) /Charlaix et al. 1984/, (—) /Robinson 1984/.

Case C6: Diffusion in a dead-end fracture

Introduction

This test case, see Figure C6-1, has previously been used to verify that a correct flow rate through a single fracture is calculated. Now, it is the diffusive transport that is in focus. Initially the fracture has a concentration (of some substance) of 1.0. A zero flux boundary condition is prescribed at $y = 10$ metres and a concentration of 0.0 is prescribed for $y = 0$ metres. The fracture position at the downstream boundary is varied in order to test a wide range of angles to the coordinate directions. Also a range of thicknesses was tested, but the height of the fracture was kept constant at 0.5 metres.

This problem has an analytical solution, for example presented by /Versteeg and Malalasekera 1995/, which reads:

$$c(x^1, t) = \frac{4}{\pi} \sum_{n=1}^{\infty} \frac{(-1)^{n+1}}{2n-1} \exp(-D_a \lambda_n^2 t) \cos(\lambda_n x^1) \quad (\text{C6-1})$$

where $\lambda_n = \frac{(2n-1)\pi}{2L}$, and t is time, L total length of the fracture, x^1 coordinate starting from the zero flux boundary and following the fracture and D_a the diffusion coefficient.

The objective of the test case is to verify that the numerical solution is in agreement with the analytical one.

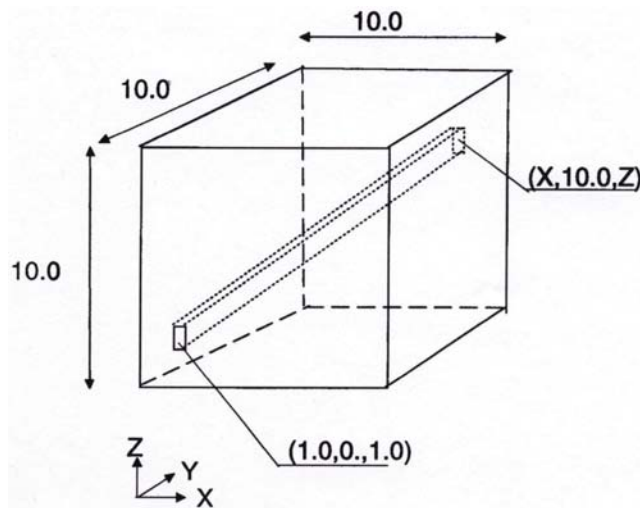


Figure C6-1. Diffusion in a dead-end fracture. Outline of situation studied. All distances in metres.

Numerical simulation

The time scale of the problem can be estimated as L^2/D_a . As we are interested in “long time storage of water” we choose $D_a = 10^{-10} \text{ m}^2/\text{s}$, which gives a time scale of the order of 10^{12} s . The integration time will be 10,000 years, which is equal to $3 \cdot 10^{11} \text{ s}$.

The simulation parameters are summarised in Table C6-1, see also Figure C6-1.

Table C6-1. Simulation parameters.

Domain	10·10·10 metres.
Initial and Boundary conditions	$c = 1, t = 0.$ $c = 0, t > 0$ at $y = 0.$ $\partial c/\partial y = 0$ at $y = 10.$
Fracture dimension	Height = 0.5 metres, thickness varied (see Result section).
Fracture position	Fixed at $y = 0$ metres boundary (see Figure C6-1), varied at $y = 10$ metres (see Result section).
Diffusion coefficient	$10^{-10} \text{ m}^2/\text{s}.$
Grid	$dx_{\max} = dy_{\max} = dz_{\max} = 0.2 \text{ m}.$

Results/discussion

Results are presented in Table C6-2. Five downstream fracture positions and four fracture thicknesses were tested. The five downstream fracture positions will give a fracture that, for the first position, is parallel to the y -coordinate while the last position gives a fracture that almost follows a diagonal in the box. Note also that the x - and z -coordinates for the zero flux boundary are different; this ensures that the fracture will have different angles to all three coordinate directions (except for the first position). The concentration at the zero flux end of the fracture is normalised with the analytically determined concentration, c_a , all after 10^4 years.

Table C6-2. Diffusion in a dead-end fracture. Concentration as represented in the grid, c , normalised with the true concentration, c_a , for various fracture thicknesses and orientations. All for a time of 10,000 years and at the zero flux boundary.

Fracture coordinates at zero flux boundary [m]	Analytically determined concentration, c_a	Concentration (c/c_a)			
		Fracture thickness (b/Δ)			
		0.1	0.5	1.0	2.0
X = 1.0, Z = 1.0	0.588	1.0	1.00	1.00	1.00
X = 3.0, Z = 2.5	0.612	1.05	1.02	1.01	1.01
X = 5.0, Z = 4.0	0.685	1.05	1.02	1.01	1.00
X = 7.0, Z = 5.5	0.772	1.02	1.01	1.01	1.00
X = 9.0, Z = 7.0	0.852	1.00	1.00	1.00	1.00
	Average	1.02	1.01	1.01	1.00

From Table C6-2 one may conclude that accurate concentrations are calculated provided b/Δ is not too small; if b/Δ is larger than 0.5 the error is less than 2%. In Case C3, it was found that the flow rate through a single fracture in a 3D domain was under-predicted with a few percent. The error in the concentrations has the same origin, as the diffusive flux is represented in the grid by a procedure that is analogous to that of the Darcy flux.

The concentration at the zero flux boundary as a function of time is given in Figure C6-2. As can be seen, the numerical solution is in fair agreement with the analytical one also for the development in time.

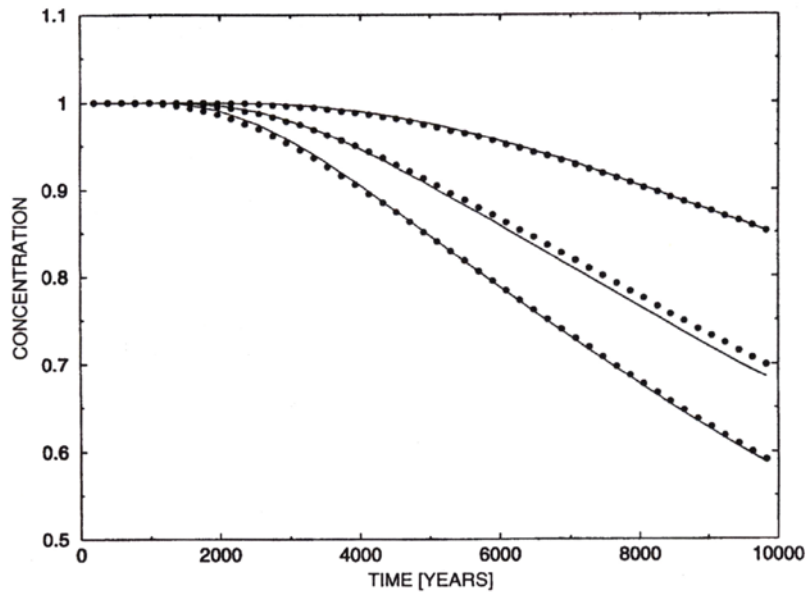


Figure C6-2. Diffusion in a dead-end fracture. Concentration at the zero flux boundary for three positions of the fracture ($x = 9.0, z = 7.0$ (top) $x = 5.0, z = 4.0$ (middle) and $x = z = 1.0$ (bottom)). Solid line gives the analytical solution.

Conclusions

Accurate diffusive transport is calculated for a single fracture of varying thickness and orientation in a 3D domain, provided the fracture thickness in relation to the grid size is not too small. If $b/\Delta > 0.5$, the maximum error in the calculated concentrations is found to be less than 2%.

Case C7: Matrix-fracture temperature problem

Introduction

This study concerns the convective-conductive processes in a fracture plane and the surrounding rock matrix, see Figure C7-1. A point heat source is located at (7.875, 0.125, 0.125) (cell centre coordinates) and the steady state temperature distribution in the fracture and the rock is sought.

An analytical solution for this case is given by /Probert and Claesson 1997/. They found that the temperature distribution is governed by a dimensionless parameter, p :

$$p = \frac{\rho_w c_w q_{wc}}{2\lambda} \quad (C7-1)$$

where

ρ_w = water density [kg/m^3]

c_w = water heat capacity [$\text{J}/\text{m}^3 \text{ } ^\circ\text{C}$]

q_{wc} = water flow in fracture [m^3/ms]

λ = heat conductivity of the rock [$\text{W}/\text{m } ^\circ\text{C}$]

For further details, see /Probert and Claesson 1997/. The objective of this test case is to compare the numerical and the analytical solution. Two different p -values will be considered.

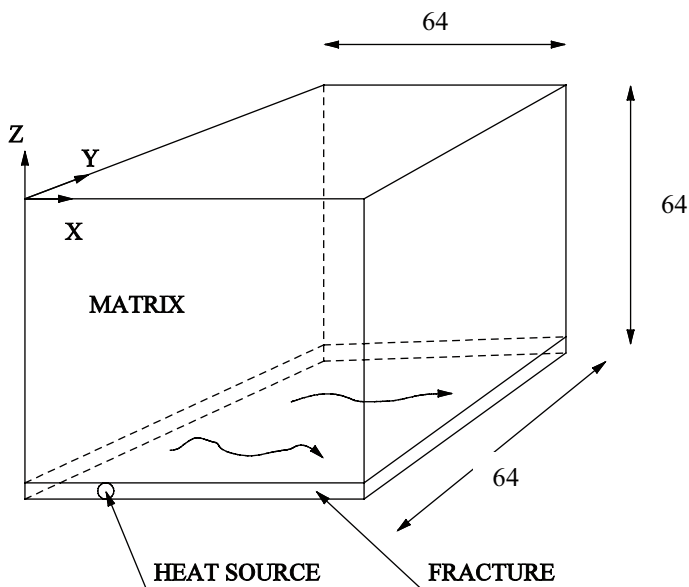


Figure C7-1. Outline of the situation studied.

Numerical simulation

The general outline of the computational domain is given by Figure C7-1. Additional input data are summarized in Table C7-1. The prescribed pressures at the $x = 0$ and $x = 64$ boundaries will give a uniform flow q_{wc} , in the x -direction.

Note that due to symmetry conditions only one quarter of the domain is specified in the numerical solution.

Table C7-1. Simulation parameters.

Domain	64·64·64 [m ³].
Boundary conditions	$P_{x=0} = 2.93 \cdot 10^5$ [Pa]. $P_{x=64} = 0$. Zero flux on other boundaries. Temperature put to zero at $z = z_{\max}$, $y = y_{\max}$ and at fracture inlet.
Heat source	600/4 = 150 [W].
Properties	Viscosity = $1.78 \cdot 10^{-3}$ [kg/ms]. Fluid heat capacity = 4,200 [J/kg °C]. Density = 1,000 [kg/m ³]. Porosity = 0.01. Permeability = 10^{-12} [m ²]. Thermal conductivity = 3.5 [W/m °C]. Rock thermal capacity = $2 \cdot 10^6$ [J/m ³ °C].
Grid	Expanding from the heat source.

Results/discussion

The numerical solution is compared with the corresponding analytical solution for $p = 1$, Figure C7-2, and $p = 5$, Figure C7-3. As can be seen, a good agreement is obtained for both p values.

The numerical solution was found to be sensitive to the boundary conditions at $z = z_{\max}$ and $y = y_{\max}$. It was hence necessary to increase the domain size in these directions until the near source temperature fields were unaffected by the boundary conditions. This explains the large domain size in these directions.

Conclusion

The temperature distribution in a fracture-matrix system is studied. A good agreement between the numerical and analytical solutions has been demonstrated.

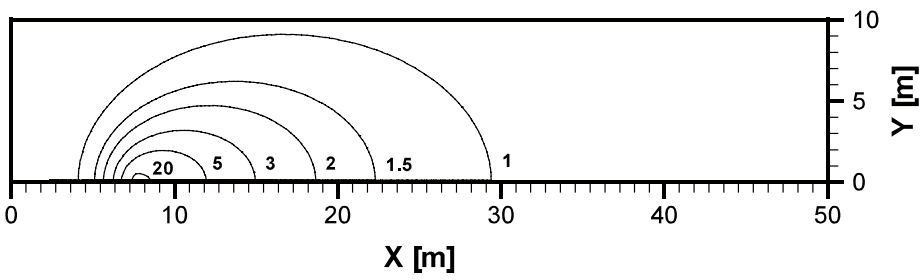
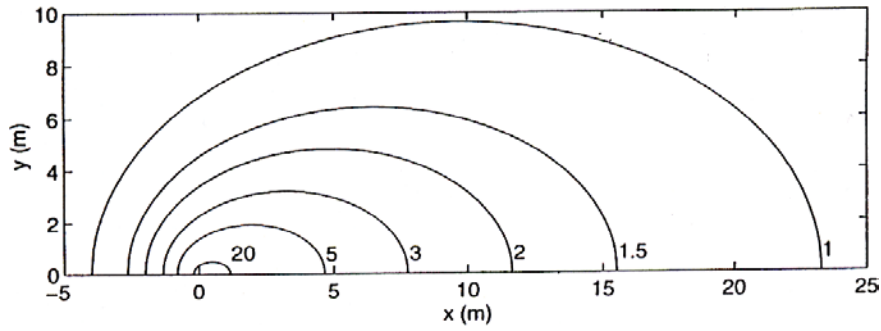


Figure C7-2. Temperature distribution in the fracture plane for $p = 1$. Analytical (top) and numerical solution. Note that the origo in the x -direction is different in the two figures.

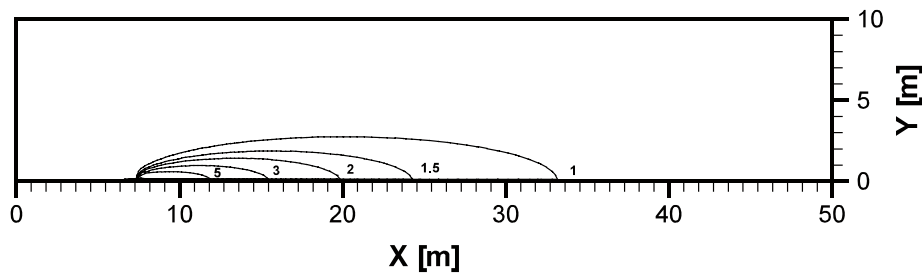
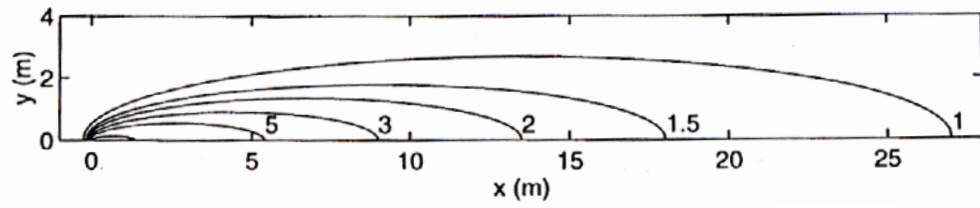


Figure C7-3. Temperature distribution in the fracture plane for $p = 5$. Analytical (top) and numerical solution. Note that the origo in the x -direction is different in the two figures.

Case D1: Taylor dispersion, PARTRACK

Introduction

If a cloud of particles is introduced in a fully developed flow between two parallel walls, the particles will be dispersed longitudinally at a rate given by /Sahimi 1995/:

$$D_L = \frac{2}{105} \frac{h^2 u^2}{D_m} \quad (\text{D1-1})$$

where D_L is the longitudinal dispersion coefficient, h half the aperture, u the mean velocity and D_m the molecular diffusion coefficient of the solute the particles represent. When we use PARTRACK to simulate Taylor dispersion we subdivide the space between the two walls into a number of layers.

The objective of this test case is to verify that PARTRACK predicts Taylor dispersion correctly.

Numerical simulation

Input data are summarised in Table D1-1.

Table D1-1. Simulation parameters.

Domain	10·0.1·5·10 ⁻⁴ [m ³].
Boundary conditions	At $x = 0$ a fixed flux is prescribed, at $x = 10$ the pressure is fixed to zero. 10,000 particles were injected as a Dirac pulse at $x = 0$.
Properties	The fixed flux conditions give a velocity of 10 ⁻⁴ m/s, other properties are of no significance. Molecular diffusion coefficient, D_m , is varied.
Grid	$dx_{\max} = 0.1$ m.

Result/discussion

Three runs, with D_m equal to 10⁻⁹, 10⁻¹⁰ and 10⁻¹¹ m²/s respectively, were carried out in order to compare the simulated dispersion with Equation D1-1. The result can be studied in Figure D1-1. From the breakthrough curves the mean arrival time and the standard deviation, σ , was calculated. The standard deviation is then related to the longitudinal dispersion coefficient, D_L ($\sigma = \sqrt{2D_L t}$, where t is the mean transport time). As can be seen a perfect agreement between the analytically determined and simulated dispersion is obtained. The breakthrough curves, also shown in Figure D1-1, show that the Taylor dispersion effect is small for $D_m = 10^{-9}$ m²/s, while a significant spread is obtained for $D_m = 10^{-11}$ m²/s. This result is of course related to the parameters and geometry used in this test case.

Conclusion

The results presented show that PARTRACK predicts Taylor dispersion in perfect agreement with the analytical solution.

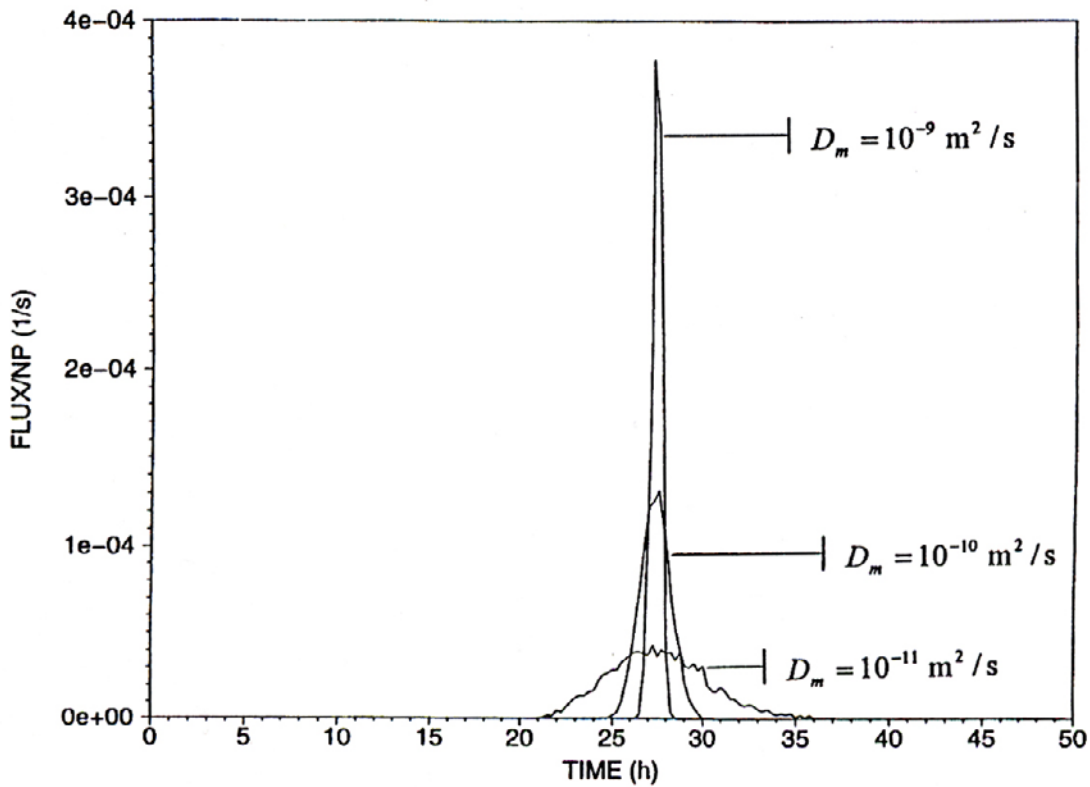
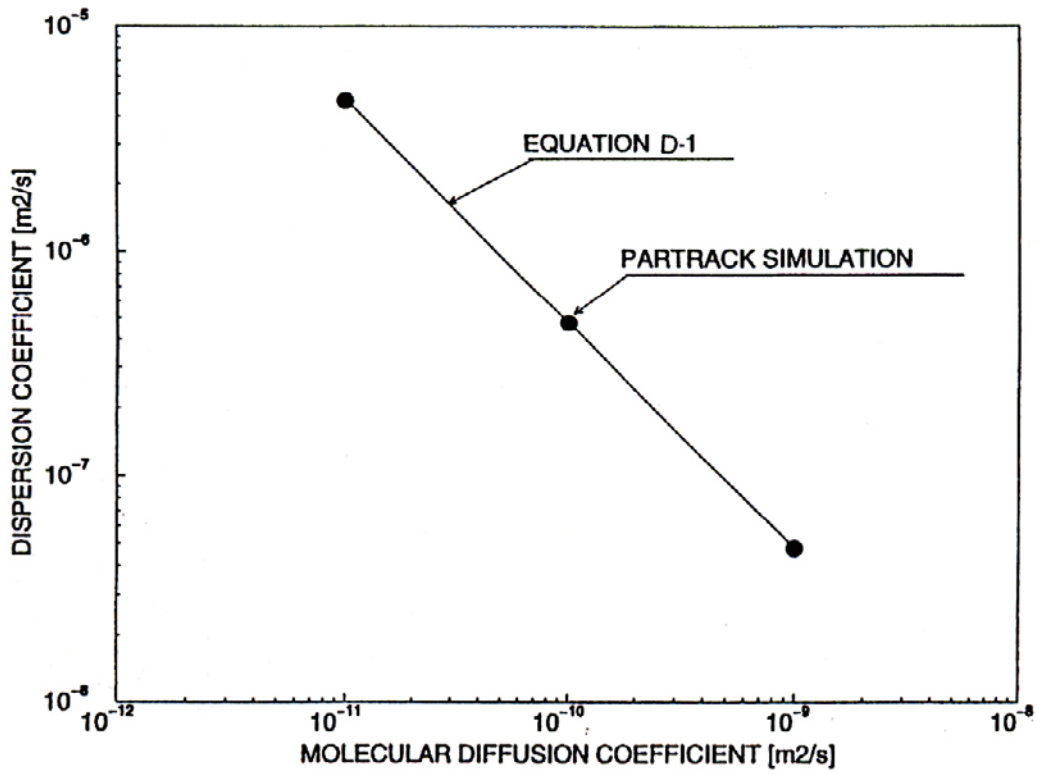


Figure D1-1. Taylor dispersion in a single fracture. Comparison with Equation D1-1 (top) and breakthrough curves

Case D2: Breakthrough curve, PARTRACK

Introduction

The objective of this study is to compare the solutions given by DarcyTools with the analytical solutions for single rate diffusion. The multi-rate diffusion model in DarcyTools is hence “degenerated” to a single rate model; this is done by specifying the late time slope, k , to $-3/2$.

The situation studied is outlined in Figure D2-1. A channel with constant width and aperture is bounded by an infinite matrix. A Dirac pulse injection is prescribed and the BTC at the outlet is studied.

The analytical solution of the equation describing this case is given by, for example, /Barten 1996/, /Cvetkovic et al. 1999/ and /Neretnieks 2002/. It can be written as:

$$m = \Theta(t - \alpha) \frac{\gamma}{2\sqrt{\pi}} (t - \alpha)^{-3/2} \exp\left(-\frac{\gamma^2}{4(t - \alpha)}\right) \quad (\text{D2-1})$$

where m is mass flux at the outlet, $\Theta(t)$ Heaviside step function and t time. The two parameters α and γ are defined as:

$$\alpha = R_m \theta_m L / q, \quad (\text{D2-2})$$

$$\gamma = L \delta_f \theta_{im} \sqrt{D_w R_{im}} / q \quad (\text{D2-3})$$

with definitions of parameters as given in Table D2-1, below.

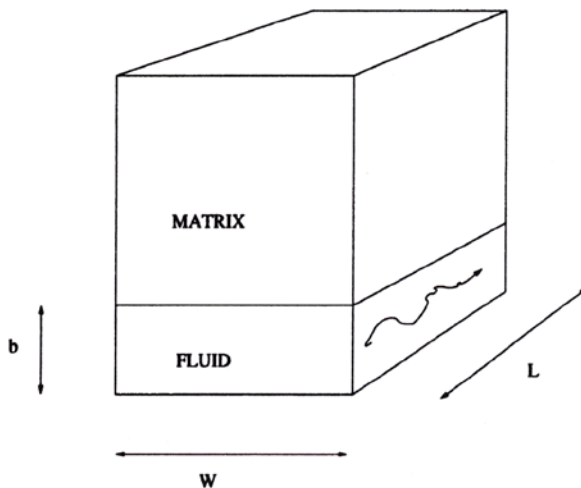


Figure D2-1. Outline of situation studied.

Numerical simulations

A reference case is given by the values specified in Table D2-1. The two parameters α_{\min} and α_{\max} are chosen to give a large enough range of capacity boxes. The specification of these does however influence the setting of β_n , the volume ratio for a non sorbing tracer. The analytical solution is for an infinite matrix, while a specification of α_{\min} implies a limitation. The method to calculate β_n for such a case is described in Report 1.

Table D2-1. Simulation parameters.

Domain	$L = 10.0, W = 0.1, b = 0.5 \cdot 10^{-3}$ Surface to volume ratio: $\delta_f = 1/b$
Properties	Porosity mobile zone: $\theta_m = 1.0$ Porosity immobile zone: $\theta_{im} = 0.05$ Retention mobile zone: $R_m = 1.0$ Retention immobile zone: $R_{im} = 1.0$ Diffusivity: $D_w = 10^{-10}$ Volume ratio: $\beta_n = 20.8$
Transport	Flow velocity: $q = 10^{-5}$ Injection: Dirac pulse $\alpha_{\min} = 10^{-9}/R_{im}$ $\alpha_{\max} = 5 \cdot 10^{-2}/R_{im}$

Result/discussion

For the reference data a perfect agreement with the analytical solution is obtained, see Figure D2-2.

For the cases to follow β was evaluated as: $\beta = \frac{R_{im} V_{im}}{R_m V_m} = \frac{R_{im}}{R_m} \cdot \beta_n$.

In Figure D2-3 the effect of changing R_m and R_{im} by a factor of five can be studied. The change from the reference case is calculated correctly.

Figure D2-4 shows consistency checks, which are based on the parameters α and γ , given by (D2-2) and (D2-3) respectively. In the first case (Figure D2-4, top), R_m , q and θ_{im} were all increased by a factor of 2.0. As both α and γ remain the same, the BTC should be unaffected. This is also found. Similarly we may increase θ_{im} with a factor of two and decrease D_w with a factor of four and still get the same BTC, which is also the case (Figure D2-4, bottom).

Conclusion

It is clear that the numerical solutions, based on a particle tracking technique, is in good agreement with the analytical solution of the governing advection/diffusion equation.

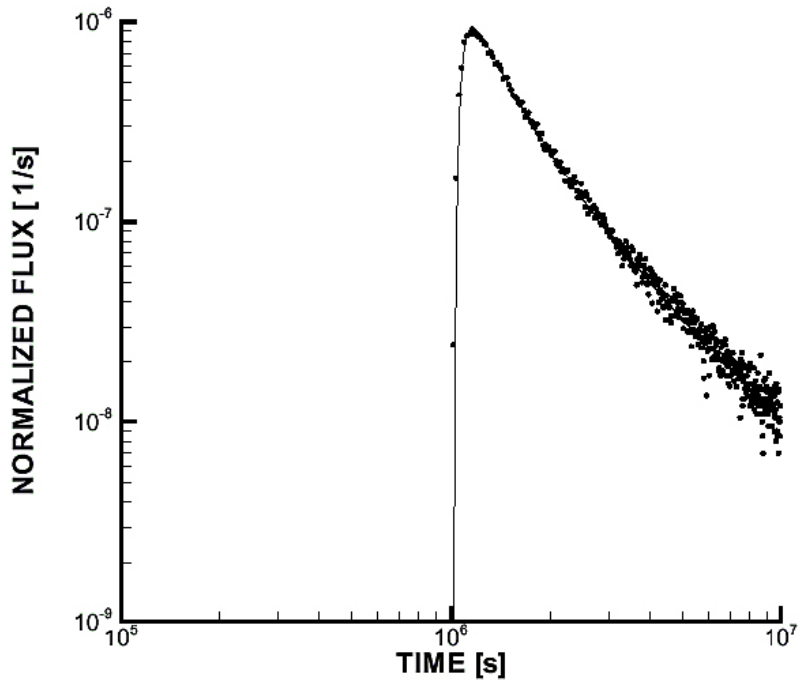
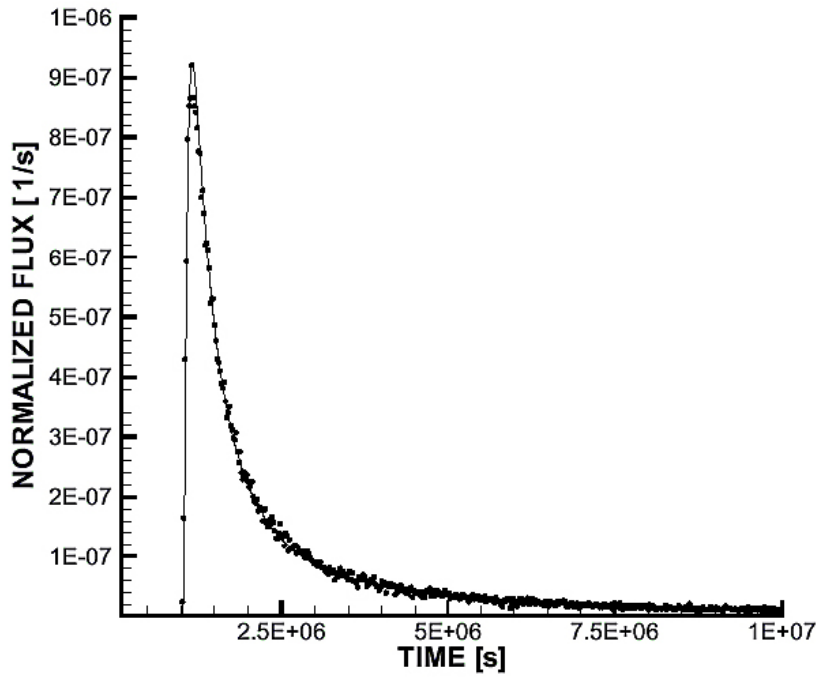


Figure D2-2. Comparison with the analytical solution for the reference parameters. Linear scale (top) and log-log scale. Solid line gives analytical solution.

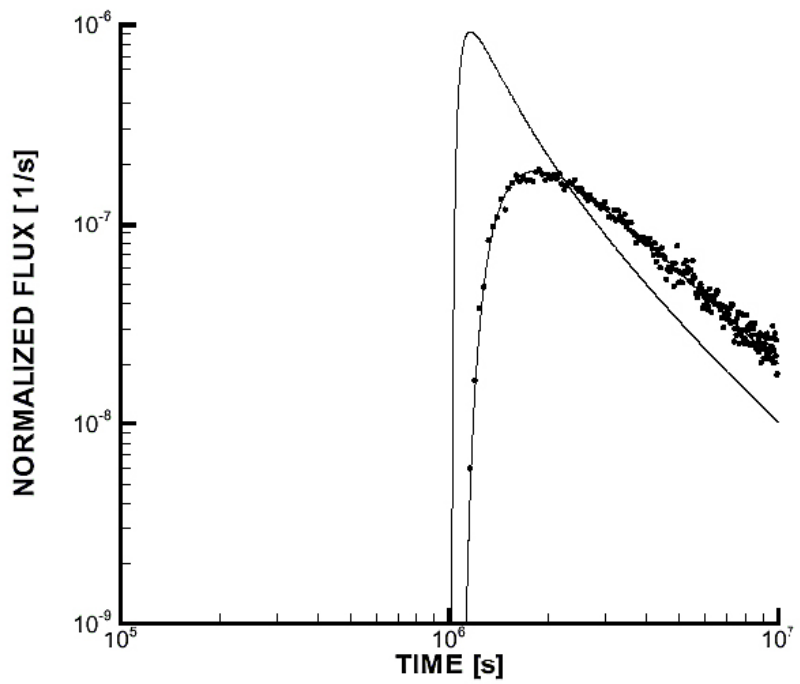
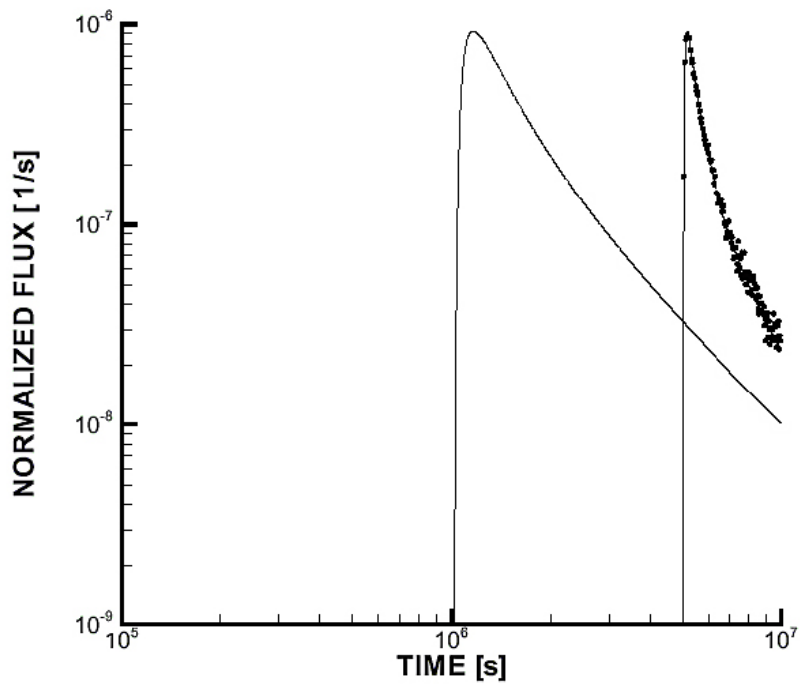


Figure D2-3. Effect of changing R_m (top) and R_{im} by a factor of five. Solid line gives analytical solution.

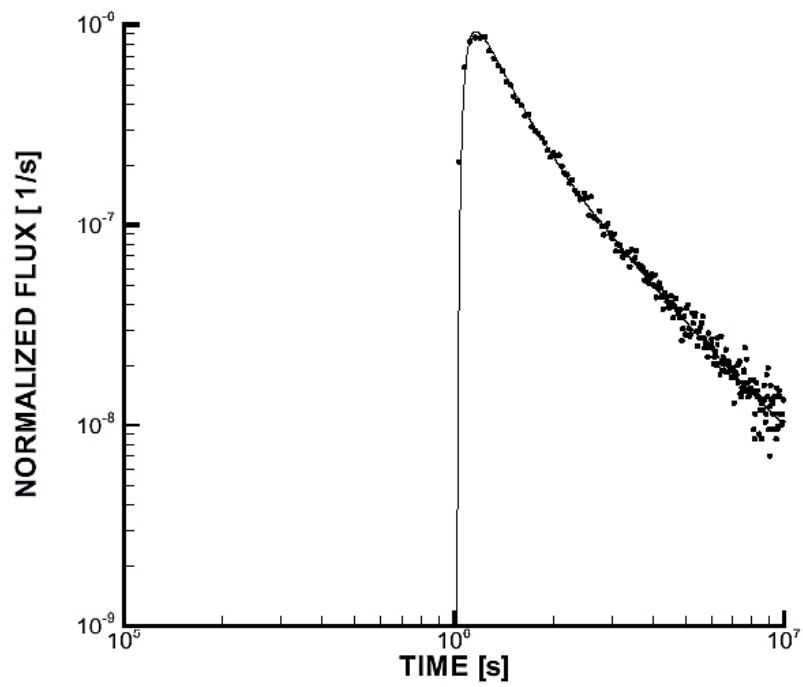
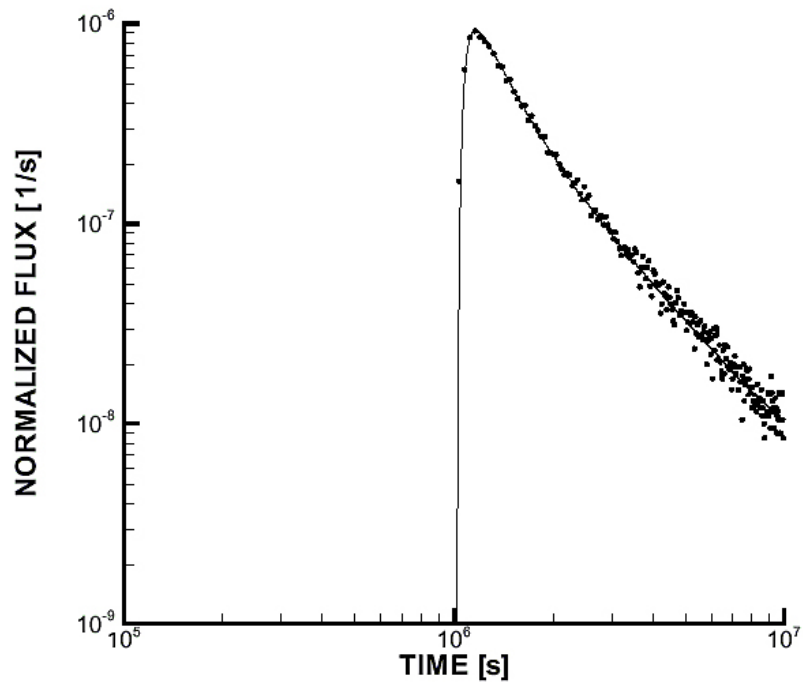


Figure D2-4. Consistency checks. R_m , q and θ_{im} increased (top), θ_{im} increased and D_w decreased.

Case D3: Breakthrough curve, adv/diff eqn

Introduction

The objective of this study is to compare the solutions given by DarcyTools with the analytical solutions for single rate diffusion. The single-rate diffusion model in DarcyTools is hence activated.

The situation studied is outlined in Figure D3-1. A channel with constant width and aperture is bounded by an infinite matrix. A Dirac pulse injection is prescribed and the BTC at the outlet is studied.

The analytical solution of the equation describing this case is given by, for example, /Barten 1996/, /Cvetkovic et al. 1999/ and /Neretnieks 2002/. It can be written as:

$$m = \Theta(t - \alpha) \frac{\gamma}{2\sqrt{\pi}} (t - \alpha)^{-3/2} \exp\left(-\frac{\gamma^2}{4(t - \alpha)}\right) \quad (\text{D3-1})$$

where m is mass flux at the outlet, $\Theta(t)$ Heaviside step function and t time. The two parameters α and γ are defined as:

$$\alpha = R_m \theta_m L / q, \quad (\text{D3-2})$$

$$\gamma = L \delta_f \theta_{im} \sqrt{D_w R_{im}} / q \quad (\text{D3-3})$$

with definitions of parameters as given in Table D3-1, below.

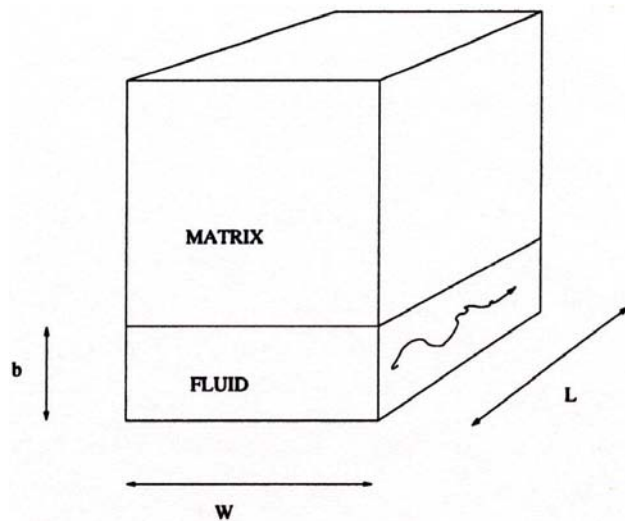


Figure D3-1. Outline of situation studied.

Numerical simulations

The case is given by the values specified in Table D3-1. The two parameters that specify the single rate model are α_D and β_n . The analytical solution is for an infinite matrix, while the numerical solution requires a specified thickness of the matrix. The thickness should hence be “large enough, not to influence the result”.

Table D3-1. Simulation parameters.

Domain	$L = 10.0$, $W = 0.1$, $b = 0.5 \cdot 10^{-3}$. Surface to volume ratio: $\delta_f = 1/b$. Thickness of matrix, $H = 0.1$ m.
Properties	Porosity mobile zone: $\theta_m = 1.0$. Porosity immobile zone: $\theta_{im} = 0.05$. Retention mobile zone: $R_m = 1.0$. Retention immobile zone: $R_{im} = 1.0$. Diffusivity: $D_w = 10^{-10}$. Volume ratio: $\beta_n = 10.0$ (calculated).
Transport	Flow velocity: $q = 10^{-5}$. Injection: Dirac pulse. $\alpha_D = D_w/H^2$.

Result/discussion

As the numerical solution is based on the advection/diffusion equation it is expected that numerical diffusion will influence the predicted break-through-curve. This is also seen in Figure D3-2, where the predicted BTC is compared with the analytical one. A fair agreement is however found.

Conclusion

The numerical solutions, based on an advection/diffusion equation, is in fair agreement with the analytical solution of the governing equation.

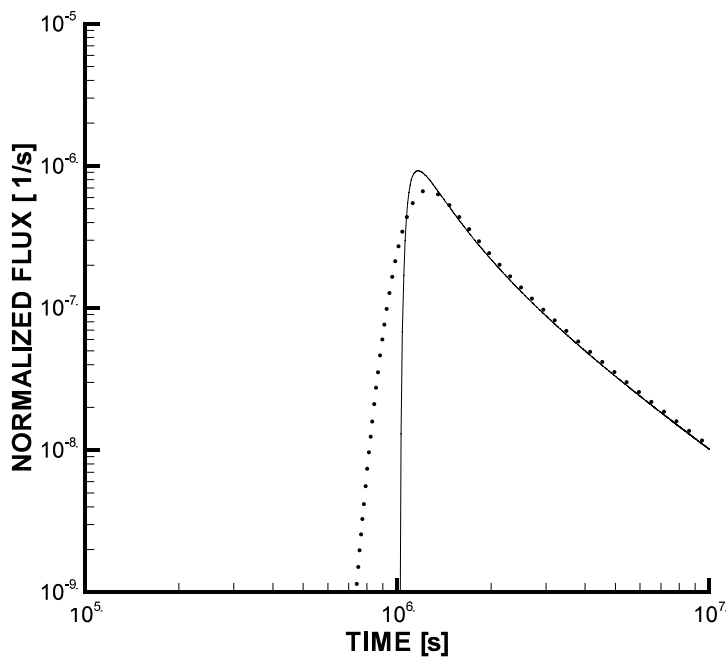


Figure D3-2. Comparison with analytical solution (solid line).

Case D4: Seven fractures in a 2D domain, PARTRACK

Introduction

The two dimensional fracture network considered is shown in Figure D4-1. A pressure gradient is applied, to give a flow from left to right with a pore velocity of about 10^{-4} m/s.

This case is of interest for the following reasons:

- It is possible to determine the flow in each part of the fracture network analytically.
- If we assume complete mixing in fracture intersections, one can determine analytically how a cloud of particles, injected at the upstream side, will leave through the outlets.

The analytical solution gives the flow-rates in each of the fracture sections. If we inject a cloud of particles in the central fracture, called fracture A-A, it will split up in fracture intersections in proportion to the flow rates (assuming complete mixing in fracture intersections). The fractions at the outlet plane are given in Figure D4-1, assuming that all fractures have the same transmissivity.

The objective is to verify that the numerical solution is in agreement with the analytical one. In particular it is of interest to see how a particle cloud is split up at intersections.

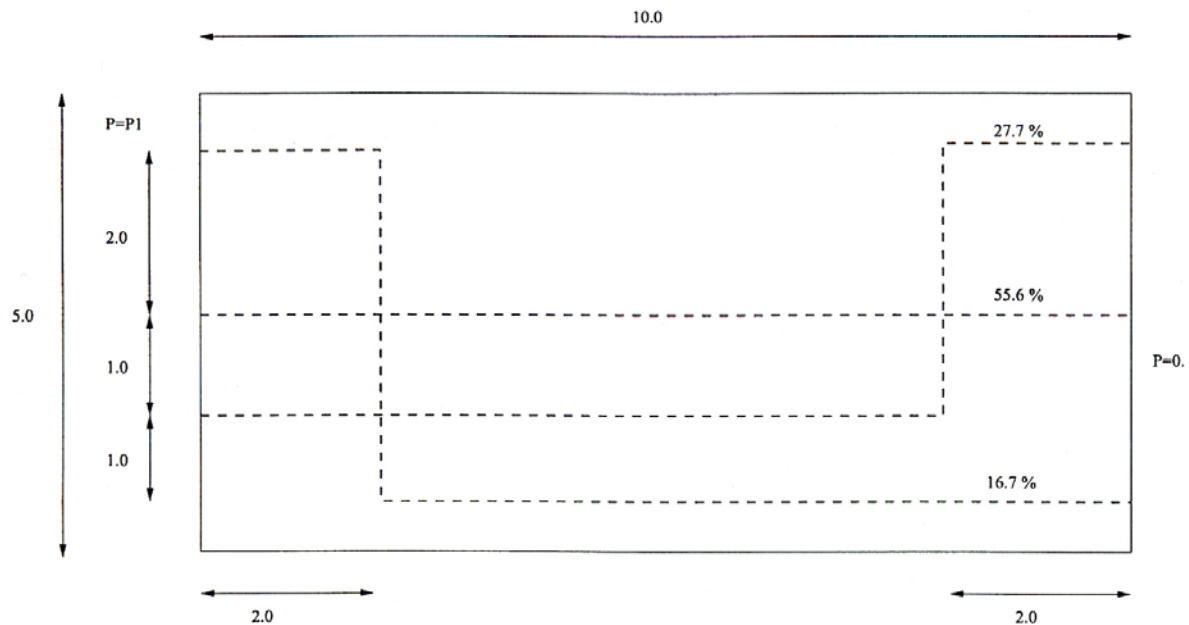


Figure D4-1. A fracture network. Outline of situation studied. The %-figures give the proportions for the split-up of a tracer cloud at the outlet boundary (assuming complete mixing).

Numerical simulations

The size of and fracture system in the domain is given in Figure D4-1. Additional input data are summarised in Table D4-1.

Table D4-1. Simulation parameters.

Domain	$2D, 10 \cdot 5 \text{ [m}^2\text{]}$
Boundary conditions	$P_{x=0} = 9,810 \text{ [Pa]}$ $P_{x=10} = 0$ zero flux on other boundaries.
Properties	Density = $1,000 \text{ [kg/m}^3\text{]}$ Viscosity = $2.0 \cdot 10^{-3} \text{ [kg/ms]}$ Permeability = $2.0 \cdot 10^{-12} \text{ [m}^2\text{]}$
Grid	$dx_{\max} = dy_{\max} = 0.025 \text{ m}$

Result/discussion

First a steady flow calculation is performed then 100,000 particles are injected in Fracture A-A at $x = 0$. From the analytical solution we know the flow in each part of the channel system and it is hence possible to calculate how a cloud of particles will split up at a fracture intersection. The underlying assumption is that the cloud will be split up in proportions to the outgoing flows at the intersection, i.e. the “fully mixed assumption”.

The result is summarised in Table D4-2. An almost perfect agreement is found.

Table D4-2. Distribution of particles at the boundary $x = 10$.

Solution	Outlet		
	Top	Middle (A-A)	Bottom
Analytical	27.7%	55.6%	16.7%
Numerical	27.5%	55.6%	16.9%

Conclusion

It has been shown that the “well mixed assumption at fracture intersections” is correctly implemented in the numerical algorithms.

Case D5: Three fractures in a 2D domain

Introduction

The two dimensional fracture network considered next is shown in Figure D5-1. A pressure gradient is applied, to give a flow from left to right with a pore velocity of about 10^{-4} m/s.

This case is of interest for the following reasons:

- It is possible to determine the flow in each part of the fracture network analytically.
- The transport time for a particle is known, whatever path it takes.
- If we assume complete mixing in fracture intersections, one can determine analytically how a cloud of particles, injected at the upstream side, will leave through the outlets.

The analytical solution gives the flow-rates in each of the fracture sections. If we inject a cloud of particles in fracture B-B, it will split up in fracture intersections in proportion to the flow rates (assuming complete mixing in fracture intersections). These fractions are given in Figure D5-1, assuming that all fractures have the same transmissivity. From the analytical solution we can thus get both the arrival time and size of each breakthrough pulse. In the numerical solution of the flow field we assume that the kinematic porosity of the fractures is equal to 0.05. The fracture thickness, b , will be varied in order to test a range of ratios b/Δ , where Δ is the grid size (equal to 0.1 metre). In all simulations 10^5 particles were injected in fracture B-B.

The main objective is to verify that the numerical solution is in agreement with the analytical one. It is a part of this objective to evaluate the sensitivity to the ratio b/Δ .

Numerical simulations

Input data are summarized in Table D5-1.

Table D5-1. Simulation parameters.

Domain	2D 10.5 metres.
P_1	9,810 Pa.
Fracture Conductivity	$5 \cdot 10^{-5}$ m/s.
Fracture thickness	b/Δ varied: 0.1, 0.5, 1.0 and 2.0.
Grid	400.200 cells, $\Delta = 0.025$ m.

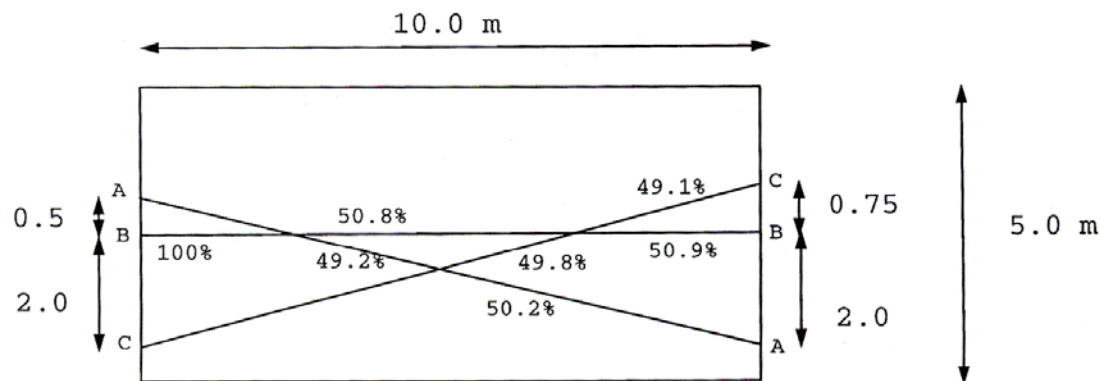


Figure D5-1. A fracture network. Outline of situation studied. The %-figures give the proportions for the split-up of a tracer cloud at the three fracture intersections (assuming complete mixing).

Result/discussion

We first calculate the flow. A cloud of particles, injected in fracture B-B, is then tracked by PARTRACK. The result can be studied in Figure D5-2. In order to understand the result one may first note that the transport time in fracture B-B is 27.8 hours and that all other pathways have longer transport times. The size of the pulses is explained by noting that 100% enters in fracture B-B, about 50% go each way in each crossing. The first pulse that leaves fracture B-B will thus contain about 25% of the injected pulse. It will however not be exactly 25% as the flow rates in the fracture sections are not exactly the same. As seen in Figure D5-2, the numerical solution is in good agreement with the analytical solution. One may question why we do not get an exact agreement. The answer is probably that we do not get the assumed split up of the particle cloud in fracture intersections. In the analytical solution we assumed that the cloud will split up in proportion to the outflows. In the numerical solution, we solve for the flow and transport in the intersection. The effect can be noted in the intersection between fractures A-A and C-C. The particles arrive in fracture A-A and should split up in about equal fractions in the two outlets. From Figure D5-2 it is seen that the numerical solution gives fewer particles in fracture A-A, as compared to the analytical solution. This is probably due to the local flow pattern in the fracture intersection. In the literature, see for example /Park and Lee 1999/, two concepts for solute transport in a fracture intersection are used; “complete mixing” and “streamline routing”. The effect described is due to streamline routing in the fracture intersection.

The results given in Figure D5-2 are based on a fracture thickness, b , of 0.05 m ($b/\Delta = 0.5$). The sensitivity to the fracture width is presented in Table D5-2, where results for $b/\Delta = 0.1, 0.5, 1.0$ and 2.0 are given. It is seen that the transport time does not vary strongly with b/Δ , while the size of the breakthrough pulse depends strongly on b/Δ (see for example fracture A-A). As discussed above, this is due to the two dimensional representation of the fracture intersection.

Conclusion

The transport times for a simple two dimensional fracture network are in agreement with the analytical solution. The simulated partitioning of a particle cloud in a fracture intersection is close to complete mixing for small fracture thicknesses, while the streamline routing effect is important when $b > \Delta$.

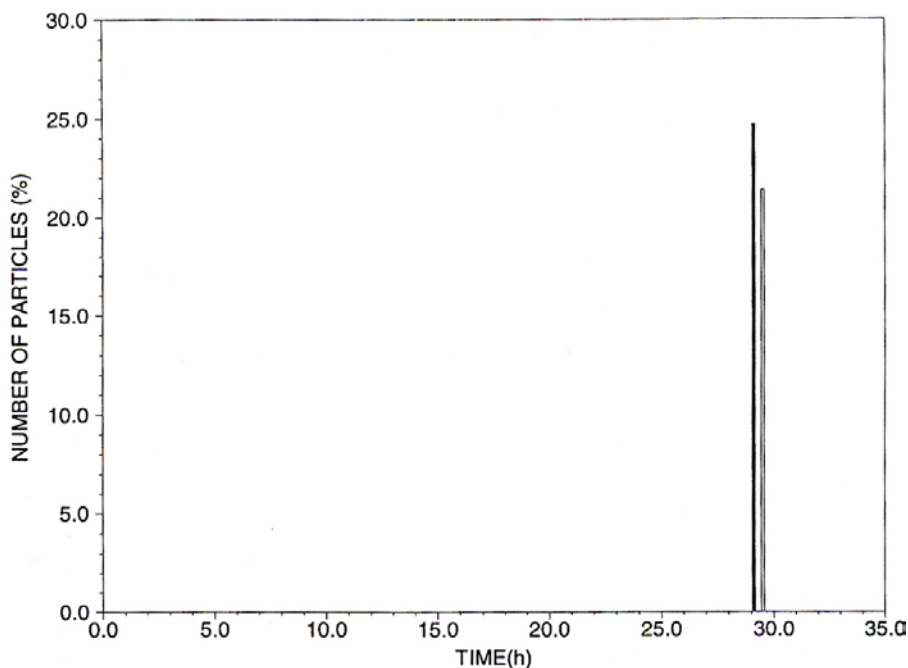


Figure D5-2. A fracture network. Breakthrough curve in fracture A-A. Solid bar gives the analytical solution.

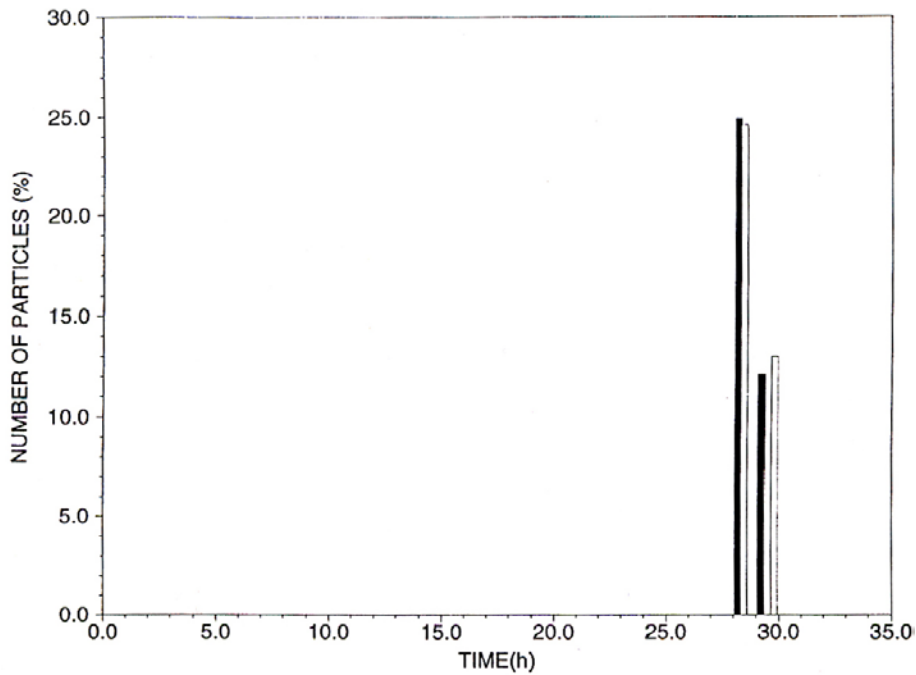
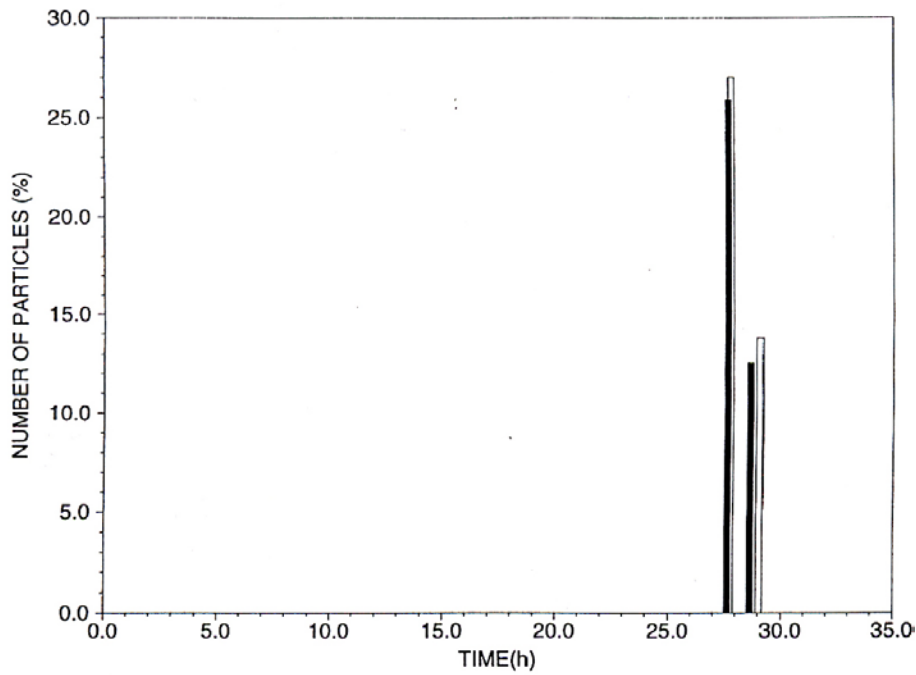


Figure D5-2. Cont. Breakthrough curves in fractures B-B (top) and C-C.

Table D5-2. A fracture network. Breakthrough curves (time, t , and fraction, f) in various fracture outlets as a function of normalised fracture thickness (b/Δ).

Breakthrough curve in fracture	Analytical solution		Fracture thickness normalised with Δ (b/Δ)							
	t_a (h)	f_a (%)	0.1		0.5		1.0		2.0	
			t/t_a	f/f_a	t/t_a	f/f_a	t/t_a	f/f_a	t/t_a	f/f_a
A-A	29.2	24.7	1.02	0.94	1.02	0.95	1.00	0.75	1.00	0.50
B-B	27.7	25.8	1.00	1.02	1.00	1.02	1.00	1.01	0.99	0.90
B-B	28.8	12.5	1.01	1.06	1.01	1.05	0.98	1.20	0.95	1.87
C-C	28.3	24.9	1.01	1.00	1.00	1.00	1.00	1.09	1.00	1.00
C-C	29.4	12.1	1.02	0.99	1.02	0.99	1.01	1.09	1.00	1.31

Case D6: Single fracture in a box, PARTRACK

Introduction

This test case is the same as used in Case C3, to evaluate how the flow rate through a single fracture varied with the orientation and thickness of the fracture. The situation studied is outlined in Figure D6-1. The pressure is held constant on two opposite faces ($y = 0.0$ m and $y = 10.0$ m) and a zero flux condition is used on all other boundaries. At the inflow boundary the position of the fracture is fixed, with centreline coordinates (1.0, 0.0, 1.0). The fracture position at the downstream boundary is varied in order to test a wide range of angles to the coordinate directions. Also a range of thicknesses were tested, but the height of the fracture was kept constant at 0.5 metres.

For each of the situations studied, a steady state flow calculation is first performed. PARTRACK is then used to calculate the transport time from the inlet to the outlet.

The objective is to verify that PARTRACK gives correct transport times for fractures of different thicknesses and orientations. As the flow and porosity is calculated in the flow model, the test case also evaluates the integrated performance of the flow and transport model.

Numerical simulations

Most of the simulations parameters are introduced in Figure D6-1, some further details are summarised in Table D6-1.

A systematic variation of the fracture thickness and the downstream position will be in focus in the simulations.

Table D6-1. Simulation parameters.

Domain	10·10·10 [m ³].
Boundary conditions	Fixed pressure difference (= 1 metre head) between two opposite faces. Zero flux on other faces.
Fracture dimensions	Height = 0.5 metres, thickness varied (see Result section).
Fracture position	Fixed at inflow boundary (see Figure D6-1), varied at outflow boundary (see Result section).
Fracture conductivity	10^{-4} m/s.
Grid	$dx_{\max} = dy_{\max} = dz_{\max} = 0.2$.

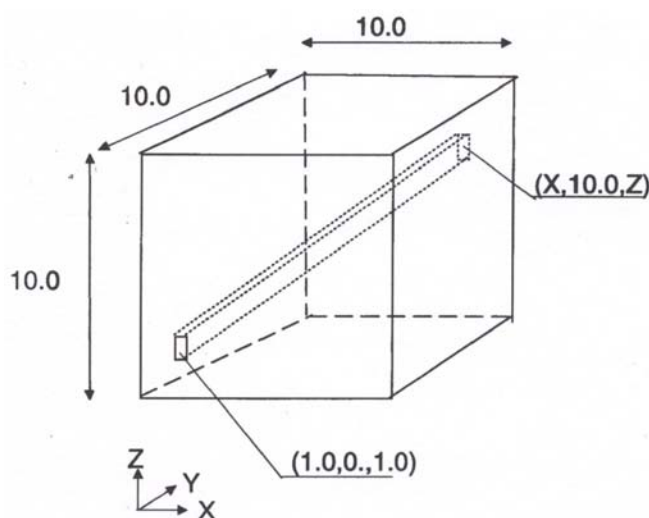


Figure D6-1. Outline of situation studied. A single fracture in a 3D domain. Outline of situation studied. All distances in metres.

Result/discussion

Results are presented in Table D6-2. Five downstream fracture positions and four fracture thicknesses were tested. The five downstream fracture positions will give a fracture that, for the first position, is parallel to the y -coordinate while the last position gives a fracture that almost follows a diagonal in the box. Note also that the x - and z -coordinates for the downstream positions are different; this ensures that the fracture will have different angles to all three coordinate directions (except for the first position). The transport times are normalised with the analytically determined transport time, t_a , which is easily obtained from the specified pressure gradient, kinematic porosity and fracture length.

From Table D6-2, one may conclude that accurate transport times are calculated provided b/Δ is not too small; if b/Δ is larger than 0.5 the error is less than 3%. In Case C3 it was found that the flow rate through a single fracture in a 3D domain was under predicted with a few percent. The error in the transport times is thus mainly due to the error in the flow rates, which can be concluded from a comparison with Table C3-2.

It is also of interest to note that the spread of the breakthrough curve in all simulations was small. Ideally all particles should arrive at the same time, but some numerical dispersion is present as particles will have different flow paths. The standard deviation of the breakthrough curve was however always less than 2% of the transport time and the numerical dispersion effect is hence small (as compared to other effects).

Conclusion

Accurate transport times are calculated for a single fracture of varying thickness and orientation in a 3D domain, provided the fracture thickness in relation to the grid size is not too small. If $b/\Delta > 0.5$, the maximum error in the calculated transport time is found to be less than 3%.

Table D6-2. A single fracture in a 3D domain. Transport time as represented in the grid, t , normalised with the true transport time, t_a , for various fracture thicknesses and orientations.

Fracture coordinates at downstream boundary [m]	Analytically determined transport time, t_a [h]	Transport time (t/t_a)			
		Fracture thickness (b/Δ)			
		0.1	0.5	1.0	2.0
X = 1.0, Z = 1.0	27.50	1.00	1.00	1.00	1.00
X = 3.0, Z = 2.5	29.02	1.06	1.02	1.01	1.00
X = 5.0, Z = 4.0	34.37	1.08	1.03	1.01	1.00
X = 7.0, Z = 5.5	42.97	1.04	1.02	1.01	1.00
X = 9.0, Z = 7.0	54.98	1.02	1.01	1.00	1.00
	Average	1.04	1.02	1.01	1.00

Case E1: Henry's problem

Introduction

Henry's problem is the most widely used, classic, test case for density stratified simulations. The basic situation in mind is that of sea water intrusion into a fresh water aquifer, see Figure E1-1. At the left boundary, the inland boundary, a fixed fresh water inflow is specified while the right side boundary has a prescribed hydrostatic pressure distribution based on a given salinity. The top and bottom boundaries are of zero mass flux type.

Henry's problem is discussed in detail in /Ségol 1994/, where also Henry's analytical solution and a number of numerical solutions are presented and discussed. The present study will be based on, and make reference to, the review of Henry's problem as given in /Ségol 1994/.

The objective of the test case is to simulate Henry's problem and compare the result with Henry's analytical solution and results from other models (all as presented in /Ségol 1994/).

Numerical simulations

The numerical simulation will be based on the parameters and boundary conditions specified in Table E1-1, see also Figure E1-1. We are seeking the steady state solution and the initial conditions are hence of no importance. The data within brackets in Table E1-1 are the values specified in /Ségol 1994/; here SI units are used throughout.

Table E1-1. Parameters for Henry's problem.

Domain	Rectangular section with a length of 200 m and a depth of 100 m.
Hydraulic Conductivity	$1.157 \cdot 10^{-5}$ m/s (= 1m/day).
Density difference	25 kg/m ³ .
Porosity	0.35.
Dispersion coefficient	$7.639 \cdot 10^{-7}$ m ² /s (= 0.066 m ² /day).
Fresh water inflow	$7.639 \cdot 10^{-8}$ m ³ /m ² , s.
Grid	Coarse: $dx_{\max} = dz_{\max} = 4$. Fine: $dx_{\max} = dz_{\max} = 2$.

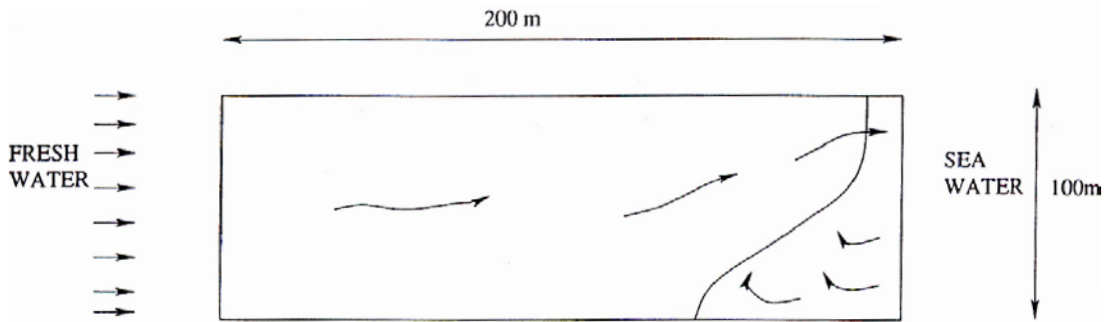


Figure E1-1. Illustration of Henry's, or the seawater intrusion, problem.

Result/discussion

Henry's analytical solution, and a number of numerical simulations, are shown in Figure E1-2. The sharp interface solution is the solution obtained if no mixing occurs between the salt and fresh water; this solution is included only as a reference. It is seen that Henry's solution gives a penetration length of about 90 metres, while the numerical models, shown in the same figure, give a penetration length of about 80 metres. DarcyTools is found to give a penetration length of about 85 metres.

This is a grid independent solution as can be seen in Figure E1-3; reducing the cell size with a factor of two does not change the penetration length.

One may question why the numerical models are not closer to the analytical solution. One possibility is the type of boundary conditions used at the "seaward side". Some model studies fixed the depth of the mixed water outflow region, while others let the model decide the depth of the division point between inflow and outflow. In the present study a hydrostatic assumption based on a fixed density difference was used for the whole vertical. Further discussions about possible causes of deviations between numerical and analytical solutions can be found in /Ségol 1994/.

Conclusion

It has been demonstrated that a grid independent solutions of Henry's problem, by DarcyTools, is in fair agreement with the analytical solution.

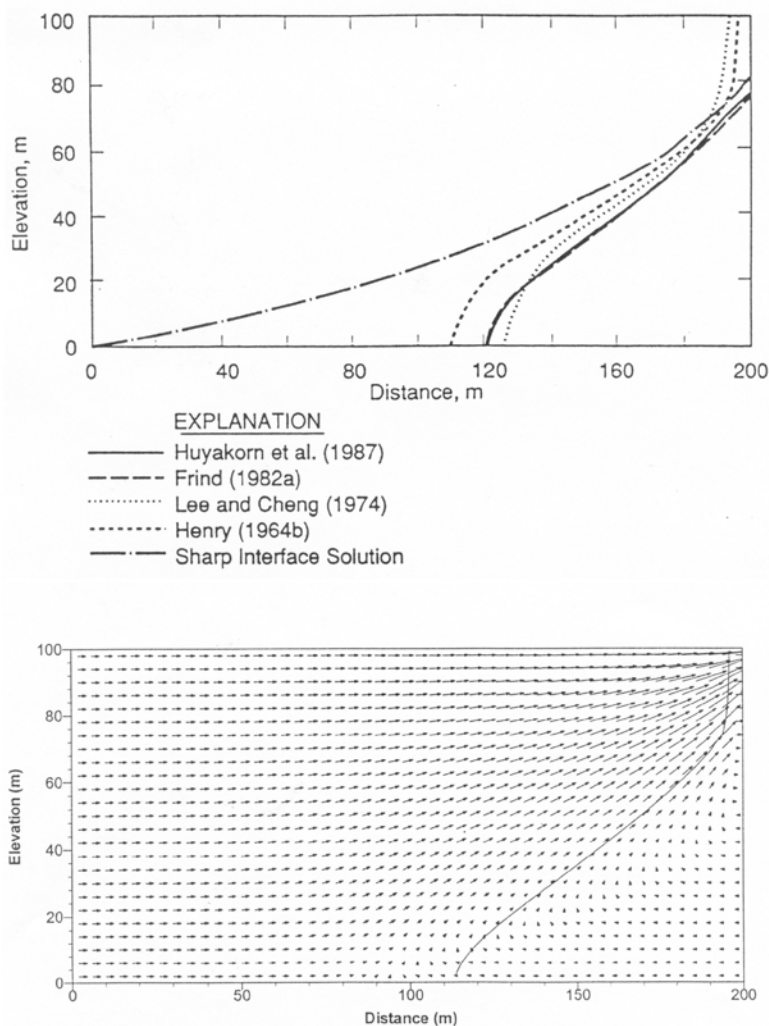


Figure E1-2. Comparison between Henry's solution and a number of numerical models (top), figure from /Ségol 1994/. Result from DarcyTools (bottom). The isochole $s = 0.5 s_{max}$ is chosen to illustrate the salt-water wedge.

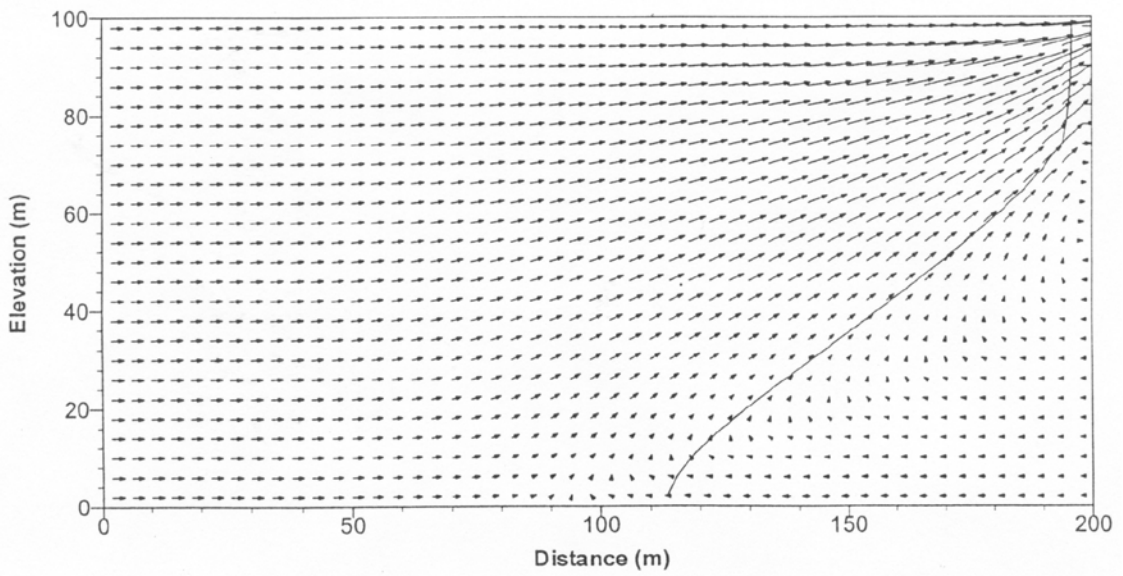
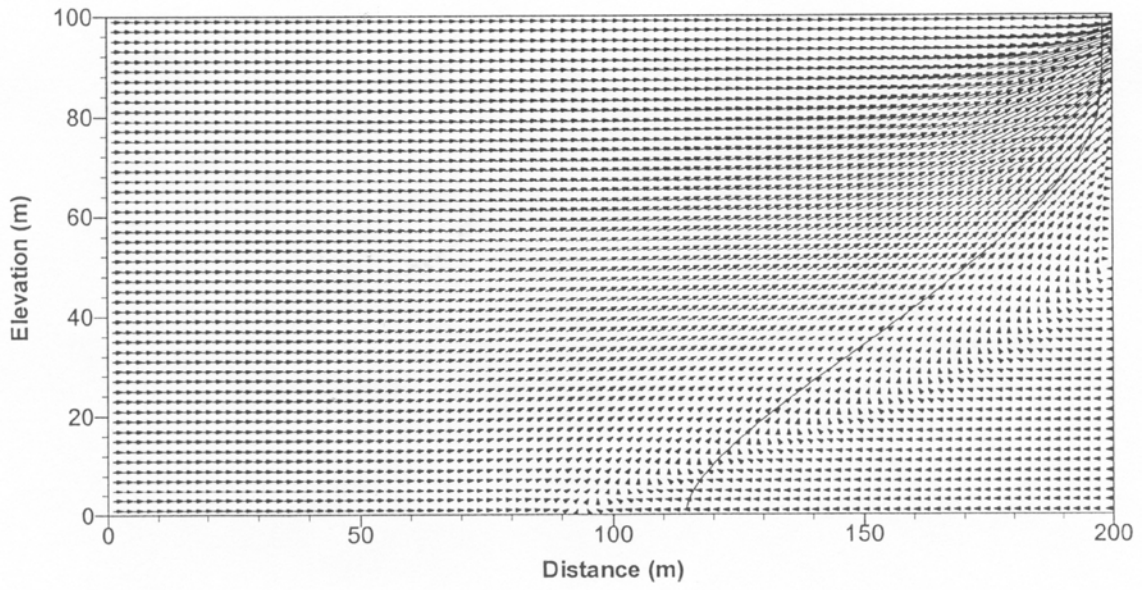


Figure E1-3. Grid independence test. Solution with maximum cell size 4 metres (top) and 2 metres.

Case E2: Two-fluid problem

Introduction

The motion of an interface between two fluids with different densities and viscosities is studied, see Figure E2-1. The buoyancy flow induced by the density difference will cause the two-fluid interface to tilt.

An analytical solution of this problem is found in /Hellström et al. 1988/. They found that the horizontal velocity at the interface is given by

$$q(z) = \kappa q_0 \frac{1}{\pi} \ln \left[\frac{1 + \sin\left(\frac{\pi z}{H}\right)}{1 - \sin\left(\frac{\pi z}{H}\right)} \right] \quad (\text{E2-1})$$

where

$$q_0 = \frac{k \Delta \rho g}{\mu_1 + \mu_2} = \text{a characteristic velocity}$$

and

$\Delta \rho$ = density difference

g = gravitational constant

k = permeability

μ = viscosity

κ = anisotropy factor (= 1 for isotropic permeability)

The objective of this test case is to compare the numerical and analytical solution for a common situation.

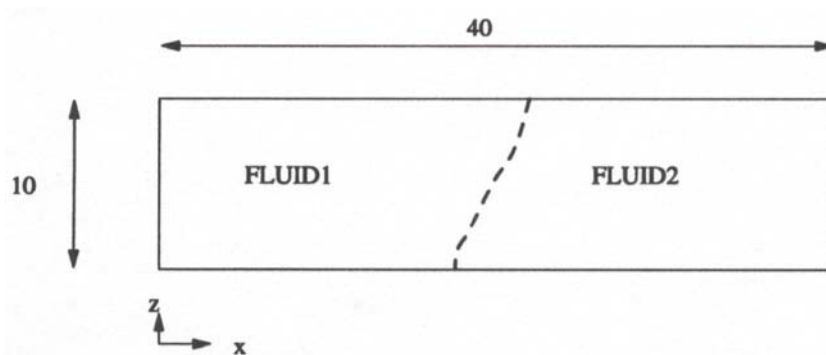


Figure E2-1. Outline of the situation studied.

Numerical simulations

The domain is outlined in Figure E2-1. A summary of input data is given in Table E2-1. It should be noted that not all of the parameters specified influence the simulations to be discussed. It should further be pointed out that the parameters are not representing any real fluid; they are only chosen to suit the present comparison.

Table E2-1. Simulation parameters.

Domain	2D, 40·10 [m ²].
Boundary conditions	Zero flux on all boundaries.
Property data	$T_1 = 10^\circ\text{C}$, $T_2 = 20^\circ\text{C}$. $\rho_1 = 1,000$, $\rho_2 = 950$ [kg/m ³]. $\mu_1 = 2 \cdot 10^{-3}$, $\mu_2 = 6 \cdot 10^{-3}$ [kg/ms]. Permeability = 10^{-12} [m ²]. Porosity = 1.0. Heat capacity aquifer = $2.0 \cdot 10^6$ [J/m ³ °C]. Heat capacity fluid = 4,200 [J/kg °C]. Thermal conductivity = 10^{-10} [W/m °C].
Grid	$dx_{\max} = dz_{\max} = 0.25$ m refined at the interface to 0.1 m.

Result/discussion

The main result of this study is the comparison of velocity profiles, shown in Figure E2-2. The agreement is very good indeed and requires no further comments.

An illustration of the velocity field is given in Figure E2-3. From this figure one can conclude that the vertical boundaries are placed sufficiently remote from the interface.

Conclusion

The tilting of a vertical interface between two fluids with different densities and viscosities has been studied. It is concluded that the numerical result agrees very well with the analytical solution.

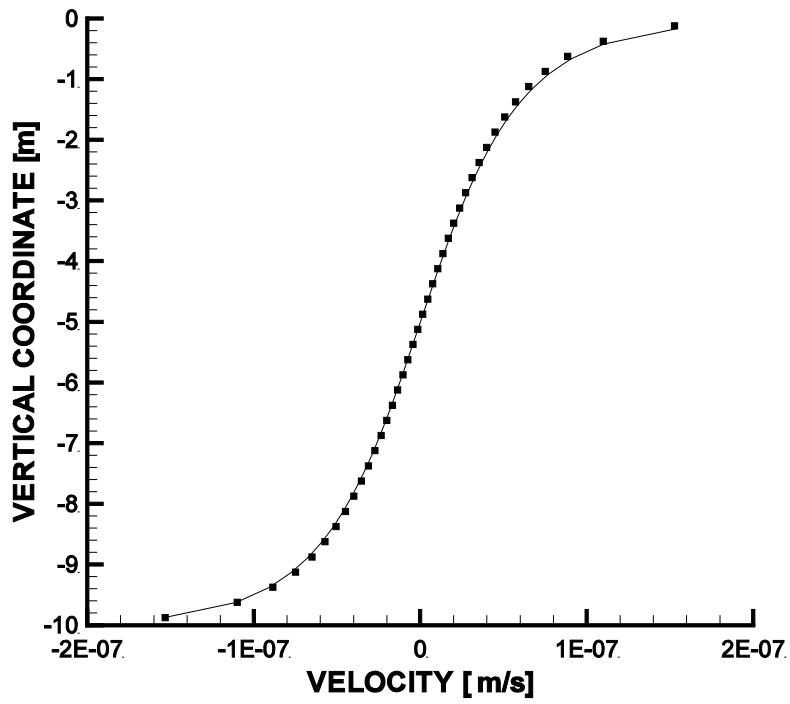


Figure E2-2. Comparison between numerical (■) and analytical (—) solution.

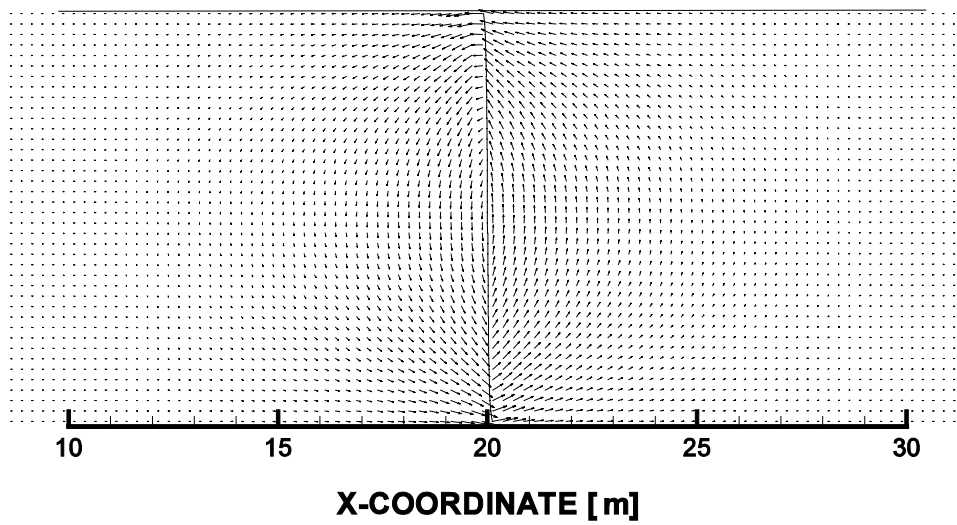


Figure E2-3. Illustration of the velocity field close to the interface..

Case E3: Coupled temperature and salinity fields

Introduction

This case considers the coupled buoyancy effect due to temperature and salinity fields. If a point heat source is placed in a stable salinity field an upward movement will result. This movement will eventually be halted by the stable salinity gradient. The task is to calculate the maximum vertical displacement.

An analytical estimate of this displacement is given in /Claesson et al. 1992/. In a porous media the maximum vertical displacement due to an instantaneous point heat source is:

$$Z_{\max} = \sqrt[4]{\frac{\bar{\alpha} E_0}{2\pi}} \quad (\text{E3-1})$$

where

E_0 = heat source [J]

$\bar{\alpha} = \frac{\alpha_T}{\alpha_c C_z^0 C}$ = buoyancy parameter [m^4/J]

α_T = thermal expansion coefficient [$1/^\circ\text{C}$]

α_c = salt expansion coefficient [$1/\%$]

C_z^0 = initial salinity gradient [$\%/m$]

C = aquifer volumetric heat capacity, rock [$\text{J}/\text{m}^3 \text{ } ^\circ\text{C}$]

The objective of this test case is to compare estimates by the above formula with the corresponding results from the numerical solution.

Numerical simulations

The heat source is placed in the middle of a box with dimensions $100 \cdot 100 \cdot 100 \text{ m}^3$, see Table E3-1 for additional data.

Note that not all of the parameters in Table E3-1 influence the simulation results to be presented here.

Table E3-1. Simulation parameters.

Domain	100·100·100 [m ³].
Boundary conditions	Zero flux on all boundaries.
Heat source	Variable.
Property data	Porosity = 0.01. Density = 1,000 [kg/m ³]. Viscosity = $2.0 \cdot 10^{-3}$ [kg/ms]. Permeability = $2.0 \cdot 10^{-12}$ [m ²]. Heat capacity, fluid = 4,200 [J/kg °C]. Heat capacity aquifer = $2.0 \cdot 10^6$ [J/m ³ °C]. Thermal conductivity = 10^{-7} [W/m °C]. Thermal expansion coefficient = 10^{-4} [1/ °C]. Salinity expansion coefficient = 10^{-2} [1/ %].
Initial salinity gradient	0.01 [%/m].
Grid	Uniform $dx_{\max} = dy_{\max} = dz_{\max} = 2$.

Result/discussion

The simulated maximum vertical displacement is in Figure E3-1 compared with the estimate from the analytical solution. The word “estimate” is used as /Claesson et al. 1992/ consider the formula as “an upper limit on the displacement” and that the formula is “normally more correct for large displacements, while it overestimates the small displacements”. The agreement found in Figure E3-1 is hence regarded as acceptable.

An illustration of the disturbed salinity field, in a vertical section through the position of the heat source, can be found in Figure E3-2. This snapshot is at a rather late stage, i.e. long after that the maximum displacement has been established.

Conclusion

The maximum displacement in a coupled temperature-salinity problem has been simulated and the results have been compared with an analytical solution. An acceptable agreement has been demonstrated.

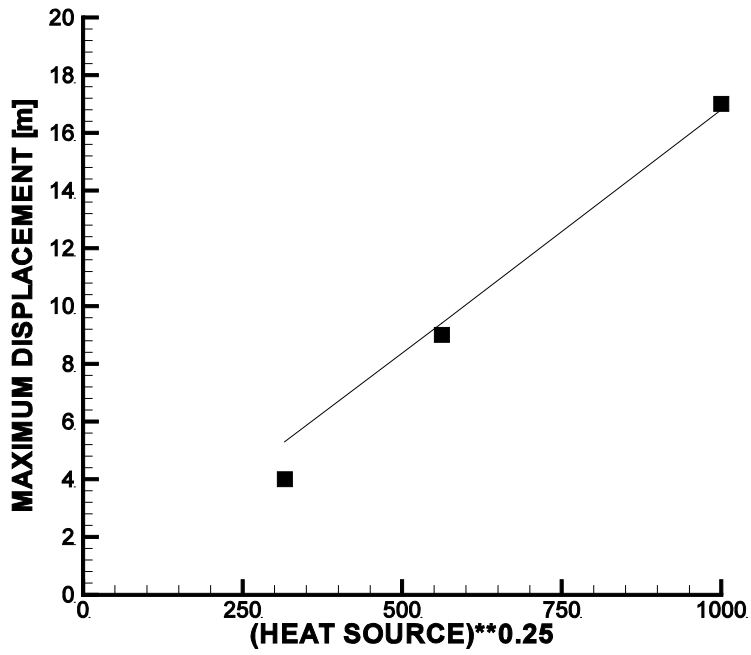


Figure E3-1. Maximum displacement as a function of the strength of the heat source. Solid line represents the analytical solution and the symbols the numerical solution.

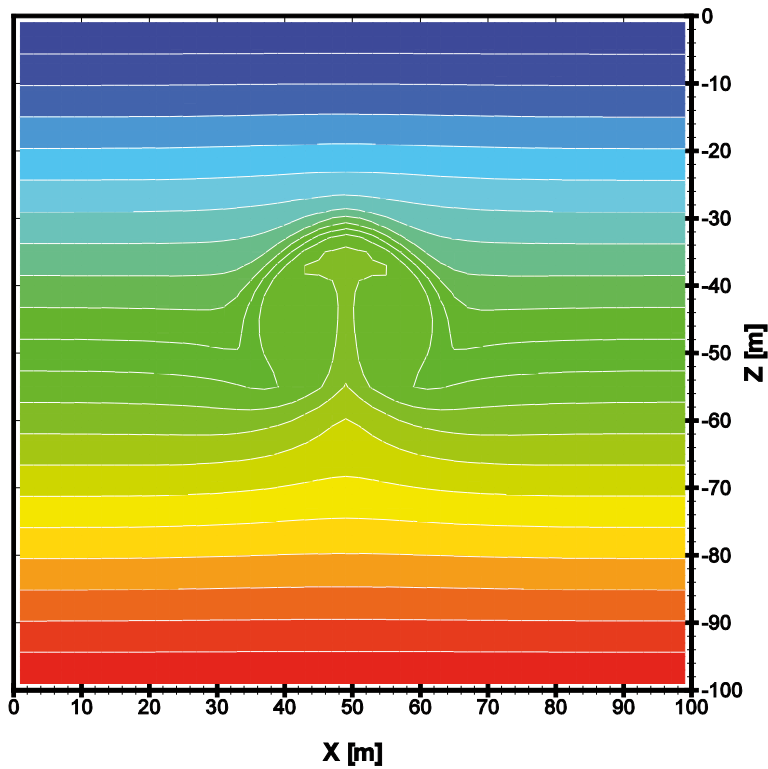


Figure E3-2. Illustration of the disturbed salinity field. Vertical section through the position of the heat source.

Case E4: Upconing

Introduction

If a well is placed in a two-layered aquifer, with a freshwater layer above a saltwater layer, a phenomenon known as upconing may take place, see Figure E4-1. It is of course the pressure drop due to the pumping that causes the rise of the interface.

An approximate solution, for small rises, is discussed in /Domenico and Schwartz 1990/. They also discuss a critical elevation at which the interface is no longer stable and saltwater flows to the well. In order to avoid this, the pumping rate, Q , should not exceed Q_{\max} , given by:

$$Q_{\max} = 0.6\pi d^2 K \left(\frac{\rho_s - \rho_f}{\rho_f} \right) \quad (\text{E4-1})$$

where d is the distance from the well to the original interface, K conductivity, ρ_s density of saltwater and ρ_f the freshwater density.

The objective of the test case is to make a qualitative comparison between results obtained by DarcyTools and Equation (E4-1). The comparison can only be qualitative as Equation (E4-1) is based on relations only valid for small interface rises.

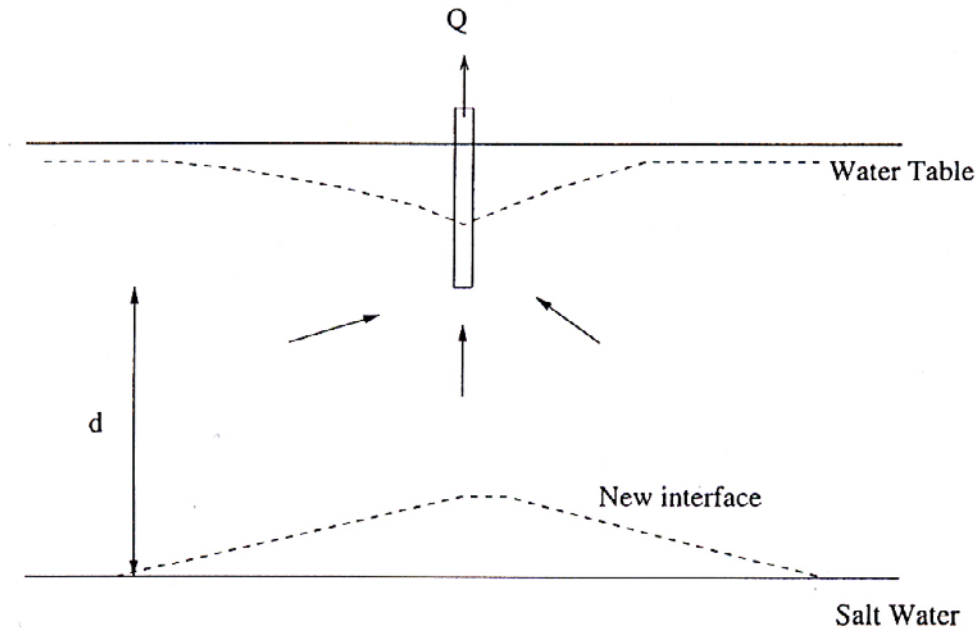


Figure E4-1. The upconing phenomenon.

Numerical simulations

In polar coordinates the problem is two-dimensional but here it will be treated as a 3D problem, as DarcyTools does not provide polar coordinates. Due to symmetry conditions we only need to consider one quarter of the domain. A summary of the simulation parameters is given in Table E4-1.

Table E4-1. Simulation parameters.

Domain	500-500-110 metres (x, y, z).
Boundary conditions.	Prescribed pressure at x_{\max} and y_{\max} . Zero flux condition on other boundaries. Salinity prescribed at bottom of domain.
Pumping rate	Varied.
Distance d (Figure E4-1)	50 metres.
Conductivity	10^{-5} m/s.
Diffusivity (salt)	10^{-9} m ² /s.
Salinity below interface	1 % ($\Delta\rho = 7.8$ kg/m ³).
Grid	$dx_{\max} = dy_{\max} = 2$ and $dz_{\max} = 1.0$.

Results/discussion

The predicted relation between the pumping rate and the salinity at the bottom of the well is shown in Figure E4-2. In this figure also the critical pumping rate, as given by Equation (E4-1), is indicated. As already mentioned we can not evaluate the result more than in a qualitative way; both DarcyTools and Equation (E4-1) do however predict a Q_{\max} of the same magnitude.

Conclusion

A qualitative agreement with the analytically predicted critical pumping rate, for saltwater intrusion into a well, has been demonstrated.

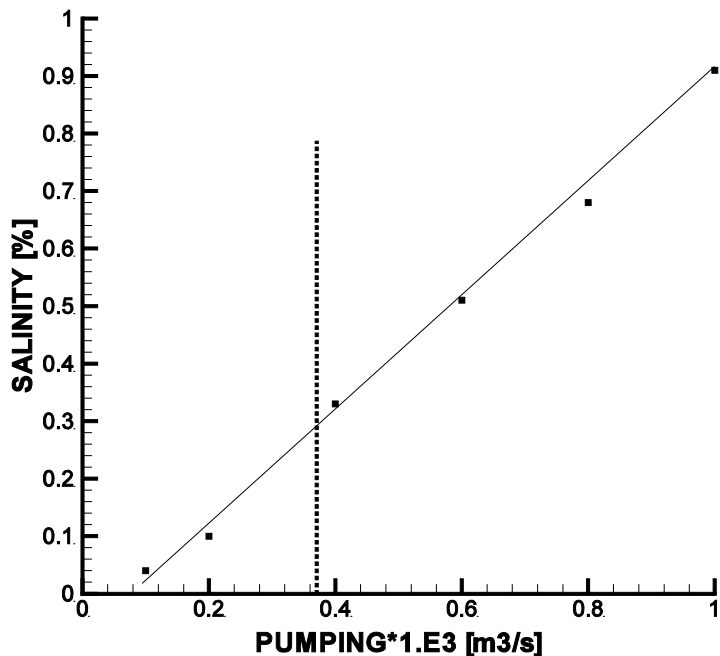


Figure E4-2. Relation between salinity at the bottom of the well and the pumping rate, as predicted by DarcyTools. Vertical line indicates the critical pumping rate according to Equation E4-1.

Case E5: The floating island

Introduction

This case is of special interest as it has some resemblance to the situation at the island of Äspö (location of the SKB Hard Rock Laboratory). The situation considered is outlined in Figure E5-1. A fresh water lens is formed below the island, due to the precipitation. As the surrounding seawater is more dense, due to its salinity, one may think of the freshwater as floating in the saltier seawater.

An analytical solution to this problem can be found in /Fetter 1994/; the groundwater height, h , as a function of distance from the shore, x , is given by:

$$h^2 = \frac{w(a^2 - (a-x)^2)}{K(1+G)} \quad (\text{E5-1})$$

where w is the recharge on the island, a half-length of the island, K conductivity and $G = \rho_f / (\rho_s - \rho_f)$, where ρ_s and ρ_f are seawater and freshwater densities, respectively.

The objective of this test case is to compare the groundwater tables as predicted by DarcyTools and as given by Equation E5-1.

Numerical simulations

The simulation parameters for this case are given in Table E5-1, see also Figure E5-1. Some comments:

- The vertical conductivity is increased in order to simulate the Dupuit assumption (as discussed in Case B2).
- As the salinity is fixed to 1.0 below sea and at the bottom boundary, the salinity will be uniform except for the region close to fresh water lens.
- The grid is generated as follows: A basic grid with a maximum size of 10 metres is refined close to the top surface where the maximum cell size is 1.0 metre.

Table E5-1. Simulation parameters.

Domain	2D, 1,000-500 metres. Upper boundary follows a sin-curve.
Conductivity	10^{-7} m/s (horizontal). 10^{-5} m/s (vertical).
Diffusivity (salt)	10^{-9} m ² /s.
Boundary conditions	Bottom: zero mass flux, salinity fixed to 1.0. Top: prescribed mass flux on island, prescribed pressure below sea level. Zero salinity on island, fixed salinity (= 1.0) below sea level.
Grid	See above.

Results/discussion

The comparison with the analytical solution is given in Figure E5-2; as can be seen a near perfect agreement is obtained. The flow and salinity distribution can be studied in Figure E5-3. For a recharge of 50 mm/year it is seen that the freshwater lens reaches a depth of about 400 metres. It may further be noted that the fresh water is discharged into the sea in a very narrow region close to the shore-line.

Conclusion

The predicted groundwater table on the floating island is in very good agreement with the corresponding analytical solution.

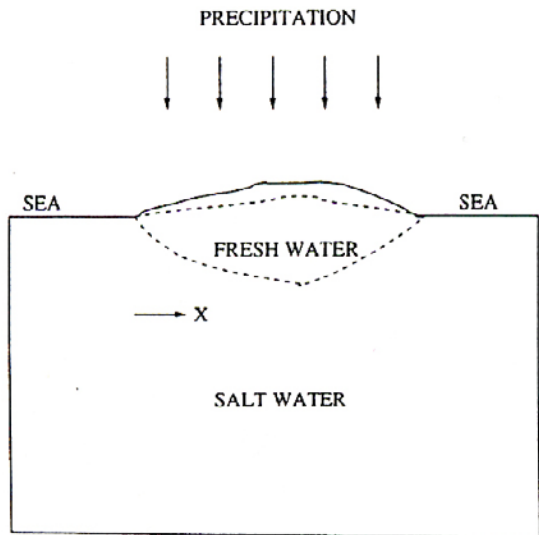


Figure E5-1. Illustration of the floating island problem.

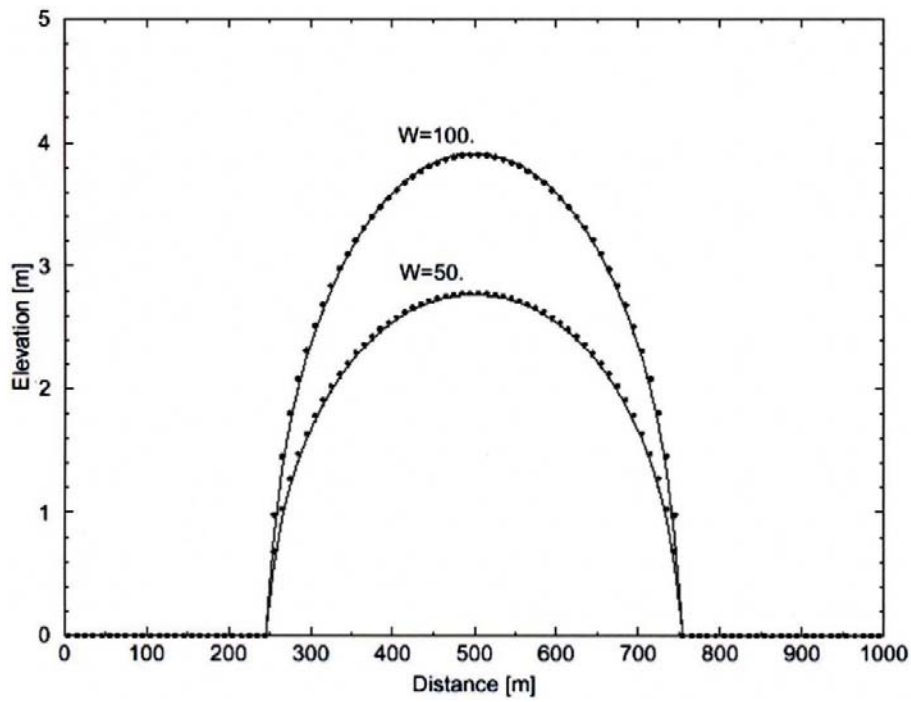


Figure E5-2. Numerically ($\cdot\cdot\cdot$) and analytically (—) predicted groundwater table for two recharges.

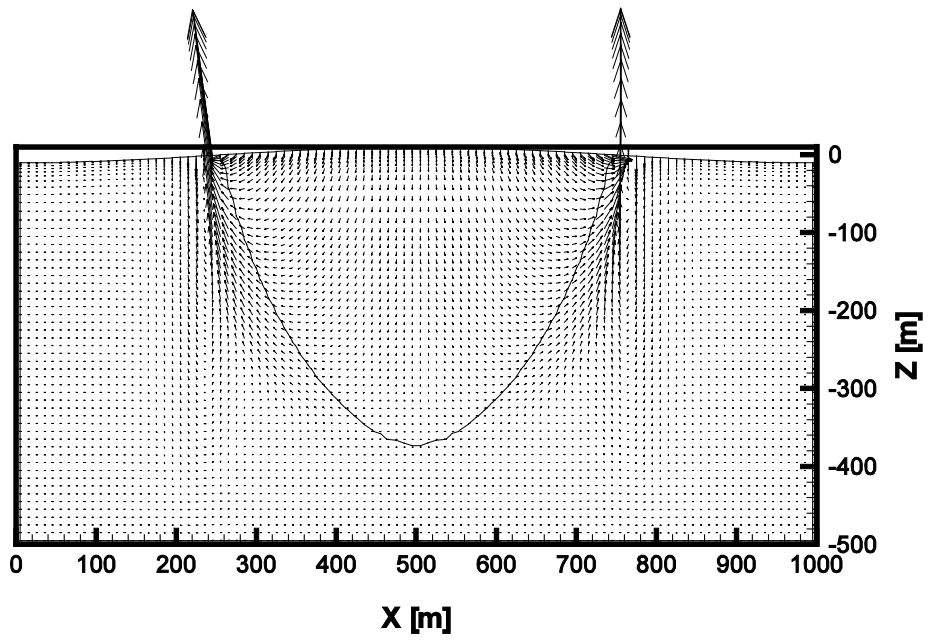


Figure E5-3. Flow and salinity distributions. The line shows the extent of the fresh water lens.

Validation cases

Case V1: A site scale validation

Introduction

This validation study is taken from the report “Impact of the tunnel construction on the groundwater system at Äspö. Task 5 Äspö task force on groundwater flow and transport of solutes; /Svensson et al. 2002/.

The hydrochemical field data at Äspö HRL has been presented as distributions of four basic water types: Meteoric, Baltic, Glacial and Äspö Brine. The Meteoric water has recently been in contact with the atmosphere and originates from precipitation, while Baltic water has its origin from the Baltic Sea. The Glacial water is believed to come from the melt water of the last inland ice about 12,000 (or more) years ago. The Äspö Brine water is characterised by its high salinity and its age; it is estimated that it has not been in contact with the atmosphere for at least 1 million years. The Äspö Brine fraction increases with depth and may be the dominating fraction below a depth of, say, 800 metres in the Äspö area.

The numerical model should be able to determine the composition, expressed as the four water types mentioned, of the water leaking into the tunnel. Two problems, which call for basic conceptual assumptions, can be identified when formulating such a model:

- Order of magnitude calculations show that water from outside the computational domain will contribute to the inflow to the tunnel already after a few years after the start of the construction of the tunnel. We thus need an assumption about the water composition outside the domain.
- The hydrochemical data show that large fractions of Glacial water are present already at a depth of a few hundred meters. As there is no source of Glacial water one would expect that this water should have been replaced by younger water during the last 12,000 years. As mentioned, the inflow to the tunnel will replace the water in the computational domain with water from outside the domain in a few years time. So, even if we specify a large fraction of Glacial water as an initial condition we would soon “run out” of this water type.

Boundary conditions

To deal with these problems we need to introduce some assumptions about the water composition at the boundaries of the computational domain. The following concepts and assumptions are introduced.

- Vertical boundaries:
 - If s (Salinity) $\leq 0.1\%$ we assume that the water is of Meteoric origin.
 - If $0.1 < s \leq 1.2\%$ we call this water type “Mixed Water High” (MWH).
 - If $s > 1.2\%$ we call this water type “Mixed Water Low” (MWL).

The reason for introducing MWB, MWH and MWL is that we can base an assumption about the composition of these waters on field data. There is also a reason for choosing the salinity value 1.2% as the division between MWH and MWL. When the inland ice had its frontline above Äspö one can expect that Glacial water penetrated very deep into the rock. At about 800 to 1,000 metres, the Äspö Brine provided a lower limit for the circulation. Presumably a mixture of Glacial and Äspö Brine waters resulted in the transition region between the two water types. At about 8,000 years ago the Litorina Sea, with a maximum salinity of about 1.2%, replaced most of the water due to its high density. The maximum penetration depth is however given by the salinity 1.2% and we can therefore assume that MWL is composed mainly of Glacial and Äspö Brine water. Based on these arguments, we assume the following for MWH and MWL:

- MWH. Composition based on field data from borehole KLX01 10% Baltic, 35% Meteoric, 45% Glacial and 10% Äspö Brine.
- MWL. 10% Baltic, 10% Meteoric, 40% Glacial and 40% Äspö Brine. This is to some degree supported by measurements in KLX02, at a depth with a salinity of 1.5%.

For the water entering through the bottom of the domain, MWB, it will be assumed that the composition is the same as for MWL.

Calibration

The model is calibrated both with respect to the hydrogeological and hydrochemical information available.

Above conceptual assumptions were discussed; it was stated that the water composition at the bottom and vertical boundaries of the domain were tentative and should be considered again in the calibration process. Three water types, MWH, MWL and MWB, were introduced, with tentative compositions from borehole measurements.

The focus of the calibration process for water composition is thus on the composition of MWH, MWL and MWB.

In the Task #5 description it was suggested that the calibration should be based on measured water composition in boreholes, with the tunnel front at position 2,900 metres. A review of the field data on water composition shows that more data are available for position 3,170 metres (April -94) and the calibration will therefore be based on conditions prevailing at that time.

Calibration criteria

In the calibration we will try to fulfil the following criteria:

- **Groundwater table for natural conditions.** The distribution can be found in /Rhén et al. 1997/. One can expect that a certain variation of the groundwater table is found, between seasons and years, and a fair agreement is hence sought.
- **Pressure response in boreholes.** During the construction of the Äspö HRL, the pressure was monitored in a number of borehole sections. The drawdowns at tunnel front position 2,875 metres can be found in /Rhén et al. 1997/; these data will be compared with simulated drawdowns.
- **Kinematic porosity.** The kinematic porosity field is based on the estimated flow aperture of each fracture or zone in the network. In the calibration process this basic distribution will be kept, but each value will be multiplied by a constant, that is to be determined. The time history of the upconing, i.e. the salinity variation in time, will be utilized for this purpose.
- **Water composition for natural conditions.** The water composition in the Äspö area was measured prior to the construction of the Äspö HRL. We will run the model for this situation, assuming steady state conditions, and compare the result with field data. In the steady state the water composition in the domain is completely determined by the boundary conditions and should thus be sensitive to the assumed compositions of MWH, MWL and MWB. A general agreement between measured and simulated distributions is the criteria set.
- **Water composition for tunnel front at 3,170 metres.** The water composition in 19 boreholes was measured at this tunnel front position. We want to ensure as close agreement as possible with these data.
- **Water composition at time 1996-05.** The measured composition in eight borehole sections, after the completion of the tunnel, will be compared to simulated values. As close agreement as possible is the objective of part of the calibration.

Calibration process

It was decided to perform the calibration in three steps. First the hydrological model was calibrated (the first two criteria above). This involved determining the conductivity for the top five layers of the model and adjusting the transmissivity of some deterministic fracture zones. It was the ambition to keep these adjustments as small as possible. Next the kinematic porosity factor was determined from the measured upconing dynamics and finally the water composition was considered. Adjustments of the compositions of MWH, MWL and MWB were evaluated, with the ambition to get as close agreement with field data as possible.

Results

The groundwater table for natural conditions is compared to measurements in Figure V1-1 and the drawdowns in borehole sections, for a tunnel front position of 2,875 metres, are given in Table V1-1. Starting with the groundwater table, it is seen that the predicted maximum ground water level is about 4 metres. A general agreement with the measured levels (given in /Rhén et al. 1997/) is also found. The calculated drawdowns in borehole sections in the domain were compared with measured ones, all for tunnel front position 2,875 metres. It was anticipated that the drawdowns should be sensitive to various realisations of the background fracture network. In order to study this five realisations of the network were generated and the drawdown for each borehole section and each realisation was calculated. The result can be studied in Table V1-1, the location of boreholes can be found in Figure 1-3 (Report 1). It is seen that different realisations are best for different boreholes. Realisation two has only two borehole sections with an error larger than 10 metres and is for this reason considered to be the best one. In the following, it is this realisation of the conductivity field that will be used, if not otherwise stated.

It was found that an increase of the kinematic porosity, based on the flow aperture, with a factor of five gives a realistic description of the upconing process, see Figure V1-2. We do not know the exact position of the upconing front and therefore both the predicted maximum salinity at a depth of 370 metres and the predicted salinity at the tunnel position 2,800 metres are given in Figure V1-2. The measurements are from boreholes SA2783 and SA2880. This calibration result is considered to be important, as it focuses on the transport velocity of a fluid property.

These results were obtained by prescribing certain conductivities to the top five layers, see Table V1-2, and by making small adjustments to the transmissivities of the major fracture zones. A small background conductivity, with a lognormal distribution, was also added to all cells. This conductivity had a value of 10^{-10} m/s north of the line $y = 7,050$ metres (in the Äspö coordinate system) and a value of 10^{-9} m/s south of this line. The standard deviation of $\text{Log}_{10}(K)$ was 0.8 for the whole domain.

The compositions of MWH and MWL given above were found to give results in fair agreement with field data, both for initial conditions and for the tunnel front at position 3,170 metres. The composition of MWB has no significant influence on these comparisons, but is important when water from the bottom boundary reach the tunnel level. The salinity at the bottom boundary, generated by the regional model, will reach 5–6% when the tunnel is completed. Borehole KLX02, at 1,500 metres, has a salinity of 7–8% and Äspö Brine fraction of 90%. Based on these data and the comparison of measured and simulated water composition at time 1996-05, the following composition for MWB was considered to be more accurate: 5% Meteoric, 5% Baltic, 10% Glacial and 80% Äspö Brine. This is the composition of MWB to be adopted. A small adjustment of the composition of MWL (giving 12% Meteoric, 12% Baltic, 45% Glacial and 31% Äspö Brine) was found to give a minor improvement of the results. With these modifications good agreement was also obtained for the comparison at time 1996-05. Some results that confirm these statements will now be given.

The calculated initial distributions are given in Figure V1-3. The sections are through the centre of the spiral part of the tunnel. The distributions are in general agreement with field data, see /Gurban et al. 1998/. Of particular significance is the band of glacial water occupying about 50% of the pore volume at a depth of about 600 metres. Point by point comparisons with field data can be found in Table V1-3. It should be mentioned that measurements are available also for depths above 300 metres. These were however not included in the table as the model predicts 100% Meteoric water for depths smaller than 200 to 300 metres. In order to be able to compare the average values for the composition, it was decided to exclude these data.

Next we consider the simulated water composition for tunnel front position 3,170 metres. Point comparisons with field data can be found in Table V1-4; the comparison in Table V1-4 is also shown as a graph in Figure V1-4. A certain agreement in proportions of different water types, as well as trends along the tunnel, can be found. It is not easy to anticipate the degree of agreement one can expect in a simulation like this. Distributions for tunnel front position 3,170 metres are shown in Figure V1-5. This figure is included as an illustration of how the tunnel affects the distributions and is not directly used in the calibration process.

Finally, the comparison for 1996-05 is shown in Table V1-5. Also in this comparison both the trends and the average compositions are in fair agreement with field data.

Conclusions

From the comparisons presented, the following conclusions are formulated:

- The hydrogeological simulations are in fair agreement with field measurements.
- The simulations of water compositions are harder to evaluate. A certain agreement in trends can however be claimed.

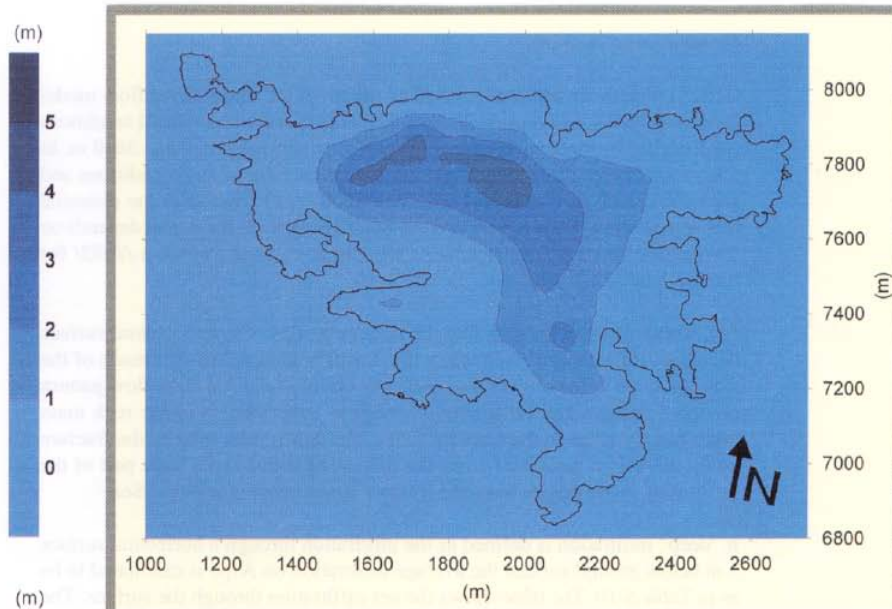


Figure VI-1. Measured (top) and calculated water table for natural conditions.

Table V1-1. Errors in calculated drawdown (calculated-measured) for tunnel front at 2,875 metres, using five realisations of the conductivity field.

Borehole section	Depth m b s l	Realisation				
		1	2	3	4	5
K02-B5	-190.00	5.37	7.84	8.53	15.56	0.72
K02-B4	-310.00	-9.58	-9.81	-11.36	-10.02	-10.31
K02-V3	-530.00	3.63	5.75	4.09	5.60	4.83
K02-V2	-830.00	-5.84	-5.50	-5.69	-5.43	-5.54
K02-V1	-870.00	-5.43	-5.21	-5.34	-5.16	-5.24
K03-C5	-210.00	6.64	5.85	8.11	7.02	5.46
K03-C4	-350.00	0.80	0.62	1.74	0.13	0.33
K03-C3	-510.00	1.78	1.20	2.28	2.51	1.57
K03-C2	-610.00	1.47	0.98	1.64	1.78	1.67
K03-C1	-670.00	0.54	0.22	0.38	0.28	0.78
K05-E4	-270.00	2.65	5.59	1.19	5.81	0.26
K05-E3	-310.00	-8.85	-4.45	-1.91	0.47	-0.15
K05-E2	-430.00	-9.44	-7.11	-5.93	-5.35	-5.54
K05-E1	-450.00	-7.46	-4.83	-4.51	-4.23	-3.68
K06-F6	-90.07	9.30	9.55	6.95	9.27	8.94
K06-F4	-250.00	-2.15	-2.92	-4.17	-5.22	-1.47
K06-F3	-290.00	11.45	16.49	15.17	14.71	13.24
K06-F2	-330.00	-2.94	0.55	-3.38	-1.26	-2.63
K06-F1	-370.00	-4.48	-0.01	-6.55	-2.89	-5.32
K07-J5	-110.00	-34.67	-27.76	-31.98	-28.15	-29.55
K07-J4	-210.00	-10.42	-6.42	-4.28	-5.17	-8.83
K07-J3	-290.00	-4.48	-1.00	-2.94	-6.21	-1.21
K07-J2	-370.00	2.50	3.47	2.52	3.05	2.88
K07-J1	-470.00	-5.41	-4.65	-5.26	-4.75	-5.07
K08-M3	-150.00	2.37	7.08	-4.10	2.76	1.04
K08-M2	-310.00	7.42	9.63	3.98	9.38	7.67
K08-M1	-450.00	-6.20	-5.50	-5.74	-5.38	-5.69
K09-AE	-90.07	0.49	1.64	0.80	1.55	0.97
K09-AD	-110.00	0.37	4.73	1.39	8.17	1.90
K09-AC	-150.00	-1.20	6.17	-0.08	5.39	7.31
K09-AB	-210.00	1.89	4.88	6.47	6.34	11.75
K09-AA	-350.00	-2.32	-2.25	-2.23	-2.64	-2.61
K10-BA	-50.35	-2.41	-2.38	-2.76	-2.41	-2.19
K11-CF	-30.48	-5.99	-6.09	-6.45	-5.58	-5.90
K11-CE	-50.35	-6.02	-6.20	-6.49	-5.50	-6.01
K11-CD	-90.07	-1.41	-1.05	-1.51	-1.39	-1.33
K11-CC	-130.00	-2.42	-2.11	-2.49	-2.11	-2.25
K11-CB	-170.00	2.79	3.03	2.81	3.21	3.04
K11-CA	-210.00	-2.07	-1.61	-1.95	-1.57	-1.72
K12-DE	-90.07	-3.02	-4.97	-6.58	-1.89	0.44
K12-DD	-110.00	-1.45	-4.02	-4.50	-3.52	1.44
K12-DC	-230.00	2.17	4.68	-1.97	3.25	1.83
K12-DB	-270.00	4.67	9.84	-0.26	4.56	6.94
K12-DA	-350.00	2.91	6.49	-1.03	3.47	3.22
K14-FE	-70.21	-1.03	-0.43	-0.69	-0.48	-0.43
K14-FD	-110.00	2.08	2.61	0.55	1.59	1.35
K14-FC	-130.00	2.88	3.56	3.04	4.65	3.02
K14-FB	-130.00	1.66	1.94	1.23	3.83	1.79
K14-FA	-170.00	2.74	0.86	2.20	5.28	2.95
K16-?D	-110.00	0.36	0.52	-3.14	0.52	1.54
K16-?C	-230.00	-8.69	-6.93	-10.48	-8.82	-8.90
K16-?B	-410.00	-5.67	-5.12	-5.32	-5.00	-5.25
K16-?A	-490.00	-4.16	-3.76	-4.35	-3.64	-4.88
KV2-B6	-50.35	1.97	-1.22	1.48	0.71	2.45
KV2-B5	-70.21	12.71	6.36	6.47	9.41	10.62
KV2-B4	-90.07	10.72	7.10	8.08	9.74	9.88
KV2-V3	-130.00	6.22	5.94	6.19	5.74	5.78
Mean error (m)		-0.99	0.21	-1.20	0.39	-0.07

Table V1-2. Conductivities for the top five cell layers, as given by the calibration process.

Layer (m)	Conductivity m/s
0–0.5	10^{-4}
0.5–1.5	10^{-4}
1.5–3.0	$4 \cdot 10^{-5}$
3.0–5.0	10^{-6}
5.0–10.0	10^{-7}

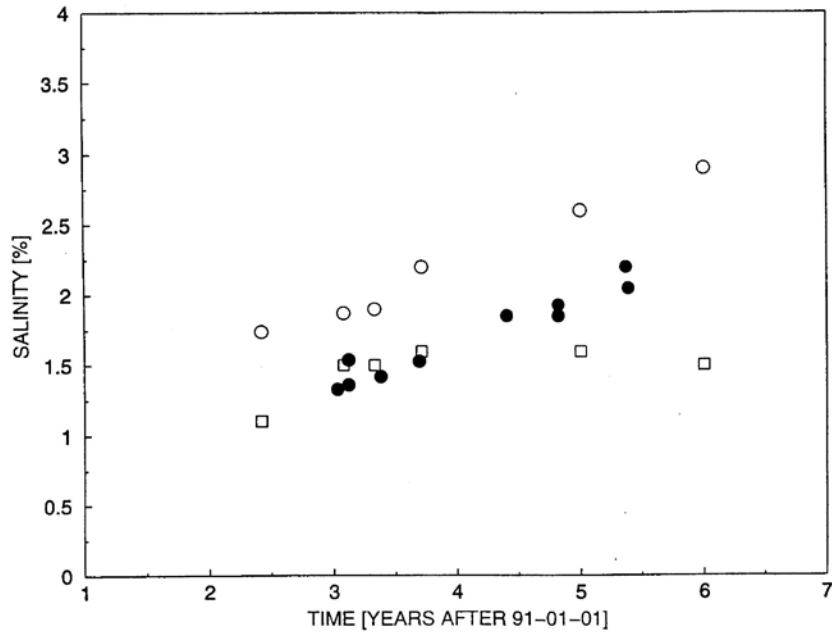


Figure VI-2. The upconing process. Salinity as a function of time at a depth of 370 metres.

- Field data (SA2783 and SA2880)
- Simulated maximum salinity.
- Simulated salinity at tunnel coordinate 2,800 metres.

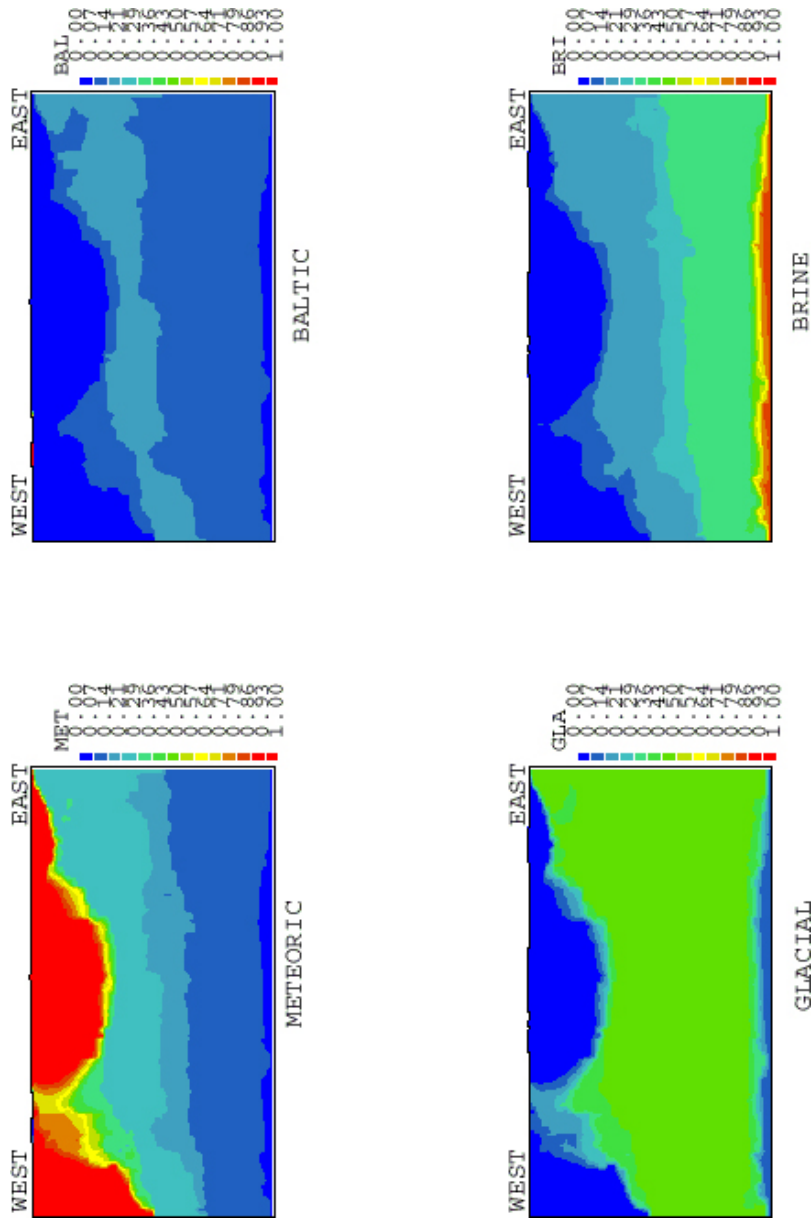


Figure VI-3. Vertical sections through the centre of the spiral part of the tunnel, showing the simulated initial distributions of various water types.

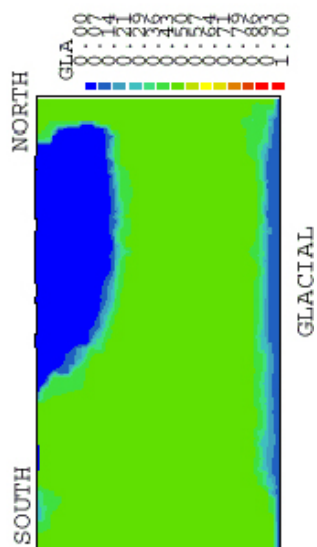
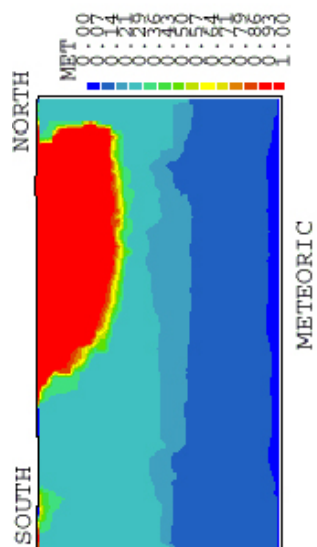
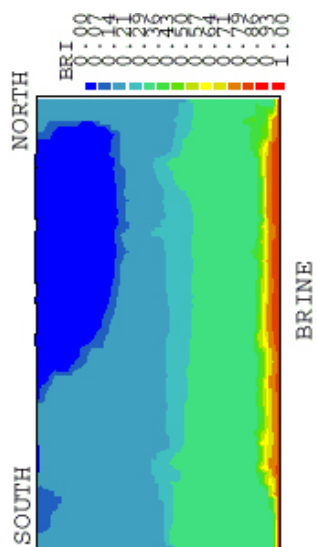
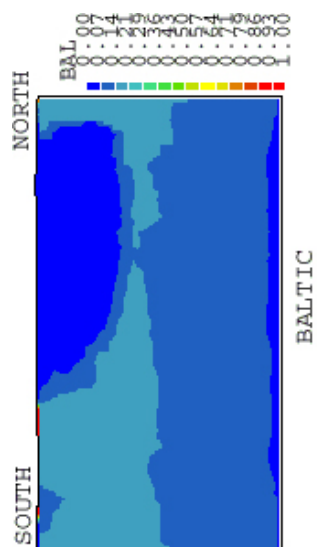


Figure VI-3. Cont.

Table V1-3. Comparison between measured and simulated water compositions in borehole sections prior to tunnel construction.

Borehole depth [m]	Measured (top) and simulated water composition			
	Meteoric	Baltic	Glacial	Äspö Brine
KAS02C	30.1	14.8	40.4	14.8
300 m	66.3	6.5	19.9	7.3
KAS02D	26.9	15.0	43.0	15.0
440 m	21.7	14.2	45.0	19.1
KAS02E	17.9	17.9	44.7	19.6
520 m	20.4	13.9	45.0	20.6
KAS02F	13.6	13.6	45.4	27.4
840 m	12.0	12.0	45.0	31.0
KAS02G	12.3	12.3	46.8	28.7
880 m	11.9	11.9	44.8	31.3
KAS03D	20.2	14.7	50.3	14.7
340 m	26.7	14.6	43.9	14.8
KAS03E	22.6	12.8	51.7	12.8
440 m	24.5	14.9	45.0	15.7
KAS03F	16.0	16.0	50.9	17.1
600 m	15.5	12.8	45.0	26.7
KAS03G	14.4	14.4	47.2	24.0
820 m	12.0	12.0	45.0	31.0
KAS03H	11.1	11.1	44.5	33.4
900 m	11.9	11.8	44.5	31.8
KAS04C	24.9	17.3	40.5	17.3
360 m	28.8	13.8	42.1	15.4
KAS06C	34.5	35.4	15.1	15.1
320 m	33.8	12.6	38.9	14.7
KAS06D	33.7	31.3	17.6	17.6
420 m	22.3	14.4	45.0	18.3
Average	21.4	17.4	41.4	19.8
	23.7	12.7	42.2	21.4

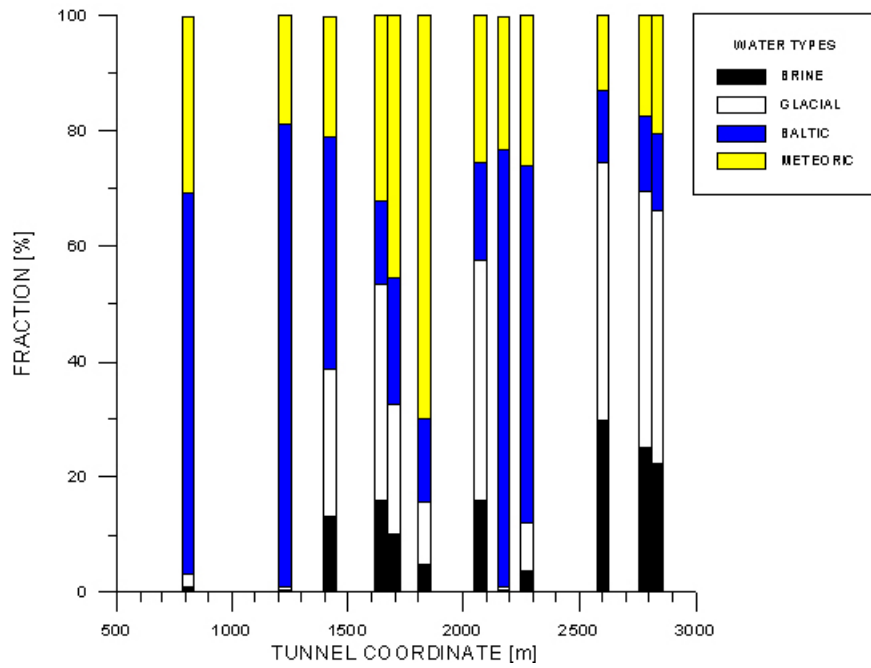
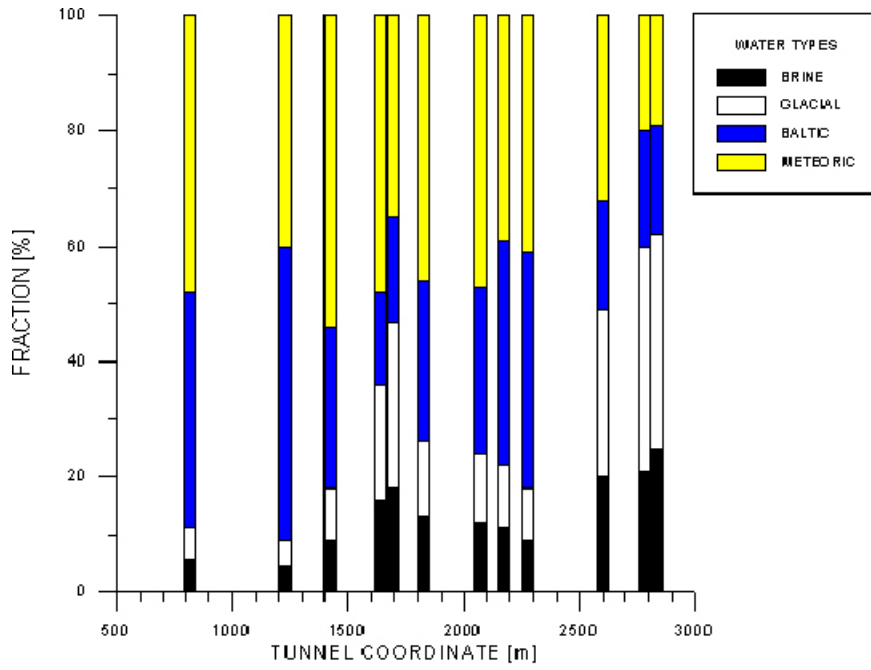


Figure VI-4. Comparison between measured (top) and simulated water composition distribution for tunnel front at 3,170 metres.

Table V1-4. Comparison between measured and simulated water composition in boreholes. Tunnelfront: 3,170 m.

Borehole depth [m]	Measured (top) and simulated water composition			
	Meteoric	Baltic	Glacial	Äspö Brine
KAS09	35.0	57.0	4.0	4.0
100 m	17.9	82.0	0.1	0.0
KAS14	32.0	64.0	2.0	2.0
100 m	21.7	77.3	0.8	0.3
SA0813	48.0	41.0	5.5	5.5
100 m	30.6	66.0	2.5	0.8
SA1229	40.0	51.0	4.5	4.5
160 m	18.9	80.2	0.7	0.2
SA1420	54.0	28.0	9.0	9.0
200 m	21.2	40.1	25.6	13.2
KAS07	60.0	32.0	4.0	4.0
200 m	18.2	81.2	0.4	0.2
SA1641	48.0	16.0	20.0	16.0
220 m	32.1	14.6	37.3	16.0
SA1696	35.0	18.0	29.0	18.0
220 m	45.5	21.8	22.6	10.0
SA1828	46.0	28.0	13.0	13.0
240 m	70.1	14.4	10.7	4.9
SA2074	47.0	29.0	12.0	12.0
280 m	25.4	17.0	41.6	16.0
SA2175	39.0	39.0	11.0	11.0
280 m	23.3	75.8	0.6	0.2
SA2273	41.0	41.0	9.0	9.0
300 m	26.2	61.9	8.2	3.8
SA2600	32.0	19.0	29.0	30.0
340 m	13.1	12.3	45.0	29.7
SA2783	20.0	20.0	39.0	21.0
360 m	17.7	12.9	44.4	25.1
SA2834	19.0	19.0	37.0	25.0
360 m	20.5	13.2	44.0	22.4
KAS08	37.0	29.0	17.0	17.0
440 m	25.6	20.4	36.8	17.2
KAS07	27.0	18.0	37.0	18.0
460 m	15.8	12.9	45.0	26.3
KAS05	16.0	16.0	45.0	23.0
480 m	13.0	12.2	45.0	29.7
KAS03	25.0	23.0	49.0	13.0
560 m	23.5	14.6	44.9	16.9
Average	36.9	30.9	19.8	12.9
	25.3	38.5	24.0	12.3

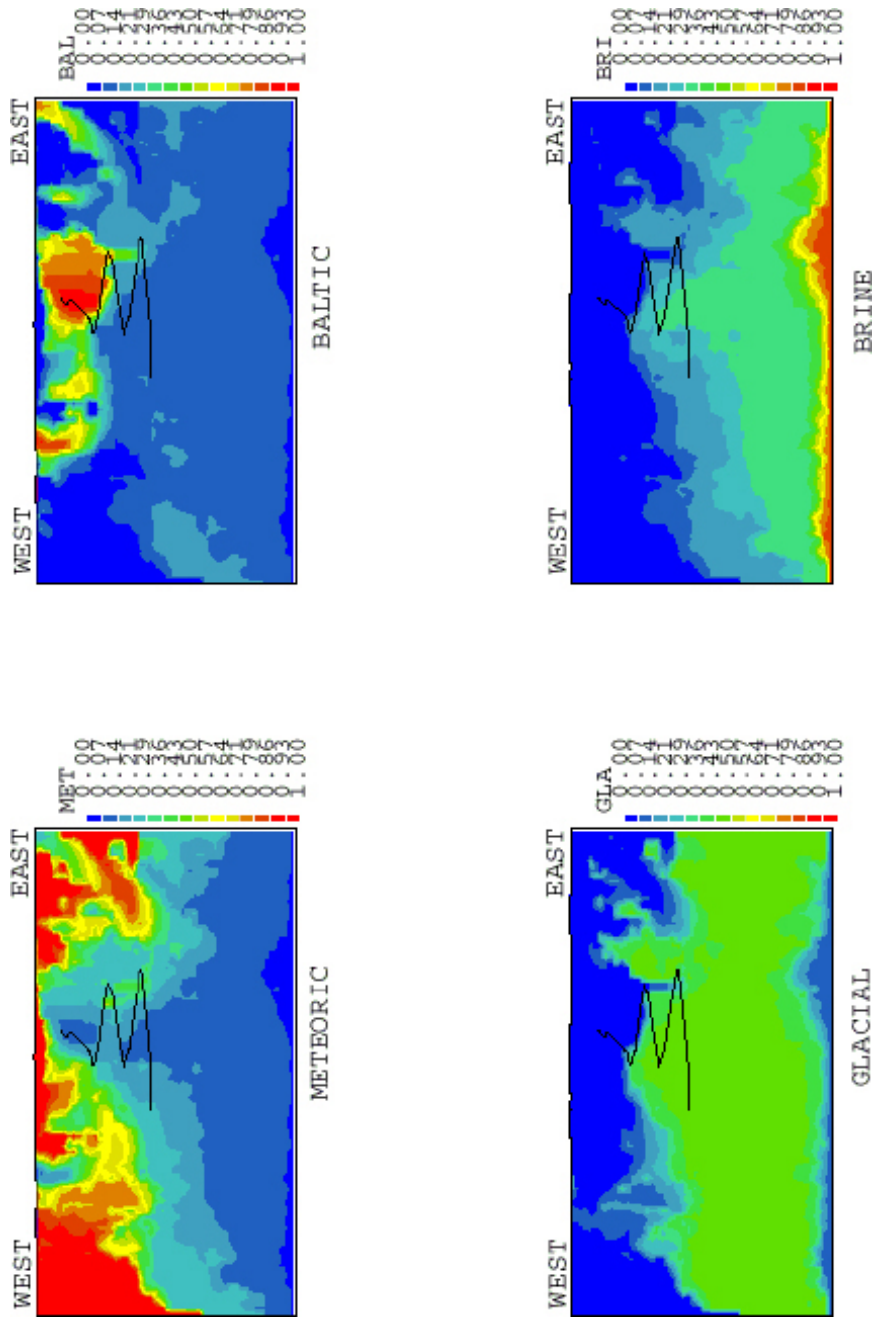


Figure VI-5. Vertical sections through the centre of the spiral part of the tunnel, showing the simulated distributions of various water types. Tunnel front position: 3,170 metres.

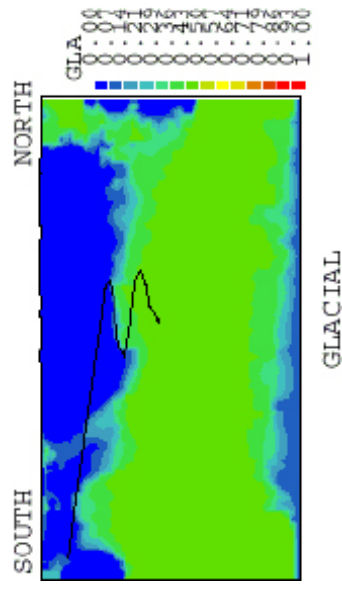
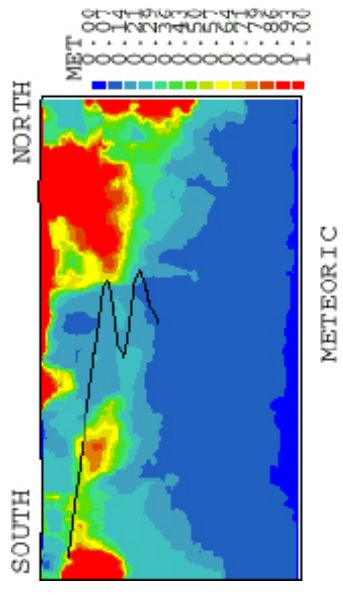
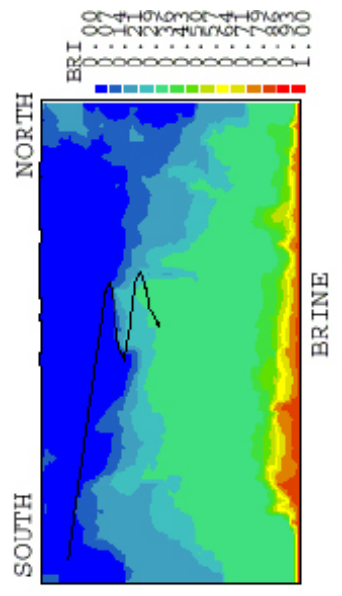
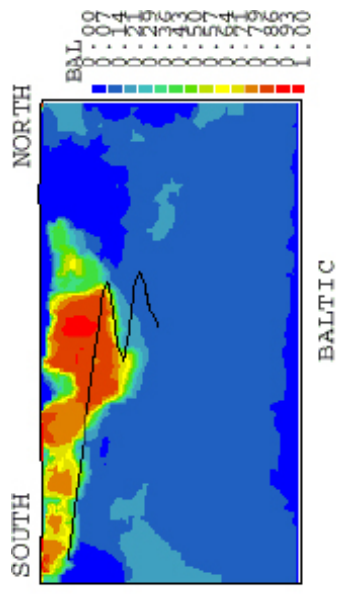


Figure VI-5. Cont.

Table V1-5. Comparison between measured and simulated water composition in boreholes at time 1996-05.

Borehole depth [m]	Measured (top) and simulated water composition			
	Meteoric	Baltic	Glacial	Äspö Brine
SA2273	46.0	38.0	8.0	8.0
300 m	30.6	64.7	3.1	1.6
Sa2600	48.0	20.0	16.0	16.0
340 m	16.5	12.4	38.2	32.8
SA2783	17.0	17.0	37.0	29.0
360 m	35.2	13.2	32.2	19.4
SA2880	18.0	18.0	34.0	31.0
380 m	35.5	18.4	31.1	14.9
KA3005	54.0	21.0	13.0	13.0
400 m	34.9	13.0	30.8	21.2
SA3067	18.0	18.0	43.0	21.0
400 m	60.2	25.3	10.8	3.7
KA3110	47.0	37.0	8.0	8.0
400 m	46.7	35.7	12.4	5.2
KA3385	38.0	18.0	25.0	18.0
440 m	18.4	13.0	42.2	26.5
Average	35.8	23.4	23.0	18.0
	34.8	24.5	25.1	15.7

Case V2: A laboratory scale validation

Introduction

The laboratory scale model (/Svensson 1999/) was the first application of the GEHYCO approach to calculate the conductivity field. Very little information about the properties of the background fracture network was available and an important part of the calibration process was to find a tentative expression for the transmissivity of the background fractures.

The boundary conditions are generated from a site scale model. For consistency, also the tunnel inflow distribution is taken from the site scale model. The transmissivities of the major fracture zones were calibrated in the site scale model and will not be the subject of calibration here. These conditions and assumptions will strongly determine the flow, pressure and salinity distributions in the present model. It is thus clear that the calibration process is quite constrained and in practice limited to the influence of the background fracture network.

The objective of the calibration is to demonstrate that the conductivity fields generated by the suggested method can be calibrated to match field data from the Äspö HRL.

Calibration criteria

The following calibration criteria were formulated:

- In a recent study, see /Rhén and Forsmark 2000/, the frequency of “High Permeability Features” (HPF) at the Äspö HRL was studied. It was concluded that fracture zones with a transmissivity $\geq 10^{-5}$ m²/s are found with an arithmetic mean distance of 75–105 metres. This includes also the deterministic fracture zones, which were found to contribute with about 48% to the total number of fractures found. The arithmetic mean distance between fractures with $T \geq 10^{-6}$ m²/s was found to be in the range 35–55 metres. We will evaluate the mean arithmetic distances for fractures with $T \geq 10^{-6}$ and $T \geq 10^{-5}$ m²/s, in the fracture network generated.
- During the construction of the Äspö HRL, the pressure was monitored in a number of borehole sections. The drawdowns at tunnel front position 2,875 metres (i.e. when the tunnel was excavated to a length of 2,875 metres) can be found in /Rhén et al. 1997/; these data will be compared with simulated drawdowns.
- The conductivity distribution for a test scale of 3 metres has been extensively studied at Äspö, (/La Pointe 1994, Rhén et al. 1997/). The corresponding distribution of cell conductivities, with $\Delta = 3$ m, will be calculated and compared with field data.

Other criteria could have been formulated, but it is believed that the above criteria will constrain the background fracture network in a useful manner. Main arguments for the criteria are:

- The frequency of HPF:s will determine the transmissivity of large background fractures.
- It is essential that the model predicts the correct pressure drops in the borehole sections in the domain, as the drawdown distribution reflects the mean conductivity of the rock.
- By studying the conductivity distribution on the 3 metre scale, we can focus on the distribution of low conductivity cells. This may be essential for transport simulations.

Calibration process

The difficult step in the calibration process is to find a strategy for how the calibration criteria can be met. The more linked the criteria are the more difficult the task is. Fortunately, the criteria above are not strongly linked and the strong influence of boundary conditions and inflows to the tunnel also make the task easier. A few trial calculations indicated that the following strategy would work:

- First determine the transmissivity distribution for the background fractures.
- The comparison of conductivity distributions on a 3 metres scale indicated that the addition of a background conductivity improved the comparison with the measured distribution (details below). The added conductivity is however of the order 10^{-10} m/s. This small added conductivity was found to have a negligible influence on the agreement for other criteria. We can thus perform this operation independently.
- The pressure drops in borehole sections are to a large extent determined by the deterministic fracture zones, which have been calibrated in earlier studies. We thus expect the drawdowns to be of the right magnitude independently of other adjustments.

Results

The main outcome of the calibration is a formula for the transmissivity of the background fractures:

$$T = \begin{cases} 10^{-5} (L/100)^2 & \left[\frac{\text{m}^2}{\text{s}} \right] \text{ for } L \leq 100 \text{ metres} \\ 10^{-5} & \left[\frac{\text{m}^2}{\text{s}} \right] \text{ for } L > 100 \text{ metres} \end{cases} \quad (\text{V2-1})$$

The frequency of High Permeability Features (HPF) was the most important criterion when establishing this relation, but of course it also ensured that the other criteria were fulfilled. Some properties of this relation include: the maximum transmissivity is of the same order as that for the deterministic zones and the transmissivity for $L = 5$ metres is $2.5 \cdot 10^{-8} \text{ m}^2/\text{s}$, which ought to ensure that the smallest fractures do not make a significant contribution to the conductivity field.

As mentioned, the test on a 3 metres scale required the addition of a small background conductivity. It was found that a lognormally distributed conductivity, with $mean(\log_{10}(K)) = -10.0$ and $std. dev(\log_{10}(K)) = -0.8$, gives good agreement with field data.

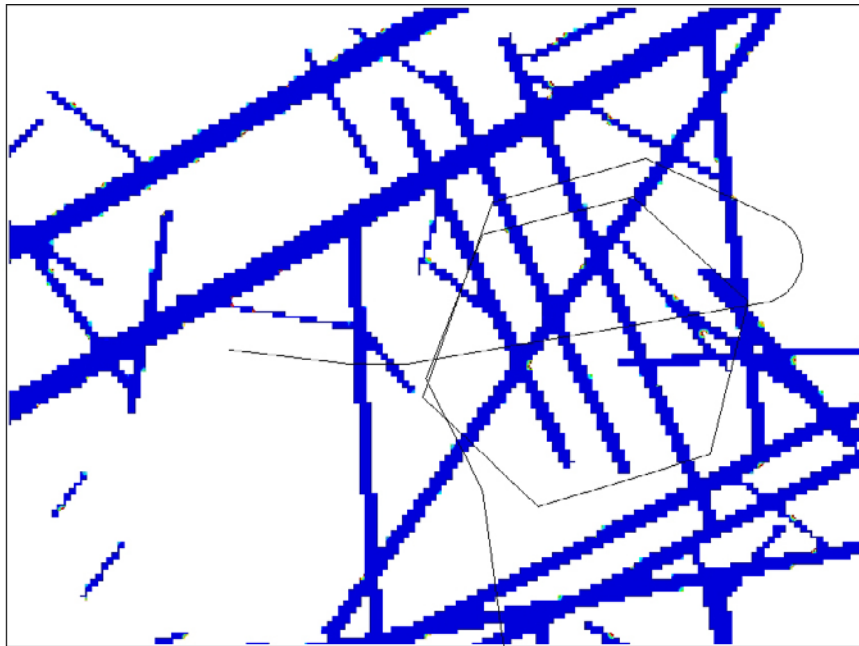
Results will now be presented, which demonstrate that the calibration criteria have been adequately fulfilled.

High Permeability Features. In Figure V2-1 illustrations of conductivity fields based on fractures with $T \geq 10^{-5} \text{ m}^2/\text{s}$ and $T \geq 10^{-6} \text{ m}^2/\text{s}$ are found. The arithmetic mean distances were calculated by drawing a number of lines in the east-west direction and count the number of crossings. It was found that the mean distance for $T \geq 10^{-5} \text{ m}^2/\text{s}$ (which includes deterministic zones) is about 80 metres and that the distance decreases to 57 metres if all fractures with $T \geq 10^{-6} \text{ m}^2/\text{s}$ are counted. The corresponding values from the field measurements are 75–105 metres and 35–55 metres, respectively. It should be noted that the two fields shown in Figure V2-1 are from different realisations; it is hence only the deterministic fracture zones that are the same in the two figures.

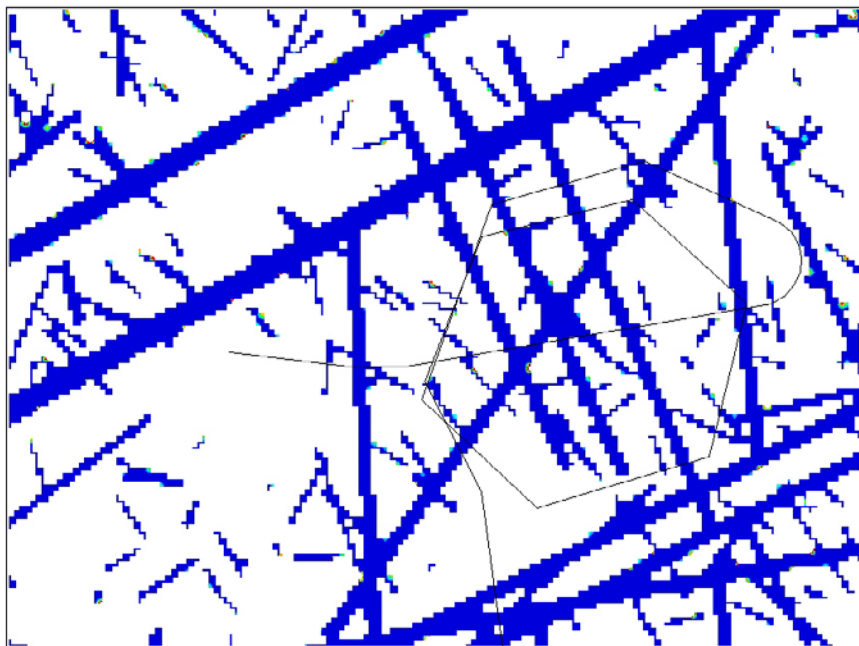
Drawdowns. The calculated drawdowns in borehole sections in the domain were compared with measured ones, all for the time when the tunnel was excavated to a length of 2,875 metres. It was anticipated that the drawdowns should be sensitive to various realisations of the background fractures. In order to study this eight realisations of the background fractures were generated and the drawdown for each borehole section and each realisation was calculated. The result can be studied in Table V2-1; the location of boreholes can be found in Figure 1-3 (Report 1). It is seen that different realisations are best for different boreholes. Recognising this pattern, it is tempting to try to optimise the comparison by using what can be called the “Method of local realisations”. We thus enclose a borehole in a volume and use fractures from the best realisation in this volume. The fracture centre is used to determine if a fracture belongs to the enclosing volume. This means that a large fracture with its centre outside the volume may still dominate the volume, which shows that there is no guarantee that the method improves the comparison in every borehole. In the vertical the volumes extended from the top to the bottom of the domain. In Table V2-1 results including local realisations can be found. When using this method one has to decide which realisation should be used outside the volumes enclosing the boreholes. This realisation is called the base realisation in Table V2-1. It is found that the locally optimised fields improve the agreement with measured drawdowns. Two measures of the agreement between measured and simulated drawdowns are given in Table V2-1, the arithmetic mean error and the goodness of fit value, defined as

$$\sqrt{\frac{\sum (a - \bar{a})^2}{n - 1}}, \text{ where } a \text{ is the error, } \bar{a} \text{ the mean error and } n \text{ the number of comparisons.}$$

Two examples of the resulting conductivity fields are given in Figure V2-2. Two base realisations are shown, but the realisations around the boreholes are in both cases from the optimum realisation. The rectangles in Figure V2-2 indicate the enclosing volumes. By studying the same rectangle in both figures, one can see that small fractures inside the two rectangles are the same. It should be underlined that this first step towards a conditioning of the background fracture network with local realisations is not an integral part of the method suggested. It is included only to demonstrate that conditioning to field data is possible.



Scale: |-----| 100 m

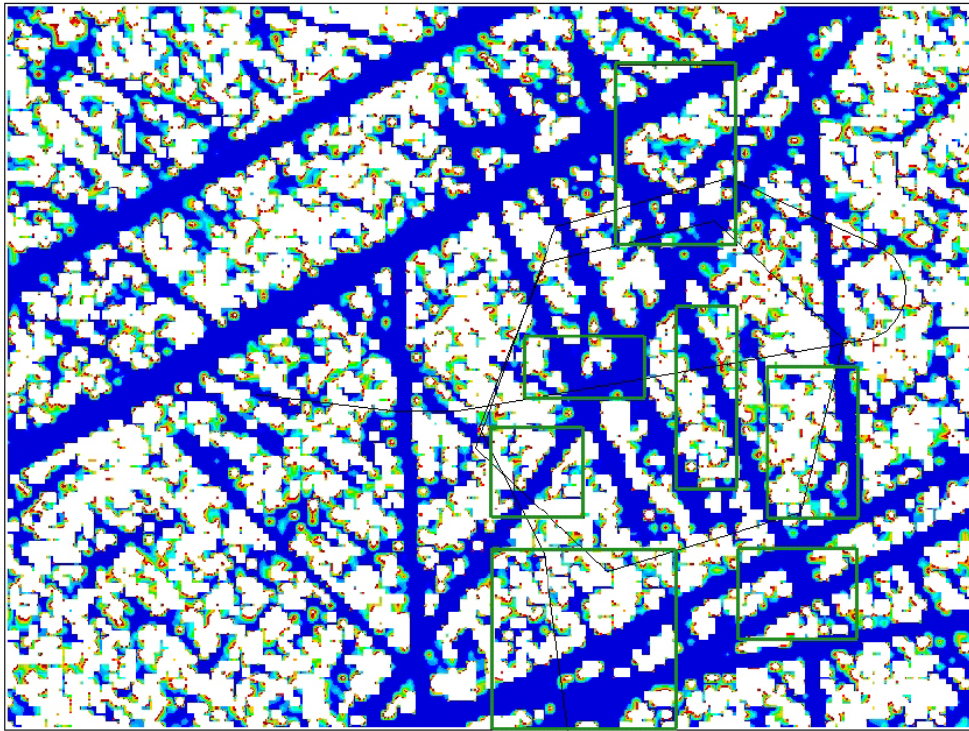


Scale: |-----| 100 m

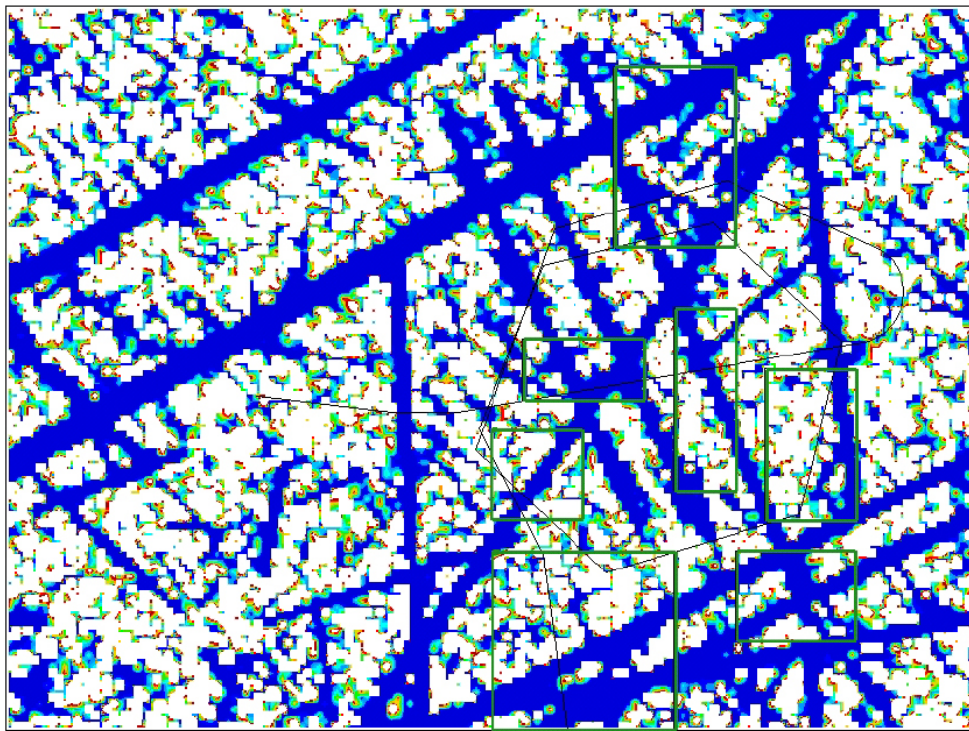
Figure V2-1. Illustrations of calculated High Permeability Features. $T \geq 10^{-5} \text{ m}^2/\text{s}$ (top) and $T \geq 10^{-6} \text{ m}^2/\text{s}$, all for a depth of 450 metres.

Table V2-1. Measured and calculated drawdowns in borehole sections for various background fracture networks. Tunnel front at position 2,875 metres.

Borehole section	Contact with major fracture zone	Measured drawdown (m)	Error (Calculated-Measured drawdown) (in m) for various realizations of the background fracture network									With local realizations	
			Realization number									Base realization	
			1	2	3	4	5	6	7	8	Best	1	4
K02-B4	no	51.50	-10.57	-9.79	-8.48	-9.85	-11.64	-10.89	-11.01	-9.92	3	-10.11	-9.38
K02-V3	yes	16.90	9.13	9.16	9.20	9.28	9.11	9.02	8.92	9.22		9.17	9.26
K05-E4	no	40.40	4.40	5.15	6.48	4.66	5.10	6.95	10.59	2.28	8	3.69	1.99
K05-E3	no	39.90	-2.22	-0.51	0.73	-0.74	0.71	1.83	-0.37	0.93		-0.56	0.41
K05-E2	no	32.50	-3.40	-2.14	-4.84	-3.61	-4.55	-4.64	-4.77	-3.13		-2.90	-3.44
K05-E1	yes	29.20	-1.41	-0.96	-3.36	-1.59	-2.56	-2.99	-3.09	-1.88		-1.58	-2.20
K06-F4	no	33.80	-2.42	-1.60	-0.68	-0.81	-0.24	-0.34	-0.95	-2.10	4	-1.11	-0.78
K06-F3	no	13.90	15.84	17.64	18.12	15.24	19.81	17.30	16.21	18.38		14.57	15.99
K06-F2	no	29.10	-1.70	0.35	-0.78	-1.44	-1.29	0.83	-1.46	-2.13		-2.82	-1.41
K06-F1	yes	30.00	-4.26	-1.13	-2.97	-2.82	-3.76	-1.20	-3.42	-2.91		-4.30	-3.35
K07-J4	no	37.50	-1.23	-0.51	-0.01	-2.07	-0.23	-5.97	0.08	0.72	8	0.68	1.09
K07-J3	no	25.20	1.78	-0.55	-0.59	-1.75	-1.42	4.04	3.86	0.20		0.65	0.83
K07-J2	yes	11.70	4.79	4.45	4.41	4.08	4.33	5.39	4.02	3.80		3.93	3.81
K08-M2	no	16.60	9.59	7.75	8.04	9.25	6.08	9.61	9.27	9.31	5	7.44	6.80
K08-M1	yes	19.50	-5.55	-5.69	-5.58	-5.59	-5.56	-5.47	-5.50	-5.60		-5.40	-5.45
K12-DC	no	25.40	3.44	2.39	3.04	3.05	3.45	2.97	2.98	1.89	1	3.52	3.47
K12-DB	no	25.30	2.31	3.39	3.17	3.26	3.63	3.97	2.62	5.09		2.61	2.30
K12-DA	yes	24.90	2.38	4.09	3.63	3.10	3.86	4.07	3.43	4.48		3.10	2.85
K16-3	no	28.00	-6.61	-6.68	-6.50	-7.72	-6.56	-5.73	-8.28	-7.04	6	-5.97	-5.77
K16-2	yes	18.60	-6.43	-6.48	-6.28	-6.51	-6.45	-6.28	-6.40	-6.48		-6.39	-6.41
K16-1	no	16.70	-5.59	-6.09	-4.79	-5.70	-4.87	-5.01	-5.04	-5.36		-5.59	-5.28
	Mean error		0.11	0.58	0.57	0.08	0.33	0.83	0.56	0.46		0.12	0.25
	Goodness of fit		6.32	6.29	6.40	6.20	6.76	6.75	6.80	6.54		5.86	5.84



Scale: |-----| 100 m



Scale: |-----| 100 m

Figure V2-2. Conductivity fields for base realisations 4 (top) and 1, see Table V2-1. The rectangles indicate volumes where fractures are taken from the optimum realisation.

Conductivity interval: $\begin{cases} \text{blue} > 10^{-8} \text{ m/s} \\ 10^{-8} < \text{red} < 10^{-9} \text{ m/s} \end{cases}$

Conductivity on a 3 metres scale. In order to collect statistics for the 3 metres scale a smaller computational domain was used. The depth interval chosen was 200 to 500 metres. The block is thus 300·300·300 m³ and with $\Delta = 3$ metres we get 10⁶ cells in the grid. Isolated fractures were not removed for this case, as this was considered to be closer to the experimental conditions. Fractures down to a size of 2.5 metres were generated. The reason for this is that the smallest fracture size generated should be comparable to the cell size.

Comparisons with field data are given in Figure V2-3, where it can be seen that the cell conductivity distribution based on this fracture network has 36% of the cells with a conductivity of less than 10⁻¹¹ m/s. A minimum conductivity of 10⁻¹² m/s was prescribed to all cells. The calculated distribution is not in agreement with the field data. However, adding a lognormally distributed conductivity with $mean(\log_{10}(K)) = -10.0$ and $std. dev(\log_{10}(K)) = -0.8$ to all cells gives a much better agreement with field data. The argument for adding a background conductivity is that it represents fractures below the cut-off length in the network. It should be noted that adding this conductivity field does not strongly influence the drawdown calculations, nor the frequency of high permeability features, presented above. It may however prove important to have also the “low conductivity connections” well described when transport simulations are attempted.

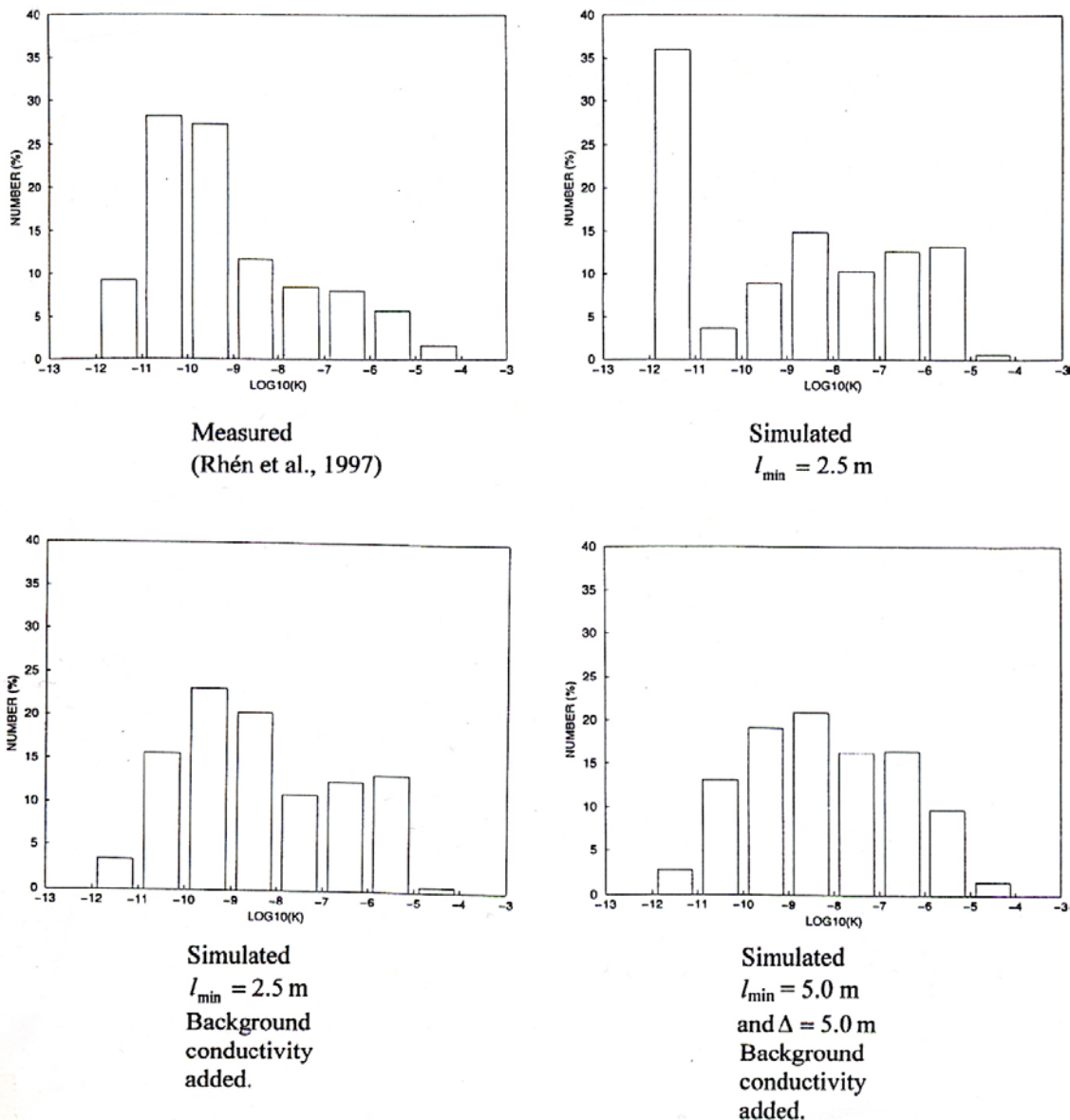


Figure V2-3. Measured and simulated conductivity distributions on a 3 metres scale and simulated distribution for 5 metres scale.

The field data are based on measurements in boreholes with a packer spacing of 3 metres. It may be questioned if it is relevant to compare these data with grid cell conductivities, with $\Delta = 3$ metres. If, as an example, we assume that the radius of influence is 3 metres in the field measurements we sample a cylinder with diameter 6 metres and length 3 metres. In order to see the influence of the cell size, the distribution for $\Delta = 5$ metres (using the main model domain) was also calculated. The result is shown in Figure V2-3. It is found that the conductivity distribution for $\Delta = 5$ metres is different and perhaps closer to the field data. Considering this uncertainty about the sampled volume, it is probably not worthwhile to strive for a closer agreement with the measured distribution. Further discussions about the field data can be found in /La Pointe 1994/ and /Rhén et al. 1997/.

Some further comparisons with data

In this section we will analyse the generated conductivity field and, when possible, compare with data. The results were not directly used in the calibration process but are anyway believed to illustrate the properties of, and add confidence to, the generated fields.

The first topic to be discussed is heterogeneity. As there is a large contrast in the hydraulic conductivity between fractures and intact rock, it is of interest to compare the heterogeneity of the generated conductivity field with field data. This can be done (/Painter 1999/) by comparing the histograms of the increments in $\log K$, as shown in Figure V2-4. The basic idea is to determine the probability of finding a certain difference in $\log_{10} K$ when moving vertically a certain distance (the “lag” in Figure V2-4). Obviously, if we had a smoothly varying conductivity field the probability to find large increments for short lags would be low. The field data shown in Figure V2-4 are from 3 metres packer tests in eight boreholes on Äspö (see /Rhén et al. 1997/). These data were analysed, with respect to heterogeneity, by /Painter 1999/.

An illustration of the heterogeneity of the generated conductivity field is given in Figure V2-5. The cell conductivity, with $\Delta = 5$ metres, along a horizontal line is shown. The line is parallel to the final part of the tunnel (i.e. section 3,400–3,600 metres), at the same depth, but roughly 100 metres south of the Äspö tunnel. The reason for sampling this volume is that conductivity measurements, with 5 metres spacing, have recently been carried out in this volume. It is clear from Figure V2-5 that large variations in conductivity from cell to cell is a characteristic feature of the field generated. Qualitatively the distribution is in good agreement with the measurements.

An often used parameter to characterise a fracture network is the fracture area per unit volume, P_{32} . In Table V2-2, the contributions from different fracture sets are given. As can be seen, P_{32} is depending on the cut-off length in the fracture network. For the present cut-off length, 5 metres, the P_{32} parameter is 0.086. If however $l_{cut-off}$ was 2.5 metres P_{32} would increase to 0.117, and if $l_{cut-off}$ was 0.5 metres P_{32} would be 0.35; all calculated from the power-law distribution. /Follin and Hermanson 1996/ summarised reported estimates based on Äspö data. They found P_{32} -values in the range 0.0664 to 2.0 m²/m³. This is a wide range, which however includes the estimates from the present model.

Concluding remarks

The main conclusion from this calibration exercise is that the suggested method to generate conductivity fields can be calibrated to match Äspö data. This was achieved by the following actions:

- Retain the transmissivities for the major fracture zones, as used in the site scale model, without modification.
- Employ a background fracture network with a fracture transmissivity that decreases with fracture size, see Equation V2-1.
- Add a background cell conductivity, which has a lognormal distribution. Also apply a lower limit (=10⁻¹² m/s) for the cell conductivity.

When comparisons with measured drawdowns in borehole sections were made, it was found advantageous to use different realisations of the background fracture network for different boreholes. This is a novel technique that seems to work well, but may require some further evaluation.

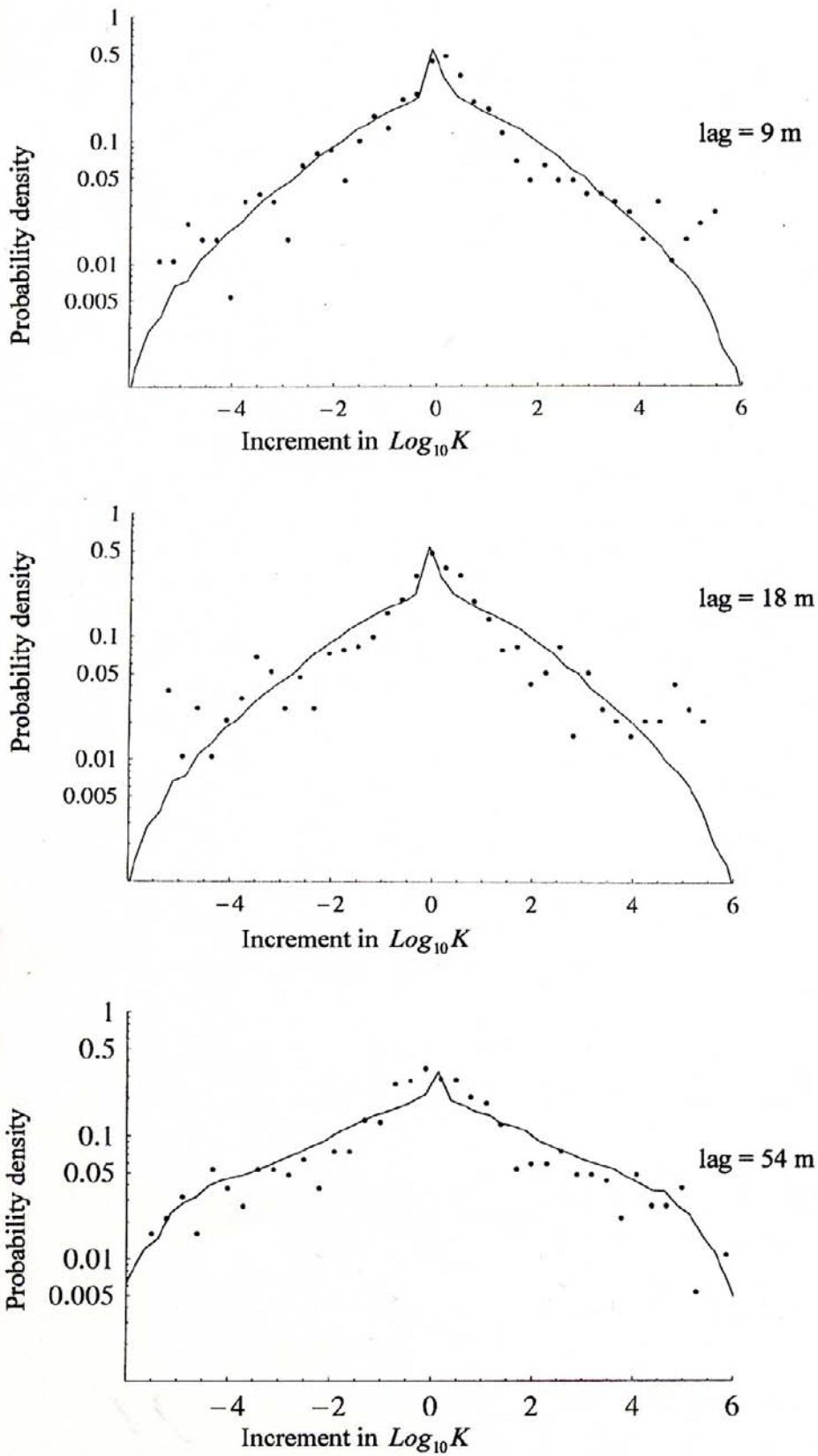


Figure V2-4. Increment histograms. Measured (•) versus simulated (-) probability distribution for different lags.

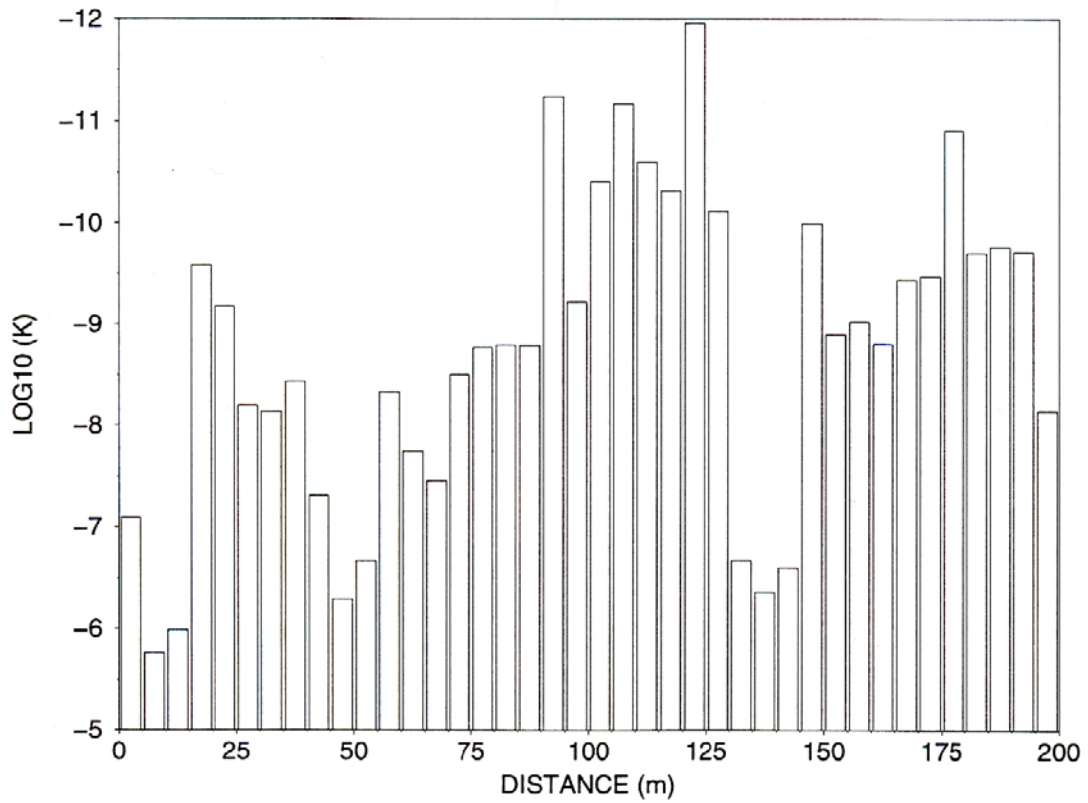


Figure V2-5. Conductivity distribution along an east-west line south of the final part of the Äspö tunnel. The conductivity in the north-south direction is shown, but other directions are similar.

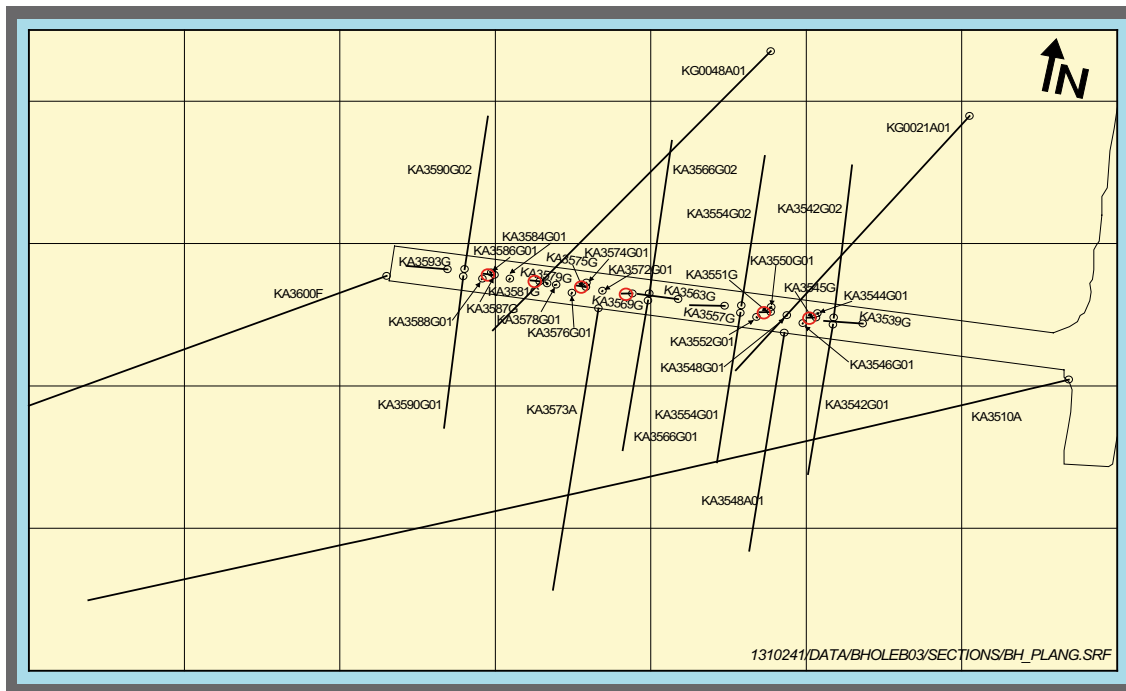
Table V2-2. The fracture intensity P_{32} , expressed as m^2/m^3 , based on deterministic fractures and the background fracture network.

Fracture length interval	P_{32} [m^2/m^3]
Determ. fracture zones	0.014
160–320	0.008
80–160	0.007
40–80	0.008
20–40	0.011
10–20	0.016
5–10	0.022
	Σ 0.086

Case V3: A repository scale validation

Introduction

This validation study is taken from (Svensson 2001/), dealing with the Prototype Repository Project, which aims to test the components in SKB:s deep repository system; see Figure 1-1 (Report 1) for the location of the computational domain and Figure V3-1 for the layout of the Prototype Repository. The objective of the report mentioned was to “develop and establish an adequate model of the groundwater pressure and salinity distributions in the domain”. More precisely five realisations that fulfilled some criteria were sought.



0 10 20 30 40 50 (m)

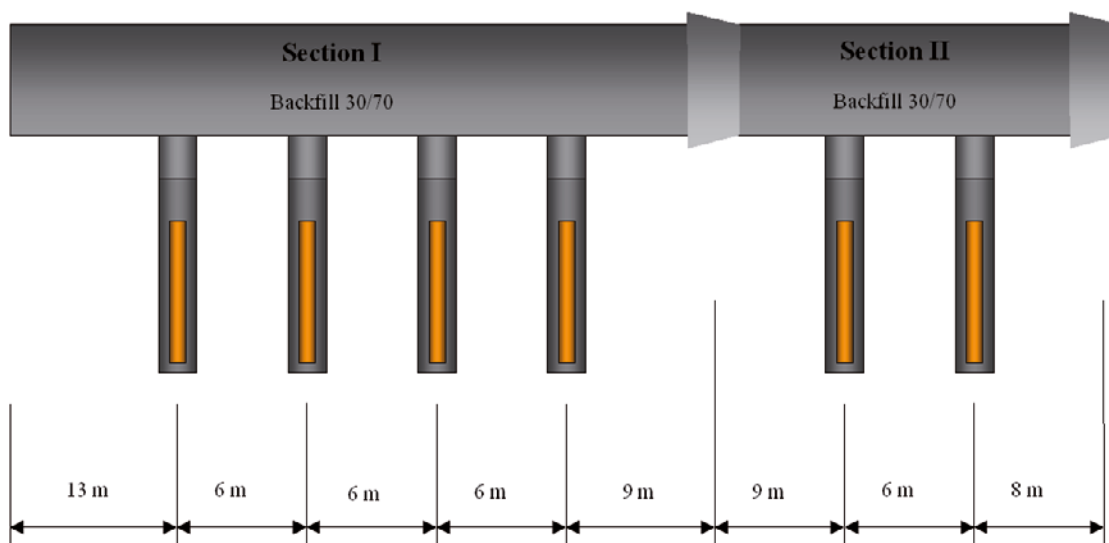


Figure V3-1. The Prototype Repository area. Six deposition holes and boreholes used for pressure monitoring.

Calibration criteria

With the objective in mind, it was concluded that the following criteria ought to constrain the model in a useful way:

- Tunnel inflows. Measurements and estimates of the inflow to different tunnel parts are available, see /Forsmark and Rhén 1999/ and /Stigsson et al. 2000/. A recent re-evaluation (Rhén I 2001, pers. comm.) of the inflow data has however revealed that the inflows are 2–3 times higher than given in the reports mentioned. Based on this information, the inflow to the tunnels has been divided into three parts, see Figure V3-2. The model should predict these inflows as closely as possible.
- Borehole pressures. Extensive data on borehole pressures, before, under and after the excavation of the deposition holes, are available, see /Forsmark and Rhén 1999/, /Forsmark et al. 2001/. The pressure measurements before the excavation will be compared with calculated pressures. Also the relation “Pressure-Distance from tunnel” will be studied as this is considered to be a well established relation from field data.
- Conductivity statistics. The conductivity distribution for the 1 metre scale has been estimated from borehole sections. This distribution will be compared with the cell conductivities in the Repository model (which has a cell size of 1 metre). It is however not obvious that field data from a packer spacing of 1 metre can be directly compared to the grid conductivities.

Calibration process

The methods and concepts, embedded in DarcyTools, have earlier been applied to larger scale problems, i.e. the Laboratory and Site scale models. The pressure distribution around a tunnel is quite a different problem and it was not clear if, for example, the type of fracture network generated would be suitable also for this problem. However, it was decided to follow the procedures from the Laboratory model as a first test. Fracture properties, orientation, intensity, etc were thus determined from the formulae given in /Svensson 1999/, also for the Repository model. In the Laboratory model a background conductivity with a lognormal distribution was used as a tuning knob; the same approach will be used for the Repository model.

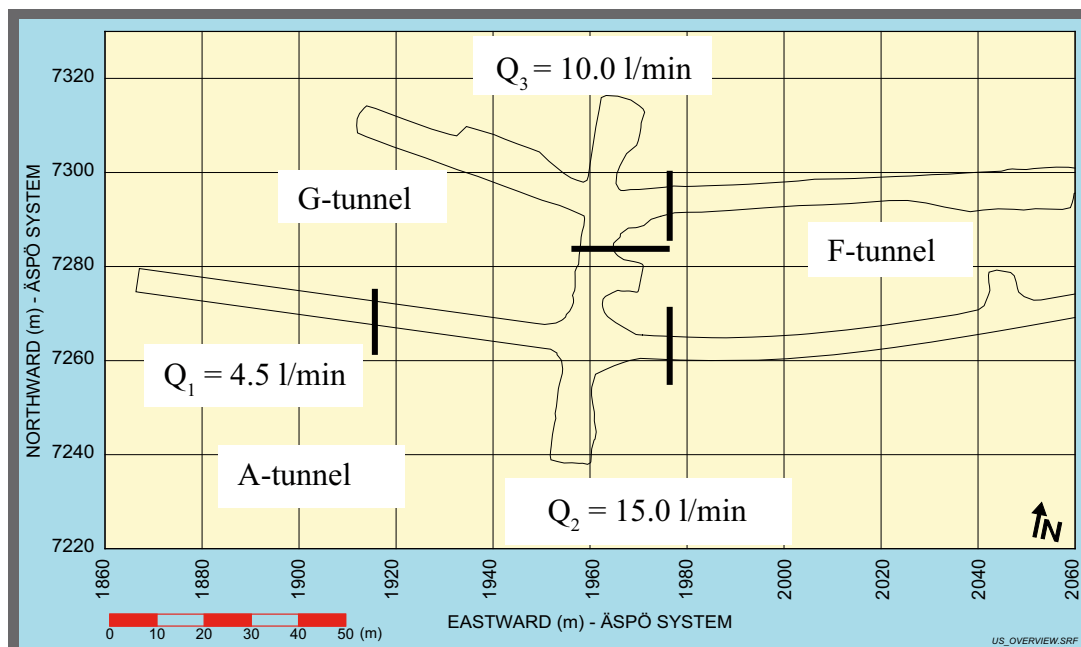


Figure V3-2. Total inflow to the tunnels is partitioned into three inflows.

Preliminary tests showed that it ought to be possible to generate five realisations that fulfilled the criteria, simply by tuning the background conductivity. The following steps can thus describe the calibration process:

- Generate a large number of realisations of the conductivity field and select the five best based on the following criteria:
 - No large fracture, with its centre outside the Repository model, should be present close to the tunnels (note that large fracture with centres inside the domain have been removed and replaced with deterministic fractures).
 - A “realistic” inflow (say 10 → 50 l/min, without skin) in each tunnel section shown in Figure V3-2. If a large fracture crossed a tunnel an inflow of perhaps several hundred l/min was generated, which means that the two conditions are partly linked. However, also a zero inflow case (or close to zero) has to be rejected, due to the first calibration criterion chosen.
- For the five realisations chosen, verify that the application of a skin around the tunnels can force the inflows to the desired values.
- Adjust the mean of the background conductivity, K_0 , to get good agreement with the pressure data from boreholes. The standard deviation (for $\log_{10} K_0$) of the added conductivity was fixed to 1.0.
- Check that the conductivity statistics for the 1 metre scale is in fair agreement with field data.

Results

Twenty realisations of the conductivity field were generated in order to select five acceptable. Some of these twenty realisations generated an inflow of several hundred l/min, others zero, in a tunnel section.

The five best could however be forced, by way of a skin factor, to give a correct inflow for all three tunnel sections shown in Figure V3-2. The skin factor multiplied all cell wall conductivities of the cells facing the tunnel. As can be seen in Table V3-1 the skin factors are in the range 0.02 → 10. The upper limit for the skin factor was set to 10.0 and, as can be seen, this skin was applied for Q_2 in realisation 3. The inflow is still a little bit lower than desired.

In Table V3-1 also the mean values for the added background conductivity are given; these are in the range $3.0 \rightarrow 6.5 \cdot 10^{-10}$ m/s. The values were determined from a comparison with measured pressures in borehole sections, see Table V3-2. In this comparison we will intentionally call the difference between the measured and calculated pressures a “difference” and not an error, as an error is something that can be identified and corrected. Anyway, the objective of the calibration, using the added conductivity as a tuning knob, was to bring down the mean difference to a small value; as can be seen in Table V3-2 this was successful. If we like, one can consider the added conductivity as representing fractures smaller than the smallest fracture generated in the network, i.e. smaller than 1 metre. A conductivity value of around 10^{-10} m/s seems to be of the right magnitude to simulate such fractures. In Table V3-2 also the number of comparisons with an absolute difference in head, smaller than 100 metres is given; this gives an additional measure of the comparison. It should be added that more pressure recordings than given in Table V3-2 are available. The ones selected are those that were classified as “best quality” in /Forsmark and Rhén 1999/.

Another way of representing the comparison of pressures in Table V3-2, is shown in Figure V3-3. Now the pressures, measured and simulated, are shown as a function of the distance to the nearest tunnel centre. As we are interested in the nearfield around the tunnels, this way of plotting the information is of interest. The first diagram in

Figure V3-3 shows the mean of all five realisations, as compared to the evaluated trend in the measured data. The trend in the measurements was estimated by fitting a straight line to the measured heads in Table V3-2. The rest of the diagrams show comparisons for each realisation. From Figure V3-3 one can conclude that the pressure head may vary with several hundred metres at a distance of, say, 10 metres from the tunnel centre. Further, the simulations show the same trend and spread as the measurements.

Table V3-1. Inflows, skins and background conductivities for the Repository model. Skin factors are given with high accuracy in order to facilitate later comparisons.

Realisation	Q ₁ l/min	Q ₂ l/min	Q ₃ l/min	Skin ₁	Skin ₂	Skin ₃	Mean conductivity added m/s [x 10 ⁻¹⁰]
1	4.5	15.0	10.0	0.0259	7.3655	0.1019	3.0
2	4.5	15.0	10.0	0.0715	0.0995	6.1238	5.0
3	4.5	13.6	10.0	0.0255	10.000	0.2430	6.5
4	4.5	15.0	10.0	0.0713	0.2595	0.0793	6.5
5	4.5	15.0	10.0	0.4360	0.0608	0.0352	3.0

Table V3-2. Comparison between measured pressures in borehole sections and simulated pressures from five realisations of the fracture network.

Borehole	Measured Head [m]	Realisation 1		Realisation 2		Realisation 3		Realisation 4		Realisation 5	
		Head	Diff.	Head	Diff.	Head	Diff.	Head	Diff.	Head	Diff.
KA3510A:3	393.2	404.3	11.1	407.4	14.2	394.6	1.3	411.2	18.0	425.5	32.2
KA3539G:1	308.2	311.3	3.1	243.7	-64.5	289.9	-18.3	291.9	-16.3	338.4	30.0
KA3542G01:1	378.7	364.5	-14.1	323.3	-55.2	304.4	-74.1	319.6	-58.9	389.8	11.4
KA3542G02:1	321.9	154.2	-167.7	240.6	-81.3	134.1	-187.8	202.6	-119.3	235.1	-86.8
KA3550G01:1	18.1	220.5	202.4	256.7	238.5	174.4	156.2	198.6	180.5	230.5	212.4
KA3550G02:1	377.6	382.1	4.5	378.8	1.2	358.9	-18.7	376.9	-0.7	405.8	28.2
KA3563G01:1	327.8	261.8	-66.0	288.2	-39.6	269.1	-58.7	269.6	-58.2	302.8	-25.0
KA3563G01:2	142.0	389.7	247.6	347.3	205.2	336.5	194.5	341.9	199.9	292.2	150.2
KA3563G01:3	142.1	187.8	45.7	218.9	76.8	206.3	-64.2	169.9	27.8	267.6	125.5
KA3566G02:1	24.6	188.5	163.9	201.6	177.0	176.8	152.2	138.1	113.4	219.2	194.6
KA3566G02:2	349.2	354.6	5.4	296.6	-52.6	333.6	-15.6	323.2	-26.0	337.6	-11.6
KA3572G01:1	353.6	298.9	-54.7	298.3	-55.3	308.9	-44.7	300.6	-53.0	304.1	-49.5
KA3573A:1	191.5	359.3	167.8	303.2	111.7	316.8	125.3	286.3	94.9	280.1	88.7
KA3573A:2	404.9	366.7	-38.2	382.7	-22.2	371.8	-33.0	373.0	-31.8	324.5	-80.4
KA3579G01:1	391.5	280.3	-111.1	315.0	-76.4	316.0	-75.5	277.3	-114.2	289.4	-102.1
KA3584G01:1	204.1	416.7	212.6	322.6	118.5	348.3	144.2	323.7	119.6	280.0	75.9
KA3590G01:1	11.5	325.8	314.3	241.0	229.5	325.2	313.7	268.8	257.3	218.6	207.1
KA3590G01:2	395.6	425.1	29.5	382.1	-13.6	396.1	0.5	379.2	-16.4	326.7	-68.9
KA3590G02:1	389.8	340.5	-49.3	272.9	-116.9	332.9	-56.9	283.8	-106.1	227.8	-162.0
KA3590G02:2	368.0	350.5	-17.6	351.4	-16.7	382.2	14.1	360.7	-7.4	332.8	-35.3
KA3590G02:3	363.4	352.2	-11.2	339.8	-23.6	374.4	11.0	349.5	-14.0	315.4	-48.0
KA3590G02:4	276.8	339.1	62.3	320.3	43.4	362.0	85.2	332.1	55.3	285.8	8.9
KA3590G02:4	100.1	311.3	211.2	239.3	139.2	317.1	217.1	270.1	170.0	65.5	-34.6
KA3593G01:2	216.1	311.7	95.6	232.1	16.0	339.3	123.2	257.9	41.8	137.4	-78.6
KA3600F:2	409.7	404.9	-4.8	276.1	-133.6	372.5	-37.2	364.3	-45.4	315.2	-94.5
KG0021A01:2	349.5	114.0	-235.6	249.2	-100.3	197.6	-152.0	234.7	-114.9	271.3	-78.3
KG0021A01:3	349.6	68.7	-280.9	268.6	-81.0	163.9	-185.6	218.4	-131.2	255.8	-93.8
KG0021A01:4	331.7	88.5	-243.2	239.1	-92.6	159.2	-172.5	225.8	-105.9	263.8	-67.9
KG0021A01:5	231.1	149.2	-81.9	188.7	-42.4	111.3	-119.8	204.4	-26.6	261.5	30.5
KG0048A01:1	386.2	267.7	-118.5	277.2	-109.0	314.4	-71.8	268.1	-18.1	241.5	-144.7
KG0048A01:2	364.0	246.2	-117.8	278.1	-85.9	289.7	-74.3	267.1	-96.9	212.3	-151.7
KG0048A01:3	370.7	206.2	-164.5	272.2	-98.5	295.6	-75.1	276.5	-94.2	269.3	-101.5
KG0048A01:4	294.0	234.4	-59.5	132.3	-161.7	283.0	-11.0	254.6	-39.4	315.9	22.0
Mean Diff		-2		-5		4		-3		-9	
Numbers with Diff < 100		18		21		20		20		23	

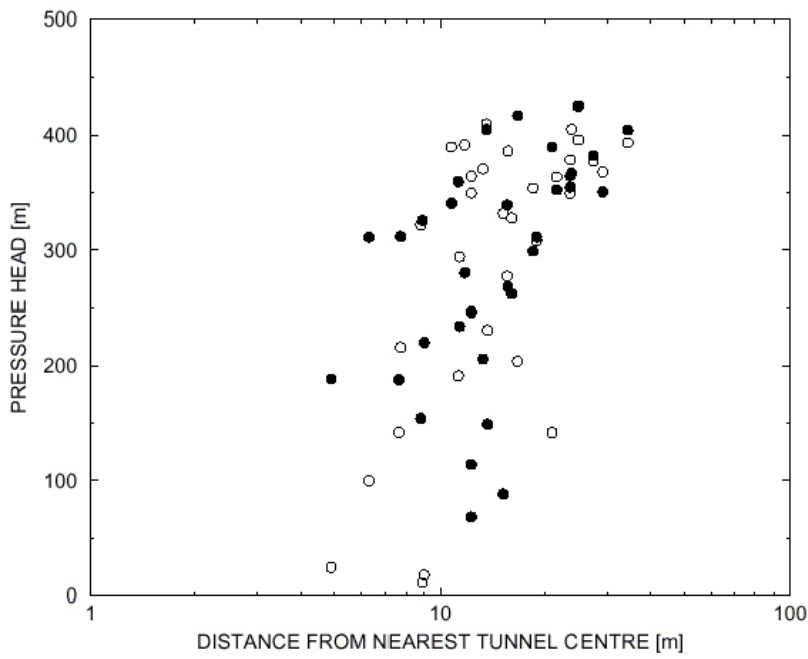
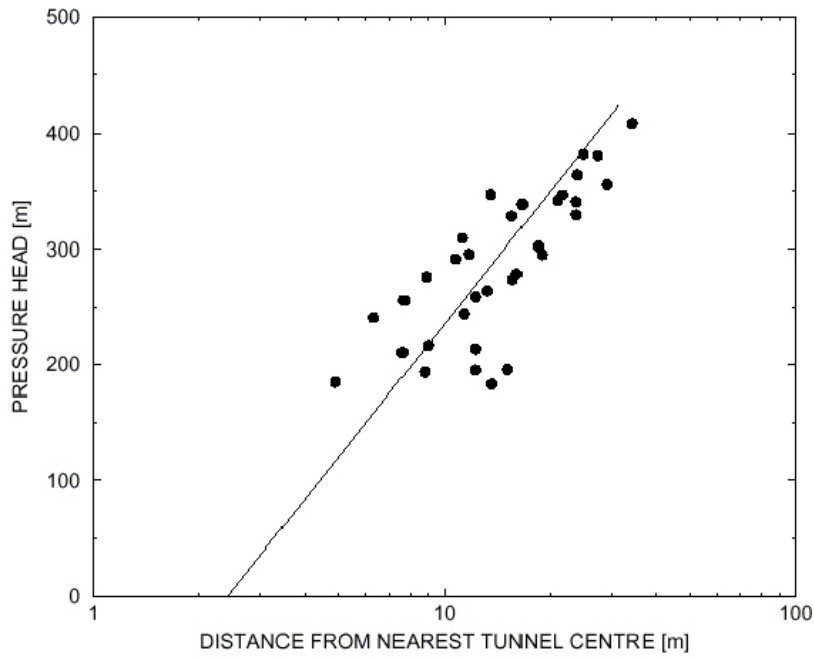


Figure V3-3. Pressure head as a function of distance to nearest tunnel centre. Average of all five realisations compared to measured trend (top); straight line represents measurements. Bottom: Realisation 1 and measured data.

- Measurements
- Simulations

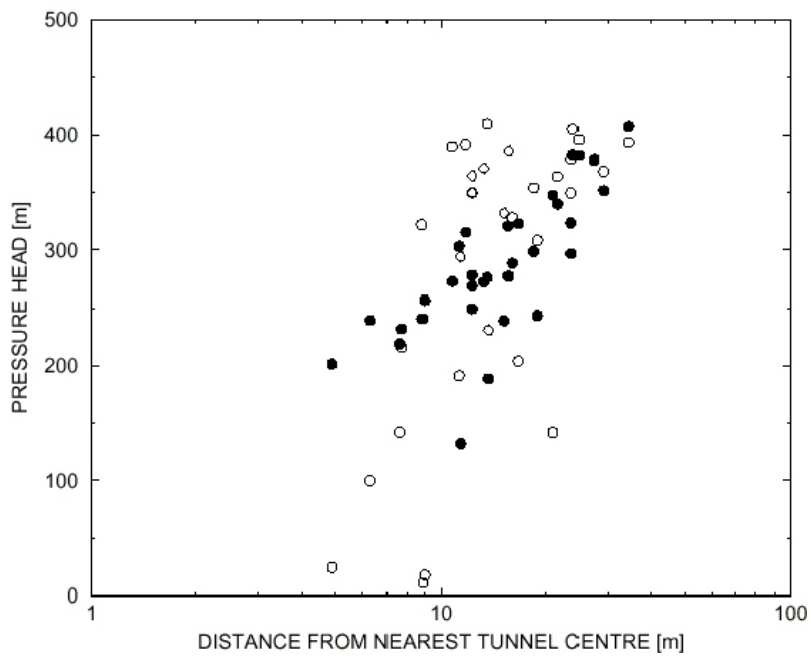
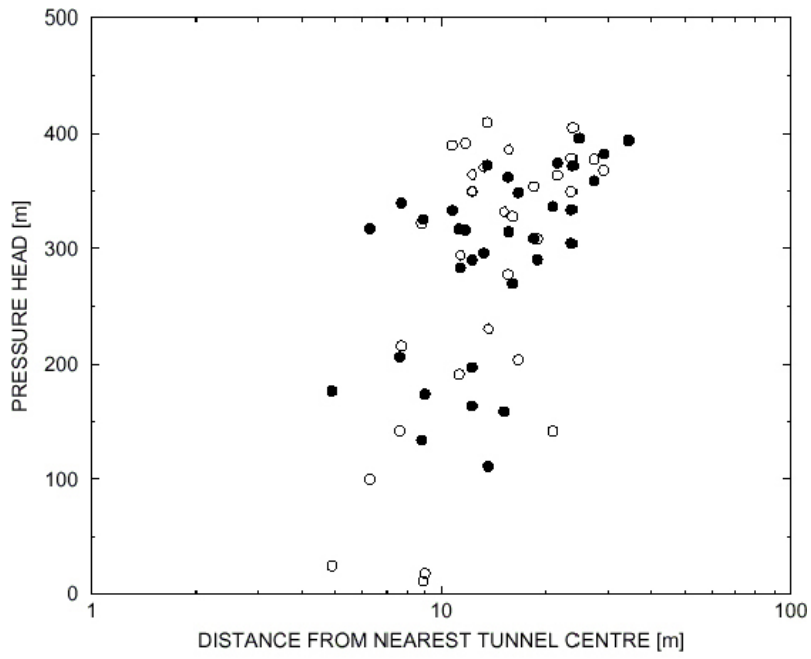


Figure V3-3. *Cont. Pressure head as a function of distance to nearest tunnel centre. Realisation 2 (top) and 3.*
 ○ Measurements
 ● Simulations

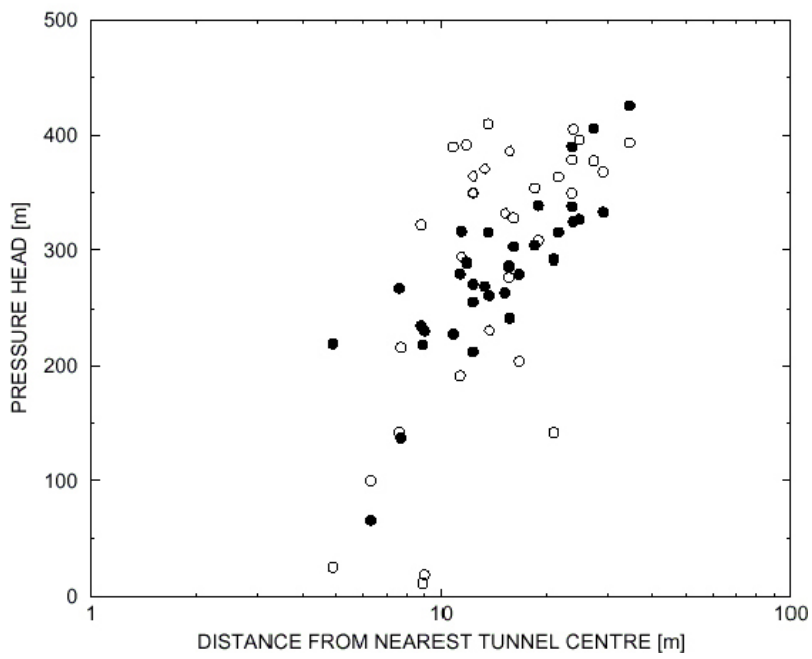
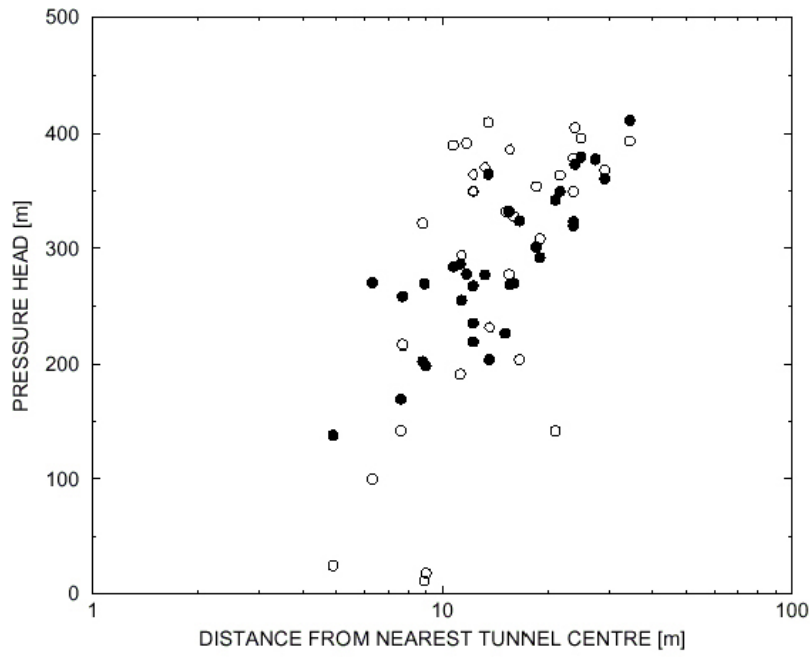


Figure V3-3. *Cont. Pressure head as a function of distance to nearest tunnel centre Realisation 4 (top) and 5.*

- *Measurements*
- *Simulations*

Finally, we will check the conductivity statistics. As mentioned above, it will be assumed that the 1 metre cell conductivities can be compared to the conductivities obtain from borehole measurements with a packer spacing of 1 metre. The distributions from the five realisations are given in Table V3-3 and in Figure V3-4 the mean of the five realisations is compared to the measured distribution. It is found that the agreement is good for conductivities above 10^{-9} m/s, while a deviation is found below this value. The distribution is however sensitive to the value of the added background conductivity for small conductivities. This is illustrated in Figure V3-4, where the distribution for a background conductivity of 10^{-11} m/s is also shown. As can be seen this will result in a perfect agreement with the measured distribution. It was however regarded as more important to optimise the agreement with the pressure measurements, and the background conductivities given in Table V3-1 are thus kept.

Concluding remarks

It can be concluded that five realisations of the conductivity field, that fulfill the calibration criteria, have been found. The agreement with measurements is generally very good.

It is worth noting that this was achieved by adding a small background conductivity, while the basic methods and parameter estimates are kept from the Laboratory scale model.

Table V3-3. Simulated conductivity distributions. Five realisations and the average distribution.

Realisation	Cumulative conductivity distribution ($\log_{10} K$, in %), K [m/s]						
	<-11	<-10	<-9	<-8	<-7	<-6	<-5
1	5	25	58	81	92	96	100
2	3	21	55	83	96	99	100
3	3	18	50	80	95	99	100
4	3	17	50	80	94	99	100
5	5	26	60	84	95	99	100
Average	4	21	55	82	94	99	100

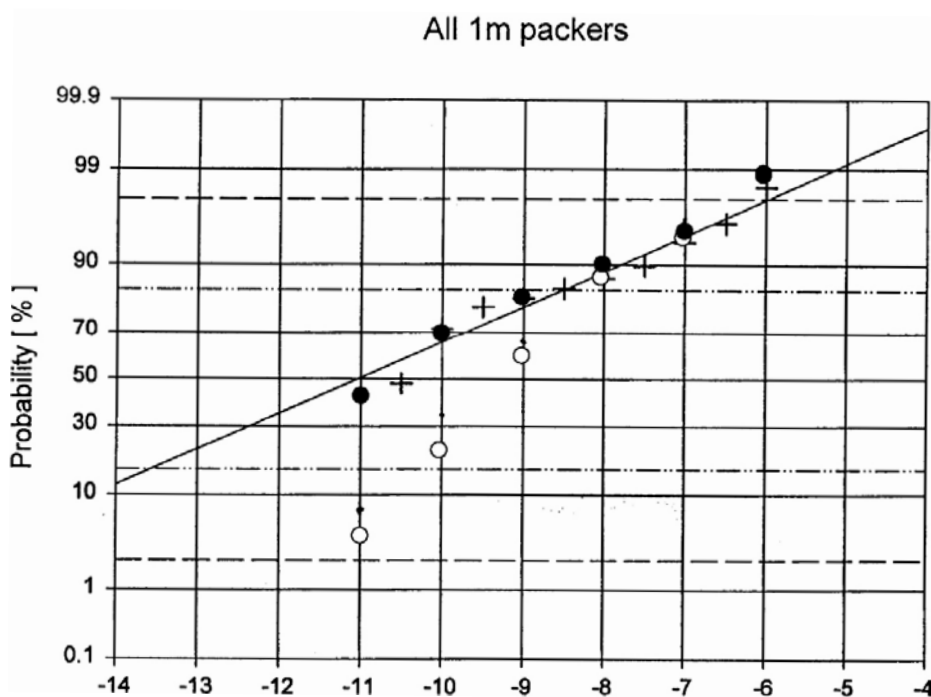


Figure V3-4. Comparison between measured (line and crosses) and simulated conductivity distribution for a scale of 1 metre. (Basic figure from /Stigsson et al. 2000/).

○ Mean of five realisations.

● Realisation 4 with an added conductivity of 10^{-11} m/s.

Case V4: An experimental scale validation

Introduction

Validation implies that the simulations should be compared with measurements. However, in this study a “somewhat derived form” of the field data will be used. The BTC:s measured in field have been deconvoluted to a unit response function, i.e. the BTC represents the expected result from a Dirac pulse input (see /Elert and Svensson 1999/). For the present purpose we will however regard the deconvoluted BTC as field data.

The objective of the validation study is to show that the numerical model can be tuned to fit the experimental BTC:s. It is however not meaningful to use all model parameters in such a tuning or to use unrealistic values on parameters. A strategy is needed.

As this is the first comparison with field data (concerned with BTC:s) it is relevant to begin with a study that focuses on the most uncertain model parameters. We will call this study phase I. The real test of a tracer transport model is however to predict BTC:s. To do predictions, the model parameters should be known or possible to estimate without reference to the measured BTC. In phase II we will use fixed model parameters and only vary property data.

The problem specification is in most respects identical to the one given for Task 6A. A general description of Task 6 and further details of this modelling exercise can be found in /Svensson and Follin 2004/. For a general description of the PARTRACK model, see Report 1.

Validation, phase I

If fracture and matrix properties, flow velocity, tracer properties, etc were all known the present model would still have two parameters that are undetermined:

- k , the late time slope. For a single rate diffusion problem we know that $k = 1.5$, but for more complex situations we can only say that $k > 1.5$. /Haggerty et al. 2000/ found, using a multi-rate model, that $k = 2.1 \rightarrow 2.2$ fits experimental data.
- α_{\max} (rate for the smallest boxes) is uncertain because it is not clear if we should associate the fastest boxes with diffusion into stagnant water or diffusive exchange with the matrix. In the later case α_{\max} should be estimated as $D_w / (t_{\min}^2 R_m)$ while one may question if R_{im} should be involved (fully or not at all) for the stagnant water interpretation.

In phase I, k and α_{\max} will hence be used as tuning knobs, with the objective to learn about sensitivity and limits. Some more conditions for the simulation:

- β_n (for non sorbing tracers) is first estimated. For sorbing tracers $\beta = R_{im} \cdot \beta_n / R_m$. R_{im} and R_m are estimated from the tracer data (see Table V4-1).
- $\alpha_{\min} = 10^{-10}$ for HTO and $D_w / D_{w,HTO} \cdot 10^{-10} / R_{im}$ for other tracers.
- The unit response BTC:s include the following tracers: HTO, Uranine, Na22, Sr85, Rb86 and Co58 (see Table V4-1).

Table V4-1. Tracer property data.

Tracer	D_w ($\cdot 10^{-9}$)	K_a	K_d	R_m	R_{im}
HTO/Uranine	2.4	0.0	0.0	1.0	1.0
Na22	1.33	$7 \cdot 10^{-7}$	$1.4 \cdot 10^{-6}$	1.0	1.95
Sr85	0.78	$8 \cdot 10^{-6}$	$4.7 \cdot 10^{-6}$	1.02	4.2
Rb86	2.0	$5 \cdot 10^{-4}$	$4 \cdot 10^{-4}$	2.0	271.
Co58	0.5	$8 \cdot 10^{-3}$	$8 \cdot 10^{-4}$	17.	542.

The first BTC discussed is for HTO, see Figure V4-1. As data are available also for Uranine (which should give a similar BTC) we include the data for Uranine as well. It is found that $\beta_n = 4$ and $k = 2.2$ give an excellent agreement with the measurements. Note that α_{\max} is not uncertain for this case.

Next Na22 is considered. It is found from the measurements that “the peak is as high as for a non sorbing tracer, but delayed”. It is not possible to obtain this effect, by the present model, without a $R_m > 1.0$. So, even if we set out to use the estimated values for R_m and R_{im} , we change R_m from 1.0 to 2.7, to get the peak arrival time right. α_{\max} is estimated to be in the range $0.68 \rightarrow 1.33 \cdot 10^{-3}$. A $k = 2.05$ and $\alpha_{\max} = 0.68 \cdot 10^{-3}$ give a fair agreement with measurements, as seen in Figure V4-2.

Strontium is the next, weakly sorbing, tracer to be studied. α_{\max} should be in the interval $0.19 \rightarrow 0.78 \cdot 10^{-3}$. A somewhat larger value, $1.3 \cdot 10^{-3}$, and a $k = 2.05$ are needed to ensure good agreement, see Figure V4-3.

For Rubidium the α_{\max} interval is $0.74 \cdot 10^{-5} \rightarrow 2.0 \cdot 10^{-3}$. A $\alpha_{\max} = 1.1 \cdot 10^{-4}$ and a $k = 1.86$ give a fair agreement, see Figure V4-4, with the measured BTC.

Cobalt is the final tracer to be discussed. The α_{\max} interval is now $0.92 \cdot 10^{-6} \rightarrow 0.5 \cdot 10^{-3}$. A $k = 2.0$ and $\alpha_{\max} = 1.5 \cdot 10^{-5}$ is the best two-parameter tuning that could be found. The agreement with the measured BTC, see Figure V4-5, is however not very good.

Validation, phase II

The objective is now to evaluate how well we can tune the model to the experimental data by only changing tracer property data, as represented by R_m and R_{im} . We then need to conclude something about k and α_{\max} from phase I. The k values range from $1.86 \rightarrow 2.2$. Let us put $k = 2.0$. α_{\max} was found to be in the expected range, except for Sr85. It is however difficult to make further interpretations of the comparisons. In lack of further evidence, α_{\max} will be based on the \log_{10} average of the two limits (i.e. the average of 10^{-5} and 10^{-3} is 10^{-4}).

Again we start with HTO and estimate β_n . Now we only have one parameter to tune as HTO is non sorbing. A $\beta_n = 10.0$ gives a fair agreement as can be seen in Figure V4-6. One should however note that $k = 2.0$ is not the best value for the part after the peak (compare with Figure V4-1).

For Na22, see Figure V4-7, $R_m = 2.0$ and $R_{im} = 1.0$ give a good agreement, with the same arguments as in phase I. The estimated values, see Table V4-1, are $R_m = 1.0$ and $R_{im} = 1.95$.

For SR85 $R_m = 2.5$ and $R_{im} = 2.0$ produce a fair agreement, see Figure V4-8. These values are of the same magnitude as estimated.

In Figure V4-9, the comparison for Rubidium is shown. $R_m = 2.0$ and $R_{im} = 30.0$ were used in the simulation ($R_m = 2.0$ and $R_{im} = 271$ in Table V4-1). However, the “average rule” for α_{\max} did not produce a good agreement for the early part of the BTC. A reduction, from $0.37 \rightarrow 0.07 \cdot 10^{-3}$, gives a significant improvement. Both curves are shown in Figure V4-9.

The same hold true for Cobalt, see Figure V4-10. The α_{\max} based on the average is $2.1 \cdot 10^{-5}$, while the better BTC is based on $\alpha_{\max} = 0.5 \cdot 10^{-5}$. For both curves the estimated $R_m (=17)$ and $R_{im} (=542)$ were used.

Concluding remarks

In the discussion section of the main Task 6 report (/Svensson and Follin 2004/) some comments about the advantages and limitations of the present model can be found. These comments are to a large extent based on the simulations presented in this Appendix.

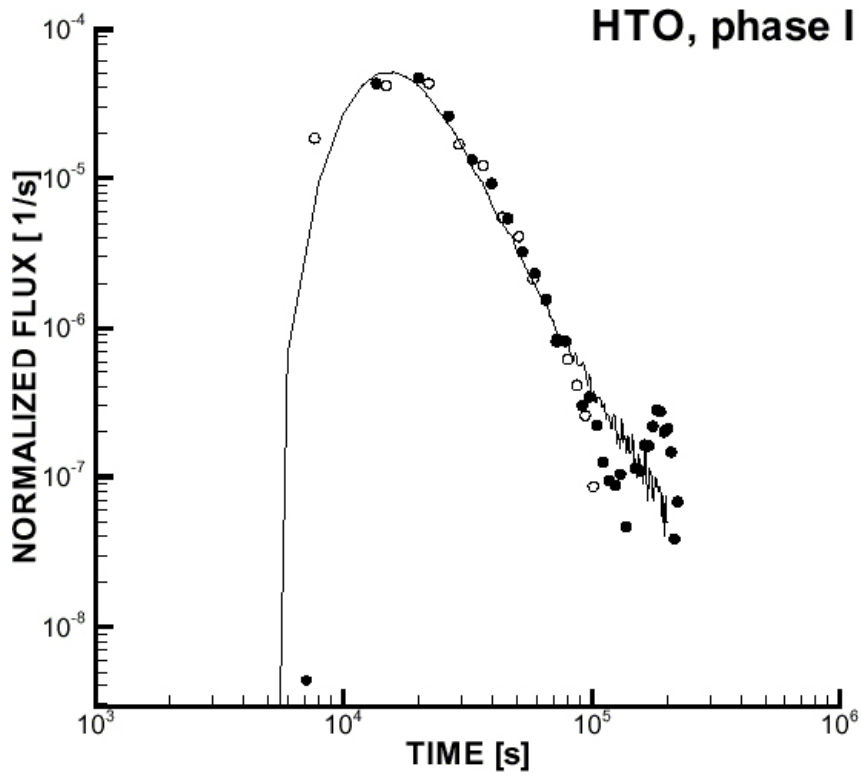


Figure V4-1. Validation, phase I. Solid line gives simulation, open circles HTO and filled circles Uranine.

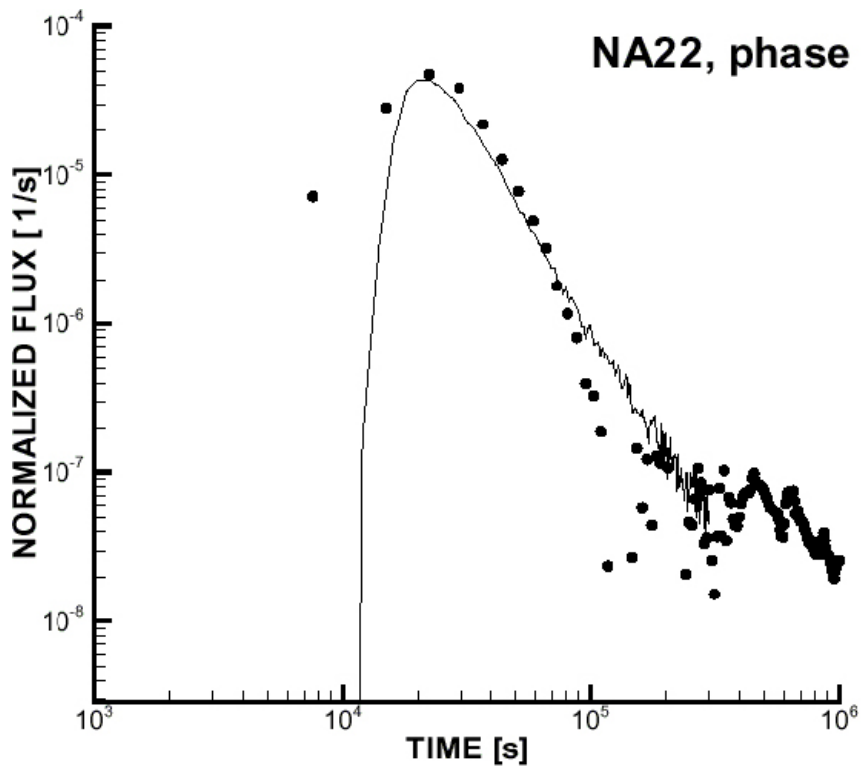


Figure V4-2. Validation, phase I. Solid line gives simulation, circles measurements.

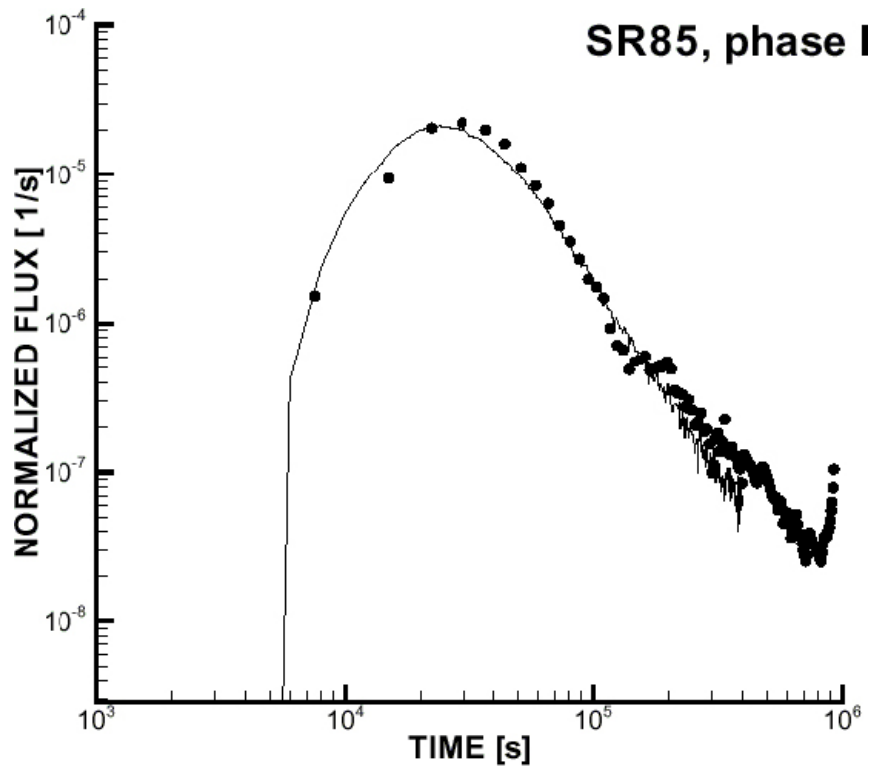


Figure V4-3. Validation, phase I. Solid line gives simulation, circles measurements.

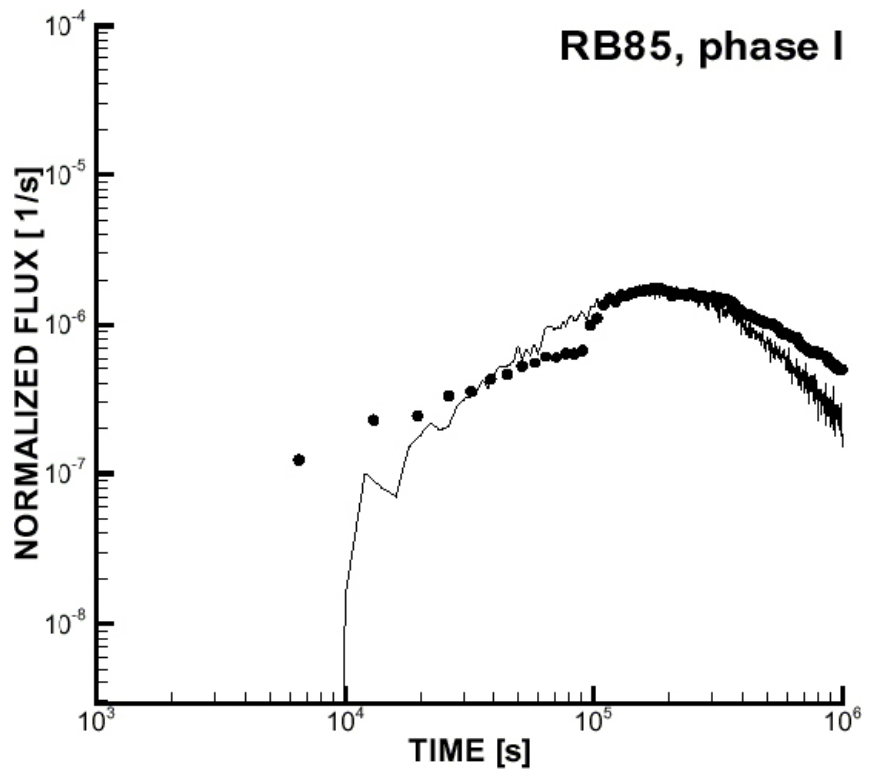


Figure V4-4. Validation, phase I. Solid line gives simulation, circles measurements.

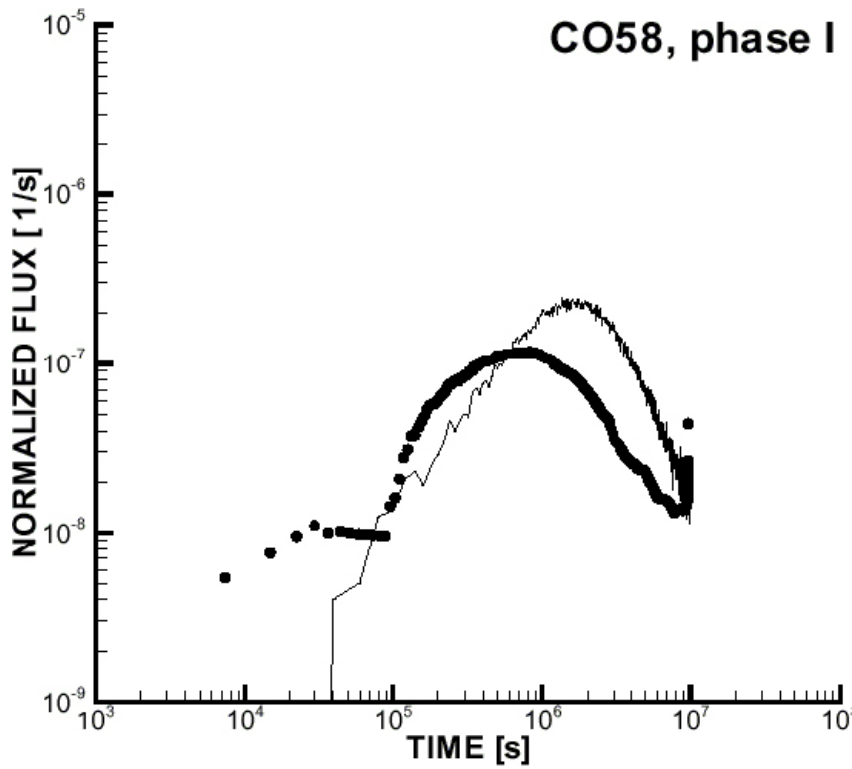


Figure V4-5. Validation, phase I. Solid line gives simulation, circles measurements.

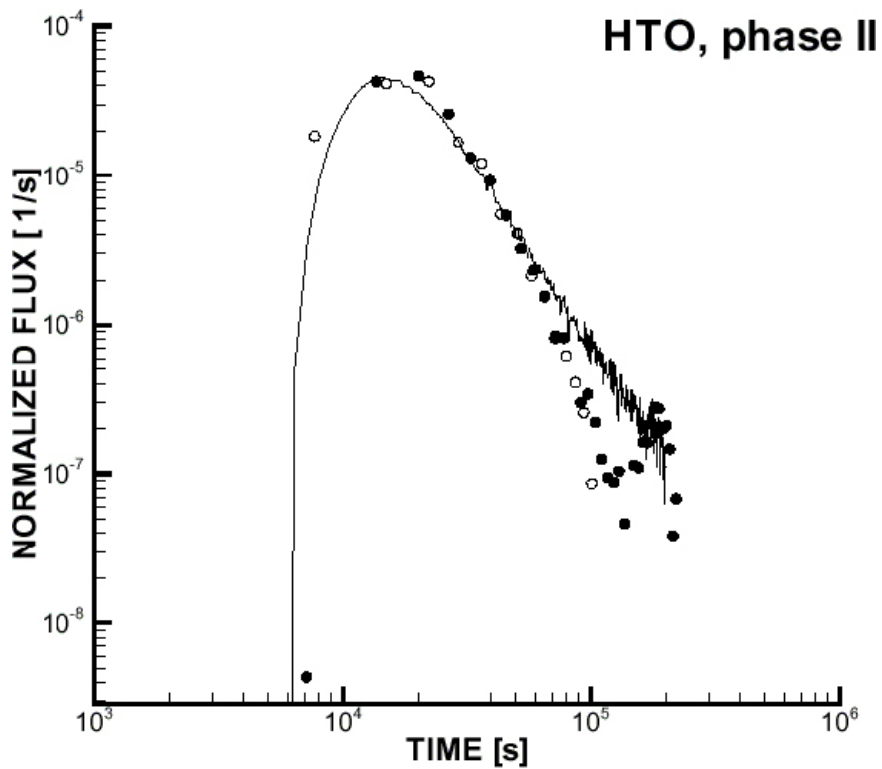


Figure V4-6. Validation, phase II. Solid line gives simulation, circles measurements. Solid line gives simulation, open circles HTO and filled circles Uranine.

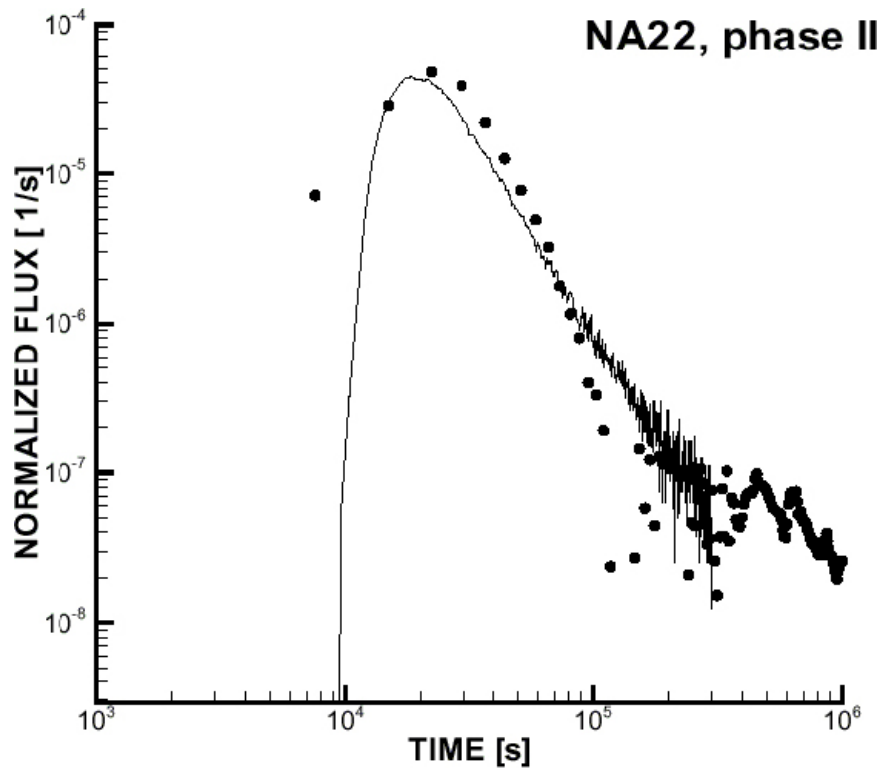


Figure V4-7. Validation, phase II. Solid line gives simulation, circles measurements. Solid line gives simulation, circles measurements.

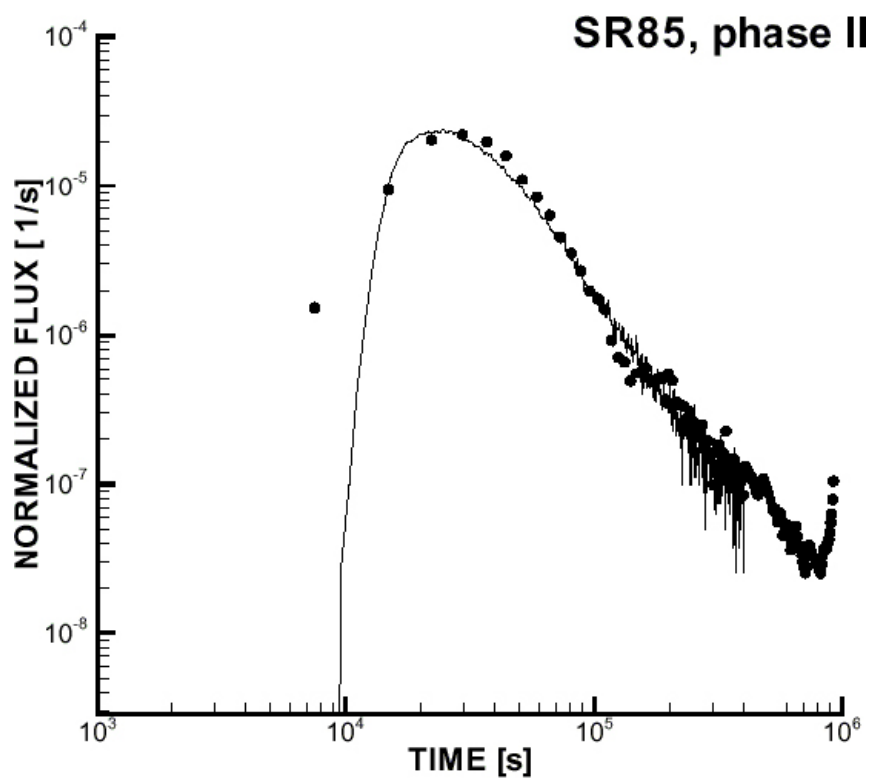


Figure V4-8. Validation, phase II. Solid line gives simulation, circles measurements. Solid line gives simulation, circles measurements.

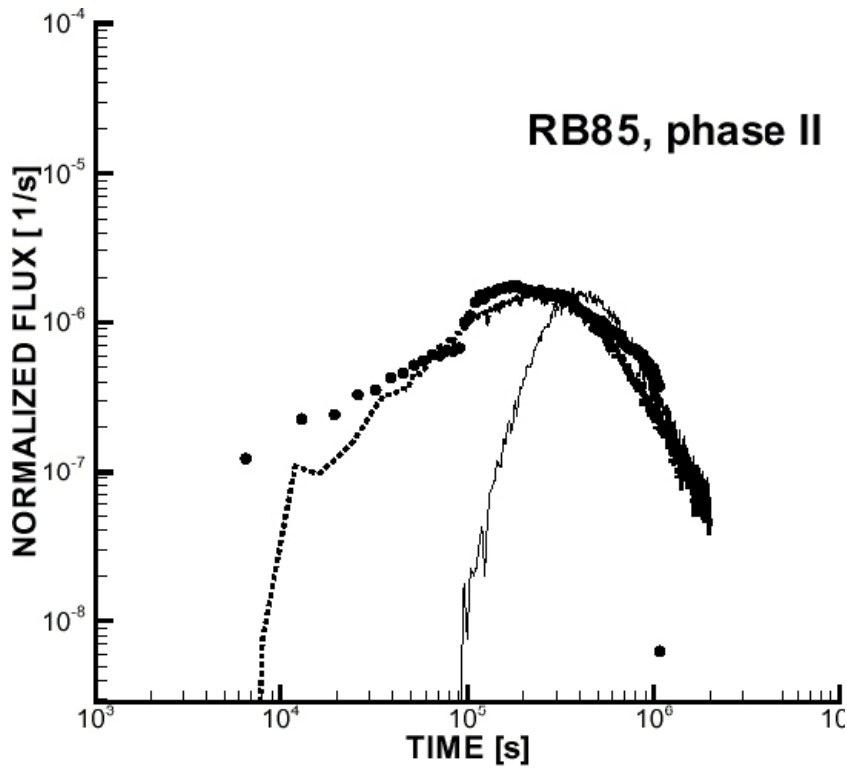


Figure V4-9. Validation, phase II. Solid line gives simulation, circles measurements.. Dashed line gives simulation with reduced α_{max} .

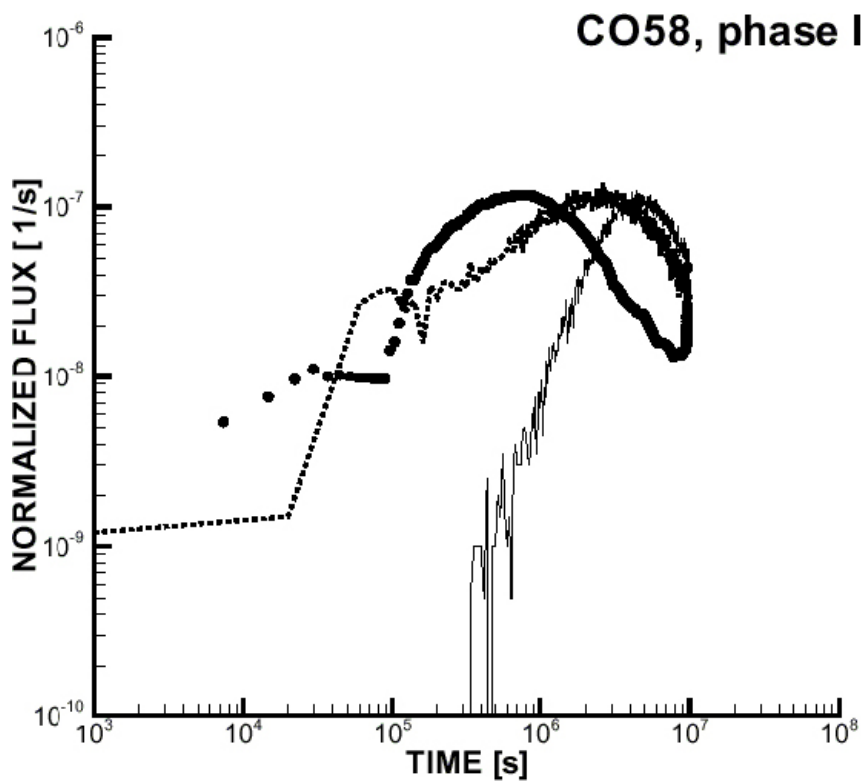


Figure V4-10. Validation, phase II. Solid line gives simulation, circles measurements. Dashed line gives simulation with reduced α_{max} .

Case V5: A pump test

Introduction

Background

Site investigations are to a large extent based on the information gathered from drilled boreholes. The core gives valuable information about the rock properties and the fracture system. If several boreholes are drilled interference tests of various kind may give further information about both the hydraulic and transport properties.

Boreholes can be of various kinds; they can be open or packed off into sections. We may further distinguish between pumped boreholes, or borehole sections, and observation boreholes. A pumped borehole will get a certain drawdown that generates an inflow to the borehole. If a steady state is reached the pumping rate is then equal to this inflow. A borehole, or a borehole section, which is not pumped, has both inflows and outflows along the borehole. For a packed off section one can assume that these are equal in magnitude. For all the kind of boreholes discussed a certain flow along the borehole will develop.

The Äspö Task Force has decided to address the question how boreholes can be analyzed by and implemented in numerical simulations model. The exercise is called Task 7. In particular, pump tests at the Olkiluoto site in Finland should be analyzed. Another, related, question is how boreholes may contribute to the general circulation at the site. It is further expected that the modelling exercises will provide information about the groundwater system in general, the hydrostructural model, advective travel times, etc.

Objectives

The present validation case concerns Task 7B and has the following objectives:

- Simulate an interference pump test carried out at the Olkiluoto site.
- Illustrate how a borehole simulation is set up in a large scale model.

The site

The site is described in the background documents for Task 7. From these we quote the following text and figures.

Geographical settings

Spent fuel from the Finnish nuclear power reactors is planned to be disposed of in a KBS-3 type repository to be constructed at a depth between 400 and 600 m in the crystalline bedrock at the Olkiluoto site.

Olkiluoto is an island of the size of about 10 km², separated from the mainland by a narrow strait, on the coast of the Baltic Sea. The repository for spent fuel will be constructed in the central part of the island (Figure V5-1). Olkiluoto Island has a continental climate with some local marine influence. In the spring, temperature is significantly lower on the island than inland. Correspondingly, the warm sea equalises the temperature differences between day and night in the fall, so that frosts are rare. The winter is usually temperate. The mean temperature at Olkiluoto in the period of 1992 to 2001 was 5.8°C. The snow thickness is usually less than 20 cm and water equivalent of snow is below 40 mm. The amount of snow varies during winter with temperature fluctuating around 0°C.

The site investigations will culminate in the construction of the Onkalo underground rock characterization facility. This construction work started in July 2004 and is expected to complete in 2010. The investigations in the Onkalo are an essential support for the application of the construction license for the repository. The application of the construction license is to be submitted to the authorities by the end of 2012.

The investigations in Onkalo will aim at further characterization of bedrock properties and to find the most suitable locations for the first deposition tunnels and holes for spent fuel canisters. Tests and demonstrations of repository technologies will also be carried out in

Onkalo. The underground parts of Onkalo consist of a system of exploratory tunnels accessed by a tunnel and a ventilation shaft. The ventilation shaft is to be located in the place of borehole KR24. The main characterization level will be located at a depth of about 400 m and the lower characterization level at a depth of about 500 m. Demonstrations and tests of repository technologies will mainly be carried out on the main level. The total underground volume of Onkalo will be approximately 330,000 m³ with the combined length of tunnels and shaft of about 8,500 m.

According to current plans, the operation of the facility would commence after 2020.

The KR14–KR18 pump tests

Two sets of test have been carried out in these boreholes.

- In 2001 to 2002 a test in open boreholes was carried out. The test can be described as “a cross hole interference test in the scale of 10–100 m, where several boreholes were pumped, one at the time”.
- In 2004 the same boreholes were used but now with a multi-packer system installed.

After this general introduction to the site we will continue with some details of direct relevance to the set-up of the numerical model.

- The potential recharge, i.e. precipitation minus evapotranspiration, is estimated to 100–150 mm/year.
- The salinity gradient is weak down to a depth of 400–500 mbsl. The salinity of the Baltic Sea around Olkiluoto is 6 g/l.
- The bedrock can be divided into an upper part, about 80 m thick, of high conductivity and a lower part which is dominated by a few (of the order of 20) large scale fracture zones.
- A number of boreholes have been drilled at the site, as is illustrated in Figure V5-1. The boreholes that will be considered in this study and shown in Figure V5-2.

Numerical model

DarcyTools will be used for the simulations; a few features of specific relevance to the present application will be listed.

- An adaptive Cartesian grid will be used. Geometrical features like topography, fracture zones, boreholes, etc can be read in as CAD files and the computational grid adapts itself to these, following a set of rules and conditions.
- New ways to represent boreholes have been evaluated in Task 7. Both the numerical resolution of the borehole and the mass conservation condition (for example inflows equal outflows for a packed off section) have been studied.
- Discrete fracture networks (DFN) have been generated and implemented in the model. A novel feature is that the DFN can be associated to sub volumes of the domain.
- DarcyTools has a built in method to handle a free groundwater table; this feature will be used.

These are some problem specific features that are employed in this study. Regarding equations we may state that the mass conservation and the Darcy equations form the foundation, while buoyancy effects are not considered; the salinity equation is hence not solved.

The grid on the top boundary is shown in Figure V5-3. A cell size of 16 m is used on the top boundary. The grid follows the topography, which was used as an input to the grid generation. Around the boreholes KR14 to KR18 a successively smaller cell size is used, as can be seen in Figures V5-3 and V5-4. At the 100 m scale a cell size of 1.0 metre is used, while the boreholes are resolved with a cell size of 0.0625 metre.

A vertical east-west section that goes through the pump test volume is shown in Figure V5-5. There are several things to note in this figure. The grid is continuous close to ground (top 80 metres) while at deeper levels the grid cells in “the good rock” have been removed. The grid cells at depth thus illustrate the fracture zones.

The following points summarize the boundary conditions employed.

- At the lateral boundaries a hydrostatic pressure distribution is prescribed.
- The bottom boundary condition is of the zero flux type.
- At the top boundary pressure is prescribed below sea level, with an account of the water depth, while a free groundwater table is simulated above the sea level. The net recharge was set to 100 mm/year.

Calibration

The calibration strategy is based on the following guidelines:

- The calibration carried out in Task 7A is kept with respect to large scale features (lakes, wetlands, etc.).
- The interference test with open boreholes is used for a calibration of the local site.

The main calibration effort thus concerns the pump test in open boreholes.

The pump test in open boreholes

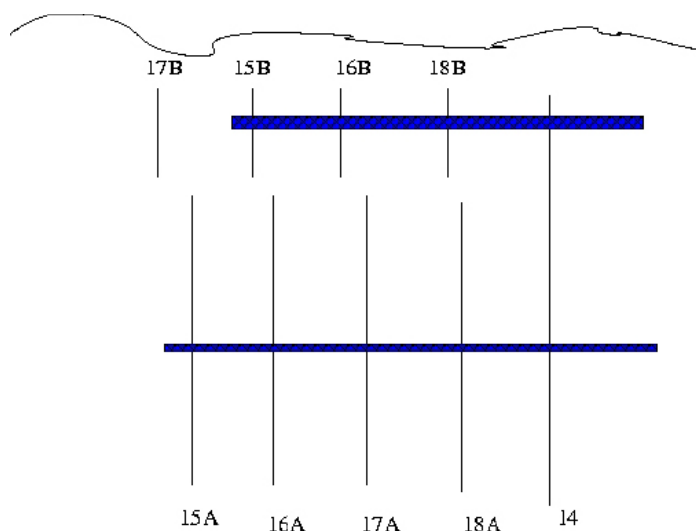
The pump test was carried out in 2001/2002 and is described in Koskinen and Rouhiainen (part of the Task delivery). The drawdown pattern is really puzzling and indicates hydraulic connections that need to be understood. In Figure V5-6 the measured draw downs and the position of the boreholes are given.

Note:

- Pumping 25 l/min in KR14 causes the same drawdown as pumping 5–7 l/min in A- holes.
- Pumping in A-holes causes a uniform drawdown in A-holes, but a lower drawdown in B-holes and KR14.
- The effect of pumping in A-holes is the same, irrespective of which hole is pumped.
- The response in KR17B is generally lower.

Suggested conceptual model

The introduction of two horizontal sheet joints, see figure below, may explain the observed draw downs, qualitatively. One may also expect that the upper sheet joint has a higher transmissivity, as pumping in KR14 with 25 l/min does not cause any large draw downs.



- Casing depths are important, especially for KR14.
- Due to the lower sheet joint a uniform response is achieved.
- Due to the upper sheet joint a weak response in KR14 is expected when pumping in A-holes.
- Pumping 25 l/min in KR14 causes a weak effect in A-holes due to the upper sheet joint.
- KR17B is not connected.

More about the sheet joints

- Have been found in boreholes at the site.
- During a pump test we expect an outflow from nearby boreholes if the boreholes are well connected. From measurements we estimate the depths of the two sheet joints to 20 and 50 mbsl.
- Transmissivities in the range $10^{-5} \rightarrow 10^{-4}$ m²/s can be expected.
- Hence, we introduce a rectangular sheet joint at 50 mbsl and a triangular (in order to exclude KR17B) sheet joint at 20 mbsl. Transmissivities from a calibration.

Sheet joints have been found at the Forsmark site; perhaps the existence of sheet joints in the upper part of the rock is the rule and not the exception?

Background fracture network (DFN)

- Power law intensity and length distribution.

$$n = \frac{\alpha}{\alpha - 1} (l_{\min}^{-\alpha+1} - l_{\max}^{-\alpha+1})$$

$$l_{\min} = 5, l_{\max} = 100, \alpha = 3.6 \text{ and } \alpha = 0.2$$

- Transmissivity law: $T = 1.5 \cdot 10^{-5} (l/100)^2$.
- Sub horizontal.
- The network is generated down to 60 mbsl (fracture centres) and may hence reach down to about 80 mbsl.

The power law parameters are explained in and found from Task 6F2 (IPR-06-21). Also the $T-l$ relation is discussed in this report.

Calibration strategy and conditions

We should look for a way to satisfy the following conditions simultaneously:

- The groundwater table should be correct (lakes, wetlands, etc). In the area of the pump test a level of 6–7 m is expected.
- The DFN should show the right frequency of HPF (High Permeability Features), i.e. number of fractures per 100 m with a T-value greater than 10^{-6} , 10^{-7} , etc m²/s. Different realisations should be tested.
- The interference test should be used to find the transmissivities of the two sheet joints.

Calibration procedure and results

In order to meet all conditions simultaneously it is important to find the interdependency between different conditions. The following procedure was adopted.

- The surface hydrology part was kept from Task 7A as it produces the right water table.
- The DFN parameters were briefly evaluated and it was found that the “standard values” produce the right HPF statistics. Different realization did not produce a big difference and the choice of the realization could be left as a “fine tuning”.
- The transmissivity of the lower sheet joint was evaluated by simulate pumping in KR15A and KR18A. A $T = 10^{-5}$ m²/s was found to work. The pump test in KR14 was used to evaluate the upper sheet joint: $T = 2.2 \cdot 10^{-4}$ is a good value. See Table V5-1.

The final part of the procedure is to evaluate three realisations of the DFN and choose one. From Table V5-1 we find that the draw downs are not very sensitive and that realization three is the best one.

The results for “No pumping” are not very sensitive to DFN realisations see Table V5-2. We choose number three as the best and all the following results are based on this realisation. The heads for “no pumping” are needed as a reference for draw downs but are also of interest as a validation; the levels are in general agreement with field data. Regarding the HPF result one should note that it is more important to get the condition $T > 10^{-6}$ m²/s right than the $T > 10^{-7}$ m²/s condition.

Results, the complete interference test

The agreement is very good, see Table V5-3, and needs no further comments. The pump tests KR16A and KR17A were not part of the calibration and are in this sense “forward predictions”.

Conclusions

The main result of this validation study is the comparison between measured and simulated draw downs (Table V5-3). A very close agreement is found.

Table V5-1. Results, the interference test. The draw downs due to pumping in KR14, KR15A and KR18A are shown for three realizations of the DFN. It is clear that the result is not very sensitive to the DFN realization used. As a simple measure of the realization the draw downs were summed up; other, and perhaps better, measures could be used.

Borehole	Measured ΔH	Simulated ΔH		
		Real. 1	Real. 2	Real. 3
KR14 pumped (25 l/min)				
KR14	6.0	6.3	6.6	6.7
KR15A	3.4	3.4	3.4	3.1
KR15B	4.4	4.6	4.8	4.0
KR16A	3.0	3.6	3.8	3.7
KR16B	3.0	4.5	4.7	4.8
KR17A	3.0	3.6	3.7	3.5
KR17B	0.2	2.7	2.8	2.6
KR18A	3.0	3.8	3.9	3.7
KR18B	5.6	4.7	4.9	5.0
	31.6	37.2	38.6	37.1

Borehole	Measured ΔH	Simulated ΔH		
		Real. 1	Real. 2	Real. 3
KR15A pumped (6.7 l/min)				
KR14	1.0	0.9	0.9	0.9
KR15A	10.0	6.6	8.4	8.6
KR15B	2.0	0.9	0.8	0.8
KR16A	3.5	2.6	2.6	2.6
KR16B	2.4	0.9	0.7	0.7
KR17A	3.0	3.0	3.1	3.1
KR17B	1.0	0.5	0.5	0.4
KR18A	3.2	3.1	3.3	3.3
KR18B	1.3	0.9	0.8	0.7
	27.4	19.4	21.1	21.1

Borehole	Measured ΔH	Simulated ΔH		
		Real. 1	Real. 2	Real. 3
KR18A pumped (5.3 l/min)				
KR14	0.8	0.8	0.8	0.8
KR15A	3.5	2.4	2.6	2.7
KR15B	0.9	0.8	0.7	0.7
KR16A	3.5	3.2	4.0	3.9
KR16B	1.5	0.8	0.7	0.7
KR17A	3.2	3.3	4.0	4.1
KR17B	0.2	0.5	0.5	0.3
KR18A	10.0	7.5	11.1	10.2
KR18B	0.8	0.8	0.7	0.7
	24.4	20.1	25.1	24.1

Table V5-2. Results, the interference test. The heads for no pumping (used as a reference for drawdowns) and the HPF statistics for three realizations.

Borehole	Heads for "no pumping"			
	Real. 1	Real. 2	Real. 3	
KR14	6.4	6.3	6.3	
KR15A	5.6	5.4	5.4	
KR15B	6.5	6.5	6.5	
KR16A	6.2	6.3	6.3	
KR16B	6.5	6.5	6.5	
KR17A	6.2	6.2	6.2	
KR17B	6.6	6.6	6.7	
KR18A	6.2	6.1	6.2	
KR18B	6.5	6.5	6.5	
Number of fractures per 100 m	Measured	Calculated		
		Real. 1	Real. 2	Real. 3
$T > 10^{-6} \text{ m}^2/\text{s}$	6	8.2	6.5	6.3
$T > 10^{-7} \text{ m}^2/\text{s}$	20	11.1	10.0	10.1

Table V5-3. The interference test. Black indicates measured draw downs, red simulated.

	KR14	KR15 A, B		KR16 A, B		KR17 A, B		KR18 A, B	
KR14	6.0	3.4	4.4	3.0	3.0	3.0	0.2	3.0	5.6
	6.8	4.0	4.9	3.9	4.7	3.7	2.5	3.9	4.9
KR15 A	1.0	10.0	2.0	3.5	2.4	3.0	1.0	3.2	1.3
	1.0	14.3	1.0	3.8	0.9	4.5	0.5	5.0	0.9
KR16 A	0.9	3.3	1.0	10.0	1.7	3.4	0.4	3.7	0.9
	0.9	3.3	0.8	13.5	0.8	4.3	0.5	4.3	0.8
KR17 A	1.0	3.5	2.0	3.9	1.5	11.0	0.2	3.7	0.9
	1.1	5.2	1.0	5.6	1.0	16.5	0.6	6.0	1.0
KR18 A	0.8	3.5	0.9	3.5	1.5	3.2	0.2	10.0	0.8
	0.8	3.9	0.7	3.8	0.7	4.1	0.4	10.0	0.7

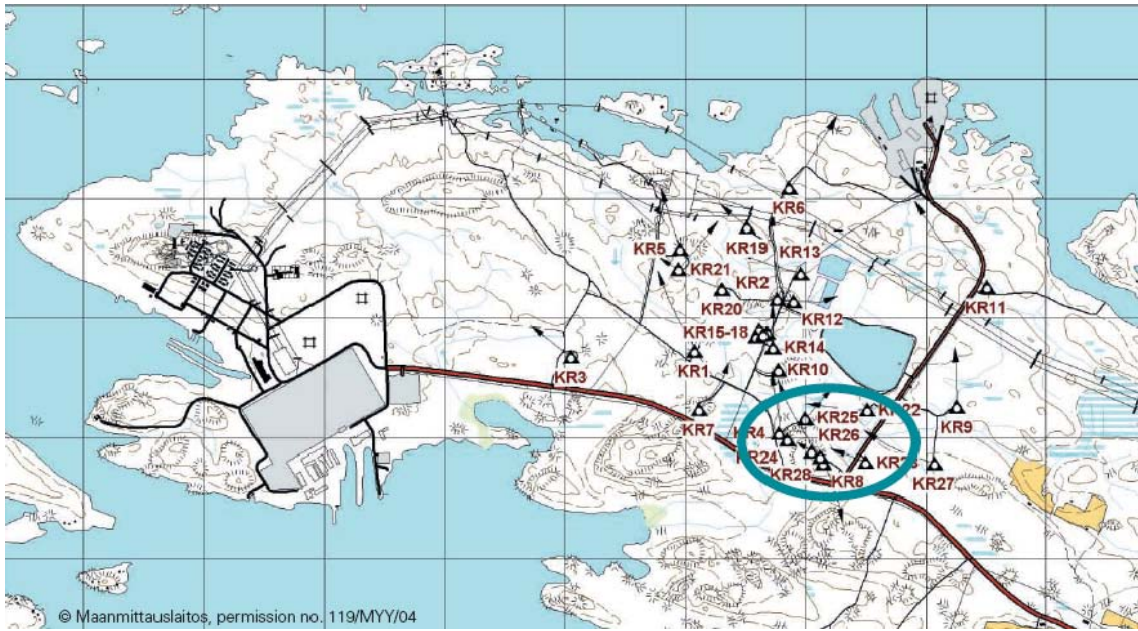


Figure V5-1. Olkiluoto Island and the location of the Onkalo (thick oval). The repository for spent nuclear fuel will be constructed in the north west of the Onkalo.

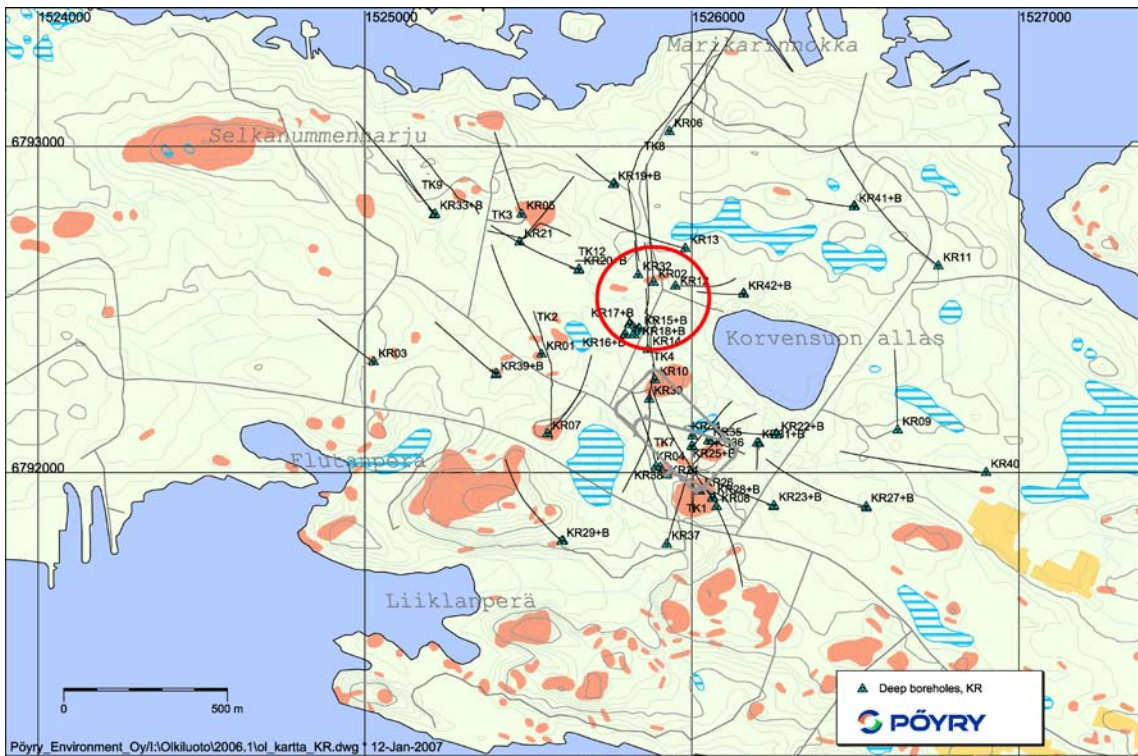
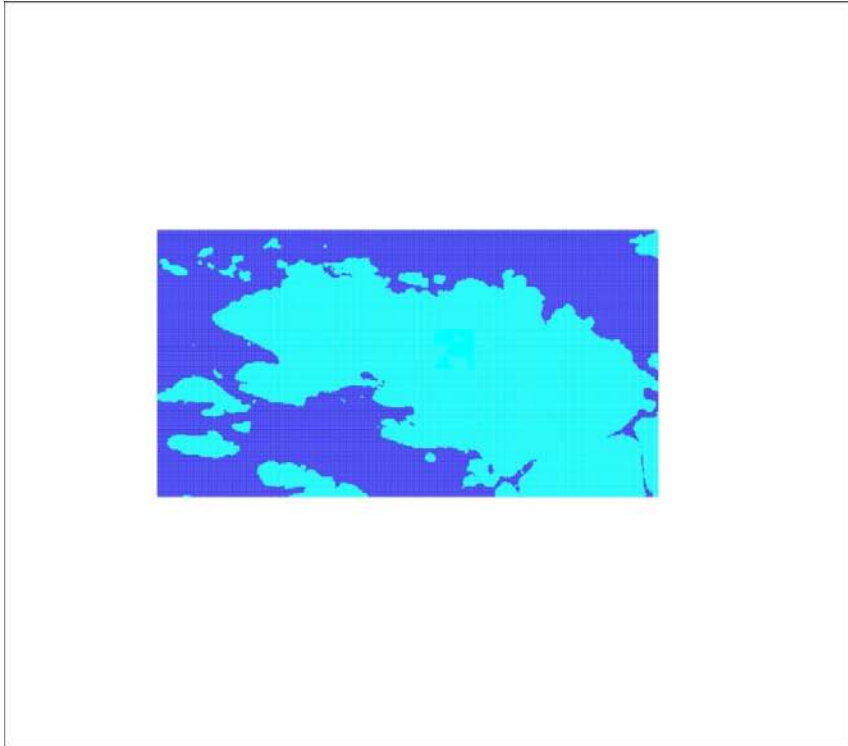
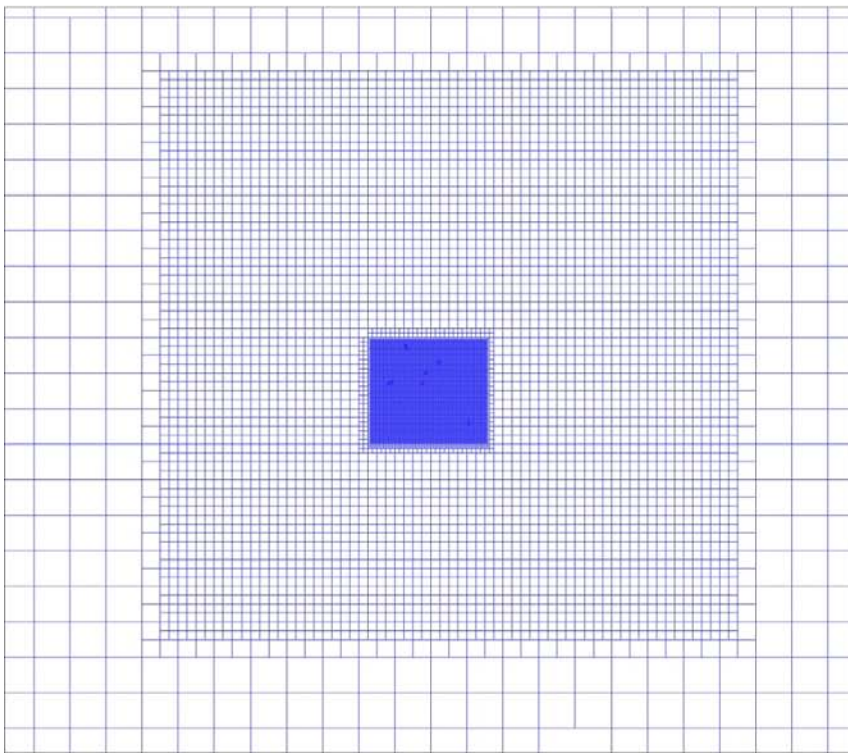


Figure V5-2. Location (red circle) of boreholes KR14 to KR18.



Regional Scale



500 m

Figure V5-3. Computational grid. Regional scale (top) and around the pump test area.

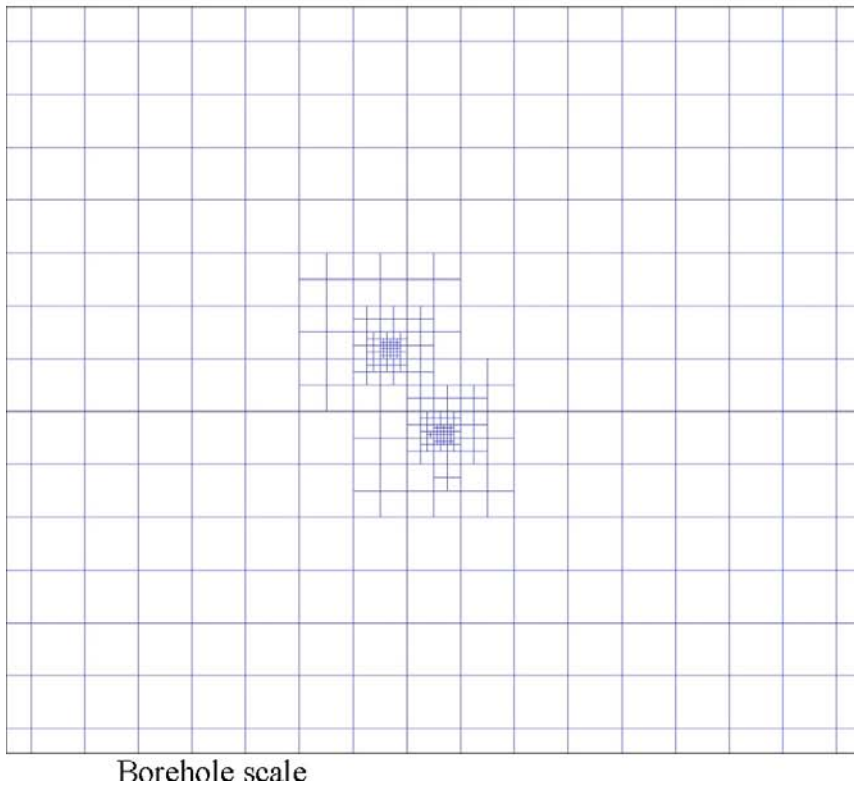
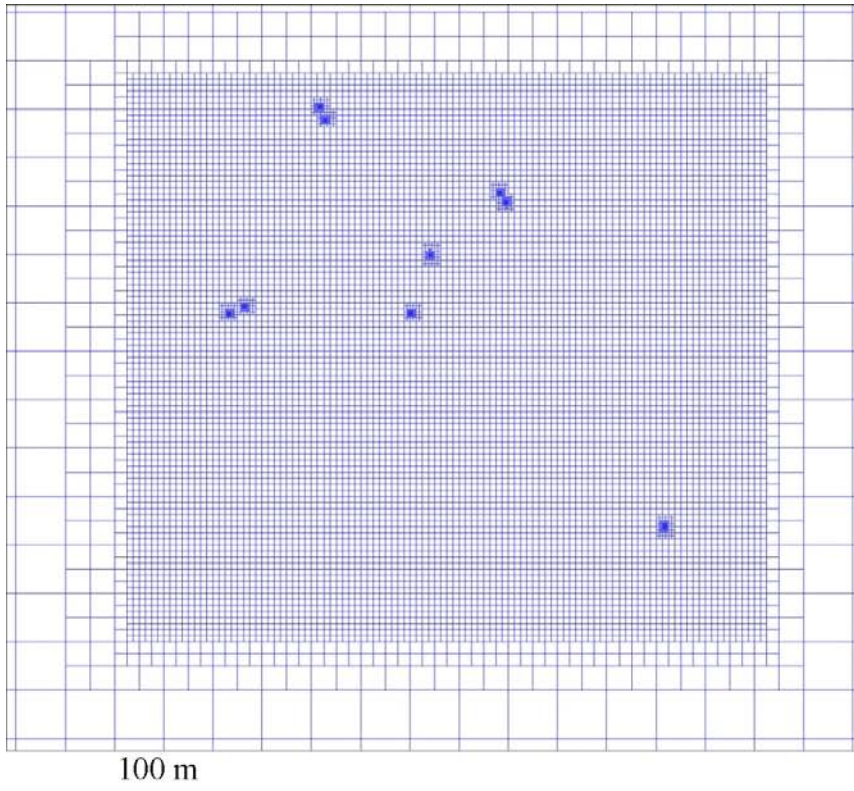


Figure V5-4. Grid around boreholes.

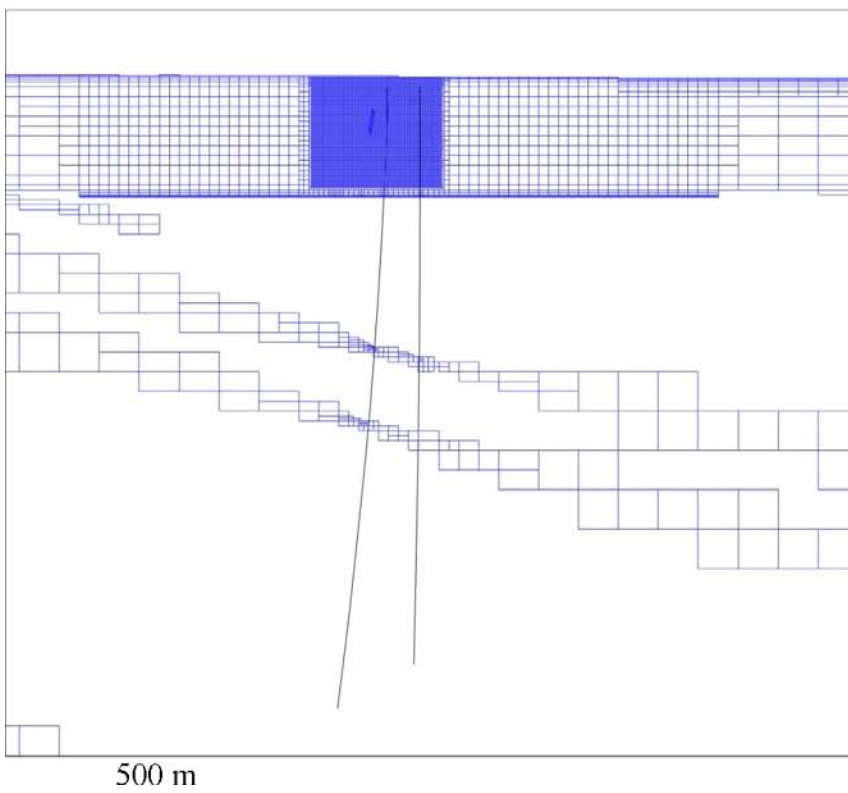
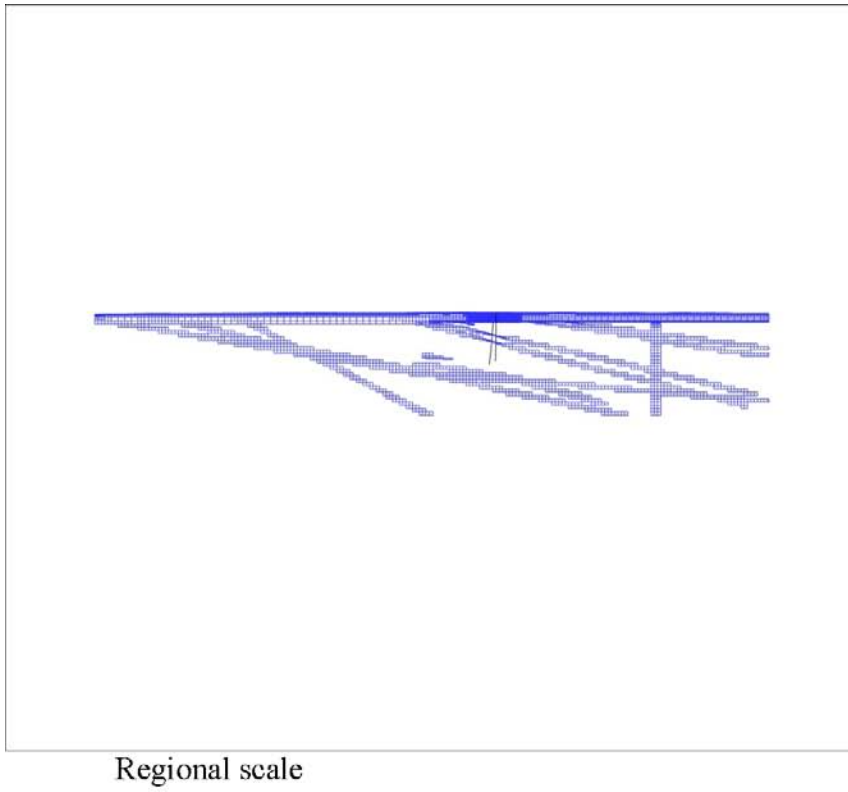


Figure V5-5. Vertical sections.

	KR14	KR15 A, B		KR16 A, B		KR17 A, B		KR18 A, B	
KR14	6.0	3.4	4.4	3.0	3.0	3.0	0.2	3.0	5.6
KR15 A	1.0	10.0	2.0	3.5	2.4	3.0	1.0	3.2	1.3
KR16 A	0.9	3.3	1.0	10.0	1.7	3.4	0.4	3.7	0.9
KR17 A	1.0	3.5	2.0	3.9	1.5	11.0	0.2	3.7	0.9
KR18 A	0.8	3.5	0.9	3.5	1.5	3.2	0.2	10.0	0.8

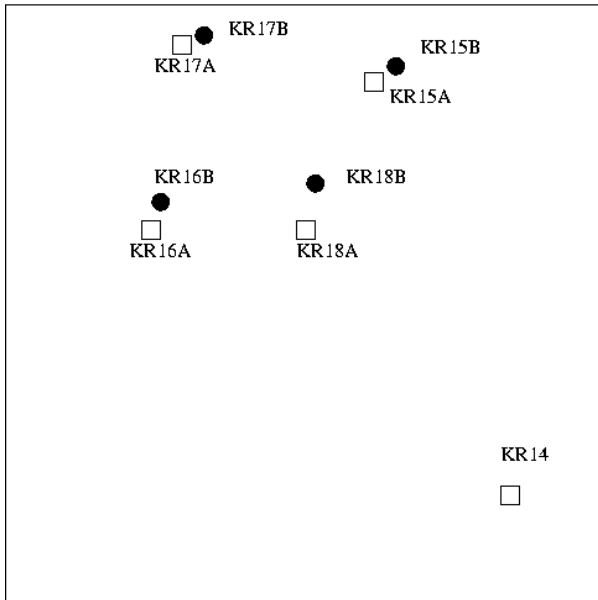


Figure V5-6. The measured draw downs (top) and position of boreholes. In the table the left column gives the pumped borehole.

Demonstration cases

Case De0: The base case

Introduction

The demo cases to be presented in this appendix all have a common base when it comes to domain size, fractures, etc. As Forsmark has been selected as a likely location for a repository, the features from this site will influence how we set up our generic base case. This is however said as a background and may explain some choices made, but all demo cases are set up to illustrate features of DarcyTools, rather than the site specific features of Forsmark.

Objective

The objective of this base case is to provide the common features of all demo cases. No flow calculations will be carried out for Case De0.

Outline of the situation studied

The ambition is to develop a set of generic cases that are simple to run and understand, but still relevant for a site. The following guide-lines have been adopted:

- Stand-alone set-ups, i.e. no input files should be required.
- Reflect the fracture network at Forsmark (sheet-joints, sparse network) and the resulting small inflow to an open repository.
- The computational domain, see Figure De0-1, is a box 1·1·1 km³ with a top surface that slopes in the x-direction. For $x < 500$ we have a land surface, for $x > 500$ we have a sea upper boundary.
- The top 20 m is considered to be a continuous soil cover. Below this level, down to 100 m, a fracture network is generated. Imbedded in this network a sheet joint is placed.
- Two vertical fracture zones connect a tunnel to the surface layer by one vertical and one horizontal fracture. The fracture zones are built up of small fractures, see Figure De0-2.
- The vertical and horizontal fractures are considered to be “single opening fractures” with an inhomogeneous property structure, see Figure De0-3.
- The tunnel is considered to be a deposition tunnel with a length of 300 m.
- Some simulation parameters are given in Table De0-1.

Table De0-1. Simulation parameters.

Fracture network	Fracture zone: $l = 5\text{--}15 \text{ m}, T \approx 7 \cdot 10^{-6} \text{ m}^2/\text{s}$ Sheet joints: $l = 5\text{--}15 \text{ m}, T \approx 3 \cdot 10^{-5} \text{ m}^2/\text{s}$ Near ground DFN: $l = 10\text{--}100 \text{ m}, T_{fr} = f(l)$
Grid	$\Delta_{\text{tunnel}} = 0.5 \text{ m}$ $\Delta_{\text{zone}} = 2 \text{ m}$ $\Delta_{\text{sheet joint}} = 2 \text{ m}$ $\Delta_{\text{fracture}} = 1 \text{ m}$ $\Delta_{\text{top boundary}} = (8, 8, 4) (x, y, z)$ $\Delta_{\text{near ground DFN}} = 4 \text{ m}$
Fractures	$T = 10^{-7} \text{ m}^2/\text{s}, \log(\text{std}) = 1$ Correlation length $\approx 3 \text{ m}$

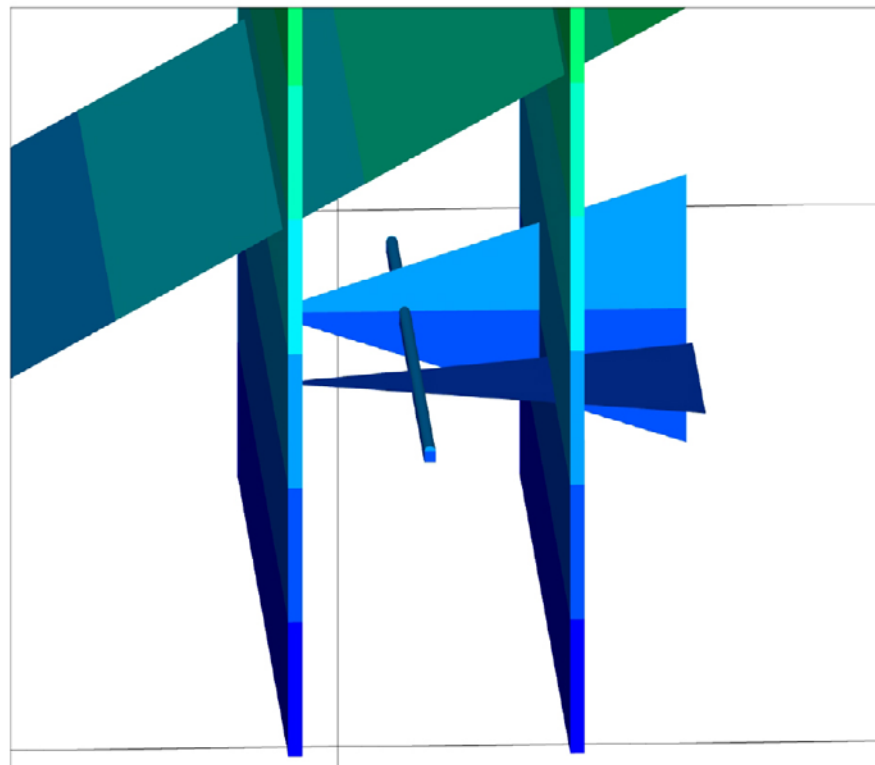
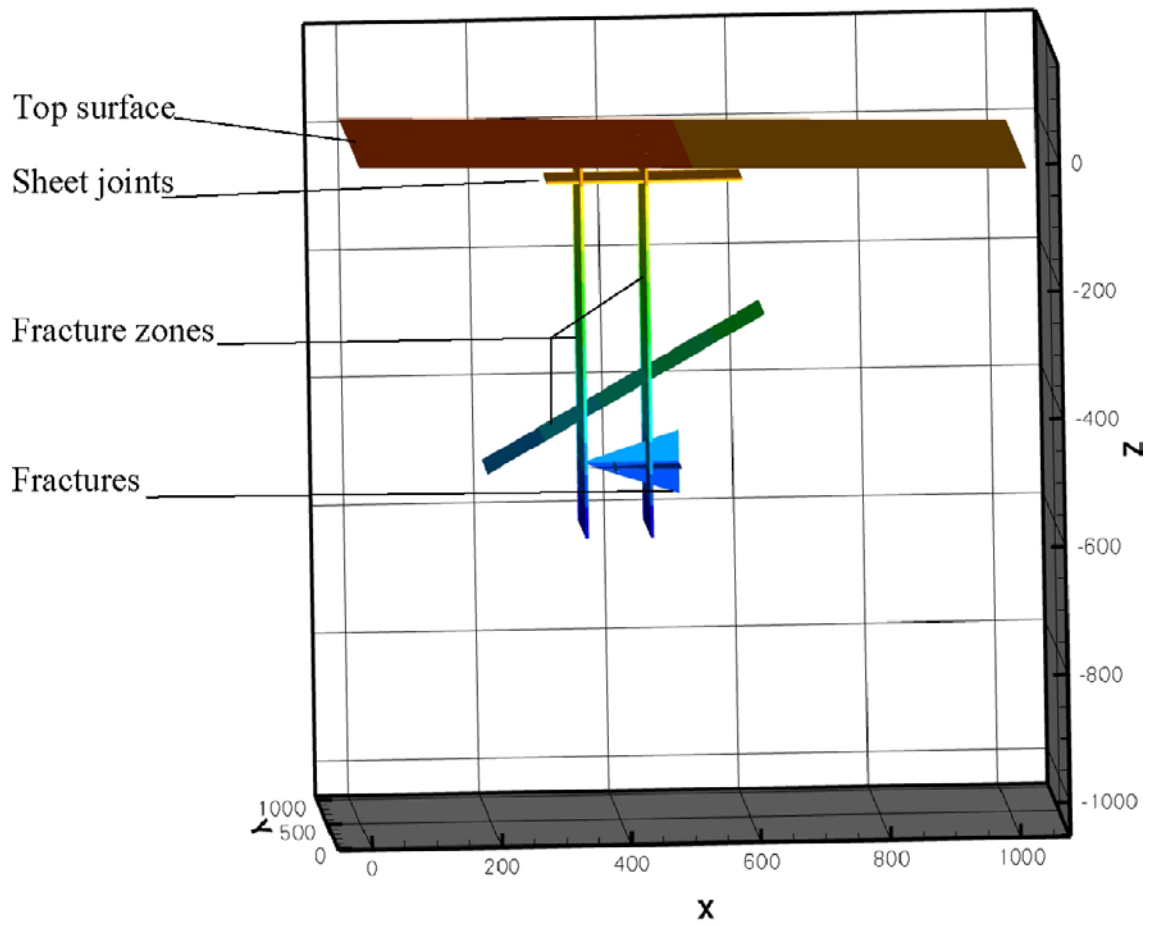


Figure De0-1. Outline of the situation considered (top) and detail around small fractures.

Concluding remarks

- The situation introduced will be the base for all demonstration cases. Each case may however introduce minor modifications; one or two zones can for example be excluded.
- The description of a case should not be expected to be complete in every detail. It is expected that a user will study the set-up where of course all details are given. All cases are part of the standard DarcyTools delivery.
- It is the intention that the demonstration cases can be used as starting points for more advanced applications.

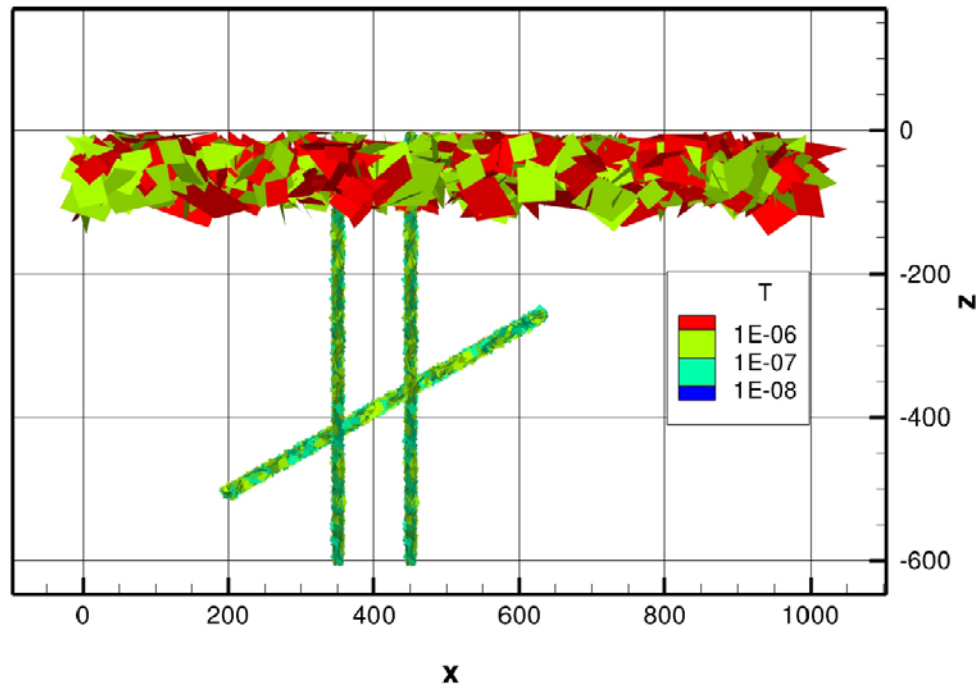


Figure De0-2. The fracture network down to a depth of 100 metres and the three fracture zones.

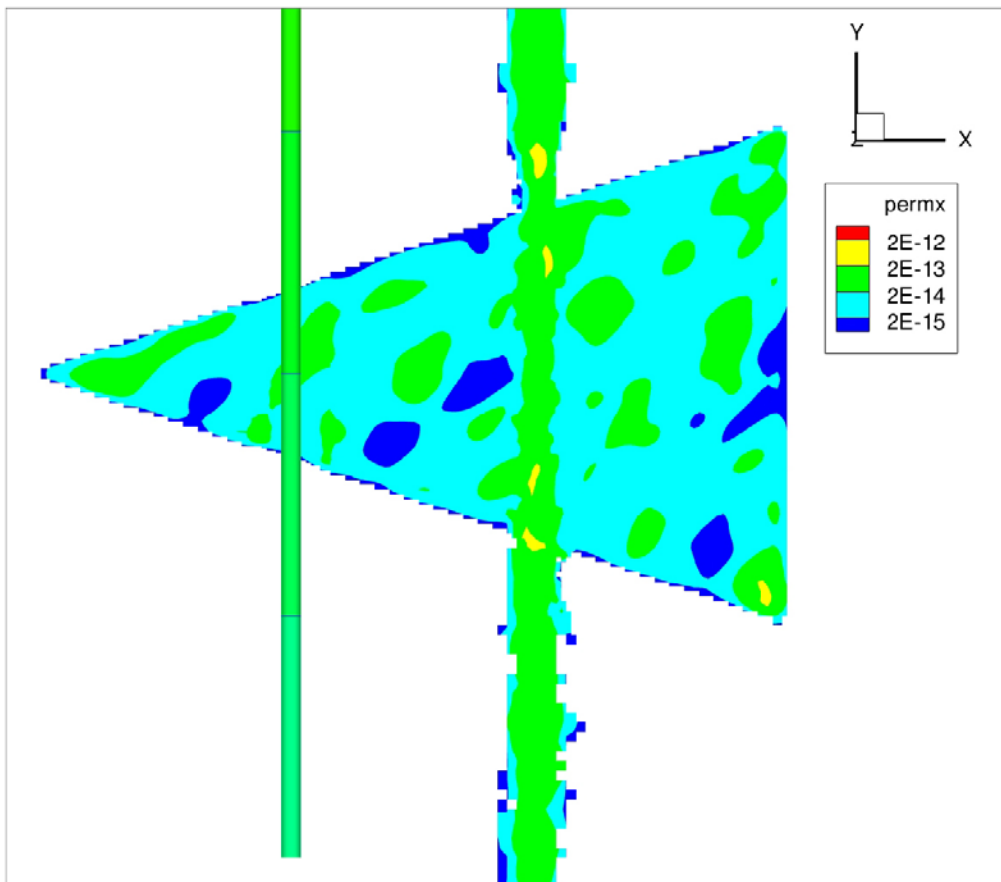
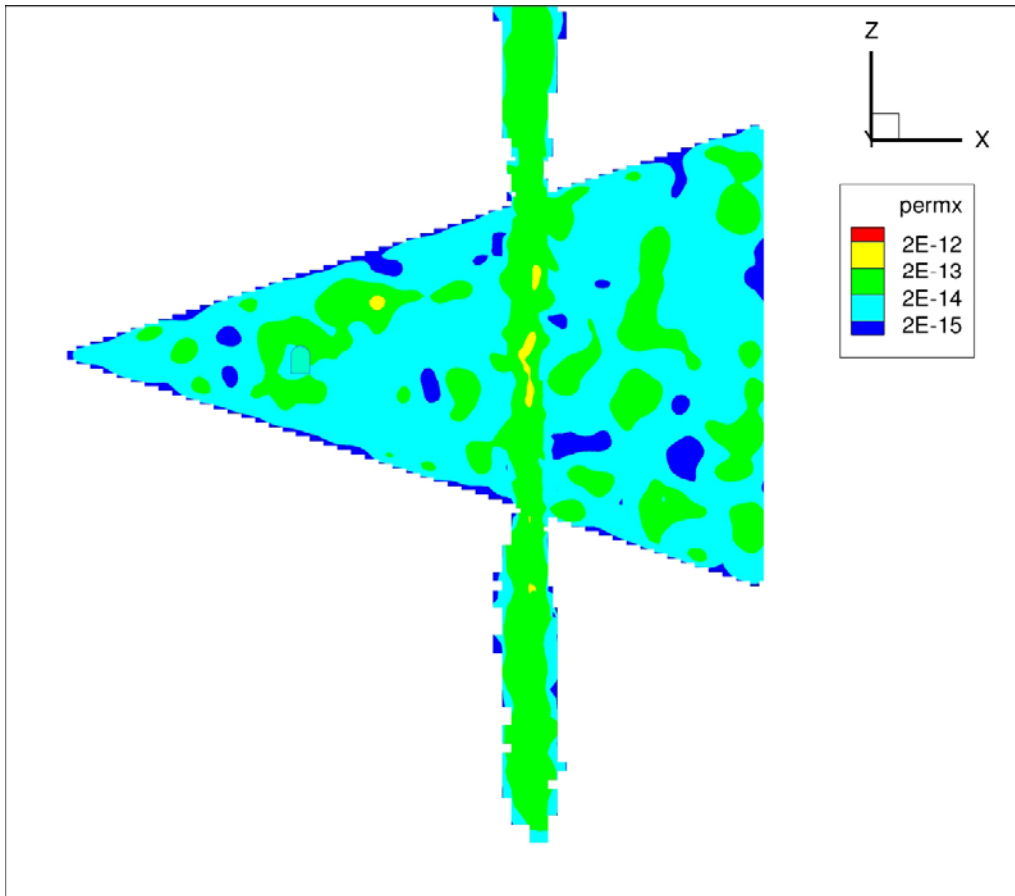


Figure De0-3. The small vertical (top) and horizontal fractures.

Case De1: The open repository

Introduction

A repository for spent nuclear fuel will have atmospheric pressure in the tunnels during the excavation and operational phases. In order to reduce the resulting water inflow grouting will be carried out. Unless the inflow is totally eliminated (which is not feasible) a disturbance in the pressure and salinity fields will result.

From several points of view it is of interest to be able to predict these disturbances:

- The ground water table will be lowered due to the tunnel inflow. The water level in lakes and wells is thus affected as well as the flow rate in streams.
- The engineered barriers are known to be affected by the salinity of the surrounding water. It is expected that water from below the tunnel will be transported to the tunnel, carrying water with high salinity (upconing). Also the oxygen saturated water from the ground surface may affect the engineered barriers.
- From a construction point of view it is essential to know the expected inflow to the repository; this in order to perform suitable grouting, design pump systems, etc.

After the closure of the repository a resaturation phase starts. Also this phase and the coupling to the host rock is of interest to simulate. Finally, one needs to consider the possible transport of radionuclides from the repository to ground level.

Considering all these aspects and the complex geometry of a repository it is realized that numerical simulations are far from trivial. A model that resolves the processes around the tunnels (on a metre scale) as linked to regional scales (on the km scale) is needed.

The present case will focus on the inflow to a single tunnel, as affected by the level of grouting.

Objectives

The demo case has the following objectives:

- Illustrate the grid generation features that were introduced in V3.3, especially the cell removal feature.
- Illustrate the grouting routine that was introduced in V3.3.

The situation considered

As compared to the base case (Case De0) we introduce the following modifications:

- Only one fracture zone is kept, namely the one at the x coordinate 450 m, see Figure De0-2.
- Grouting is considered in the two single opening fractures.

The resulting grid (after cell removal) is illustrated in Figure De1-1.

Results

In this section some brief comments to the simulation results will be given.

We start with the pressure distribution at 50 mbsl, see Figure De1-2. As all cells without a crossing fracture have been removed, the figure illustrates both the grid and the fracture network at this level. In the central part the sheet joint, with a more intense network, can be identified as well as the vertical fracture zone (at $x = 450$ metres). The pressure distribution reflects the specification at the upper boundary; at $x = 0$ the head is about 10 metres and for $x > 500$ (below sea) a zero dynamic pressure is found.

The flow close to the tunnel is shown in Figure De1-3. The channelling in the fractures is of course due to the transmissivity distribution.

Trajectories are illustrated in Figure De1-4. Cells with an inflow to the tunnel larger than 0.01 l/min are used as starting points for the trajectories and these are then back-tracked all the way up to ground level.

Finally some results using the new grouting routine will be discussed. A new command with the following parameters is introduced:

`<grout> laymin, laymax, pmin, pmax, pval </grout>`. The laymin and laymax parameter specifies cells around the tunnel in layers, starting from the tunnel wall. Parameters pmin, pmax and pval mean “if the permeability is in the interval pmin to pmax, then it is replaced by pval”. This applies to all cell walls. Which cells that are affected by the layer specification can be controlled visually.

In Figure De1-5, the layers are illustrated as well as the total inflow to the tunnel for two penetration lengths and a range of grouting conductivities. The grouting conductivity is the maximum allowed conductivity in the layers. The inflow without any grouting is about 0.1 l/s. A real world repository may have about 300 deposition tunnels and the total inflow to these tunnels can then be estimated to 30 l/s.

Running the case

The following steps should generate the results just described:

1. Copy cifstep1.xml to cif.xml and issue the commands RUNGGN and RUNFGN. This first grid is a coarse grid without any removed cells. The fracture network is generated and isolated fractures are removed. We only need to do this once and we therefore store the network in a file called “fractures”.
2. Copy cifstep2.xml to cif.xml and prpgenstep1.f to prpgen.f. Issue the command BLDMYPGN.
3. Next issue the command RUNMYPGN. A file, DE1RRC, is created which has information about cell removal and grid refinement.
4. RUNGGN is next; now the grid is refined and cells removed.
5. The fracture network is represented in the new grid by RUNFGN.
6. Repeat steps 3 to 5 in order to converge the process. Three times are probably enough.
7. Copy prpgenstep2.f to prpgen.f and issue the commands BLDMYPGN and RUNMYPGN.
8. The grid and property files are now generated and the case can be started by RUNDTS, as usual.

Discussion

The case opens the road for a number of studies concerning inhomogeneous fractures, zones built up of small fractures, grouting alternatives, inflows to tunnels, etc.

Conclusions

The case illustrates a wide range of issues that are important when simulating the inflow to an open repository.

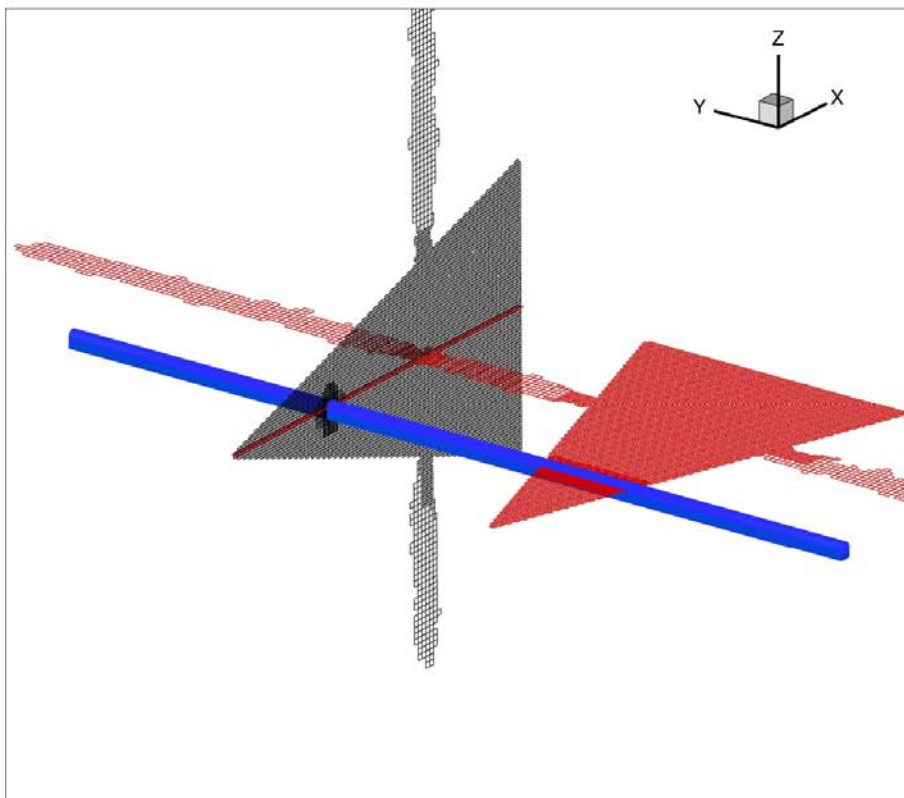
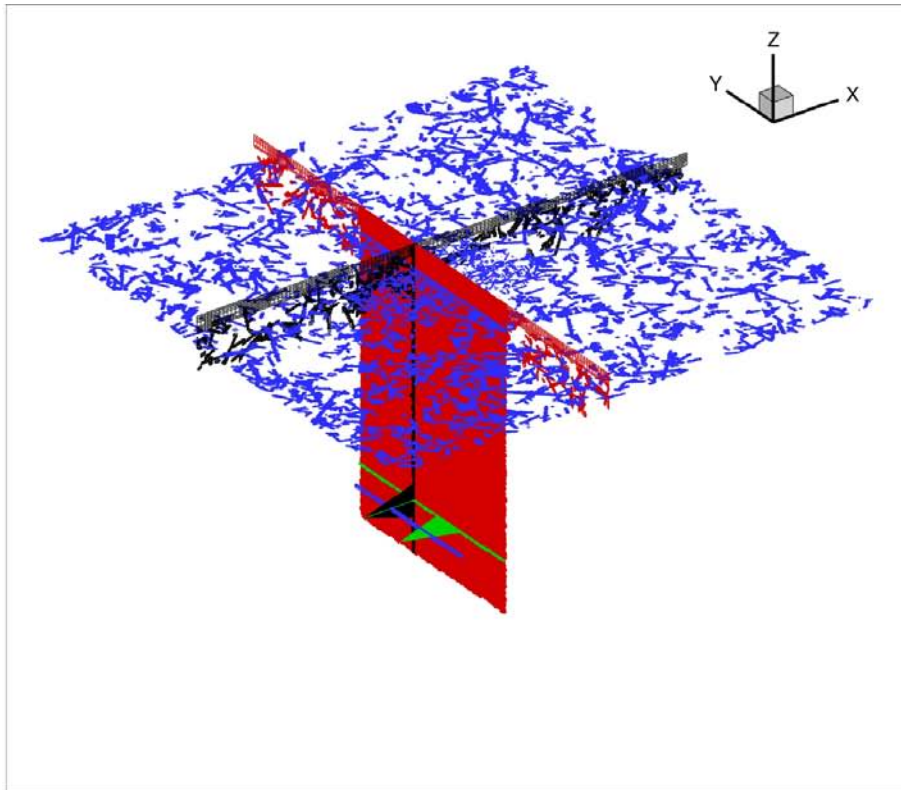


Figure. De1-1. Grid. The upper figure shows two vertical and one horizontal section. The lower figure shows the details around the tunnel.

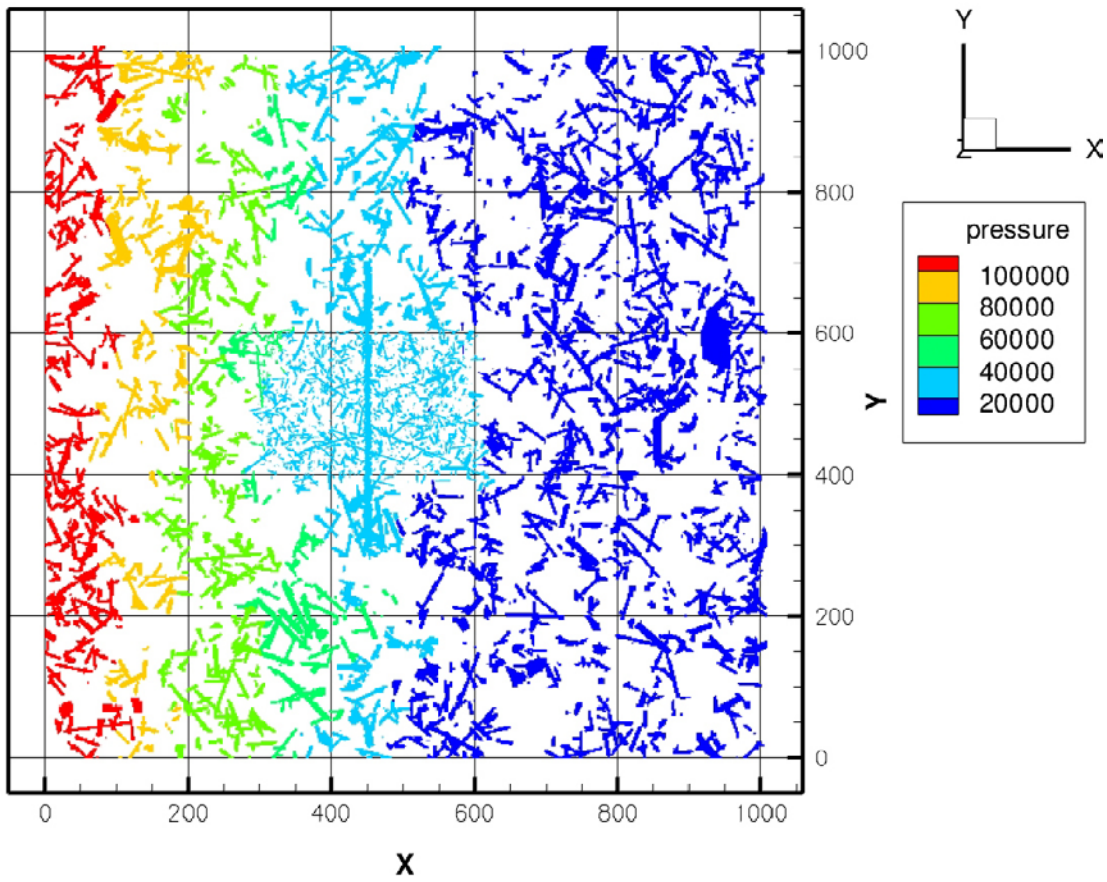


Figure De1-2. Pressure distribution (in Pa) at 50 mbsl.

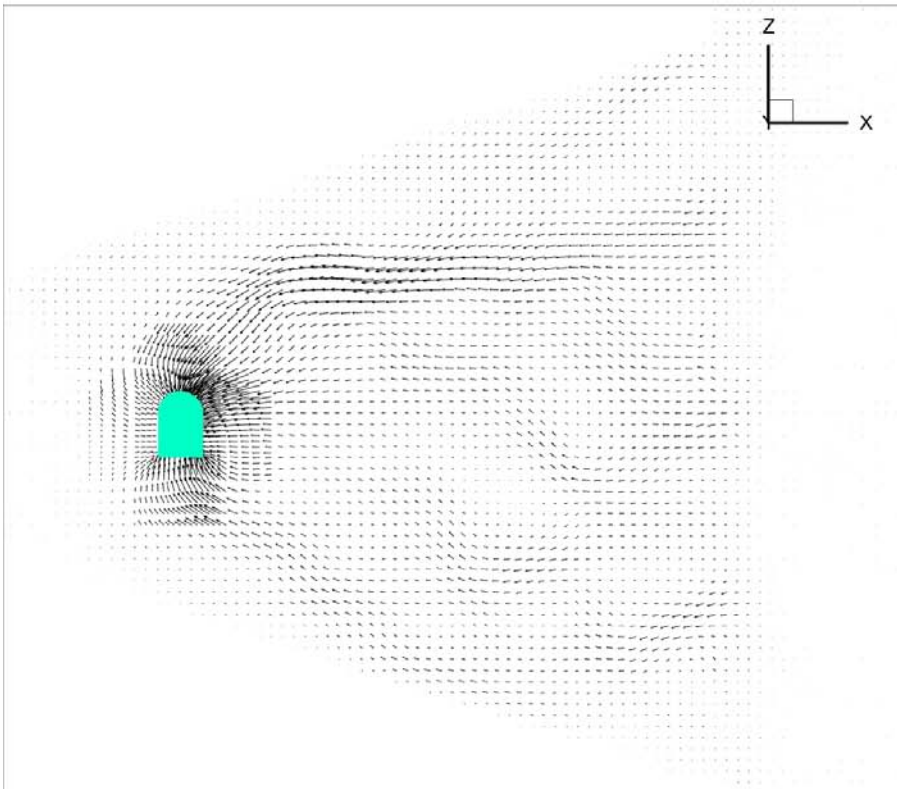
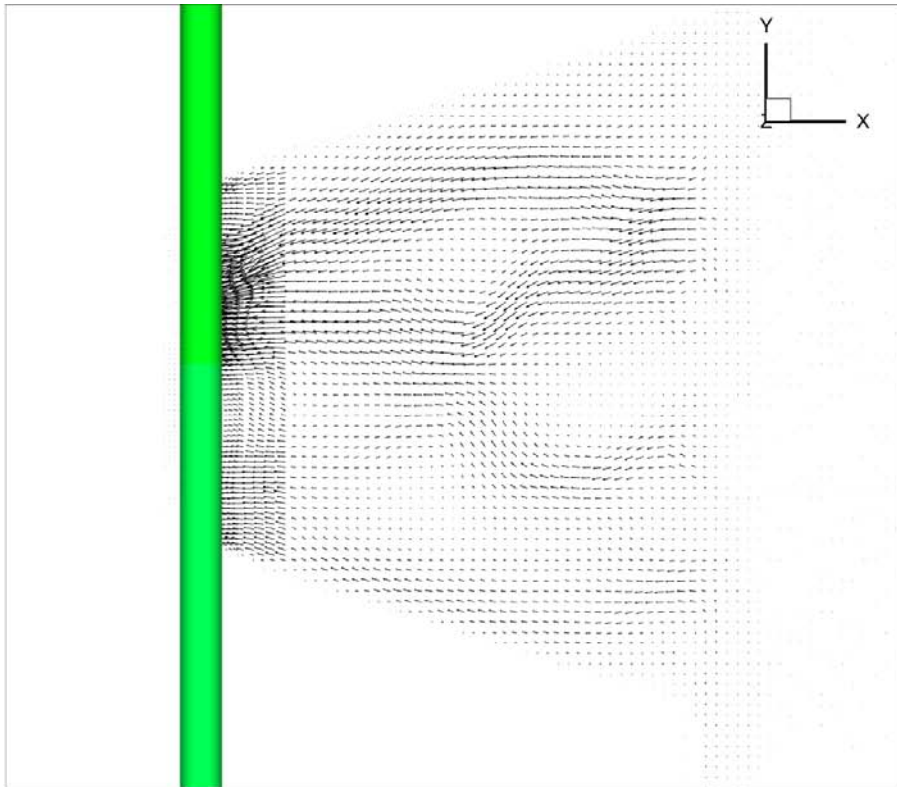


Figure De1-3. Flow distribution in the horizontal (top) and vertical fracture.

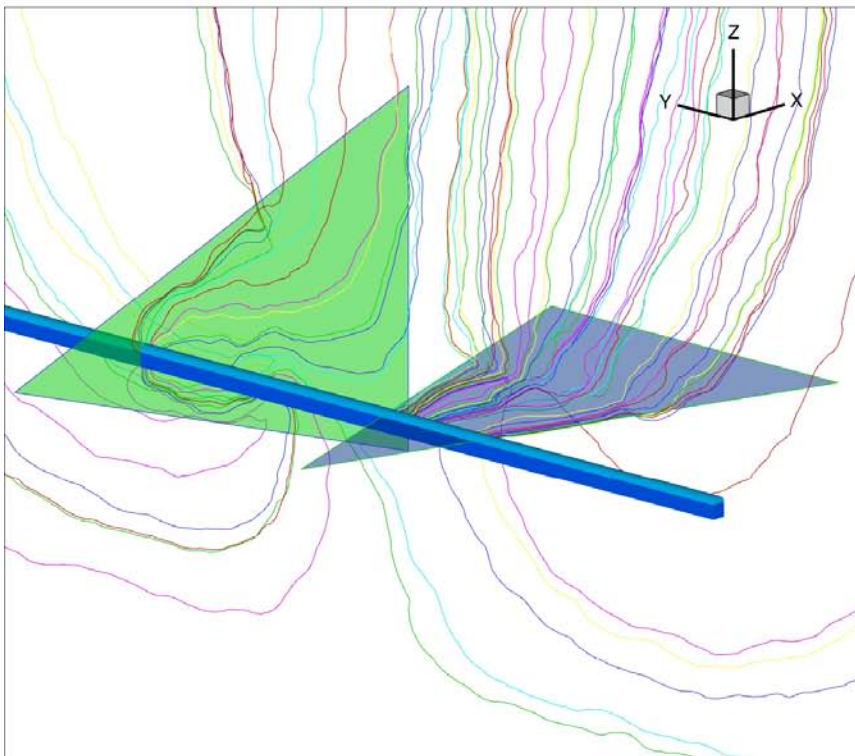
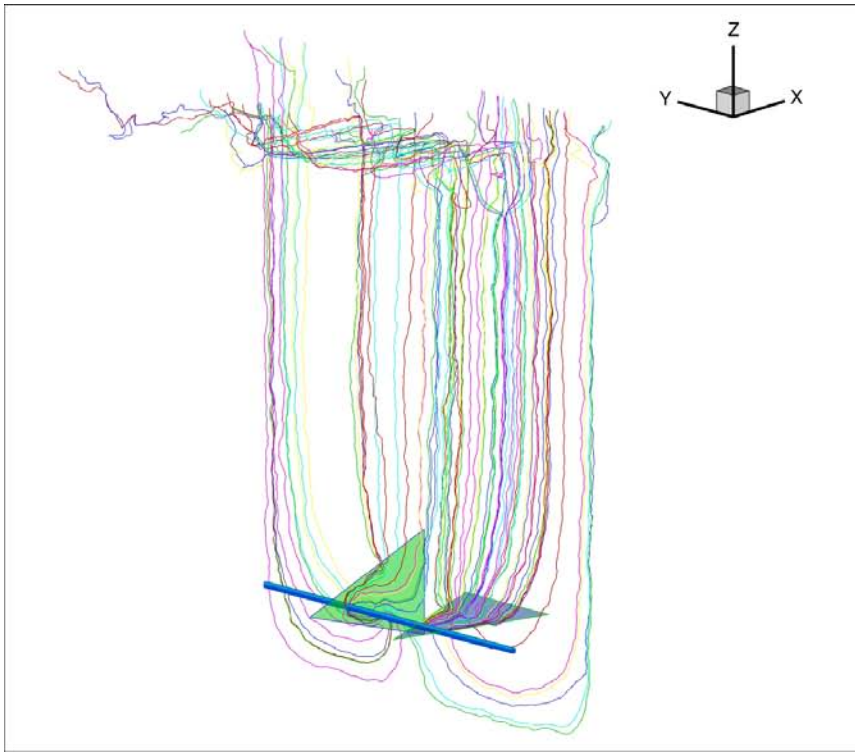


Figure De1-4. Trajectories. The top figure shows the trajectories as back-tracked from inflow points all the way up to ground level. Details in the fractures are shown in the bottom figure.

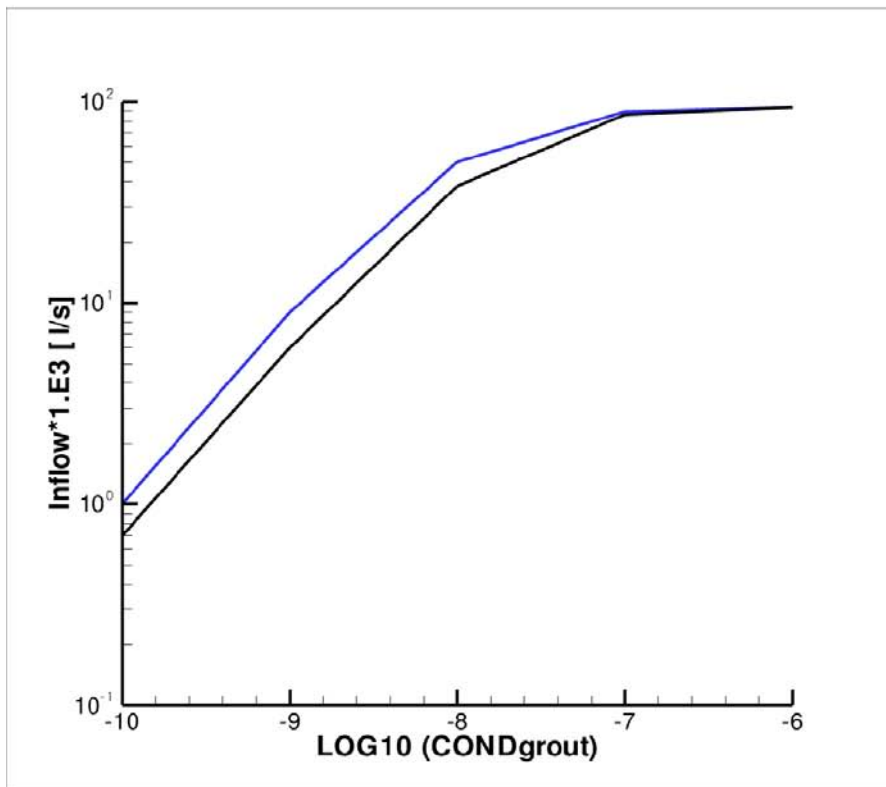
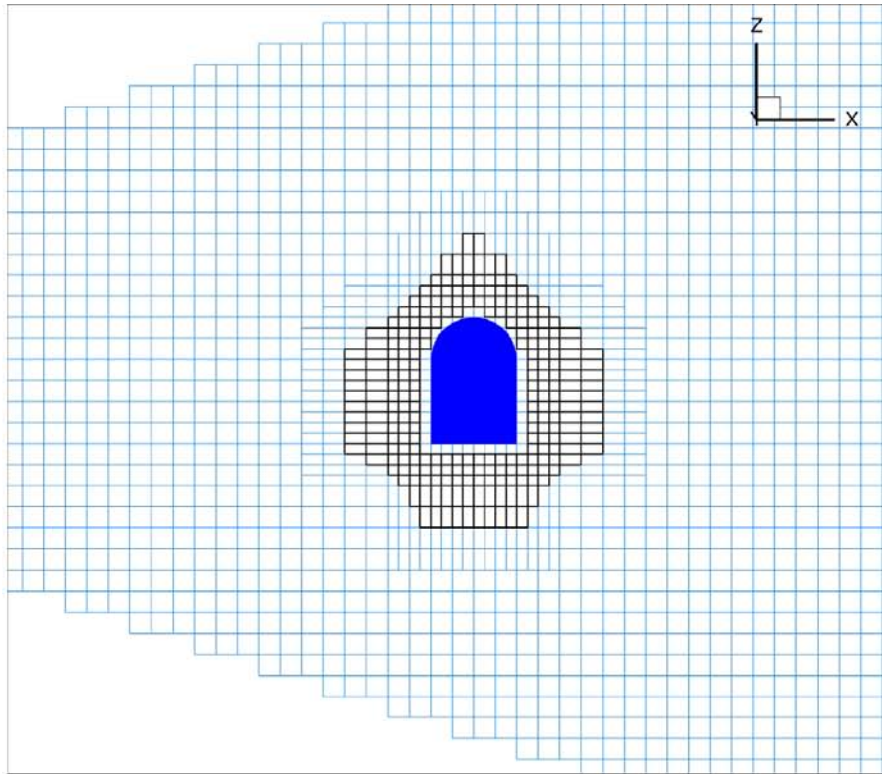


Figure De1-5. Illustration of cells that are affected by grouting (top) if layers 1–5 are specified. The bottom figure shows total inflow for two penetration lengths and a range of grouting conductivities. The blue line represents a grout penetration depth of 2–3 metres, and the black a depth of 5–7 metres.

Case De2: Transport from a canister to ground level

Introduction

The layout and location of a repository is made with respect to major deformation zones. It is however impossible to avoid contact with smaller fractures. A deposition hole may hence be crossed by a small fracture, which in turn is in contact with larger fractures and zones.

Transport from a leaking canister through this fracture network up to ground level, is one of the fundamental problems in repository analysis. It is instructive to classify deposition holes as follows:

- No contact with fractures. In this case transport through the rock matrix needs to be analyzed: this transport is however slow.
- Contact with a dead-end fracture. A dead-end fracture has no flow and the transport is hence due to diffusion.
- Contact with a fracture with a flow. This is of course the most dangerous case, as advection may provide a fast link to a zone.

Here we will study a case with flow around the canister, see Figure De2-1.

Objectives

The main objectives of the case are to illustrate the flow around a deposition hole and the transport from the deposition hole to ground level.

The situation considered

The basic situation is given by Case De0. The tilted fracture zone and vertical small fracture are however not included. The deposition hole, blue cylinder in Figure De2-1, is specified as a 10 metre long cylinder with a radius of 1 m. The grid resolution of the hole is 0.5 m.

As the deposition hole is considered to be closed there is no inflow to the hole. The flow around the hole is driven by the pressure difference between the two vertical zones, which in turn is due to the sloping ground surface.

Results

Flow vectors around the deposition hole are shown in Figure De2-2. The heterogeneity in the fracture is well illustrated. The near field is resolved with a grid size of 0.5 m, which is extended some distance from the hole. One may note that the flow goes right through the hole, which hence does not block the flow. This could have been done but here we are not interested in such detailed features.

Instead it is the transport from the hole up to ground level that is the main objective, see Figures De2-3 and De2-4. It is sometimes difficult to see a perspective view and for this reason three plane views are also included. The particles first move through the horizontal fracture, then vertically through the deformation zone and then turn towards the sea through the sheet joints. Most reach the sea bed at $x = 600$ m, while some continue even further out.

Running the case

The following steps should generate the results just described:

1. Copy cifstep1.xml to cif.xml and issue the commands RUNGGN and RUNFGN. This first grid is a coarse grid without any removed cells. The fracture network is generated and isolated fractures are removed. We only need to do this once and we therefore store the network in a file called “fractures”.
2. Copy cifstep2.xml to cif.xml and prpgenstep1.f to prpgen.f. Issue the command BLDMYPGN.
3. Next issue the command RUNMYPGN. A file, DE2RRC, is created which has information about cell removal and grid refinement.
4. RUNGGN is next; now the grid is refined and cells removed.
5. The fracture network is represented in the new grid by RUNFGN.
6. Repeat steps 3 to 5 in order to converge the process. Three times are probably enough.
7. Copy prpgenstep2.f to prpgen.f and issue the commands BLDMYPGN and RUNMYPGN.
8. The grid and property files are now generated and the case can be started by RUNDTS, as usual.

Discussion

The results presented are certainly quite schematic and one should directly like to see, for example, breakthrough curves, F-factor statistics and various sensitivity studies. Another possible extension would be to introduce matrix diffusion. These “cliff-hangers” are left for further studies.

Conclusions

An illustration of transport simulations from a single canister, exposed to flow, to ground level has been carried out. Results are schematic but plausible.

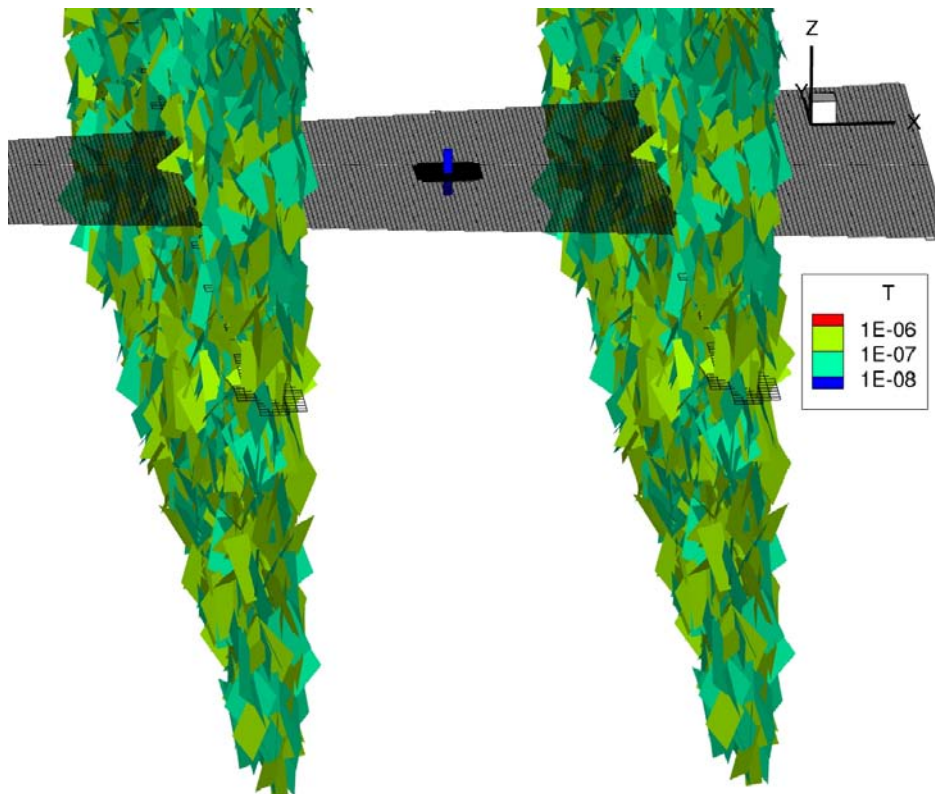


Figure De2-1. A canister (blue cylinder) crossed by a single horizontal fracture, which in turn is in contact with two vertical fracture zones.

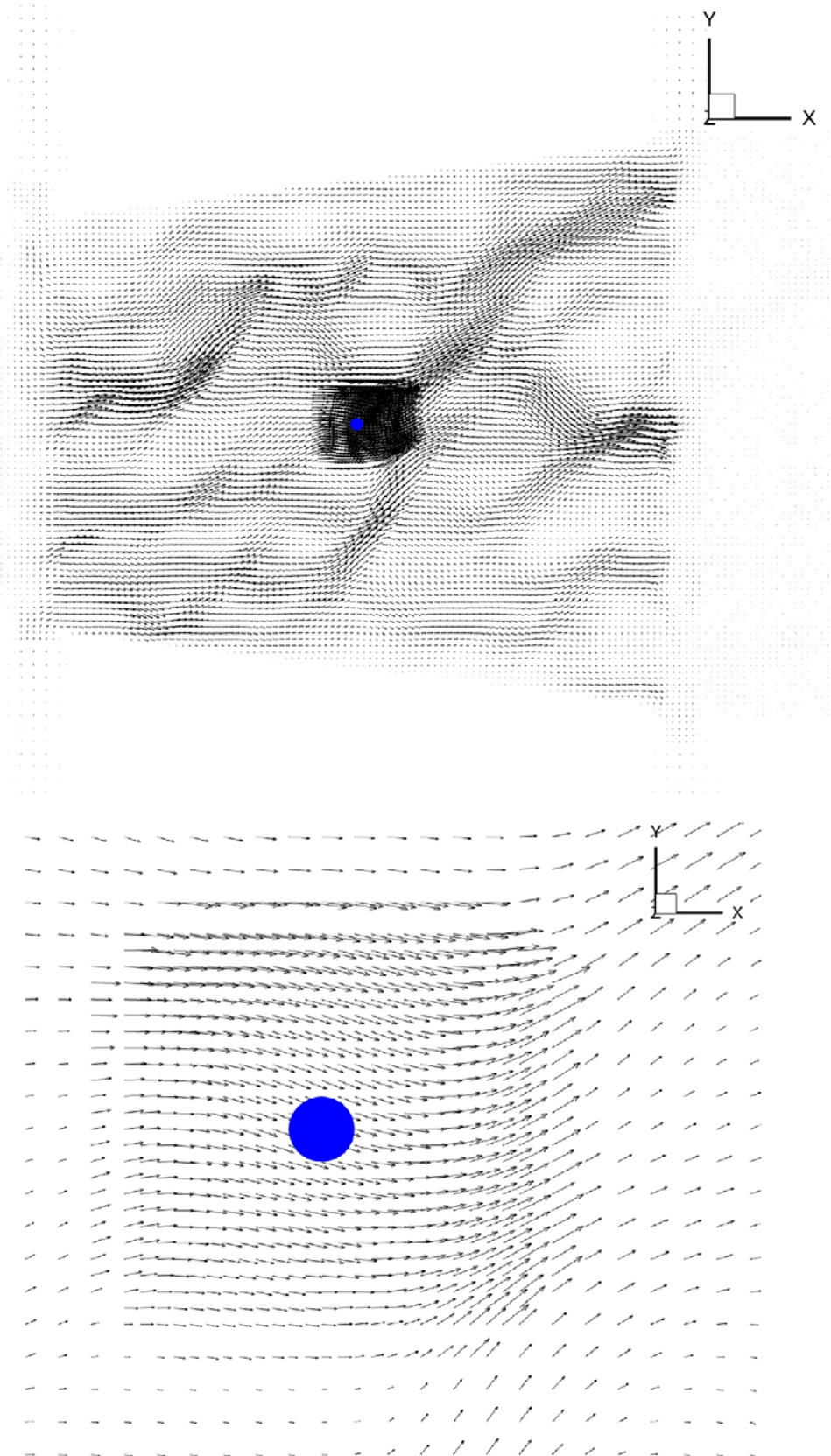


Figure De2-2. Flow vectors in the horizontal fracture (top) and close to the canister.

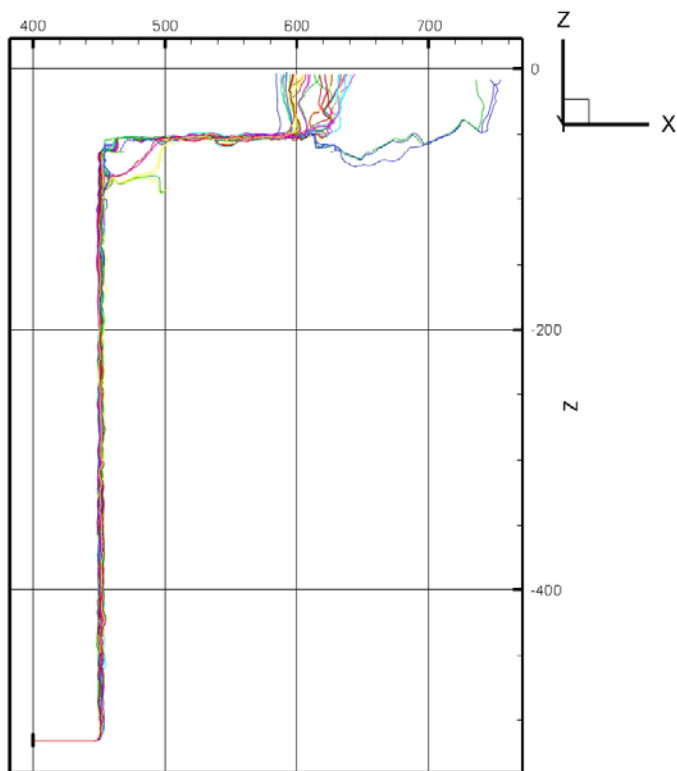
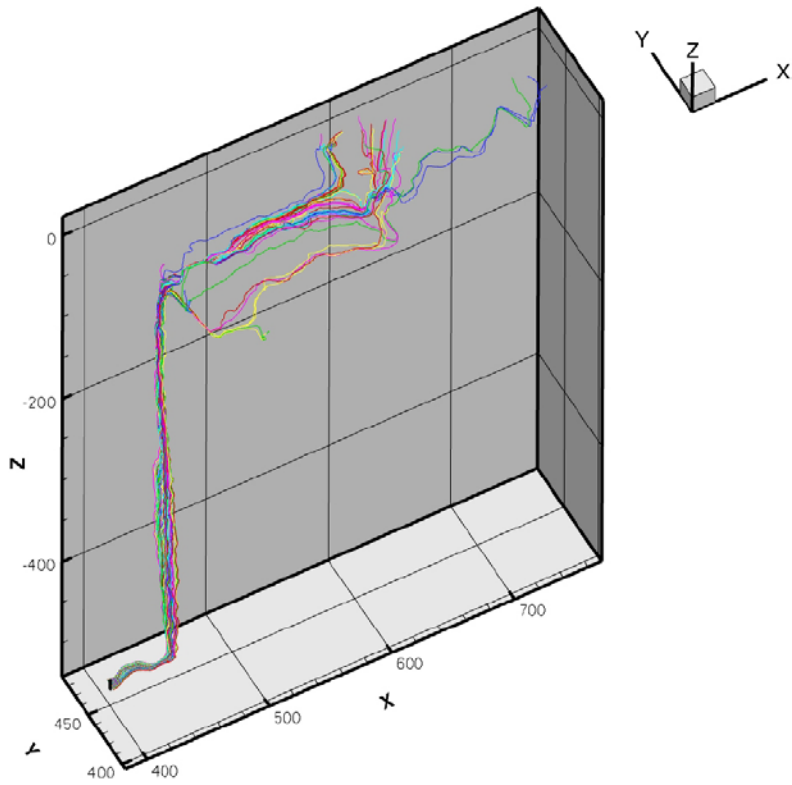


Figure De2-3. Trajectories from the canister to ground level. Perspective view (top) and xz-plane.

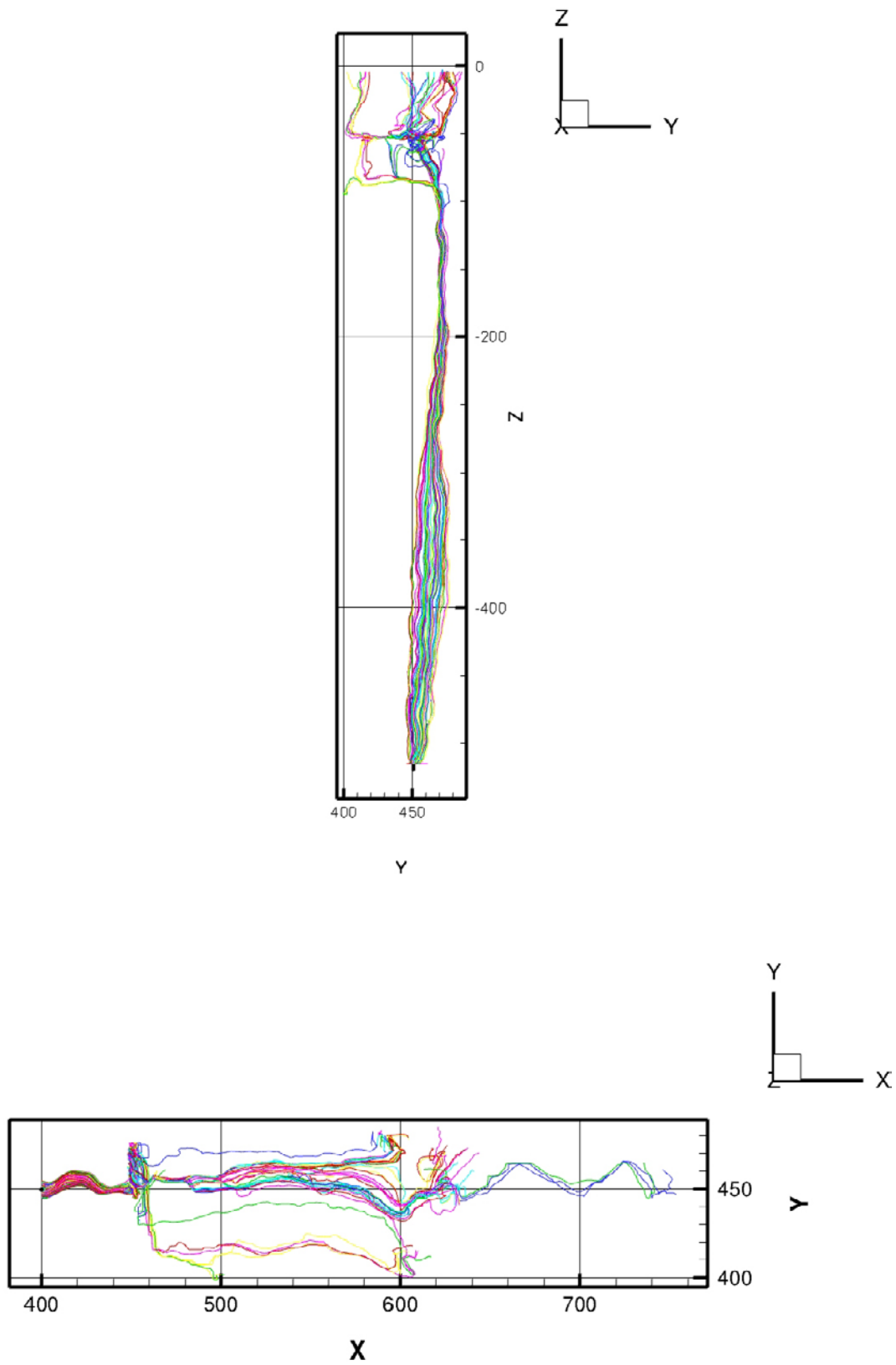


Figure De2-4. Trajectories from the canister to ground level. yz-plane (top) and xy-plane.

Case De3: Transient paleo simulation

Introduction

At the Äspö site, ground water with a glacial signature has been found already at a depth of a few hundred metres. This means that this water has remained in the rock for at least 10,000 years, i.e. since the last glaciation. This fact is important when considering the salinity field in a repository analysis. It is presently believed that the best way to obtain the initial salinity distributions for a site investigation is to simulate the period from the last glaciation. Both the level and salinity of the Baltic Sea then needs to be included as boundary conditions.

Objectives

It is the intention to show that water can be stored in the rock for 10,000 years. The transient development of the salinity field will be simulated, using the transient boundary conditions mentioned.

The situation considered

The starting point is the situation outlined in CaseDe0. The two small fractures and the repository will however now be removed, see Figure De3-1. In this figure also the fracture network close to ground is shown. The reason for the tilted zone is as follows; the initial condition for the simulation is zero salinity (glacial water) in the whole domain. The salinity specified as a boundary condition is always larger than zero and if the zero salinity remains somewhere after 10,000 years of simulation, we have shown that glacial water can be stored. The top part of the tilted zone is where glacial water can be expected as the glacial water has fresh water density.

In Figure De3-2, the level and salinity of the Baltic Sea during the last 10,000 years are shown. This is thus the boundary condition at the top boundary.

Results

The main result of the case is given by Figure De3-3, which shows the salinity distribution after 10,000 years. It is clear that the water of zero salinity, specified as the initial condition, is still present in the top of the tilted zone.

Some further results are shown in Figure De3-4. After 10,000 years the circulation pattern is “downwards in the left zone and upwards in the right one”. The zero salinity water seems to be fairly stagnant, as no flow vectors appear.

Running the case

The following steps should generate the results just described:

1. Copy cifstep1.xml to cif.xml and issue the commands RUNGGN and RUNFGN. This first grid is a coarse grid without any removed cells. The fracture network is generated and isolated fractures are removed. We only need to do this once and we therefore store the network in a file called “fractures”.
2. Copy cifstep2.xml to cif.xml and prpgenstep1.f to prpgen.f. Issue the command BLDMYPGN.
3. Next issue the command RUNMYPGN. A file, DE3RRC, is created which has information about cell removal and grid refinement.
4. RUNGGN is next; now the grid is refined and cells removed.
5. The fracture network is represented in the new grid by RUNFGN.
6. Repeat steps 3 to 5 in order to converge the process. Three times are probably enough.
7. Copy prpgenstep2.f to prpgen.f and issue the commands BLDMYPGN and RUNMYPGN.
8. The grid and property files are now generated. As the case involves FIF we need to issue BLDMYDTS and RUNMYDTS, in order to start the simulation.

Discussion

This demo case puts forward an argument why glacial water can be stored for 10,000 years; it is the fresh water density of the glacial water that makes it hard to replace it in an upward going dead-end fracture or zone. This may not be the only explanation. One could, for example, argue that matrix water is hard to replace and for this reason should have a substantial contribution of glacial water.

Here we have used the salinity field to indicate the glacial water. A more thorough analysis should use FLIP (the FLuid Population method), see Validation case V1.

Conclusions

The transient development of the salinity field during 10,000 years has been simulated. It has been demonstrated that water can remain in the domain for such a time period. This in turn may explain the presence of glacial water at shallow depth at the Äspö site

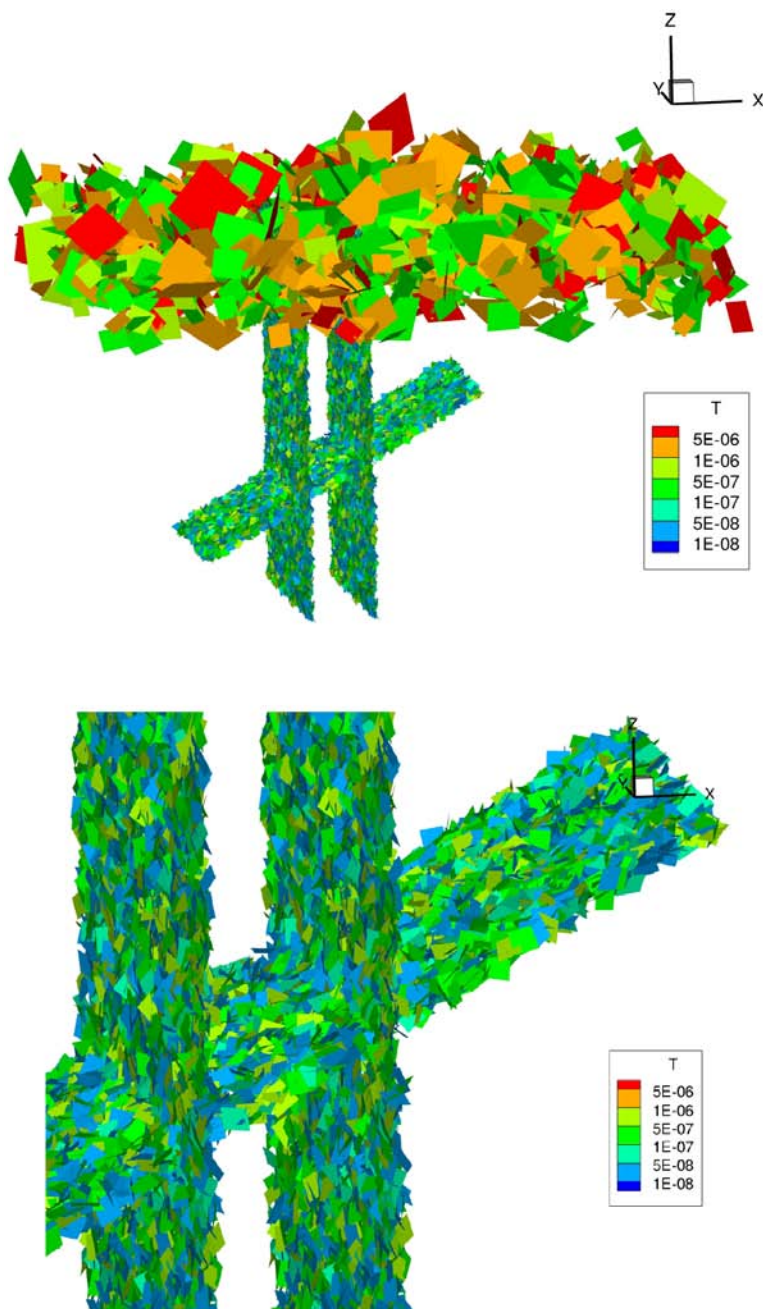


Figure De3-1. The fracture network. The whole domain (top) and close-up view.

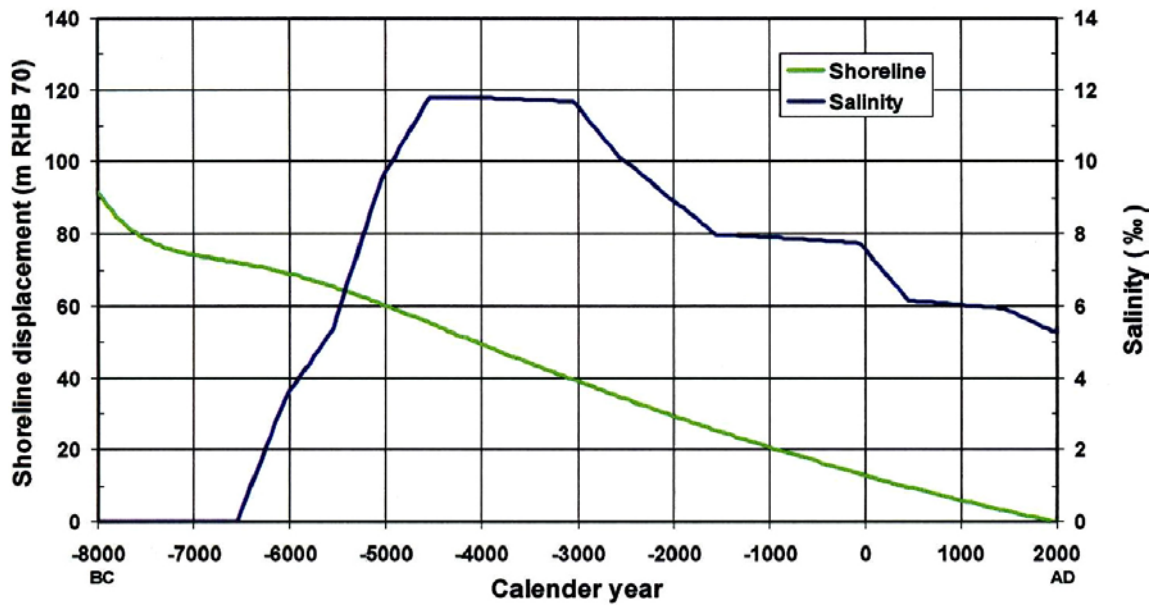


Figure De3-2. Water level and salinity of the Baltic Sea during the last 10,000 years.

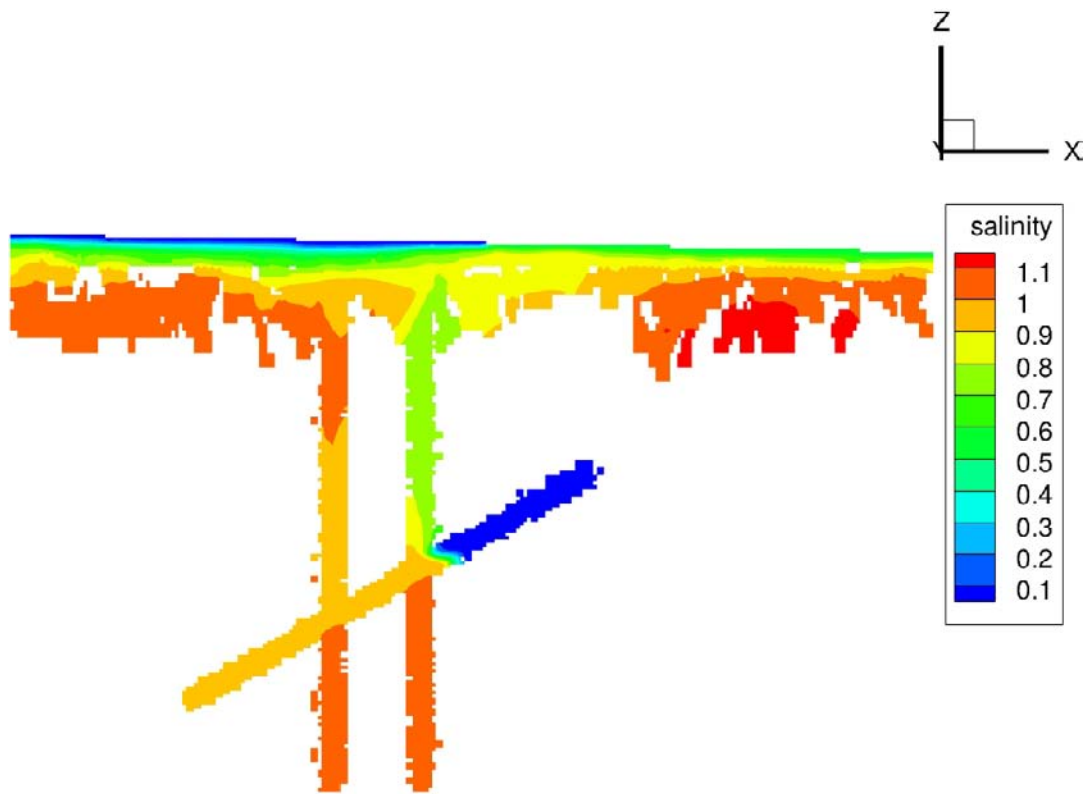


Figure De3-3. The salinity distribution after 10,000 years of integration.

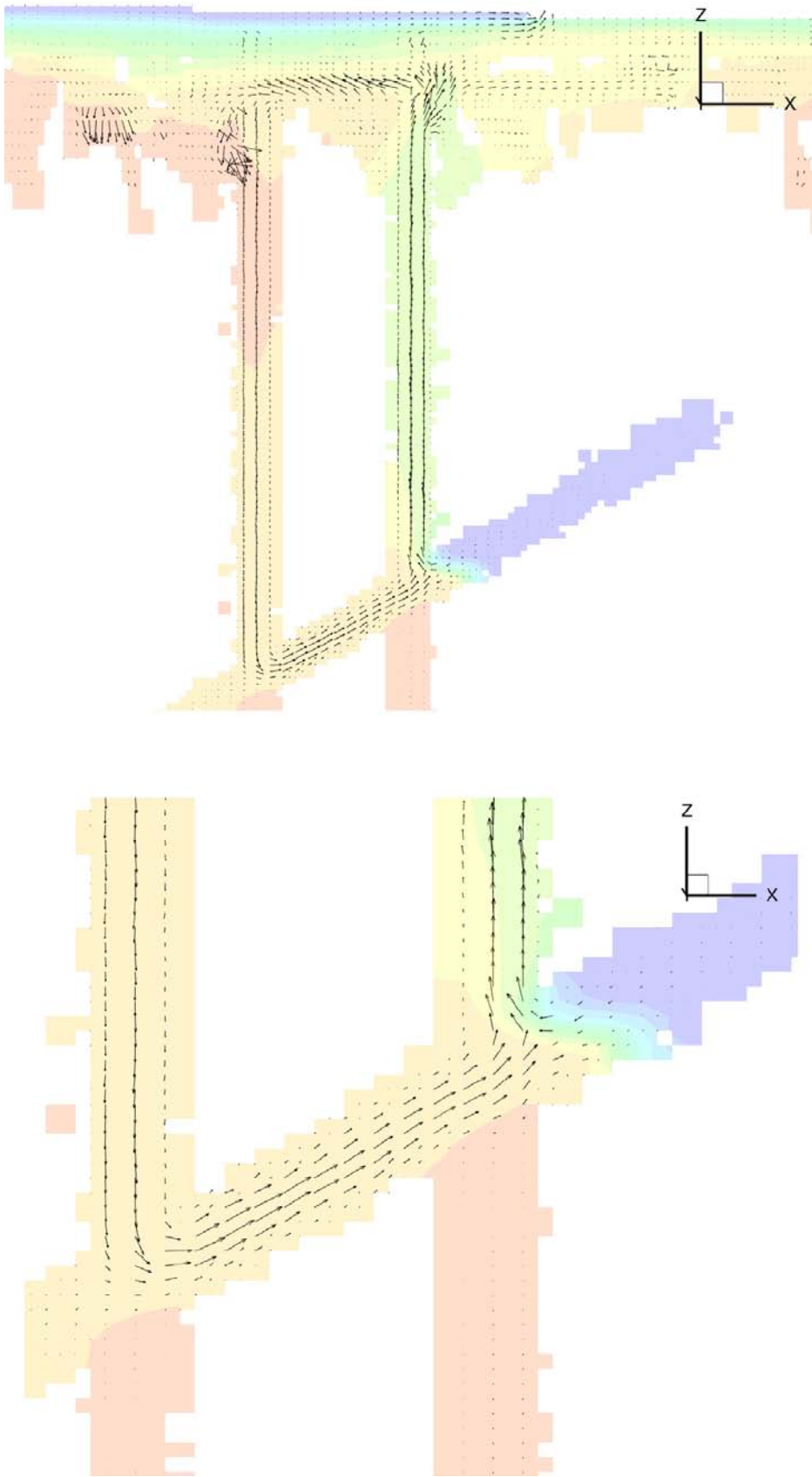


Figure De3-4. Flow field for the whole domain (top) and detail. Salinity field shown as transparent contours.

Case De4: A steady state pump test

Introduction

Site investigations are to a large extent based on the information gathered from drilled boreholes. The core gives valuable information about the rock properties and the fracture system. If several boreholes are drilled interference tests of various kind may give further information about both the hydraulic and transport properties.

Boreholes can be of various kinds; they can be open or packed off into sections. We may further distinguish between pumped boreholes, or borehole sections, and observation boreholes. A pumped borehole will get a certain drawdown that generates an inflow to the borehole. If a steady state is reached the pumping rate is then equal to this inflow. A borehole, or a borehole section, which is not pumped, has both inflows and outflows along the borehole. For a packed off section one can assume that these are equal in magnitude. For all the kind of boreholes discussed a certain flow along the borehole will develop.

Objective

Demonstrate how a steady state pump test can be simulated.

The situation considered

The starting point is the situation outlined in Case De0. The small vertical fracture is however removed, see Figure De4-1. In this figure the sheet joints (in blue colour) and the horizontal fracture (red) are shown together with the two boreholes. It is the borehole that goes through the sheet joints that is the pumped borehole. A pumping rate of 25 l/min is specified.

Results

The steady state pressure distribution is given in Figure De4-2. In the pumped borehole a drawdown of about 8 metres is calculated and in the bottom part of the fracture system the drawdown is 2–4 metres.

The inflow distribution to the pumped borehole can be studied in Figure De4-3. When looking at the permeability field in this figure one should remember that the zones and the sheet joints are built up of many small fractures. As the grid is fine close to the boreholes, the variation in permeability is resolved in this region.

The outflow to the tilted zone from the observation borehole is shown in Figure De4-4. For the observation hole we must have mass conservation and this outflow is hence balanced with an inflow close to ground level. We can hence conclude that this observation hole will have a downward flow for most of its length.

Running the case

The following steps should generate the results just described:

1. Copy cifstep1.xml to cif.xml and issue the commands RUNGGN and RUNFGN. This first grid is a coarse grid without any removed cells. The fracture network is generated and isolated fractures are removed. We only need to do this once and we therefore store the network in a file called “fractures”.
2. Copy cifstep2.xml to cif.xml and prpgenstep1.f to prpgen.f. Issue the command BLDMYPGN.
3. Next issue the command RUNMYPGN. A file, DE4RRC, is created which has information about cell removal and grid refinement.
4. RUNGGN is next; now the grid is refined and cells removed.
5. The fracture network is represented in the new grid by RUNFGN.
6. Repeat steps 3 to 5 in order to converge the process. Three times are probably enough.
7. Copy prpgenstep2.f to prpgen.f and issue the commands BLDMYPGN and RUNMYPGN.
8. The grid and property files are now generated. As the case involves FIF we need to issue BLDMYDTS and RUNMYDTS, in order to start the simulation.

Discussion

Only fully open boreholes have been simulated in the present demo. A packed-off section is however treated in a similar manner and it is mainly a task of adding more coding in the FIF file.

Packed-off sections have been simulated in work for the Äspö Task Force (Task #7). In that project also the flow along the borehole was analyzed in detail. This flow is of interest for several reason, one may for example compare the simulations with field data obtained with the Posiva Flow Log.

Conclusions

It has been shown how a steady state pump test can be simulated. A high resolution grid allows a detailed description of the flow and pressure around both pumped and observation boreholes.

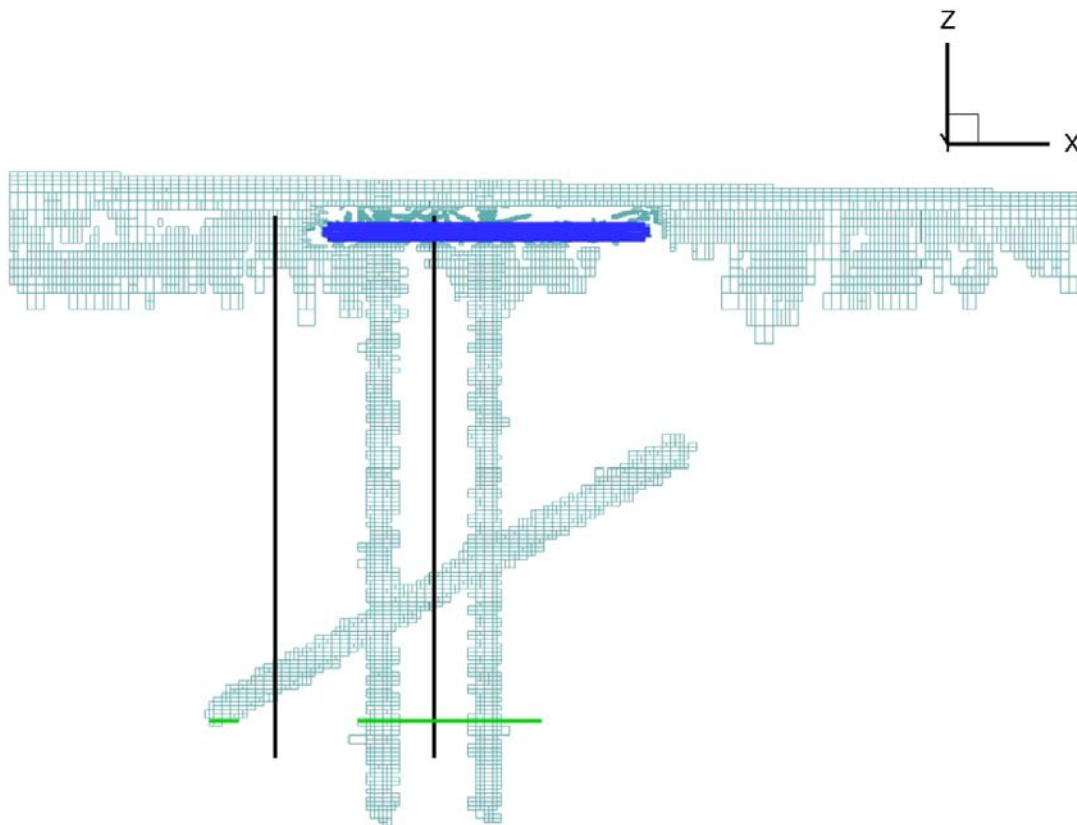


Figure De4-1. Outline of the situation studied. Sheet joints are coloured blue, the horizontal fracture red and boreholes black.

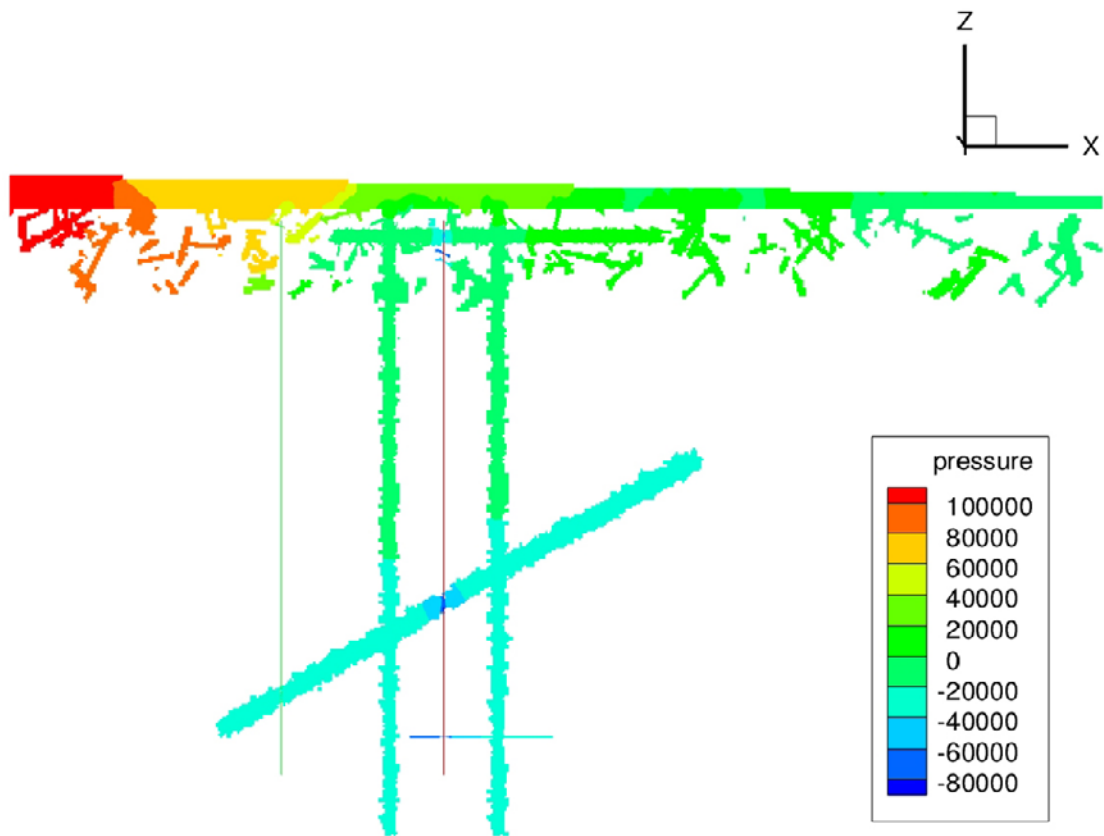


Figure De4-2. Pressure distribution in a vertical plane through both boreholes.

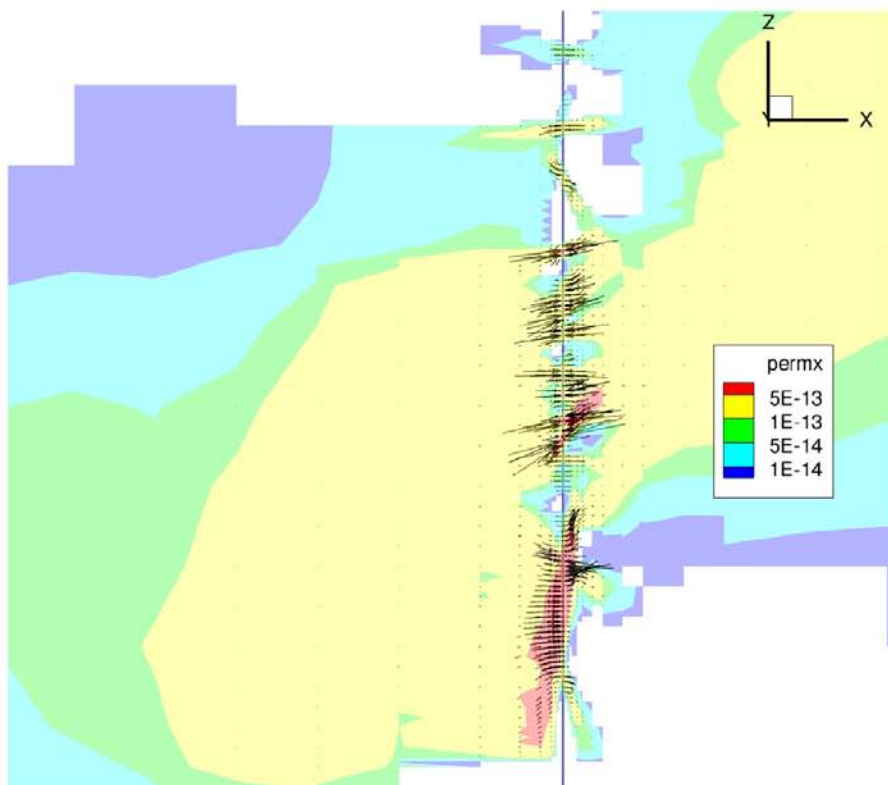
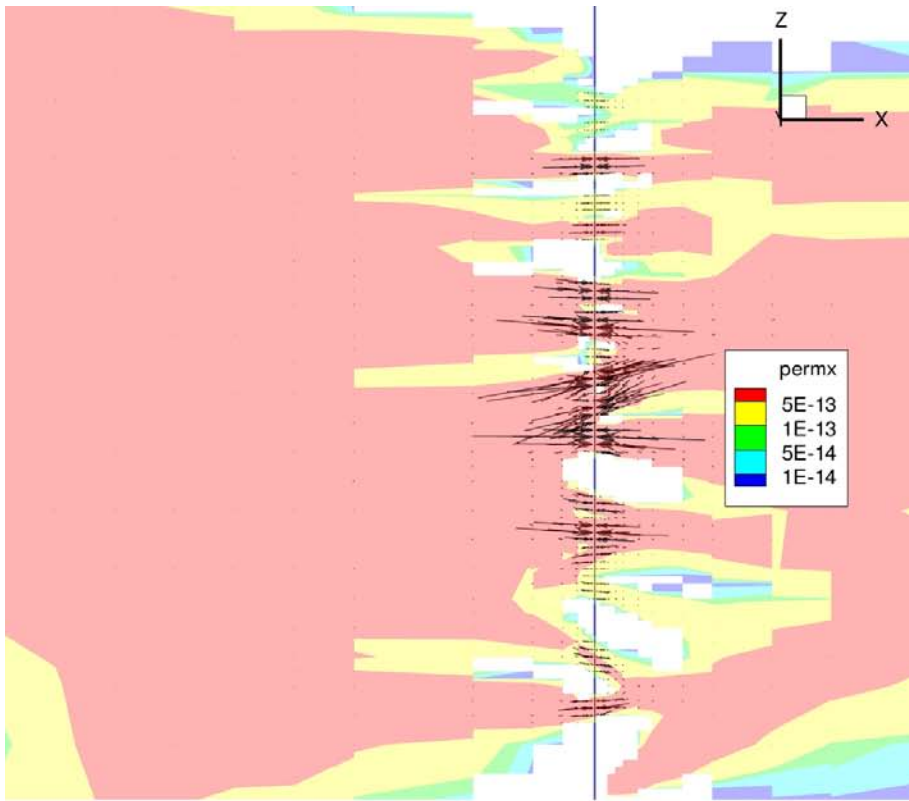


Figure De4-3. Inflow to the pumped borehole. From the sheet joints (top) and the tilted zone.

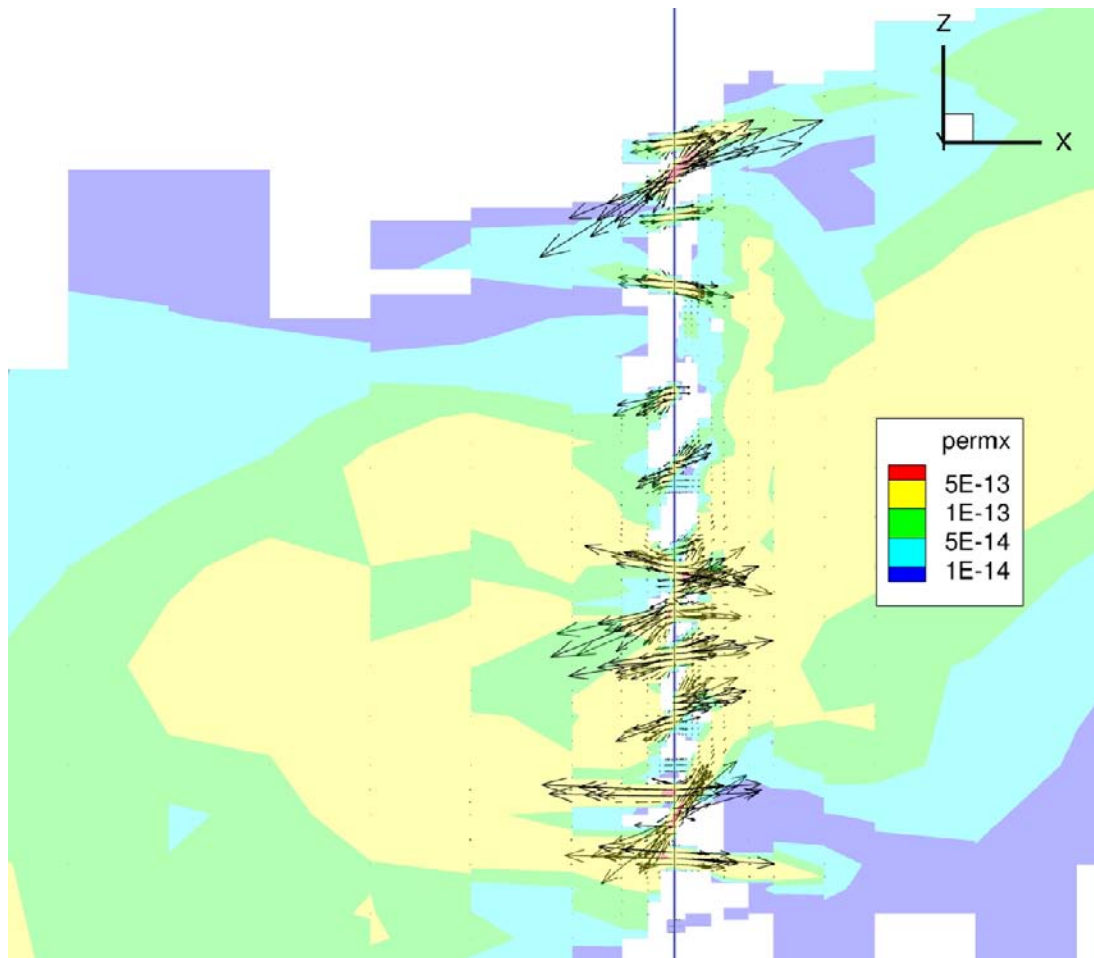


Figure De4-4. Outflow from the observation borehole to the tilted zone.

Case De5: Hydration of the tunnel backfill

Introduction

A safety assessment of a repository requires that all stages (excavation, waste emplacement, etc) of a repository are analyzed and understood. In this case the time after the waste emplacement will be in focus. One important issue during this phase is the saturation of the backfill of the tunnels. After the installation of the backfill 30–50% of the pore space is filled with air; this volume will eventually be filled with water and it is the time scale for this hydration process that needs to be estimated.

There are several reasons why this time scale is of interest:

- The needed properties of the backfill are those representing saturated conditions. During the hydration phase non-ideal properties can hence be expected.
- In the unsaturated state the heat transfer properties are affected by the air in the backfill, resulting in a lower thermal conductivity.
- During the saturation process the flow will generally be towards the repository (filling up the air volume). Considering that this flow may advect properties, the water may for example have high salinity, it may have implications.

Earlier studies /Börgesson et al. 2006/ have concluded that both the properties of the backfill and those of the surrounding rock may control the time scale of the hydration. Börgesson et al. studied the saturation of the buffer and the backfill using advanced two-phase models. These models provide realistic simulations based on fundamental physical laws and well tested empirical relations. The drawback of this approach is that it is presently hard to include an adequate description of the fracture network in the rock. For this reason a much simpler approach was tested in /Svensson 2006/. The problem was treated as a single-phase problem using the storativity term to “create” the volume which represents the air volume to be filled with water.

Objective

The main objective of the work to be presented is to demonstrate a simple method for the hydration of the backfill in repository tunnels. The method should be applicable to a realistic repository outline, embedded in a rock with a water carrying fracture network.

The situation considered

Physical processes

A number of complex interacting physical processes are active during the saturation phase. In Figure De5-1 an illustration of the more important processes is given. The illustration does not claim to be complete (if for no other reason, the author’s lacking knowledge) but it is anyway clear that we are dealing with three phases (solid, air and water) with an air phase that is subject to compression and dissolution in the water phase. With reference to Figure De5-1 the following aspects of the situation considered are emphasized:

- In the rock a fracture network provides the water up to the tunnel face.
- The saturation front is defined by the zero pressure line. Ahead of the saturation front the pressure is < 0 and it is > 0 behind the front.
- In the unsaturated part water is transported by matrix suction and may also be transported as vapour diffusion.
- The air initially present in the backfill may disappear by several processes: dissolution in the water, gravitational rise and by diffusion and advection when dissolved in the water. When pressure rises a significant compression of the air (which reduces the volume) can be expected.
- Temperature and salinity levels and gradients may affect most processes.

The SIMSAT method

If all, or most, of the processes discussed above should be included in a numerical simulation model we probably need to stay with one- or two-dimensional models. Our objective is to simulate hydration in a realistic repository geometry and a simpler approach is for this reason sought. As a basis for such an approach the following is suggested:

- Stay within the single phase framework and use the storativity term to “create” the space that the inflowing water should fill. It is assumed that the volume of this space is known and as we know the total pressure rise a suitable storativity value for the backfill can be calculated.
- Assume that the inflow of water is governed by the pressure gradients and the resistance in the rock, the saturated part of backfill and the wetting front. This means that we can use a standard Darcian flow formulation.

Only two features need to be introduced

1. A storativity that “creates” the air volume.

Alt 1. The constant $S_s = \rho g \Delta n / \Delta p$

Alt 2. The dynamic $S_s = \rho g n \, dS/dP$

where dS/dP is the derivative of the retention curve.

Alternative 2 is used in this project.

2. Relative permeability

The van Genuchten retention curve is used in this project.

Case specification

The flow resistance is dominated by the resistance in the backfill. For this reason there is little to gain by including all near surface features. Instead we only use a domain in the z-interval $-600 \rightarrow -450$ mbsl, and fix the pressure in the vertical fracture zone to 5 MPa at these boundaries. It is the vertical fracture zone at $x = 450$ that is kept; the two others are not used (see Figure De0-2). The flow to the wetting front in the tunnel is hence from the boundary of the vertical zone then through the two small fractures and finally through the saturated part of the backfill. A view of the grid is given by Figure De5-2.

Results

The hydration of the backfill is a very slow process. Results will be presented for the situation after 500 years; at this time only a small part of the tunnel is saturated.

The pressure distribution after 500 years is shown in Figure De5-3. The initial pressure in the backfill ($-4 \cdot 10^{-7}$ Pa) is found in most of the tunnel. Flow vectors at the same time are given by Figure De5-4.

Running the case

The following steps should generate the results just described:

1. Copy `cifstep1.xml` to `cif.xml` and issue the commands `RUNGGN` and `RUNFGN`. This first grid is a coarse grid without any removed cells. The fracture network is generated and isolated fractures are removed. We only need to do this once and we therefore store the network in a file called “fractures”.
2. Copy `cifstep2.xml` to `cif.xml` and `prpgenstep1.f` to `prpgen.f`. Issue the command `BLDMYPGN`.
3. Next issue the command `RUNMYPGN`. A file, `DE5RRC`, is created which has information about cell removal and grid refinement.
4. `RUNGGN` is next; now the grid is refined and cells removed.
5. The fracture network is represented in the new grid by `RUNFGN`.
6. Repeat steps 3 to 5 in order to converge the process. Three times are probably enough.
7. Copy `prpgenstep2.f` to `prpgen.f` and issue the commands `BLDMYPGN` and `RUNMYPGN`.
8. The grid and property files are now generated. As the case involves FIF we need to issue `BLDMYDTS` and `RUNMYDTS`, in order to start the simulation.

Discussion

The strong point of the SIMSAT (SIMplified SATuration) method is the possibility to use it in a real world case. A repository with a complex layout, embedded in a rock with a fracture network can hence be analyzed.

Conclusions

It has been demonstrated how the hydration of the tunnel backfill can be simulated in DarcyTools. For the case considered it is found that only a small part of the tunnel is saturated after 500 years.

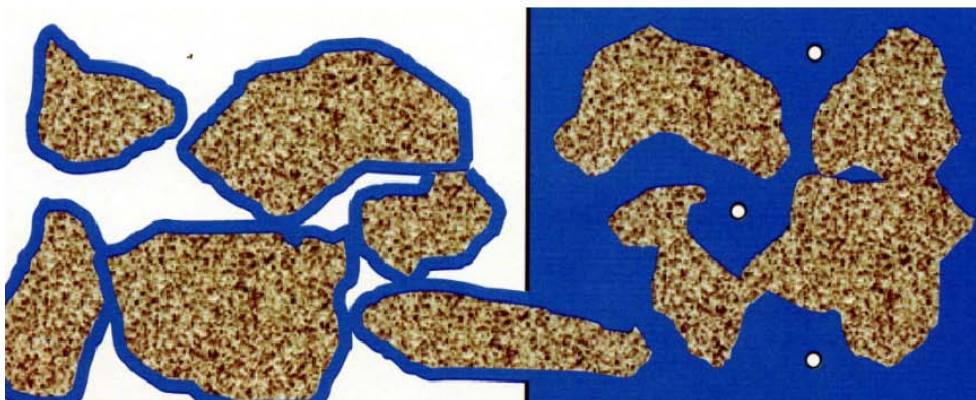
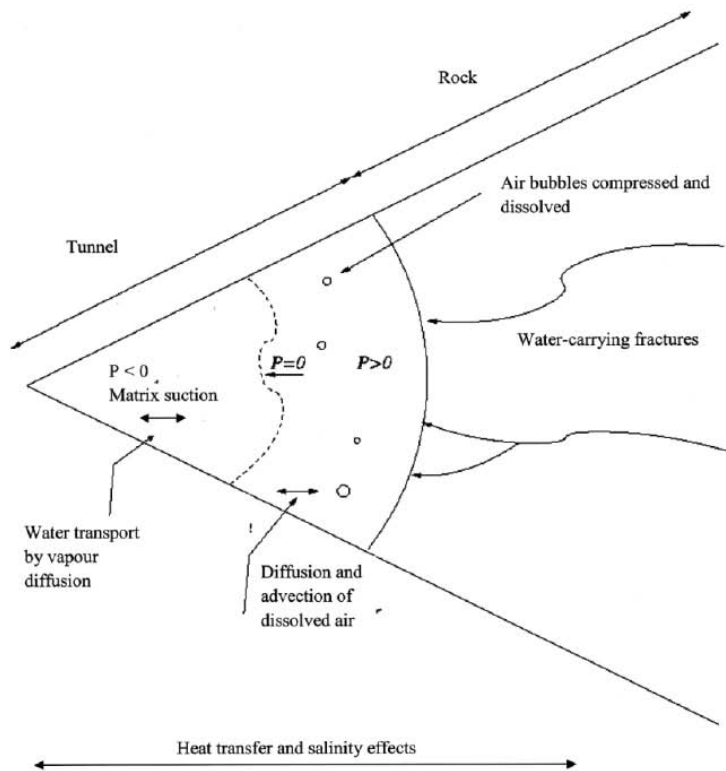


Figure De5-1. Physical processes active during the hydration of the backfill.

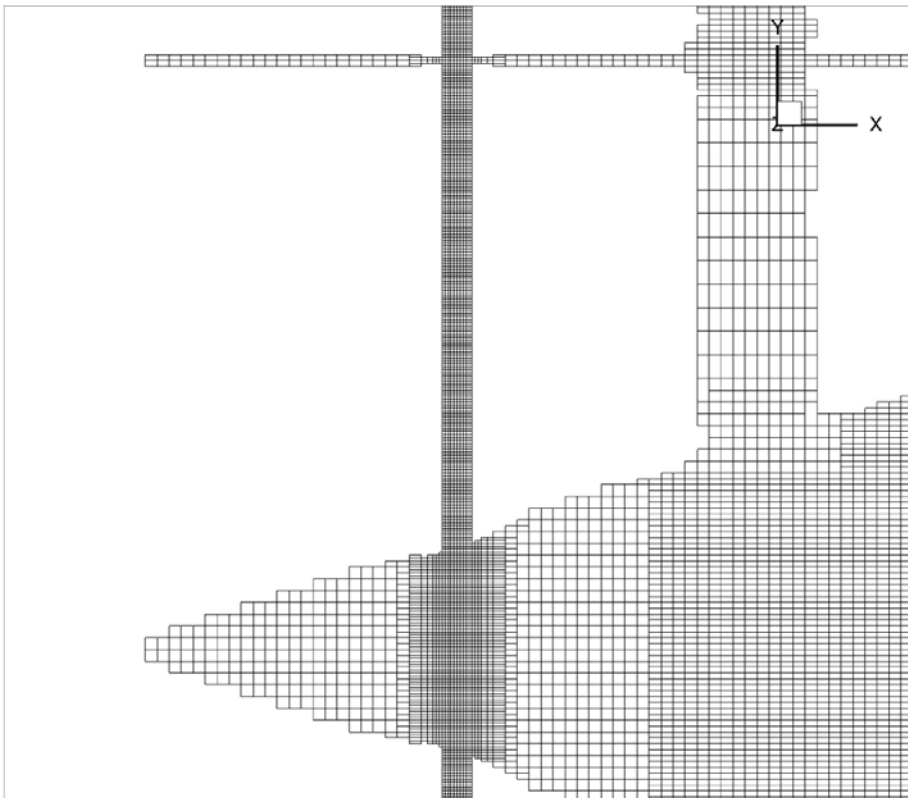
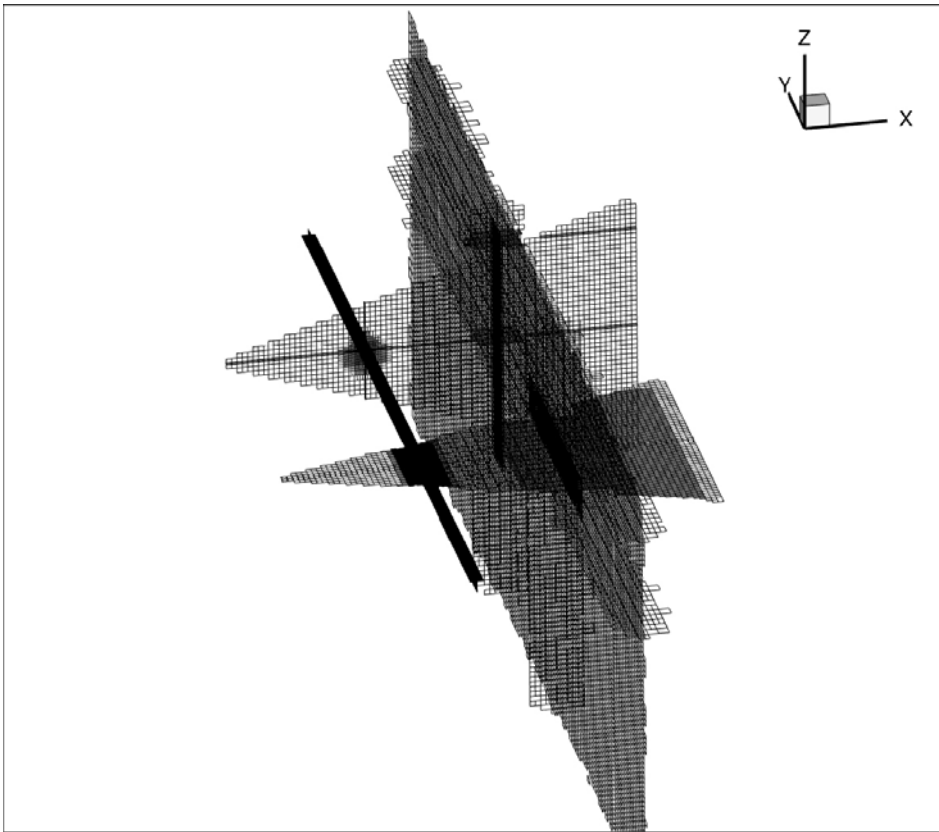


Figure De5-2. Computational grid. Perspective view (top) and a horizontal view showing the tunnel.

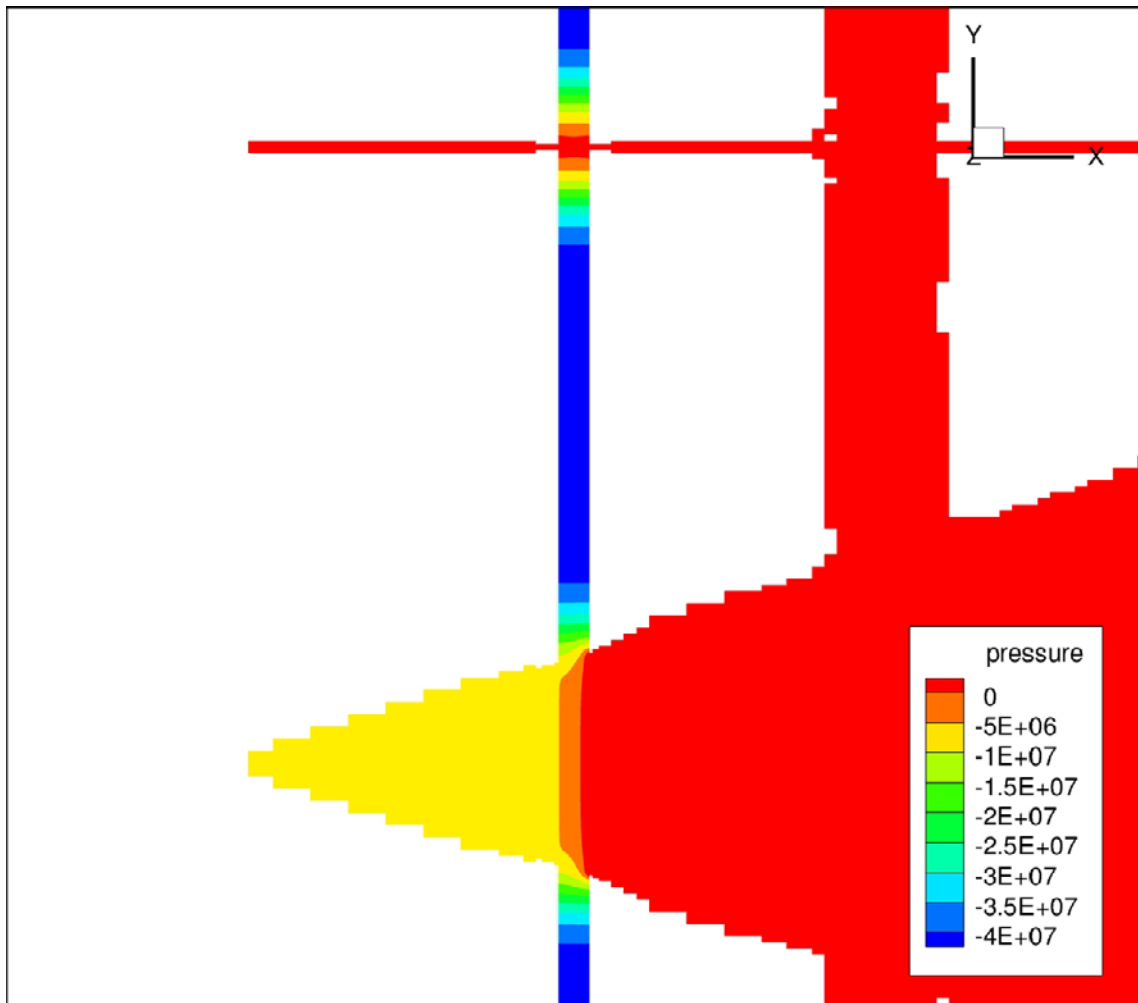


Figure De5-3. Pressure distribution after 500 years.

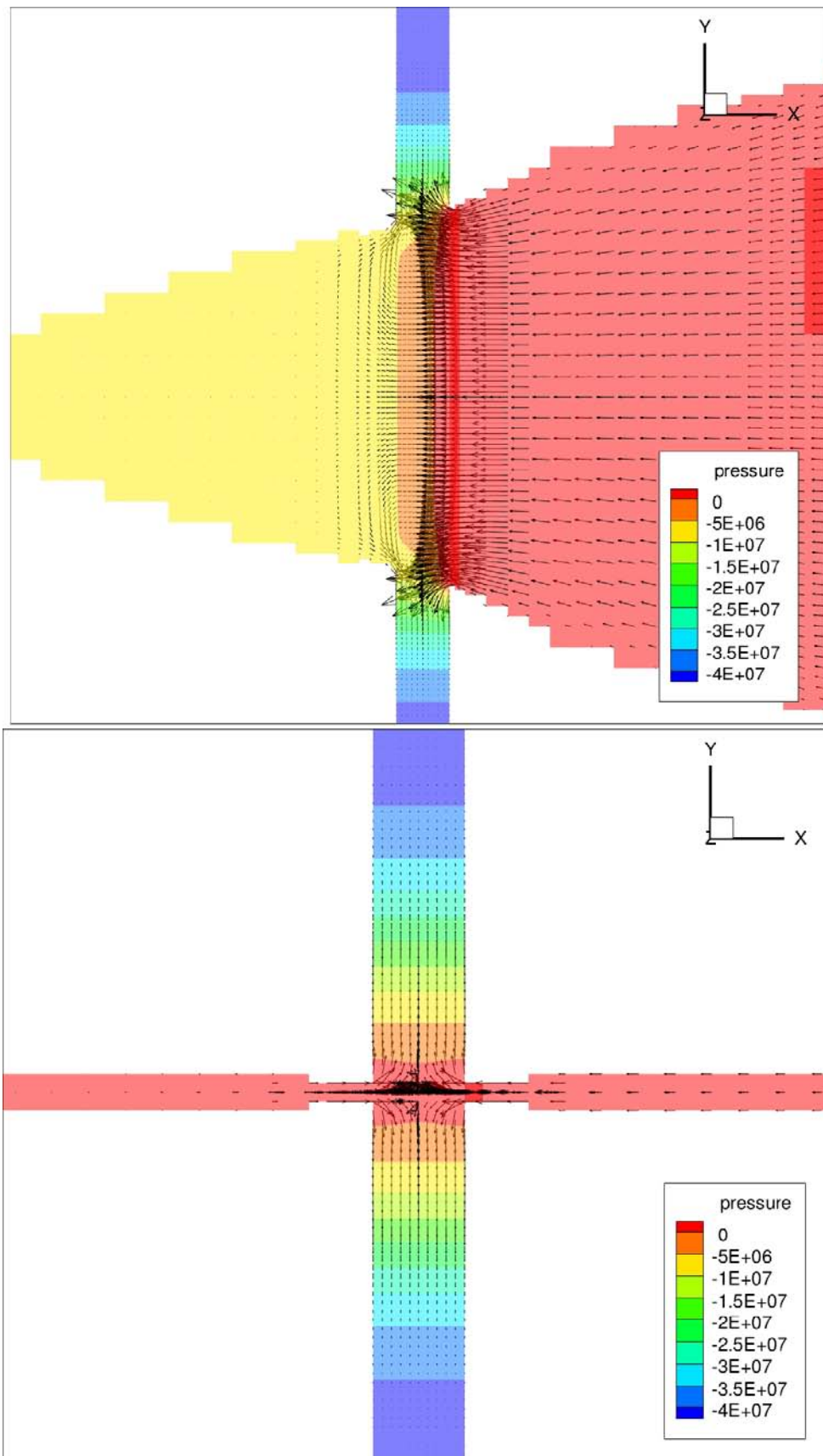


Figure De5-4. Flow vectors after 500 years. Horizontal (top) and vertical fracture crossing with tunnel.

Case De6: Surface hydrology

Introduction

Numerical models of unconfined groundwater flows can be developed for a number of purposes:

- The rainfall – runoff relation may be needed for water power production control.
- Management of a freshwater reservoir for drinking-water supply.
- Agricultural.

In this demo case the objective will be governed by the needs related to the disposal of radioactive waste in a repository, located at a depth of about 500 metres in a crystalline rock. In this connection the following considerations can be formulated:

- The groundwater table gives rise to pressure gradients that influence the flow in the fractured rock down to several hundred metres.
- At a coastal site these pressure gradients interact with the pressure gradients created by salinity variations (cf the Ghüben-Herzberg relation). The groundwater table and the salinity field largely determine the flow pattern in the domain.
- A leaking canister may release radioactive material that can be transported to ground level. The exit positions of the radionuclides is of great interest and these are determined by the near surface circulation pattern.
- During the construction of a repository, it is expected that the groundwater level may be lowered substantially. It is essential to be able to determine and control this effect.

More examples could be given, but it is probably clear that the groundwater table (hereafter grwt) is an essential part of the flow and transport problems related to a repository.

Objectives

The demo case has the following objectives:

- Demonstrate the working of the algorithm that determines the level of the ground water table. In particular the sensitivity to the near ground conductivities is studied.
- Introduce lakes and streams as objects, i.e. lakes and streams have a volume (not usually the case in DarcyTools simulations).
- Show how a horizontal variation in net precipitation (PME) can be included.

The situation considered

The idealized case studied is outlined in Figure De6-1. The domain is $1,000 \cdot 1,000 \cdot 112 \text{ m}^3$, where the vertical coordinate runs from 100 mbsl to 12 m above sea level (top of hills). Two ditches supply water to a lake and from the lake a stream carries the water to the sea, which is kept at the constant level of 0.0 m. A net recharge of 150 mm/year is prescribed in the base case.

Further details are given in Table De6-1.

Results

The computational grid resolves the features introduced in Figure De6-1 in great detail, see Figure De6-2. In particular we note that the lake, ditches and the stream are resolved, i.e. the grid is refined to the level that cells are present inside these objects.

In the base case the net recharge (P-E) is uniform and the hydraulic conductivity at ground level is set to $5.0 \cdot 10^{-3} \text{ m/s}$. The conductivity is given an exponential decay, see Table De6-1, with a minimum value of 10^{-8} m/s . This distribution has some resemblance to data based on field measurements, see Figure De6-3. Variations of the base case, as well as the base case, are illustrated in Figures De6-4 and De6-5. We study

what happens in a section at $x = 250$ m, i.e. right through the two hills. From Figure De6-5 we find that a linear variation in recharge along the y-coordinate (from 100 to 200 mm/year) has a very small influence on the pressure distribution. However increasing the top conductivity by an order of magnitude has a larger impact.

The flow pattern in the big hill is shown in Figure De6-6. The recharge is transported sub-horizontally in a rather thin layer right below the ground water table.

Finally we study “the flow pattern of raindrops”. Hence, particles are released uniformly close to ground and followed all the way to the sea, see Figure De6-7. As seen, many possible flow paths are possible.

Running the case

The following steps should generate the results just described:

1. Copy cifstep1.xml to cif.xml and issue the commands RUNGGN.
2. Copy prpgenstep1.f to prpgen.f and issue the commands BLDMYPGN and RUNMYPGN.
3. The grid and property files are now generated and the case can be started by RUNDTS, as usual.

Discussion

It should be pointed out that the coupled surface-ground water simulation discussed is far from trivial. The following aspects are emphasized:

- A small variation in the ground water elevation generates large variations in flow rate due to the exponential conductivity distribution.
- The flow in the stream, lake and the ditches is governed by the supply from the groundwater. However, the pressure distribution is “anchored” by the sea level and the pressure increase up to the start of the ditches is hence a delicate balance.

This first example of the coupled problem with explicit resolution of the surface water is however encouraging.

Conclusion

The coupled surface ground water problem has successfully been solved. Probably future site models should adopt the method to resolve the flow in ditches, streams and lakes illustrated in this demo case.

Table De6-1. Simulation parameters.

Domain	1,000 (x)·1,000 (y)·112 (z) m
Grid	Basic grid: 16·(x)·16 (y)·4 (z) m At top: 8 (x)·8 (y)·0.25 (z) m Rivers and ditches: Vertical: 0.125 m Across: 1.0 m Along: 8 m
Boundary conditions	At top: PME = 150 mm/year on land, fixed pressure at sea. All other boundaries are zero flux boundaries.
Conductivities	Cond _{top} = $5.0 \cdot 10^{-3}$ m/s, with an exponential decay. Cond _{stream} = 0.2 m/s Cond _{ditch} = 0.2 m/s Cond _{lake} = 0.2 m/s

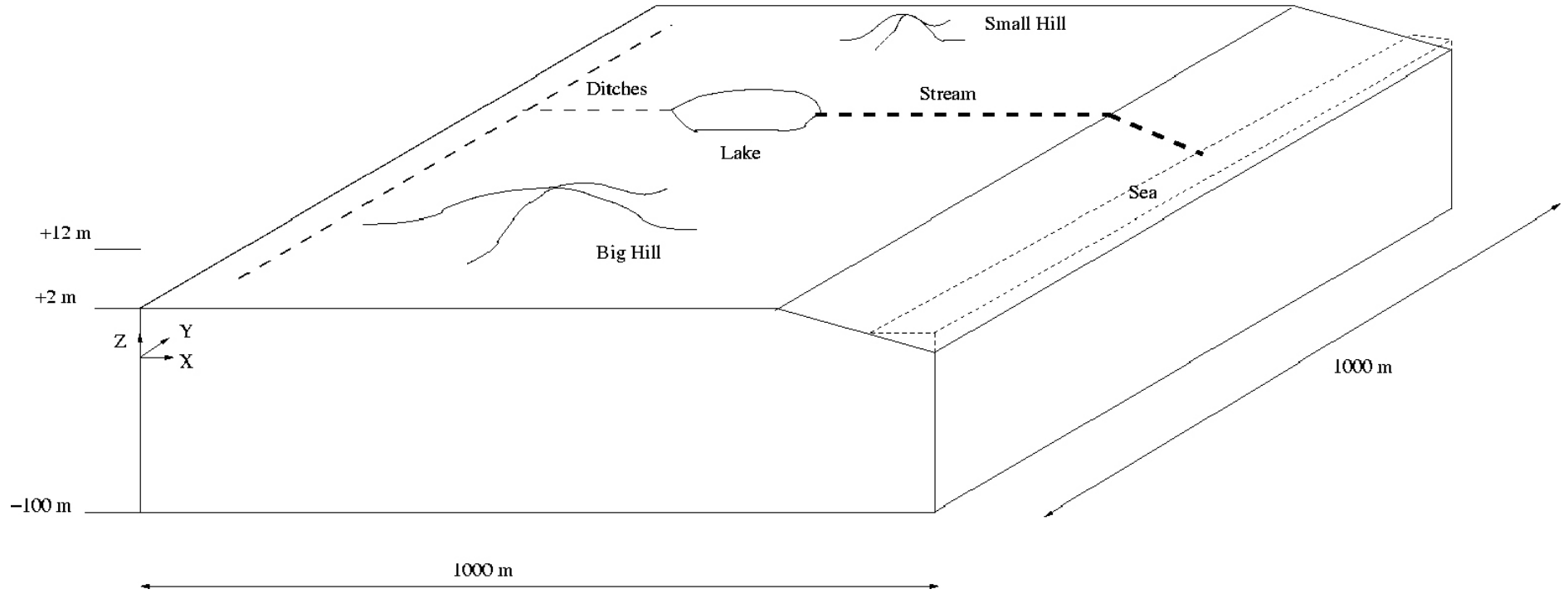


Figure De6-1. Outline of the situation studied.

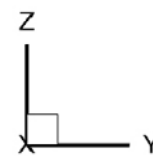
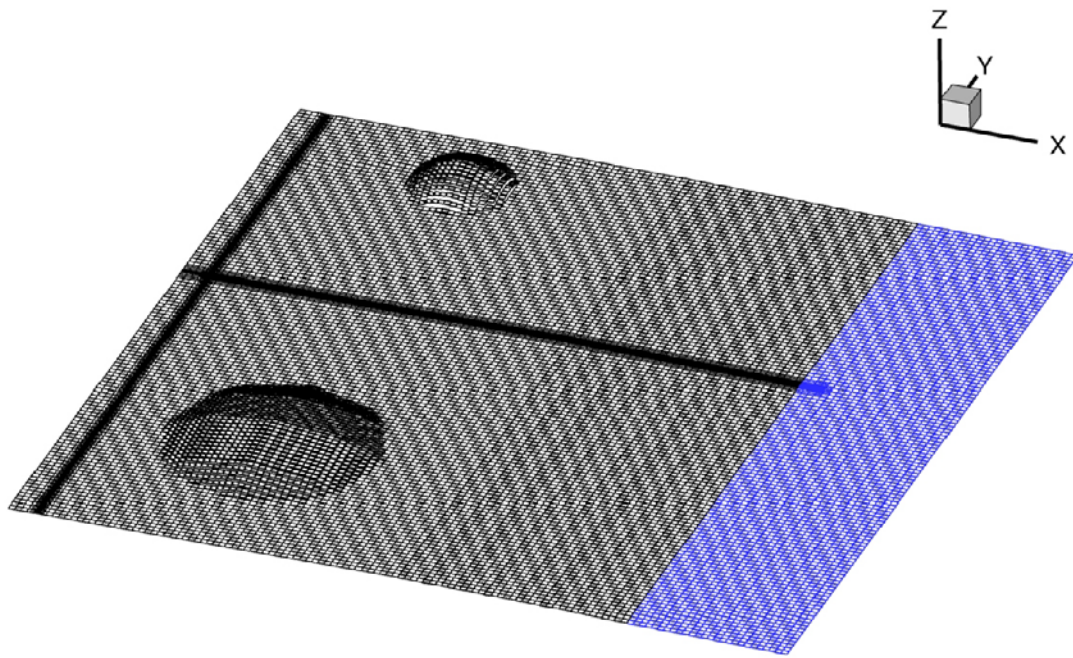


Figure De6-2. Computational grid. At ground level (top) and a section through the stream, where the cells are 0.13·1.0 m (z, y). In the top figure the blue grid marks the sea.

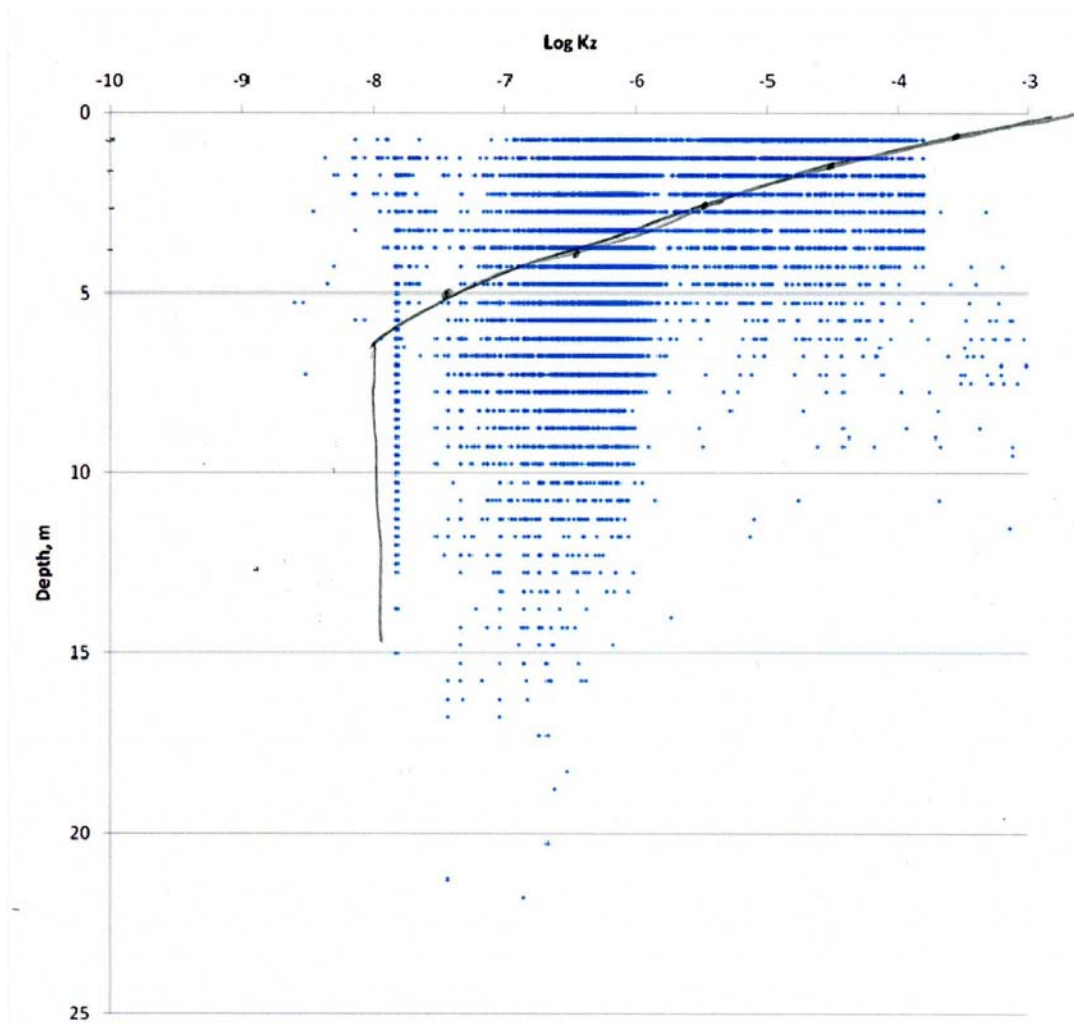


Figure De6-3. The vertical conductivity distribution. Solid line gives the isotrop conductivity used in the model, while the dots are based on field data.

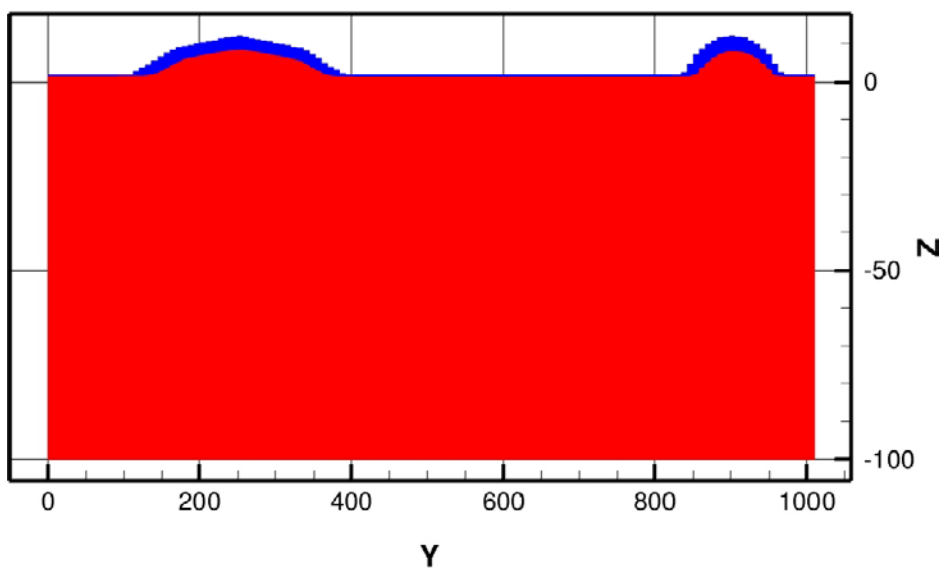


Figure De6-4. Illustration of the ground water level at a section $x=250$ m. Blue colour indicate unsaturated conditions.

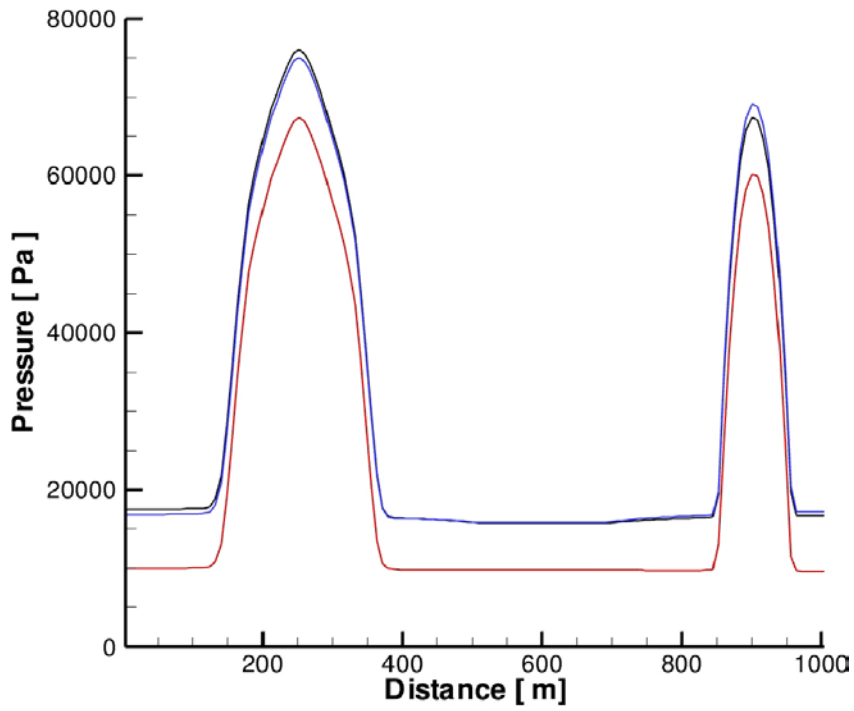


Figure De6-5. Pressure distribution near ground at section $x = 250$ m. Black line gives the base case, blue a variation along the y-coordinate of PME and red an increased conductivity.

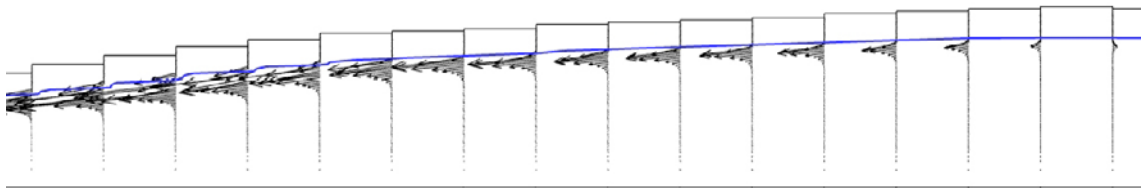


Figure De6-6. Flow distribution in a vertical section through the big hill. Blue line gives the grw table.

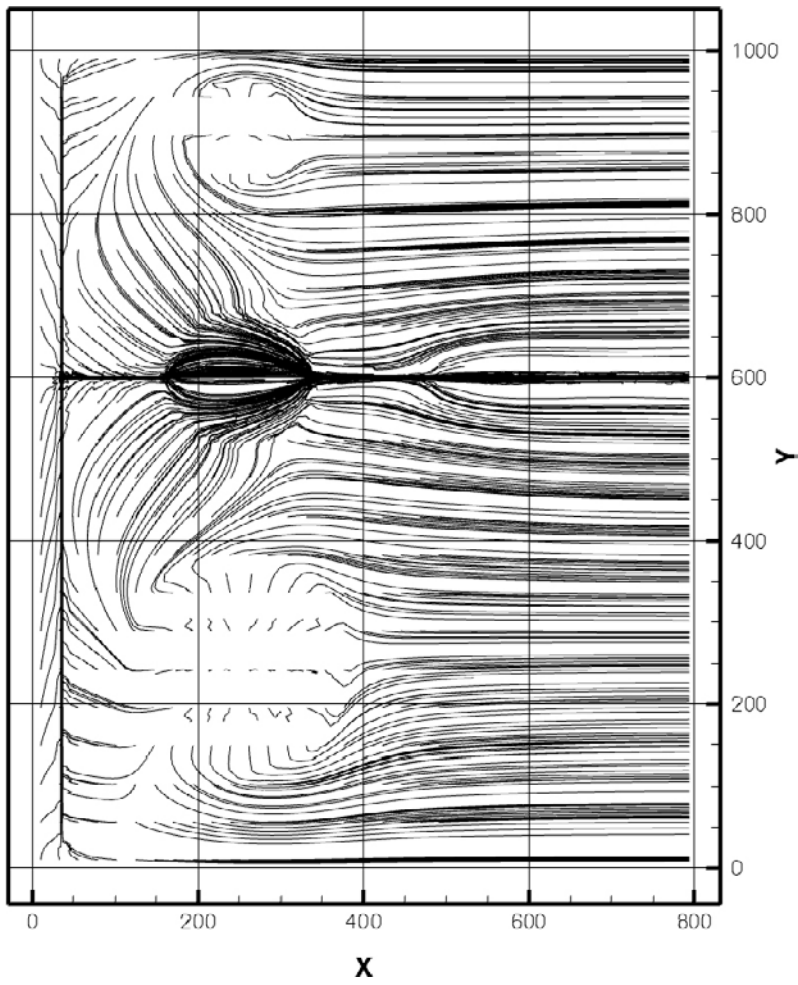


Figure De6-7. Trajectories of raindrops uniformly introduced on the square $x: 0 \rightarrow 500$ m, $y: 0 \rightarrow 1,000$ m.

Case De7: Glaciation

Introduction

It is anticipated that spent nuclear fuel will be stored in deep repositories. Even if a repository is located in a crystalline rock of low permeability a leak from the repository may find its way to the biosphere. The transport takes place in the fracture system in the rock. Future climate changes may change both the fracture system and the flow within it and it is thus important to assess the magnitude and effects of these expected future impacts on a repository.

In this demo case the transient response due to an advancing inland ice will be studied. We will keep the same domain size (1·1·1 km³) as for other demo cases even if it is realized that a much larger domain is needed for realistic results.

The case will build upon demo case De2 “transport from a canister to ground level”. The flow rate through the fracture that crosses the canister will be studied as the ice passes.

Objectives

The study has the following objectives:

- Illustrate how an advancing inland ice can be simulated in DarcyTools.
- Relate the ice movement to the flow around a canister; this is expected to be an issue of importance.

The situation considered

As mentioned, the starting point for the set-up is case De2 and the reader is hence referred to this case for full details about the set-up.

In Figure De7-1, the ice-front movement is illustrated as well as the zones and fracture close to the canister. We see that two vertical fracture zones, built up of many small fractures, are connected by a smaller fracture that is in contact with the canister. The smaller fracture is given a transmissivity of 10⁻⁷ m²/s. It is the flow through the small fracture that will be studied as the ice front passes the domain.

The ice is assumed to advance with a speed of 100 metres/year. The icefront has an angle of 45° to the coordinate axes and hence enters the domain in the upper left corner. The shape is given by the following equation:

$$h = H \cdot \left(1 - \left(\frac{x}{L} \right)^{\frac{4}{3}} \right)^{\frac{3}{8}}$$

Where h is the ice sheet elevation, x the distance from the ice sheet centre, H the ice thickness at the centre and L the length of the ice sheet.

Results

The pressure and flow are illustrated in Figure De7-2. In the vertical section we have a maximum pressure head of 320 metres which of course is due to the ice load. Flow vectors are shown for the small fracture that crosses the canister. The black area results from the increased resolution around the canister.

The main result of the case is the flux through the small fracture versus time shown in Figure De7-3. The flux increases from 0.05 to 3 litres/hour due to the advancing ice.

Running the case

The following steps should generate the results just described:

1. Copy cifstep1.xml to cif.xml and issue the commands RUNGGN and RUNFGN. This first grid is a coarse grid without any removed cells. The fracture network is generated and isolated fractures are removed. We only need to do this once and we therefore store the network in a file called “fractures”.
2. Copy cifstep2.xml to cif.xml and prpgenstep1.f to prpgen.f. Issue the command BLDMYPGN.
3. Next issue the command RUNMYPGN. A file, DE7RRC, is created which has information about cell removal and grid refinement.
4. RUNGGN is next; now the grid is refined and cells removed.
5. The fracture network is represented in the new grid by RUNFGN.
6. Repeat steps 3 to 5 in order to converge the process. Three times are probably enough.
7. Copy prpgenstep2.f to prpgen.f and issue the commands BLDMYPGN and RUNMYPGN.
8. The grid and property files are now generated. As the case involves FIF we need to issue BLDMYDTS and RUNMYDTS, in order to start the simulation.

Conclusion

It has been shown how an advancing inland ice front can be simulated in DarcyTools. The ice movement has been related to the flow around a canister.

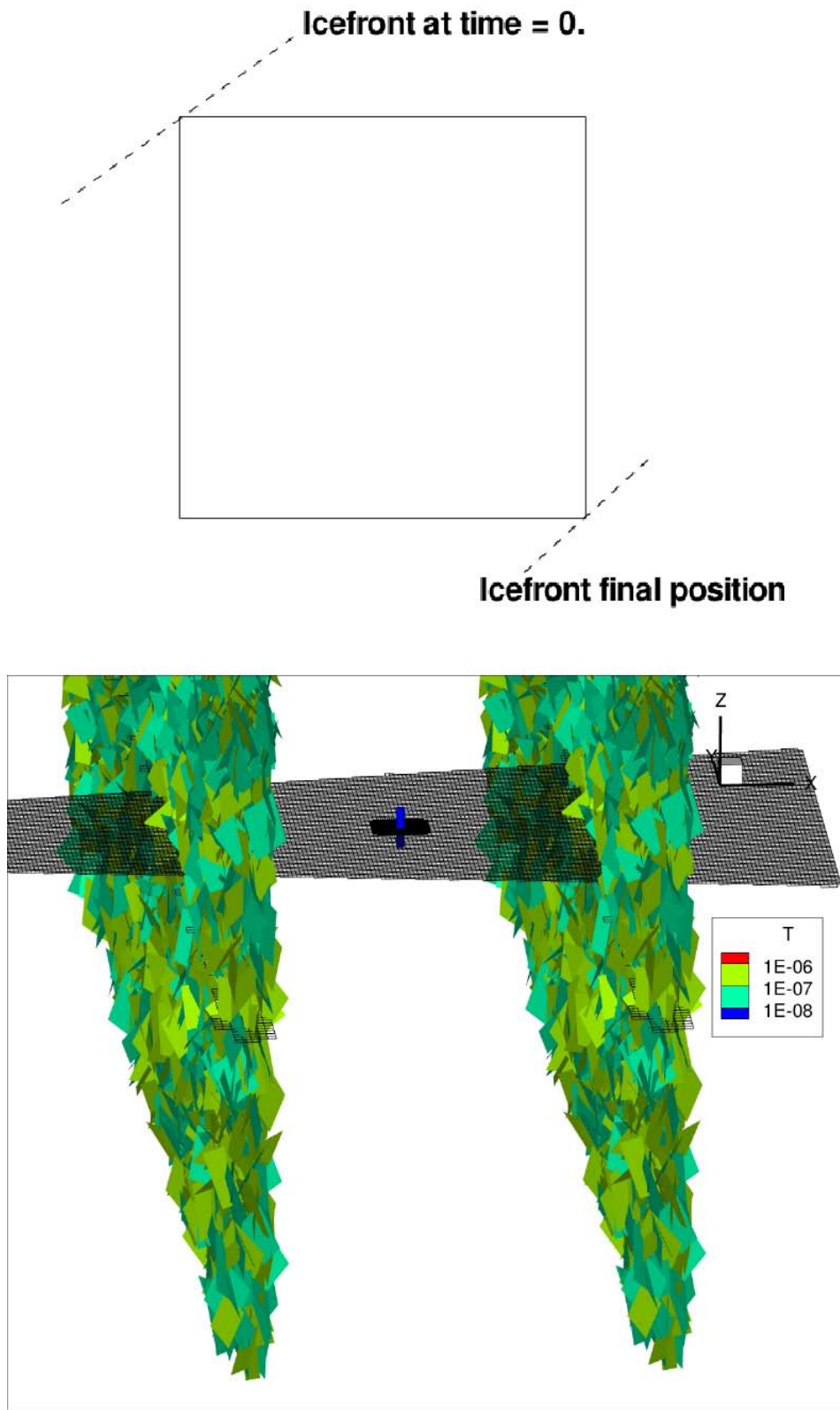


Figure De7-1. The movement of the icefront (top) and the fracture system around the canister.

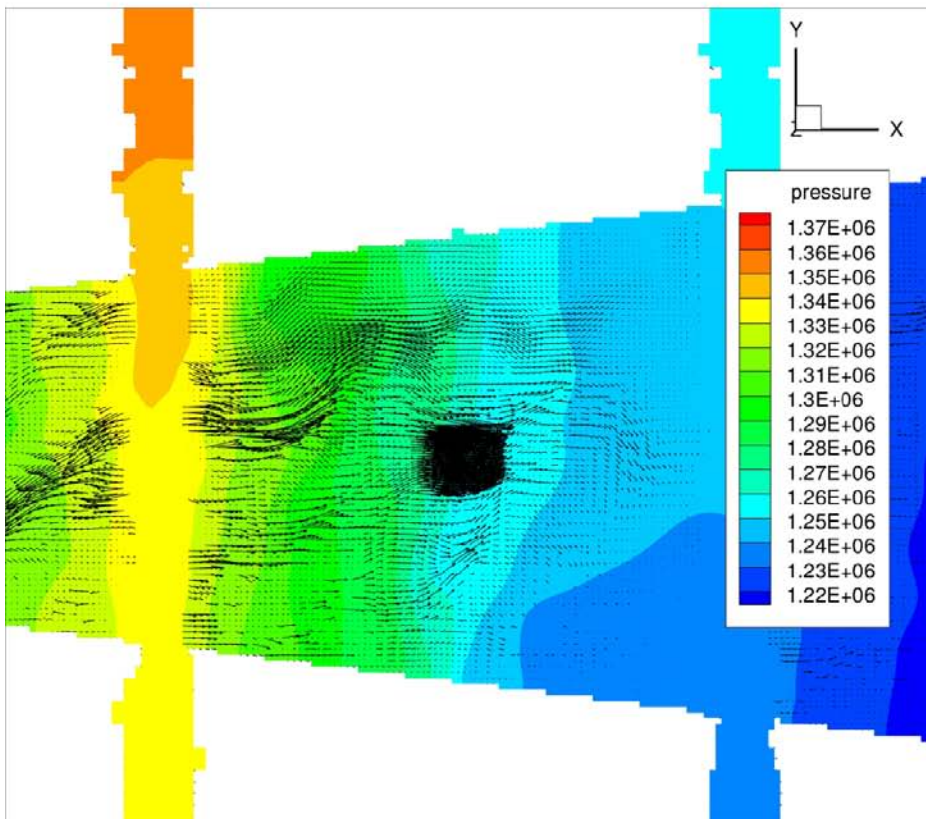
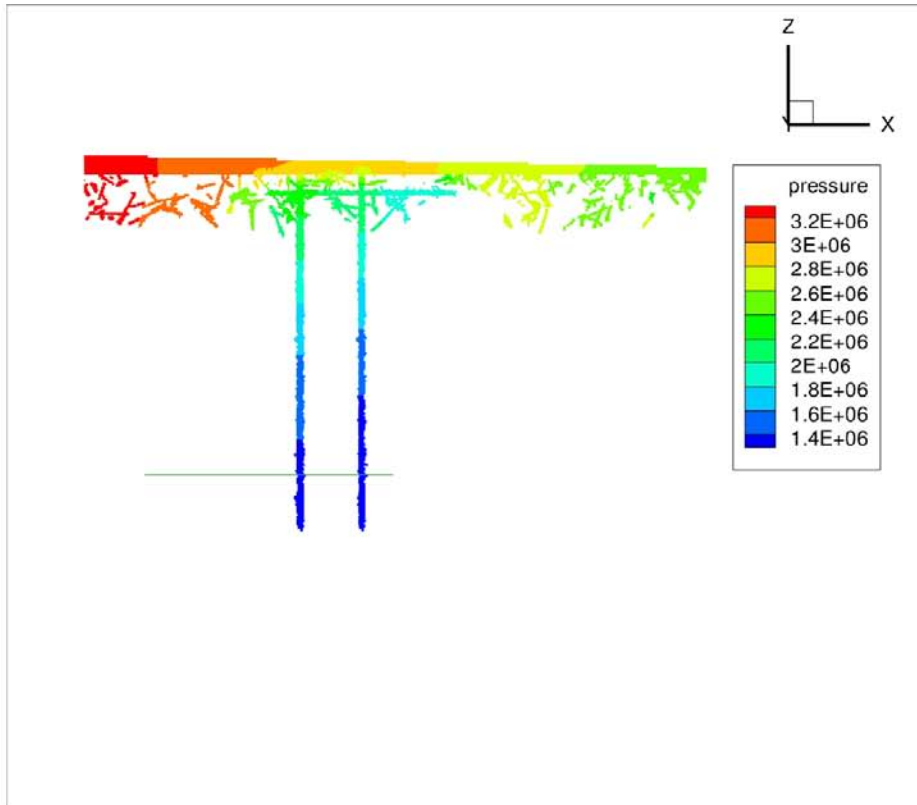


Figure De7-2. Pressure distribution (top) and flow and pressure around the canister.

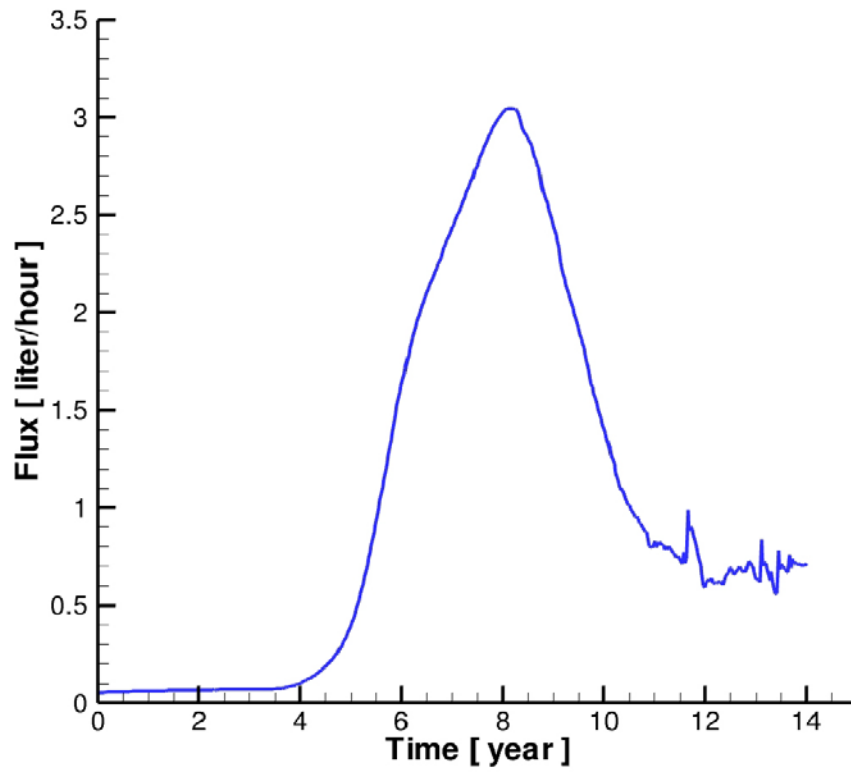


Figure De7-3. The flux through the fracture that crosses the canister, as a function of time.